Crowded field spectroscopy and the search for intermediate-mass black holes in globular clusters

Sebastian Kamann
Leibniz-Institut für Astrophysik Potsdam (AIP)

Dissertation
zur Erlangung des akademischen Grades
doctor rerum naturalium (Dr. rer. nat.)
in der Wissenschaftsdisziplin Astrophysik

Eingereicht an der Mathematisch-Naturwissenschaftlichen Fakultät
der Universität Potsdam

Potsdam, den 06. Februar 2013

Abstract

Globular clusters are dense and massive star clusters that are an integral part of any major galaxy. Careful studies of their stars, a single cluster may contain several millions of them, have revealed that the ages of many globular clusters are comparable to the age of the Universe. These remarkable ages make them valuable probes for the exploration of structure formation in the early universe or the assembly of our own galaxy, the Milky Way. A topic of current research relates to the question whether globular clusters harbour massive black holes in their centres. The attention that is drawn to this question results from the firm evidence that exists for even more massive black holes, so-called supermassive black holes, residing in the centres of galaxies. The black holes that are assumed to reside in globular clusters would therefore bridge the gap from stellar mass black holes, that represent the final stage in the evolution of massive stars, to supermassive ones. For this reason, they are referred to as intermediate-mass black holes.

The most reliable method to detect and to weigh a black hole is to study the motion of objects inside its sphere of influence. The measurement of Doppler shifts via spectroscopy allows one to carry out such dynamical studies. However, spectroscopic observations in dense stellar fields such as Galactic globular clusters are challenging. In astronomical observations stars do not appear point-like, but with a finite width given by the point spread function (PSF). The PSF is the result of the diffraction processes that the starlight encounters on its way through the earth' atmosphere and the telescope. In dense stellar fields, these processes cause the images of the individual stars to overlap in the observed data. As classical spectroscopy does not preserve any spatial information, it is impossible to separate the spectra of overlapping stars and to measure their velocities. Yet methods have been developed to perform imaging spectroscopy. The most widely used technique in this respect is integral field spectroscopy, where a continuous area on the sky is covered by a dense grid of spectra. This results in a three-dimensional data structure in which every spatial pixel contains an entire spectrum. As shown in this work, such data allows one to reconstruct the PSF and thus to deblend overlapping objects.

In the course of this work, the first systematic study on the potential of integral field spectroscopy in the analysis of dense stellar fields is carried out. To this aim, a method is developed to reconstruct the PSF from the observed data and to use this information in the extraction of the stellar spectra. Based on dedicated simulations, predictions are made on the number of stellar spectra that can be extracted from a given data set and the quality of those spectra. Furthermore, the influence of uncertainties in the recovered PSF on the extracted spectra are quantified. The results clearly show that compared to traditional approaches, the new method makes a significantly larger number of spectra accessible to a spectroscopic analysis. This systematic study goes hand in hand with the development of a software package to automatize the individual steps of the data analysis: the reconstruction of the PSF, the determination of the positions of the stars and finally the extraction of the stellar spectra. In particular with regard to the latter step, the usage of advanced algebraic algorithms allows for a very efficient analysis of the data.

The second part of this work centres around the application of the method to data of three Galactic globular clusters, M3, M13, and M92, observed with the PMAS integral field spectrograph at the Calar Alto observatory in Spain. The aim of these observations is to constrain the presence of intermediate-mass black holes in the centres of the clusters based on an analysis of the kinematics of the stars in the direct vicinities of the cluster centres. This is only possible if a sufficiently large sample of stars is probed kinematically. The application of the new analysis method yields samples of about 80 stars per cluster. These are by far the largest spectroscopic samples that have so far been obtained in the centre of any of the three clusters. In the course of the further analysis, Jeans models are calculated for each cluster that predict the velocity dispersion based on an assumed mass distribution inside the cluster. The comparison to the observed velocities of the stars shows that in none of the three clusters, a massive black hole is required to explain the observed kinematics. Instead, the observations rule out any black hole in M13 with a mass higher than 13 000 solar masses at the 99.7% level. For the other two clusters, this limit is at significantly lower masses, namely 2 500 solar masses in M3 and 2 000 solar masses in M92. In M92, it is possible to lower this limit even futher by a combined analysis of the extracted stars and the unresolved stellar component. This component consists of the numerous stars in the cluster that appear unresolved in our data. The final limit of 1 300 solar masses is the lowest limit obtained so far for any massive globular cluster.

Zusammenfassung

Kugelsternhaufen sind dichte, gravitativ gebundene Ansammlungen von teilweise mehreren Millionen Sternen, die ein fester Bestandteil jeder massiven Galaxie sind. Aus der Untersuchung der Kugelsternhaufen in unserer Milchstraße weiß man, dass das Alter von vielen dieser Objekte vergleichbar ist mit jenem des Universums. Dieses hohe Alter macht sie zu wertvollen Forschungsobjekten, beispielsweise um die Entstehung der Milchstraße und die Strukturbildung im frühen Universum zu verstehen. Eine aktuelle wissenschaftliche Fragestellung befasst sich damit, ob Kugelsternhaufen massive schwarze Löcher in ihren Zentren beherbergen. Die Bedeutung dieser Frage ergibt sich daraus, dass es eindeutige Hinweise darauf gibt, dass sich extrem massereiche, sogenannte supermassive schwarze Löcher, in den Zentren von Galaxien befinden. Jene schwarzen Löcher, die in den Zentren von Kugelsternhaufen vermutet werden, würden daher eine Brücke von den stellaren, die durch den Kollaps massereicher Sterne entstehen, zu den supermassiven schwarzen Löchern schlagen. Man bezeichnet sie daher auch als mittelschwere schwarze Löcher.

Die sicherste Diagnostik, um schwarze Löcher zu detektieren und ihre Masse zu bestimmen ist, die Bewegung der Objekte innerhalb ihrer gravitativen Einflusssphäre zu vermessen. Spektroskopische Untersuchungen vermögen dies über die Dopplerverschiebung von Spektrallinien. Jedoch sind spektroskopische Untersuchungen in dichten stellaren Feldern wie Kugelsternhaufen schwierig. Aufgrund der Turbulenz in der Atmosphäre und dem endlichen Auflösungsvermögen des Teleskops erscheinen die Sterne in den Beobachtungen nicht punktförmig, sondern mit einer durch die Punktspreizfunktion (PSF) gegebenen Breite. In dichten stellaren Feldern führt dies dazu, dass die Sterne überlappen. Da klassische spektroskopische Verfahren jedoch nicht bildgebend sind, lassen sich die Beiträge der Einzelsterne zu einem beobachteten Spektrum nicht trennen und die Geschwindigkeiten der Sterne können nicht vermessen werden. Bildgebende spektroskopische Verfahren bieten jedoch die Möglichkeit, die PSF zu rekonstruieren und basierend darauf die Spektren überlappender Sterne zu trennen. Als Integralfeld-Spektroskopie bezeichnet man ein Verfahren, in dem ein Himmelsauschnitt mit einem dichten räumlichen Raster von Spektren beobachtet wird. Dadurch entsteht eine dreidimensionale Datenstruktur, in welcher jeder Bildpunkt ein komplettes Spektrum enthält.

Im Rahmen der vorgelegten Arbeit wird das Potential der Integralfeld-Spektroskopie in der Beobachtung dichter stellarer Felder zum ersten Mal systematisch analysiert. Hierzu wird eine Methodik entwickelt, die das Extrahieren von Einzelsternspektren über eine Rekonstruktion der PSF aus den vorhandenen Daten erlaubt. Anhand von Simulationen werden Voraussagen darüber gemacht, wie viele Sternspektren aus einem gegebenen Datensatz extrahiert werden können, welche Qualität diese Spektren haben und wie sich Ungenauigkeiten in der rekonstruierten PSF auf die Analyse auswirken. Es zeigt sich hierbei, dass die entwickelte Methodik die spektroskopische Analyse von deutlich mehr Sternen erlaubt als klassische Verfahren. Parallel zu dieser systematischen Studie erfolgt die Entwicklung einer dezidierten Analysesoftware, die folgende Schritte ausführt: die Bestimmung der PSF, die Messung der Positionen der einzelnen Sterne und schließlich die Extraktion aller zugänglichen Sternspektren. Insbesondere im letzten Schritt gelingt es, den Prozess mittels ausgereifter algebraischer Verfahren sehr effizient zu gestalten.

Im zweiten Teil der Arbeit wird die entwickelte Methodik auf Daten von drei Kugelsternhaufen angewendet, die mit dem PMAS Integralfeld-Spektrographen am Calar Alto Observatorium in Spanien aufgenommen wurden: M3, M13 und M92. Ziel dieser Beobachtungen ist es, anhand der Geschwindigkeiten der beobachteten Sterne Aussagen darüber zu treffen, ob sich mittelschwere schwarze Löcher in den Zentren der Haufen befinden. Dies ist nur möglich, wenn man eine große Anzahl von Sternen in der Nähe des Zentrums analysiert. Die Anwendung der Analysesoftware auf diese Daten liefert Spektren für eine Stichprobe von ungefähr 80 Spektren pro Kugelsternhaufen. Dies sind bei Weitem die größten spektroskopischen Stichproben, die je im Zentrum eines der drei Haufen beobachtet wurden. Im weiteren Verlauf der Analyse werden Jeans Modelle für jedes der drei Objekte gerechnet. Diese erlauben basierend auf einer angenommenen Massenverteilung innerhalb des Kugelsternhaufens eine Vorhersage der Geschwindigkeitsdispersion der Sterne. Der Vergleich mit den gemessenen Geschwindigkeiten zeigt, dass in keinem der drei Haufen ein schwarzes Loch benötigt wird, um die Dynamik der zentrumsnahen Sterne zu erklären. Im Gegenteil, die Beobachtungen können zu 99,7-prozentiger Sicherheit ausschließen, dass sich in M13 ein schwarzes Loch mit einer Masse größer 13 000 Sonnenmassen befindet. In den anderen beiden Haufen liegt diese Grenze noch bei deutlich geringeren Massen, nämlich bei 2 500 Sonnenmassen in M3 und 2 000 Sonnenmassen in M92. In M92 ist es außerdem möglich, das Limit noch weiter herabzusetzen durch eine zusätzliche Analyse der unaufgelösten stellaren Komponente. Diese Komponente besteht aus dem integrierten Licht all jener Sterne, die zu schwach und zahlreich sind als dass sie aus den verfügbaren Daten einzeln extrahiert werden könnten. Das entgültige Limit von 1 300 Sonnenmassen ist das geringste, welches bisher in einem massiven Kugelsternhaufen gemessen wurde.

Contents

Chapter 1

Introduction

Sebastian Kamann

ABSTRACT

Globular clusters are intriguing objects. Seen with the naked eye, they are indistinguishable from plain stars. But already the first observations with telescopes revealed a nebular structure. However, as telescopes grew larger, Charles Messier and William Herschel were able to resolve the nebulae into individual stars. This historical overview in a nutshell already illustrates a problem that astronomers still face today. The stellar densities in these massive star clusters are so high that it is challenging to separate one star from the other. Highly sophisticated observing and analysis techniques are required to unveil the true nature of the clusters, like their remarkably old ages or the peculiarities in their stellar populations. Still many questions remain unanswered. One of those concerns the presence of massive black holes in the cluster centres, formed from the matter left by dying stars. The detection of such black holes could help to explain how their even more massive counterparts located in the centres of galaxies formed.

In the following, a short review is presented on the current state of astrophysical research within the topic of this thesis. An overview is given on the fundamental properties of globular clusters, including formation scenarios, the connection to other galaxies apart from our own and the recent developments with regard to the stellar populations in the clusters. Afterwards, the focus is put on the peculiar kinematics of the cluster stars. Phenomena such as core collapse are described and an overview on the dynamical models developed for globular clusters is given. These models form the basis of the ongoing search for massive black holes. The status of this search, from the theoretical and the observational side, is presented. Towards the end of this introduction the current observational challenges are outlined with a clear focus on spectroscopy. This discussion on the prospects and current limitations of crowded field spectroscopy is not only valid for globular clusters but for crowded stellar fields in general.

1.1. Globular Clusters

The latest edition of the famous catalogue of Milky Way globular clusters by Harris (1996) lists 157 objects. New clusters are still being discovered, preferentially behind the dense clouds of gas and dust that shield our view towards the Galactic centre (e.g., Borissova et al. 2011). Throughout the last century globular clusters have been considered as some of the most intriguing building blocks of our Galaxy. They were a major argument in the Great Debate of 1920 – Harlow Shapley's idea that the Milky Way encompasses the whole unviverse was largely based on (overestimated) distance measurements of globular clusters. When the colour-magnitude diagrams of globular clusters became sufficiently deep to study their stellar populations (Arp et al. 1953; Sandage 1953), the scientific focus gradually changed from distances to ages. Sandage (1953) estimated a remarkable age of 5 Gyr for M3. In the following decades it became evident that globular clusters are the oldest objects for which reliable age measurements are feasible. Owing to this characteristic, they became the most important benchmark for the verification of cosmological models. Those had to yield ages that were at least comparable to those of the Galactic globular clusters. As both, the measured ages of the clusters and those predicted by the cosmological models, got narrowed down it turned out that the two are comparable (Riess et al. 1998; Perlmutter et al. 1999). This emphasizes the utter importance of globular clusters for our understanding of the early universe and the formation of the Milky Way. In the following, we review what is known about the clusters today and highlight some open questions.

1.1.1. The Galactic globular cluster population

While the clusters themselves were for a long time considered perfect examples for homogeneous stellar populations, differences in the chemical composition of the individual clusters have already been known ever since the pioneering work of Mayall (1946). Kinman (1959) and Morgan (1959) discovered a correlation between the metallicity of the clusters and their position relative to the Galactic plane. The objects that showed metal-rich spectra were concentrated towards low Galactic latitudes whereas clusters with metal-poor spectra were scattered throughout the halo of the Galaxy. From the analysis of the metallicities and kinematics of a large sample, Zinn (1985) concluded that the Galactic globular cluster population can be separated into two distinct subpopulations, with a transition happening at a metallicity of $[\mathrm{Fe/H}] \sim -0.8$. This dichotomy is illustrated in Fig. 1.1 that shows the distribution of known globular clusters, colour-coded with respect to their metallicity, in Galactic coordinates. Further evidence for a bimodality in the population of Galactic globular clusters comes from the analysis of their relative ages (Rosenberg et al. 1999; De Angeli et al. 2005; Marín-Franch et al. 2009). A large group of old coevally-formed clusters is complemented by a second group of relatively younger clusters with an intrinsic age spread, with the former group encompassing all metal-poor clusters.

The results suggest that metallicity is the main parameter that influences the properties of a globular cluster. This is, however, not the whole story as becomes evident from the so-called *second parameter problem*. It refers to the variety of horizontal-branch morphologies that is observed in clusters with compa-

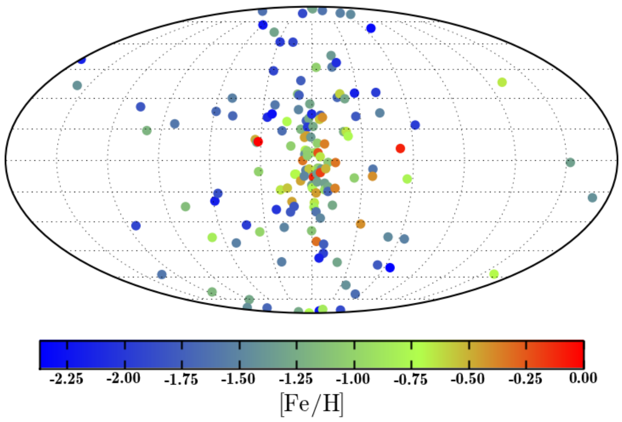

Fig. 1.1. The distribution of known galactic globular clusters in the Galactic coordinate system. The colour-coding of the datapoints that represent the individual clusters indicates their metallicity. Coordinates and metallicities are taken from the catalogue of Harris (1996).

rable metallicity. This phenomenon, first recognized from the peculiar properties of M13 (Arp 1955; Sandage & Wallerstein 1960), triggered an ongoing search for possible second parameters, including helium content (Johnson & Bolte 1998), density (Fusi Pecci et al. 1993) or mass (Recio-Blanco et al. 2006). Cluster age might be considered the most promising candidate (Sarajedini & King 1989; Dotter et al. 2010), but the increasing complexity that is revealed nowadays not only within the Galactic population but also within individual clusters (cf. Sec 1.1.3) shows that the reduction of the whole population of Galactic globular clusters to a few parameters involves a non-negligible degree of simplification.

1.1.2. Globular clusters as probes of galaxy growth

It was mentioned already that owing to their ages, globular clusters are valuable for cosmology. But this is not the whole story. The history of the mass assembly of a galaxy is partly conserved in the properties of its system of globular clusters. As massive star clusters, they must have formed during the epochs of massive star formation. Furthermore, their ages imply that they are able to survive over a Hubble time without being disrupted by the tidal forces of the host galaxy. While the system of our own Galaxy can be studied in great detail, it only provides insight into a single galaxy. However, large globular cluster systems are ubiquitous in massive galaxies and smaller systems have been detected in a number of local dwarf galaxies (see review by Brodie & Strader 2006). The study of extragalactic globular clusters has revealed some remarkable analogies between the individual systems, not only with respect to their ages (e.g., Cohen et al. 1998) or luminosity functions (Harris 2001) but also concerning the bimodality between a red and a blue subpopulation (Zepf & Ashman 1993; Gebhardt & Kissler-Patig 1999; Larsen et al. 2001). Like in the Milky Way, evidence has been found that the two branches possess distinct kinematics (Kissler-Patig & Gebhardt 1998; Harris 2001; Côté et al. 2003) or distributions (Geisler et al. 1996; Kissler-Patig et al. 1997).

To explain the bimodality in the system of Galactic globular clusters, Searle & Zinn (1978) proposed a scenario in which the tightly bound clusters at small galactocentric distances were formed in-situ, i.e., during the collapse of the protogalaxy, while the loosely bound clusters of the outer halo were assembled over a larger timespan. Many of the more recent works on the formation of globular clusters discuss similarly bimodal approaches, but usually different scenarios are assumed nowadays for the red and the blue branch of the population, respectively.

The formation of globular clusters in the proto-galactic clumps suggested by Searle & Zinn in the framework of a hierachichal model of galaxy formation was discussed by Peebles (1984) who associated globular clusters with the first halos that condense at high redshift, with gas masses $\sim 10^6 M_\odot$. Such halos would later build up the Galaxy via subsequent merging. Such a scenario is supported by cosmological simulations (e.g. Moore et al. 2006). The evidence against dark matter halos around globular clusters (e.g. Moore 1996; Baumgardt et al. 2009) can be explained because such halos are likely to be removed over a Hubble time (Mashchenko & Sills 2005; Baumgardt & Mieske 2008).

In the cosmological ΛCMD model, the successive build-up of the halo suggested by Searle & Zinn can be attributed to the accretion of satellite galaxies (Abadi et al. 2006). In this picture, a fraction of the globular cluster population in a galaxy would directly relate to the accretion event, either because new clusters are formed during the event (Hilker et al. 1999), or because the dense parts of the satellite are stripped of their surroundings. Observational evidence for the latter scenario is given, e.g., by the location of M54 in the core of the Sagittarius stream (Ibata et al. 1994; Layden & Sarajedini 2000). Mackey & Gilmore (2004) and Forbes & Bridges (2010) estimate that about 1/4 of the Galactic globular cluster population has extragalactic origin. Furthermore, Cote et al. (1998) showed that the observed colour bimodality can be reproduced under the assumption that the metal-poor cluster are accreted whereas the metal-rich clusters constitute the initial population of a massive galaxy. Intriguingly, cosmological models favour the inverse behaviour, namely an in-situ or pre-galactic origin of the metal-poor component (Moore et al. 2006; Brodie & Strader 2006).

The assembly of globular clusters with extragalactic origin does not necessarily need to involve the accretion of dwarf galaxies. Kissler-Patig et al. (1999) suggested a scenario in which the central elliptical in a galaxy cluster "steals" globulars from neighbouring galaxies via tidal stripping.

Galaxy merging has also been proposed as a formation channel for the red (metal-rich) subpopulation by Ashman & Zepf (1992). The formation of young massive clusters that is observed in major mergers such as the Antennae (Whitmore & Schweizer 1995) provides evidence for this scenario, although it is still a matter of debate whether these clusters will resemble globular clusters after evolving for a Hubble time (Brodie & Strader 2006). The attractiveness of the merger scenario is obvious as it allows one to directly use the globular cluster population as a tracer of a galaxy's star formation history. For example, in the massive elliptical galaxy NGC 1316 the population of intermediate-age globular clusters was used by Goudfrooij et al. (2001) to date a merger that is suggested by the morphology of the galaxy ~3 Gyr in the past. However, the importance of merging for the properties of a globular cluster population is not established. Striking cases like NGC 1316 are rare and there are some puzzling differences in the specific frequencies of globular clusters in spiral or elliptical hosts that seem at odds with the merger scenario (Harris & van den Bergh 1981; Forbes et al. 1997).

The current picture on the formation of globular clusters might be summarized in saying that several scenarios have been

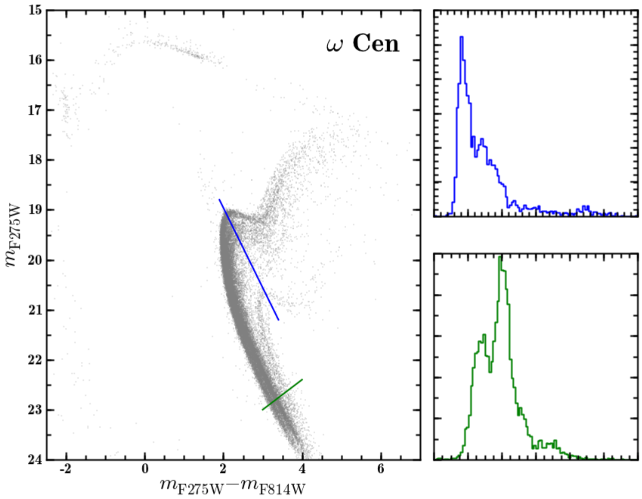

Fig. 1.2. The complex stellar populations of ω Centauri. A UV-IR colour-magnitude diagram is shown in the large panel to the left. For two representative regions marked by solid lines, we show a histogram of the distribution of the stars along the lines in the smaller panels to the right. (Figure prepared using data taken from the publication of Bellini et al. 2010).

proposed that, taken by themselves, have trouble in explaining the full spectrum of observed properties and that a definite answer on the importance of the different scenarios is still missing.

1.1.3. Stellar populations

New clues on the formation of globular clusters might come from the detailed study of their stellar populations. For several decades, globular clusters were considered the best examples for simple stellar populations, created in a single star-formation event several giga-years in the past (Renzini & Fusi Pecci 1988). The most massive cluster in the Galaxy, ω Centauri, has always been a notable exception. Not only did its population of stars show an intrinsic spread in abundances (Cannon & Stobie 1973; Freeman & Rodgers 1975), also its internal structure (Norris et al. 1997) or retrograde orbit (Dinescu et al. 1999) separated it from the remaining population of Milky Way clusters. The bulk part of the observations can be explained under the assumption that ω Centauri is the remnant of an accreted dwarf galaxy (e.g. Bekki & Freeman 2003), a scenario that also served as an explanation for its peculiarity with respect to the other clusters.

A colour-magnitude diagram of this remarkable cluster is presented in Fig. 1.2. Some striking features are clearly visible, such as three distinct main sequences (Anderson 1997; Bedin et al. 2004) or the complex morphology around the turn-off, showing evidence of four different stellar groups (Villanova et al. 2007). With respect to the main sequence splitting, it is worth noting that the bluer of the two principal main sequences is more metal-rich than its redder counterpart (Piotto et al. 2005), an observation that can only be explained by assuming significant helium enrichment in the blue main sequence.

Recent results suggest, however, that ω Centauri is not so distinct from the rest of the Galactic globular clusters after all. It might just be the most extreme case among a population that is more complex than previously thought. Studies based on photometry obtained with the *Hubble* space telescope (HST) have been very successful in identifying multiple populations in Galactic globular clusters. Evidence based on a split or a broadening of the main sequence was found in, e.g., NGC 2808 (Piotto et al. 2007) or 47 Tuc (Anderson et al. 2009; Milone et al. 2012b). Furthermore, in a larger sample of clusters including M54 (Sarajedini & Layden 1995), NGC 1851 (Milone et al. 2008) or NGC 6388 (Moretti et al. 2009, using ground-based observations with adaptive optics) the complex morphology of the (sub)giant branch clearly indicates the presence of more than a single stellar population. Recent results suggest that similar features are quite common in the colour-magnitude diagrams of globular clusters (Piotto et al. 2012).

Another piece of evidence for the complexity of the stellar populations in globular clusters comes from spectroscopy, relating the peculiarities observed in the colour-magnitude diagrams to variations in individual elements. Quantitative spectroscopy revealed that intrinsic variations in the overall metallictity of the cluster stars are indeed restricted to some, usually massive clusters, such as ω Centauri (Gratton et al. 2004; Carretta et al. 2009a). On the other hand, variations in light elements seem to be almost ubiquitous in the Galactic population. The best-known example for such variations is the Na-O anticorrelation (e.g. Carretta et al. 2009b; Gratton et al. 2012). The observation of this anticorrelation in unevolved stars by Gratton et al. (2001) showed that it is not a result of stellar evolution. Instead, it strongly suggests a scenario in which the clusters experienced at least two bursts of star formation, with the second-generation stars forming from the gas enriched by the first population. Hydrogen burning at high temperatures will enrich the cluster with sodium at the cost of oxygen (Denisenkov & Denisenkova 1989), thus explaining the anticorrelation. Remarkably, the enriched stars seem to represent the major part of the cluster population (Carretta et al. 2009b). To explain such a high degree of enrichment, it is suggested that the clusters were much more massive at the time of formation (Bekki & Norris 2006; D'Ercole et al. 2008). The loss of stars from the first population is then an attractive possibility to build the Galactic stellar halo (Baumgardt et al. 2008), even though today only a few percent of the halo stars are within globular clusters (Freeman & Bland-Hawthorn 2002).

Based on the ubiquity of the anticorrelations in light elements, a new definition for globular clusters has been proposed by, e.g., Carretta et al. (2010), in the sense that globular clusters are those star clusters that show an anticorrelation. Indeed, currently the challenge seems to find globular clusters that are genuine single stellar populations. A promising candidate in this respect is Ruprecht 106 (Geisler & Villanova 2012).

1.2. Globular cluster dynamics

The high stellar densities of up to $10^5 M_\odot/{\rm pc}^3$ in globular clusters has drawn the attention of astronomers to their internal dynamics early on. Dynamical models are constructed to describe the complex dynamics. Furthermore, the effects of dynamical evolution are investigated, such as two-body relaxation, core collapse, the disruption and creation of binaries or the formation of massive black holes. An overview on these phenomena will be given in the following.

1.2.1. Relaxation

A direct consequence of the large stellar densities is that each star in the cluster will have experienced plenty of gravitational encounters with other cluster members over its lifetime. These encounters cause the stars to “loose the memory” about their

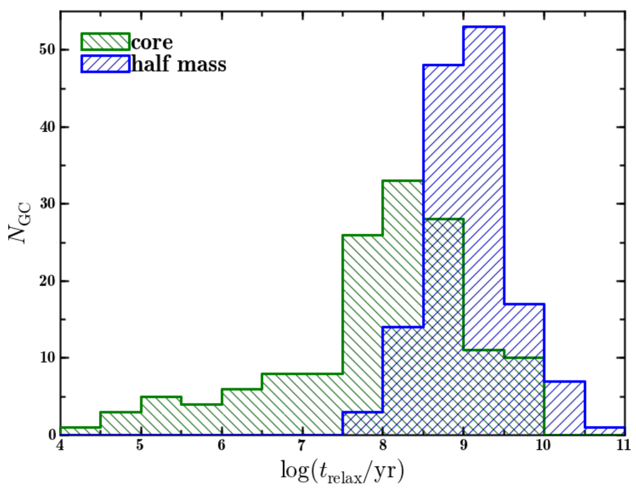

Fig. 1.3. Relaxation times of Galactic globular clusters. The green histogram depicts the relaxation times in the cluster cores, the half-mass relaxation times are shown as a blue histogram. The data is taken from the catalogue of Harris (1996).

initial velocities, a process known as relaxation. A simple formula can be derived to estimate the relaxation time of a star, as a function of its velocity v, the number N of stars in the cluster and the cluster radius R (Binney & Tremaine 2008):

$$t_{\mathrm{relax}} = \frac{0.1N}{\ln N} \cdot \frac{R}{v} \,. \tag{1.1}$$

Assuming typical values of $N = 10^6$ stars, a truncation radius of $r_{\mathrm{t}} = 30\mathrm{pc}$ and a velocity dispersion of $\sigma = 5\mathrm{km/s}$ yields a relaxation time of 40 Gyr. This simple calculation neglects that the number of gravitational encounters a stars experiences depends on its location inside the cluster. Stars inside the highly crowded centre will have drastically shorter relaxation times compared to those on wide orbits. To illustrate this, the distribution of relaxation times of Galactic globular clusters inside the core and the half-mass radius is shown in Fig. 1.3. The core radius r_{c} is defined as the radius where the surface brightness drops to half its central value, the half-mass radius r_{h} includes half of the total cluster mass. Typical values in the Galaxy are $r_{\mathrm{c}} = 1\mathrm{pc}$ and $r_{\mathrm{h}} = 3\mathrm{pc}$ (Binney & Tremaine 2008). As expected, the relaxation times in the core are shorter than those inside the half-mass radius. The fact that all cluster have core relaxation times $< 10\mathrm{Gyr}$ and that the half-mass relaxation times exceed 10 Gyr only in a few massive clusters (like ω Centauri or NGC 2419) shows that Galactic globular clusters experienced significant relaxation over their lifetime. Note that the relaxation times depicted in Fig. 1.3 were not calculated using the simple estimate of Eq. 1.1 but are based on kinetic theory (see Spitzer 1987).

A direct consequence of relaxation is mass segregation. The gravitational encounter between two stars tends to redistribute the kinetic energy equally among the counterparts. Thus, a more massive star will on average be decelerated and sink towards the centre while a less massive star will be accelerated onto a wider orbit. The amount of mass segregation that is observed (e.g. King et al. 1995, in NGC 6397) is in good agreement with theoretical predictions. Another effect of energy equipartition in gravitational encounters is that the amount of stars removed from the cluster over its lifetime, e.g. via tidal stripping, is a function of stellar mass, with low-mass stars being preferentially stripped (e.g. Vesperini & Heggie 1997).

From an observers point of view, the relation between relaxation and a possible anisotropy in the velocity distribution of the stars deserves special attention. For example, an increase in radial anisotropy towards the centre of a cluster can mimic the presence of a massive black hole (Binney & Mamon 1982). Though possible, constraining the anisotropy profile from observations is challenging, therefore predictions from theory are particularly helpful. On the one hand, it is known that relaxation diminishes existing anisotropies with time (Fall & Frenk 1985). On the other hand, new anisotropies can be induced by relaxation, e.g. via the scattering of low-mass stars on radial orbits (Hénon 1971). Simulations of isolated clusters seem to confirm that radial anisotropy develops as a consequence of relaxation. However, more realistic simulations that take the loss of stars due to tidal effects into account (Giersz & Heggie 1997; Takahashi & Lee 2000; Baumgardt & Makino 2003) show that any induced anisotropy stays small and is restricted to the outer envelope of the cluster.

The most drastic effect of relaxation is core collapse, the result of a gravo-thermal instability. A rather intuitive explanation for this phenomenon was formulated by Antonov (1962) and later expanded by Lynden-Bell & Wood (1968). In a globular cluster the core is "hotter" than the halo, in the sense that the velocity dispersion rises inwards. Now relaxation will cause a heat flow directed outwards as stars that gain energy in two-body interactions are scattered onto wider orbits. At the same time, stars that loose kinetic energy fall deeper into the potential well, thereby accelerating again and causing a gradual collapse of the core. The cluster core has negative heat capacity, it looses energy while getting hotter. Under certain conditions this apparent paradox can increase the temperature difference between core and halo, leading to an enhancement of the collapse. A review of the work that has been done over the last decades on the details of core collapse is beyond the scope of this work and can be found, e.g., in Meylan & Heggie (1997). Observationally, the most striking evidence for a core collapse is the power-law like increase in the central surface brightness profiles observed in some Galactic globular clusters, such as M15 or NGC 6293 (Trager et al. 1995; Noyola & Gebhardt 2006).

1.2.2. Binarity

The distribution of relaxation times depicted in Fig. 1.3 suggests that a large fraction of the Galactic globular cluster population should show evidence of core collapse. Yet the fraction of cluster that have undergone core collapse is only ~20% (Djorgovski & King 1986). Goodman & Hut (1989) suggested that initial binaries affect the evolution of core collapse. Binaries will on average segregate towards the centre as a consequence of their relatively large mass where they act as a heat source. In superelastic scattering processes kinetic energy is transferred to the single star and the binary binding energy is increased. This "binary burning" phase can delay the onset of core collapse significantly (e.g. Fregeau et al. 2003). As core collapse proceeds, binaries get accumulated in the core and binary-binary encounters become more important. These provide yet another heat source that is capable of stopping the collapse (e.g. Gao et al. 1991).

Binary-binary interactions tend to reduce the binary fraction, primarily via destruction of one participant (e.g. Mikkola 1983; Hut et al. 1992b). Additionally, remaining binaries might be scattered onto larger orbits or experience coalesce to form a single star (Bacon et al. 1996). On the other hand, formation scenarios for binaries exist in the form of tidal capture (Fabian et al. 1975) or three-body interactions. This may result in a equilibrium state characterized by the formation and destruction of binaries.

The strong influence that binary stars likely have on the outcome of core collapse shows their importance for the overall evolution of globular clusters. Additional evidence for the importance of binaries comes from the observed population of blue stragglers in globular clusters. The formation scenarios that are evoked for these peculiar objects, namely mass overflow from a companion or stellar mergers, both require binarity. However, it was for a long time assumed that primordial binaries are absent in globular clusters. Early radial velocity studies such as the one by Gunn & Griffin (1979) in M3 did not result in the detection of spectroscopic binary stars. Those were detected, however, in follow-up observations (Pryor et al. 1988, also see Hut et al. 1992a for a review).

Recent studies of the binary fraction are mainly based on HST photometry (e.g. Milone et al. 2012a, and references therein). The photometric detection relies on the fact that binaries are unresolved at the distance of a globular cluster and therefore appear redder than single stars of equal brightness. The binary fraction might thus be estimated from the asymmetric scatter of stars on the red and blue side of the main sequence. Spectroscopic studies are challenging because of the highly crowded stellar fields that must be observed. For this reason, they have so far been limited to less dense clusters, such as M4 (Sommariva et al. 2009). On the other hand, they offer the possibility to make the desirable change from pure fractions to orbital parameters in the future.

All studies are consistent with binary fractions that are significantly lower than in the field or in open clusters, where detected frequencies typically exceed 50% (Duquennoy & Mayor 1991). Only a minority of the Galactic globular cluster population has binary fractions higher 20% (Sollima et al. 2007) and in many clusters, the detection rates are below 10%. However, the reason for this is probably not that the initial binary fractions in globular clusters were low. Instead, current simulations such as those by Ivanova et al. (2005) that take stellar evolution into account require very high initial fractions up to 100% in order to explain the observed ones. The reason for this is that the dynamical processes that are at work will destroy many binaries over several giga-years of cluster evolution. The destruction of binaries involved in interactions with other binaries was already mentioned. Furthermore, soft binaries, defined as those with orbital velocities smaller than the velocity dispersion of the cluster, will already be disrupted in interactions with single stars. Finally, stellar evolution provides another path for binary destruction, e.g. via supernova explosions or common envelope phases.

1.2.3. Massive black holes

The idea that globular clusters may host massive black holes has fascinated astronomers for decades. Initially they were suggested in order to explain the excess of central light observed in some surface brightness profiles (Wyller 1970; Peebles 1972) or the detection of X-ray sources in the clusters (Bahcall & Ostriker 1975). Nowadays, it is well established that core collapse and the evolution of dense binary stars are the responsible mechanisms for those phenomena. But still the search for the black holes has lost nothing of its appeal.

Several mechanisms for the formation and growth of massive black holes have been proposed. Miller & Hamilton (2002) studied the possibility that an initial seed with a mass $\sim 50M_\odot$ gradually grows to masses $\sim 10^3M_\odot$ via mergers with stellar mass black holes. The timescale of this growth process is comparable to the lifetime of a globular cluster, i.e. several giga-years. The possibility to grow a black hole of similar mass on a much shorter timescale $\sim$10 mega-years via runaway merging of stellar-mass black holes was investigated by Mouri & Taniguchi (2002). On the other hand, Portegies Zwart & McMillan (2002) argued for the direct formation of a black hole with $\sim 10^3M_\odot$ following the runaway merging of massive stars in dense clusters with short relaxation times. A pitfall of the latter scenario might be that from the viewpoint of stellar evolution, stars as massive as those resulting from runaway mergers are poorly understood. It is well possible that stellar winds constrain the resulting black hole to somewhat smaller masses (e.g. Glebbeek et al. 2009).

Clearly, the presence of a massive black hole in its centre will influence the dynamical evolution of a globular cluster. It might also imprint its presence on observable properties of a cluster. Bahcall & Wolf (1976) investigated the stellar density in the vicinity of the black hole in a purely analytical way and found it to have a power law cusp, $n(r) \propto r^\gamma$, with $\gamma = -7/4$. The same result can be obtained from a consistency argument by requesting that the gravitational energy released by stars swallowed by the black hole must be carried outwards via relaxation (Shapiro & Lightman 1976; Binney & Tremaine 2008). Numerical simulations yield consistent results (e.g. Cohn & Kulsrud 1978). However, as demonstrated by Baumgardt et al. (2005), the power-law cusp present in the surface brightness profile might be significantly shallower than expected from the projected stellar density ($\gamma = -3/4$). An effect attributed to mass segregation and the resulting overabundance of dark stellar remnants near the centre. On the other hand, Gill et al. (2008) find that mass segregation is efficiently suppressed in clusters harbouring a massive black hole because the black hole "reheats" massive stars that have sunk to the centre. The central surface brightness slope has been identified as a valuable tracer for the presence of massive black holes by Miocchi (2007) or Noyola & Baumgardt (2011). However, it is still a matter of debate whether the presence of a shallow surface brightness cusp requires a black hole (as argued by Noyola & Baumgardt) or not (see Vesperini & Trenti 2010).

Not only the central behaviour of the surface brightness profile is suggested as a tracer for a massive black hole, also its overall shape. The black hole can efficiently prevent the cluster from core collapse because it represents an additional central heat source. Based on this idea, Trenti et al. (2007) predict that the host clusters will have a large ratio of core to half-light radius. However, Hurley (2007) and Noyola & Baumgardt (2011) find similar ratios in simulated clusters without black holes.

An photometric tracer not related to the surface brightness profile was suggested by Miocchi (2007), namely the existence of extreme horizontal branch stars. The tidal forces during close encounters with the black hole are assumed to strip the outer shell of giant stars and reveal the hotter internal layers in this scenario.

So far, only indirect tracers for the existence of massive black holes have been mentioned. To prove the existence or absence of a black hole beyond doubt requires direct constraints. The observation of the dynamics of the cluster stars is the most promising possibility in this direction. Those studies are the subject of Sect. 1.3. Before, dynamical models are introduced as they are of fundamental importance for meaningful dynamical studies.

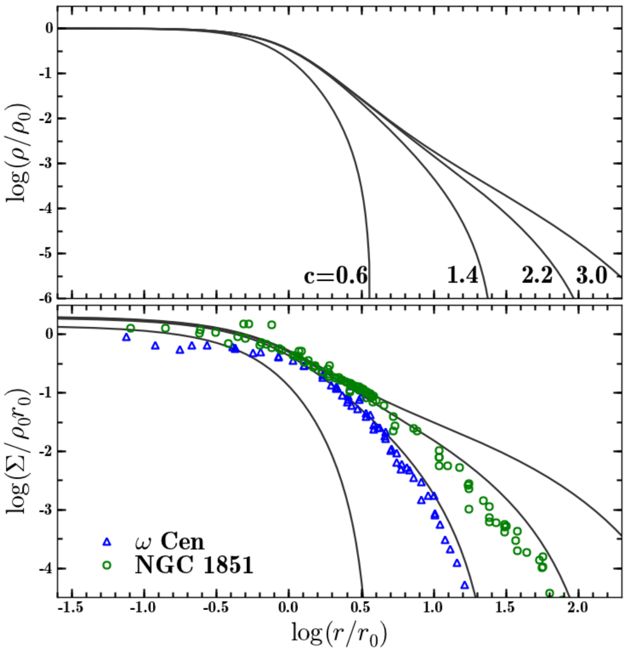

Fig. 1.4. Comparison of King models with different concentration. The upper panel shows the volume density, normalized to the central value, as a function of radius, normalized to the King radius. In the lower panel, the surface densities obtained via projection of the curves in the upper panel are shown and compared to the measured surface brightness profiles of two Galactic globular clusters, NGC 1851 (green circles) and ω Centauri (blue triangles). The data for the two clusters are taken from Trager et al. (1995).

1.2.4. Models

Not surprisingly, a gravitationally-bound system containing $\sim 10^6$ stars is by far too complex for an analytical solution in which every single star is considered. Instead, one tries to construct models that describe the kinematics inside globular clusters. There are three main approaches to do this that are discussed below.

Parametric approaches

One possibility is to describe the cluster in a statistical sense, with the help of a stellar distribution function $f(\mathcal{E})$ that is a smooth representation of the distribution of the cluster members in phase space. This approach to describe a globular cluster has been pioneered by Michie (1963) and King (1966) who introduced a family of models, the King models, that is still widely used to describe a globular cluster. A detailed discussion about King models can be found in Binney & Tremaine (2008). In the following, only the most important characteristics of King models are summarized. They are based on a distribution function given by

$$f_{\rm K}(\mathcal{E}) \propto \begin{cases} \sigma^{-3/2}\left(\exp\left\{\mathcal{E}/\sigma^2\right\} - 1\right) & \mathcal{E} < 0\,; \\ 0 & \mathcal{E} \geq 0\,, \end{cases} \tag{1.2}$$

which only depends on the relative energy $\mathcal{E} = \Psi - v^2/2$ of a star of unit mass with velocity v in a gravitational potential Ψ. The quantity σ can be considered a normalization constant for our purposes. The basic idea behind Eq. 1.2 is that for $\mathcal{E} \ll 0$ the distribution function approaches the Maxwell-Boltzmann distribution of a collisionless gas. However, the unaltered Maxwellian distribution predicts a diverging total mass of the system (see Binney & Tremaine 2008), therefore the distribution function is lowered as $\mathcal{E}$ approaches zero. The physical justification for such an approach is that the probability of stars escaping from the cluster increases with their relative energy until they become unbound at $\mathcal{E} = 0$. Since the potential Ψ decreases with increasing radius, the range of possible velocities narrows. At a limiting radius, the truncation radius $r_{\rm t}$, no orbits are allowed any more and the density drops to zero. In the framework of King models, radii are usually measured relative to a scale radius r_0, the so-called King radius. It does not have a physical meaning, in particular it is generally not equal to the core radius $r_{\rm c}$ at which the projected surface density has half of its central value. However, if one defines the concentration of a model as $c = \log(r_{\rm t}/r_0)$, then the properties of a King model are fully defined for a given value of c. To illustrate this, Fig. 1.4 shows the densities predicted by King models with different concentration. The projected surface densities are also plotted and compared to the surface brightness profiles compiled by Trager et al. (1995) for the globular clusters NGC 1851 and ω Centauri. One can see that King models yield a fair representation of the measured profiles. Trager et al. provide concentrations of $c = 2.24$ for NGC 1851 and $c = 1.24$ for ω Centauri.

A basic assumption going into Eq. 1.2 is that the velocity distribution inside the cluster is isotropic. An extension to anisotropic systems is possible, however. Michie & Bodenheimer (1963) discussed King-Michie models in which the distribution function includes an additional dependence on the angular momentum. Such models have been used in the classical work by Gunn & Griffin (1979) to describe the globular cluster M3. A further generalization that can be applied in rotating systems has been used by Lupton et al. (1987) in a study of the cluster M13 which shows evidence for rotation in its outer parts. More recently, McLaughlin & van der Marel (2005) studied a large sample of Galactic globular clusters and found that the truncation predicted by King models is too sharp and instead a distribution function with a shallower truncation introduced by Wilson (1975) yields a better representation of the measured profiles.

The advantage of models like those just described is that from the distribution function one can not only derive morphological observables, such as the surface brightness profile (cf. Fig. 1.4) but also kinematical ones. The first velocity moment of the distribution function yields the mean velocity of the system. Similarly, the second velocity moments are related to the velocity dispersion of the cluster. In turn this means that under the assumption that the stars in the cluster obey a certain distribution function such as Eq. 1.2, it is straight forward to find the parameter(s) of the model that provide the best fit with respect to a set of observations. For example, under the assumption of a King profile, the measured surface brightness profile will constrain the concentration c of the profile as well as the King radius r_0. An additional measurement of the velocity dispersion will constrain the mass-to-light ratio and thereby the depth of the potential well so that the King model is completely defined. On the other hand, assuming a certain distribution function can already introduce systematic uncertainties. Consider the case where a massive black hole is located at the cluster centre. In that case, there will be two counteracting effects. While the stellar system will try to reach thermal equilibrium, the black hole will scour it from sources on orbits with small pericentres. Yet distribution functions $\propto \exp\left\{-\mathcal{E}/\sigma^2\right\}$ are only valid for thermal equilibrium. Also, Eq. 1.2 assumes stars of equal mass, obviously a strong simplification which can be overcome by constructing multi-mass King profiles.

Non-parametric approaches

Alternatively, one can use a non-parametric approach to investigate the dynamical state inside a cluster, as advocated by Merritt (1993). Its application to globular clusters has been pioneered by Gebhardt & Fischer (1995). The idea behind the approach is to obtain intrinsic cluster properties via a deprojection of (a smooth representation of) measured ones. For example, deprojecting the surface brightness profile via an Abel transform yields the luminosity density. Similarly, intrinsic velocity moments can be obtained from measured ones. The usefulness of non-parametric approaches becomes obvious from the Jeans equations that provide a possibility to link the observationally accessible properties to the gravitational potential of the cluster. Gebhardt & Fischer used the isotropic spherical Jeans equation to infer densities, mass-to-light ratios and finally distribution functions using measurements of the surface brightness and velocity dispersion profile in four clusters (M15, 47 Tuc, NGC 362 and NGC3201) and find significant disagreement with King models. The globular cluster ω Centauri was studied in a similar fashion by Merritt et al. (1997).

The Jeans equations can also be used in a slightly different way, namely by starting from an assumption about the gravitational potential and then calculating the velocity moments following from this potential. This method, introduced by Binney et al. (1990), has been extensively used in the search for supermassive black holes in the centres of galaxies (e.g. Magorrian et al. 1998). The basic idea behind it is to obtain the gravitational potential produced by stars from the surface brightness profile, include an additional component accounting for a putative black hole and then find the mass of the black hole that yields the best representation of the observed velocity distribution. The approach is also commonly used in the search for massive black holes in globular clusters, cf. Sect. 1.3. The formalism behind this is discussed in more detail in Chapter 4.

A fundamental limitation of the Jeans modelling approach is that it can only be used if simplifying assumptions about the system are included, such as spherical or axis symmetry (Binney & Tremaine 2008). A method that works in triaxial systems was presented by Schwarzschild (1979). The idea behind this approach is to calculate a large library of stellar orbits in a gravitational potential resulting from a given mass density. The system is divided into spatial cells and the (non negative) weight of each orbit is determined by requesting that in each cell the sum of the contributions from all orbits yields the mass that corresponds to the local density. Initially, Schwarzschild modelling was applied to galaxies (e.g. Richstone & Tremaine 1985; Gebhardt et al. 2003). Globular clusters are considerably less complicated dynamical systems than galaxies and in many cases Jeans modelling is sufficient to describe their kinematics. Nevertheless, the work on ω Centauri (e.g. van de Ven et al. 2006) or M15 (van den Bosch et al. 2006) demonstrates that the application of Schwarzschild models is a promising development.

Evolutionary models

Finally, it should be noted that the presented approaches represent equilibrium models. Besides those, evolutionary models exist that follow the dynamical evolution of the cluster, resulting from gravitational encounters among stars or between stars and a massive central black hole. The most commonly used evolutionary models rely on N-body simulations (e.g. Baumgardt & Makino 2003) or a solution of the Fokker-Planck equation (e.g. Drukier et al. 1992). A major advantage of this class of models is that they can predict properties that are difficult to access observationally, such as the mass-to-light ratio (e.g. Dull et al. 1997, for M15) or the degree of mass segregation in the cluster. Also, they allow for a comparison between model and data at different evolutionary stages. On the downside, evolutionary models are computationally quite expensive. N-body models are limited currently to $\sim 10^5$ stars (e.g. Jalali et al. 2012) and therefore still do not reach the number of stars present in a massive cluster.

1.3. Supermassive black holes and the search for intermediate-mass black holes

In Sect. 1.2.3 the possibility was discussed that globular cluster host massive black holes. Apart from the implications for our understanding of the dynamics inside the clusters, such objects are of relevance in another astrophysical domain, namely the buildup and evolution of galaxies.

1.3.1. Black hole-bulge relations in galaxies

There is nowadays firm evidence that supermassive black holes (SMBHs) are almost ubiquitous in the centres of massive galaxies. Two remarkable examples in this respect are our own galaxy, where a black hole with a mass $4 \cdot 10^6 M_\odot$ is the only explanation for the observed orbits of nearby stars (Eckart & Genzel 1996; Ghez et al. 2008; Gillessen et al. 2009) and the nearby galaxy NGC 4258 in which the maser emission of a central gas disk allows a precise mass estimate of $M_{\rm BH} = 3.8 \cdot 10^7 M_\odot$ (Herrnstein et al. 2005).

A ground-braking discovery was the dependence of the masses of SMBHs on fundamental properties of the surrounding bulges of the host galaxies. Based on the limited data available back then (8 galaxies with detection of an SMBH), Kormendy & Richstone (1995) found evidence for a correlation between the mass of the SMBH and the luminosity or mass of the bulge. The significance of this result was strongly enhanced by the study of Magorrian et al. (1998) based on a sample of 30 galaxies with secure detection of SMBHs. That black hole mass correlates with both, luminosity and mass of the bulge, can be explained via the fundamental plane relation between luminosity and mass-to-light ratio (Bender et al. 1992; Magorrian et al. 1998). The rather large scatter present in the original Magorrian et al. relations could be significantly reduced in later studies, e.g. by Marconi & Hunt (2003) or Häring & Rix (2004). A similarly tight relation between the black hole mass and the velocity dispersion of the bulge stars was discovered independently by Ferrarese & Merritt (2000) and Gebhardt et al. (2000a). All three relations are presented in Fig. 1.5.

A common interpretation of these scaling relations is that the growth of the SMBH and the host galaxy are intimately linked. Usually, this link is explained by an evolutionary phase in which star formation and black hole growth are triggered by gas supply. Accretion onto the black hole causes the ignition of an active galatic nucleus (AGN) that shuts down both growth processes via a feedback mechanism (Silk & Rees 1998).

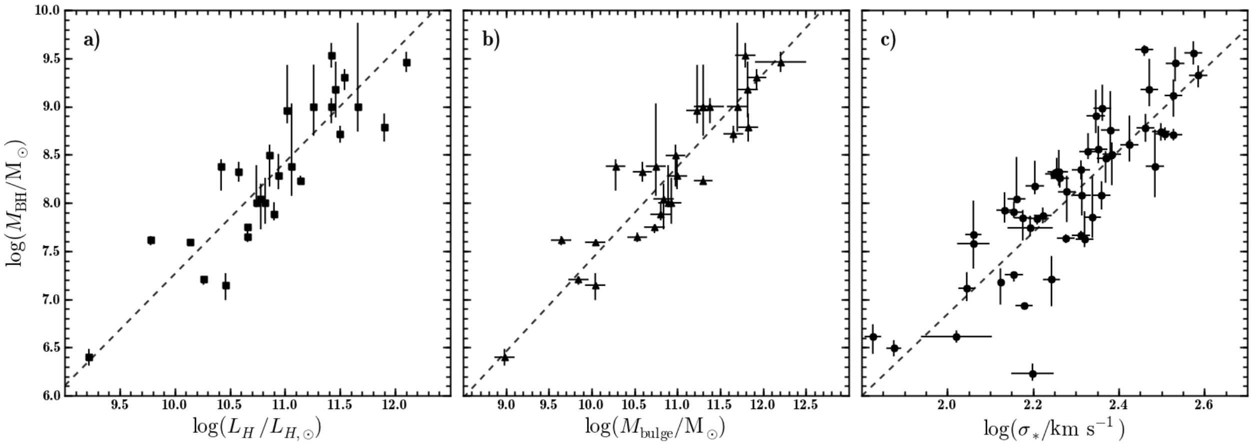

Fig. 1.5. Scaling relations observed between the masses of SMBHs and fundamental properties of the surrounding bulges, namely H-band luminosity (a), virial mass (b) and velocity dispersion (c). The data shown in panels (a) and (b) are taken from the compilation of Marconi & Hunt (2003), with the dashed line indicating the best fitting power law obtained by the same authors. The data in panel (c) are taken from Gültekin et al. (2009). Again, the best fitting power law is given as a dashed line.

1.3.2. The need for intermediate-mass black holes

The mass range covered by detected SMBHs is roughly $10^5 - 10^{10}{\rm M}_\odot$. Together with the firm evidence for stellar mass black holes with masses $\lesssim 10^2 M_\odot$, this results in rather paradoxical demographics of known black hole masses: There are abundant populations of black holes in two very different mass regimes, while the mass range in between the two extrema seems to be almost deserted concerning observational evidence. The massive black holes that were discussed in the context of the dynamical evolution of globular clusters in Sect. 1.2.3 offer an intriguing possibility to bridge the gap. Since such black holes would be intermediate between the stellar-mass and the supermassive ones, they are usually referred to as intermediate-mass black holes (IMBHs).

The fact that black holes with masses $> 10^5{\rm M}_\odot$ are observed in a hierarchical universe implies that they have grown to such high masses. Additionally, the observation of powerful AGN at high redshifts (e.g. Fan et al. 2001) implies that the build-up must have happened in the early universe. Current theoretical work (see Volonteri 2010 for a review) favours a build-up starting from less massive (10^2–$10^4 M_\odot$) seeds. Not all scenarios for the formation of such seeds are related to globular clusters, like the explosion of population III stars (Madau & Rees 2001). However, the ages and high stellar densities of the clusters make them valid candidates to host the seeds.

A simple-minded extrapolation of the black hole-bulge relations to the typical masses and velocity dispersions of globular clusters predicts black holes with exactly the required mass range. Obviously, the extrapolation of a power law over several orders of magnitude is very uncertain. There is evidence that already in the regime of low-mass galaxies the scaling relations are not valid any more (e.g. Greene et al. 2010). However, while these galaxies are often disk-dominated or of irregular morphology, globular clusters might be considered to be mini-bulges.

It is intriguing that the theoretical predictions for IMBHs in globular clusters yield consistent results. Gürkan et al. (2004) performed Monte Carlo simulations of dense clusters and found that 0.1% of the cluster mass participates in the runaway collision, a ratio similar to that between SMBH mass and bulge mass. A similar result was obtained by Miocchi (2007) in a semi-analytical way based on modified King models. Miocchi predicted the influence of a IMBH on the concentration and central surface brightness slope of a cluster and used this information to assign black hole masses to Galactic clusters. The resulting relation between black hole mass and cluster mass was in agreement with the one for galaxies, while the correlation involving the velocity dispersion was less step, with black hole mass scaling $\propto \sigma^{1.2}$ instead of $\propto \sigma^{4.8}$.

1.3.3. Observational evidence for intermediate-mass black holes in globular clusters

The first cluster for which the central dynamics were studied in detail is M15. Gebhardt et al. (2000b) suggested the presence of non-luminous matter towards the centre to explain the peculiar kinematics. The detailed study by van der Marel et al. (2002) and Gerssen et al. (2002, 2003) showed that no IMBH is required to explain the central kinematics of M15 if a justifiable increase in the central mass-to-light ratio is assumed. Later studies by McNamara et al. (2003) and van den Bosch et al. (2006) based on extended data sets reach a similar conclusion.

The cases of the most massive clusters, both in the Galaxy and in M31, are discussed controversially. The initial detection of an IMBH in G1 in the Andromeda galaxy by Gebhardt et al. (2002) was contested by Baumgardt et al. (2003). However, later observations by Gebhardt et al. (2005) seem to support the initial result, yielding a black hole with a mass of $1.8 \cdot 10^4 M_\odot$. The possibility that an IMBH resides in G1 was strengthened by the detection of a possible accretion signal both in radio and X-ray observations (Ulvestad et al. 2007; Kong et al. 2010, but see Miller-Jones et al. 2012). In ω Centauri the situation seems to be even more complex. The claim by Noyola et al. (2008) on the detection of an IMBH was not confirmed by Anderson & van der Marel (2010) and van der Marel & Anderson (2010) who find no strong evidence for an IMBH and attribute the discrepancy to the result of Noyola et al. mainly to an imprecisely determined cluster centre in the former study. However, Noyola et al. (2010) determine yet another centre for the cluster and again conclude that an IMBH is required to explain the central stellar kinematics.

A larger sample of 8 massive cluster was recently studied by Lützgendorf et al. (2011, 2012b,a). The clusters were preselected as likely candidates to host a black hole according to their photometric properties, especially the central slopes of their surface brightness profiles. However, only in 3 clusters (NGC 1904, NGC 6266, and NGC 6388) the analysis suggests the presence of an IMBH while for the rest of the sample upper limits are provided. The upper limits as well as the reported detections are still consistent with the above-mentioned extrapolation of the SMBH scaling relations. The same is true for the upper limits found by other studies in 47Tuc (McLaughlin et al. 2006) or NGC 6266 (McNamara et al. 2012).

In summary, it is safe to say that the results obtained so far yield an inconclusive picture about whether and which clusters might contain IMBHs. Additional constraints might come from the detection of the accretion signal in deep radio observations. Recently, Strader et al. (2012) reported stringent upper limits on the radio fluxes in the centres of Galactic globular clusters. However, the transformation of such measurements into mass limits requires strong assumptions about the accretion process that are not well understood. Clearly, more useful kinematical data for a larger sample of clusters will be needed in order to make progress.

1.4. Observational challenges

1.4.1. Crowded stellar fields

A main observational difficulty in the search for IMBHs is that although its influence on the evolution of a cluster can be significant, its immediate footprint in the velocities of the cluster stars is limited to the very central regions. This can be shown by estimating the size of the *sphere of influence* (Binney & Tremaine 2008), defined as the volume inside the radius where the velocity dispersion of the cluster stars equals the Keplerian velocity of a star orbiting the black hole:

$$R_{\mathrm{infl}} = \frac{GM_{\mathrm{BH}}}{\sigma^2} \tag{1.3}$$

If a black hole mass of $10^4 M_\odot$ is assumed in a cluster with $\sigma = 10\mathrm{km/s}$ at a distance of 10 kpc, the radius of the sphere of influence is 0.4 pc, corresponding to $9''$ projected onto the sky. An area of similar size around the centre of the cluster M13 is shown in Fig. 1.6 as it looks like in an HST observation. Although a huge number of stars are visible, only a handful of them have been observed spectroscopically so far. The reason for this is that traditional spectroscopic techniques do not preserve the spatial information in the way that photometric techniques do. That this is a major nuisance particularly in crowded stellar fields like the centre of a globular cluster becomes obvious from the large discrepancy between the number of photometrically and spectroscopically studied stars in Fig. 1.6.

1.4.2. Crowded field photometry

In data that fully preserve the spatial information, it is possible to reconstruct the point spread function (PSF) of an observation. The PSF represents the spatial intensity distribution created by a star (or another point-like source) in the plane of the detector. It is largely determined by two processes, the turbulent atmosphere above the telescope and the diffraction of the stellar light in the optical system of the telescope. The former factor is obviously not important for space-based observations. Knowledge of the PSF allows one to cleanly separate the images of even heavily blended stars (a technique that is referred to as *deblending*).

The era of crowded field photometry really began in the 1980s with the advent of CCDs in astronomical imaging. Very sophisticated analysis tools have been developed to handle the computational challenges involved in the analysis. To illustrate those challenges, consider an observed field containing N stars. Each star contributes 3 unknown parameters: its flux and its coordinate in x and y. Therefore, even if the PSF is known, the solution has to be optimized for $3N$ parameters. Fig. 1.6 just shows a small cutout of an observed image that already gives an impression of the complexity of the optimization process. To make it feasible, the algorithms work iteratively. After an initial step in which the stars are detected and a first guess is made for their fluxes and positions, a routine is called that loops over the detected stars and improves the initial guesses for each star individually. A further complication is that usually the PSF has to be recovered from the observations. The individual software tools, like `romaphot` (Buonanno et al. 1983), `daophot` (Stetson 1987), or `dophot` (Schechter et al. 1993) differ in the way the PSF is recovered or in the details of the implementation of the iterative fitting scheme, yet their overall analysis approach is similar. For HST data, dedicated analysis tools have been developed (e.g. Dolphin 2000; Anderson & King 2000) which make use of the advantage that the PSF can be accurately predicted for HST observations. These tools allow one to create impressively detailed colour-magnitude diagrams like the one shown in Fig. 1.2.

1.4.3. The need for spectroscopy in crowded stellar fields

The large majority of spectroscopic studies in globular clusters rely on multi-object spectroscopy, a technique in which individual fibres, each with a diameter of $1-2''$, are placed onto the stars of interest. Consequently, these stars must be sufficiently isolated so that no other stars contribute significantly to the observed spectrum – otherwise systematic uncertainties are unavoidable. For example, the analysis of hot blue horizontal-branch stars in the cluster NGC 6388 by Moehler & Sweigart (2006) yielded significantly lower surface gravities and masses for these stars than predicted by any model. Moehler & Sweigart argue that this result is caused by residual background light that potentially decreased the depths of the Balmer line cores.

Another avenue for kinematical studies is through proper motions determined from imaging studies (e.g. McLaughlin et al. 2006; Anderson & van der Marel 2010). However, such studies are observationally very expensive because they usually require HST and observations over a timespan of years. Furthermore, the information obtained in proper motion studies is complementary to that coming from spectroscopic radial velocities. For example, proper motions cannot be used to study the periods of binaries because even at the resolution of HST, binaries are unresolved at the typical distance of a globular cluster.

Spectroscopy is also indispensable to study the chemical composition of the cluster stars. The results presented in Sect. 1.1.3 show the level of detail that can be achieved in the determination of abundances nowadays. Although limited by the lack of spatial information, multi-object spectroscopy has proven to be a very valuable technique in this respect. For the reasons mentioned, those studies concentrated on the outskirts of the clusters that are less dense and therefore easier to observe.

Finally, although globular clusters might be the most obvious examples for crowded stellar fields they are by no means the only one. Entities such as open stellar clusters, the Galactic bulge or nearby galaxies can have similarly high stellar densities. The complexity of the latter two with respect to kinematics or chemical abundance patterns is often significantly higher than in globular clusters. As an example, we briefly discuss local dwarf galaxies. The intimate link between these objects and

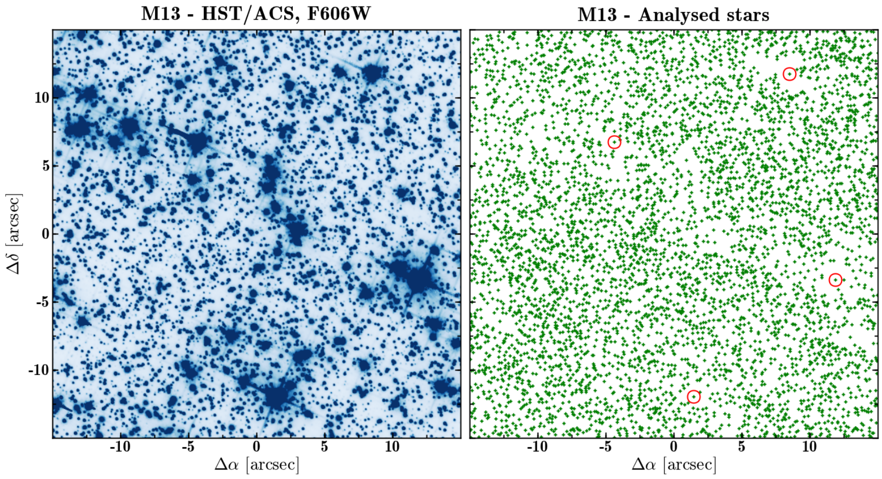

Fig. 1.6. Available data in the central 30″ × 30″ of M13. The left panel shows a *V*-band image of M13 obtained from the *Hubble Legacy Archive*. In the right panel, small green dots indicate stars that are included in the photometric catalogue of Anderson et al. (2008). Each star that has been observed spectroscopically is marked by a large red circle.

globular clusters was already mentioned in Sect. 1.1.2. Many dwarf galaxies have velocity dispersions comparable to those of globular clusters (e.g. Battaglia et al. 2008). As they are usually located at larger distances, proper motions are more difficult to measure and spectroscopy becomes even more important also for kinematical studies. For example, multi-object spectroscopy by Tolstoy et al. (2004) revealed a bimodality in the old stellar population in the Sculptor galaxy and provided evidence for distinct kinematics of the two subpopulations. Adapting spectroscopic observing techniques to the demands of crowded stellar fields will strongly increase the stellar samples for which such measurements are possible and therefore allow one to probe even deeper into the peculiarities of the stellar populations.

1.4.4. The development of crowded field spectroscopy

Several steps have already been taken to adapt spectroscopic techniques to the requirements of crowded stellar fields. Longslit spectroscopy preserves the spatial information along the slit, so that it becomes possible to pin down the position of individual stars along the slit. This technique was used in M15 by Dull et al. (1997) and van der Marel et al. (2002) to investigate the central kinematics. Yet stellar blends perpendicular to the slit cannot be accounted for and the recovery of the PSF from the observation is barely possible without additional information. Thus uncontaminated spectra are only obtained for moderately blended stars. For this reason, only with the high spatial resolution of HST it was possible to constrain the presence of an IMBH.

Imaging spectroscopy does not suffer from such problems because spectroscopic data are obtained over a continuous field-of-view and therefore the same analysis techniques can in principle be applied as for plain imaging data. There are two rather complementary approaches on performing imaging spectroscopy. Fabry-Perot imaging involves the successive scanning of a narrow spectral range with monochromatic images. It yields a “datacube” with two spatial dimensions and a spectral one. Insofar as data analysis is concerned, each monochromatic image can be analysed using the PSF-fitting techniques mentioned above. The spectrum of each star will then be the combination of all its monochromatic fluxes. Since such instruments can achieve very high spectral resolutions, they are well suited to study the dynamics of Galactic globular clusters (see Gebhardt & Fischer 1995; Gebhardt et al. 2000b).

Integral field spectroscopy on the other hand yields a similar data structure, but all the data are observed simultaneously. This is a significant advantage because to first order the PSF and the source coordinates will be the same in all images. Wavelength dependent atmospheric effects will introduce some variation of those properties in spectral direction, but these variations can be modelled so that the data from the whole cube can be analysed in a coherent way. Furthermore, the wavelength range that is covered is usually much broader compared to a Fabry-Perot instrument. This allows one to put more relaxed constraints on the required spectral resolution because the information from all available spectral lines can be used to determine velocities or metallicities. Those advantages come to a prize, however. Most integral field spectrographs have a limited number of spatial pixels ($\lesssim$ 1000), thus the covered field-of-view is small, a circumstance that makes the determination of a reliable PSF extremely challenging. This is likely the reason why integral field spectroscopy is still a scarcely used technique in the observation of crowded stellar fields. And in most existing studies the analysis is restricted to the identification of spatial pixels in which the spectrum is dominated by the light of an individual star (e.g. Eisenhauer et al. 2005; Evans et al. 2011). It is worth noting that the studies that have used integral field spectroscopy to search for IMBHs so far (Noyola et al. 2008, 2010; Lützgendorf et al. 2011, 2012b,a) did the opposite – regions around bright stars were excluded in order to study the unresolved light.

However, it is possible to obtain the PSF in integral field data. The first successful applications in this directions were performed in extragalactic applications to deblend the light contributions of an AGN and its host galaxy (e.g. Christensen et al. 2006). Wisotzki et al. (2003) were the first to use PSF fitting techniques in a moderately crowded field, filled with multiple images of a lensed quasar instead of stars. Since upcoming instrumentation, especially MUSE (Bacon et al. 2010), will also significantly improve on the number of spatial pixels in a datacube, integral field spectroscopy is a very promising technique for the investigation of crowded stellar fields.

1.5. Aims and outline of this work

The aims of this work are twofold and can be divided into a technical aim and a scientific aim. On the technical side, we want to enhance the potential of integral field spectroscopy for the investigation of crowded stellar fields. Our aim is to perform the first systematic study on the prospects and limitations of crowded field spectroscopy using integral field spectrographs. This involves the development of an algorithm and a software code to deblend and extract single stellar spectra from integral field data. In the course of this development we have to find a way to reliably recover the PSF despite the limited field of view of an average spectrograph. On the other hand, the fact that for many potential target fields, high resultion imaging data is already available will likely help us in the analysis. In this respect, we aim to quantify how much we gain in using priors from an available catalogue of sources. The most important aspect is of course the quality of the deblended spectra. Depending on the brightness and position of the stars, spectra with very different signal-to-noise ratios will be obtained. For the future usability of the software, it will be very important to predict what quality we can expect for the spectrum of a star in a crowded field under given observing conditions. Finally, the software should also be applicable to the significantly more complex data that will be delivered by future instruments. This detailed technical work is the subject of Chapter 2.

The scientific part of this work is dedicated to the search for intermediate-mass black holes in globular clusters. To this aim, integral field data were obtained in the central regions of the Galactic clusters M3, M13 and M92. The analysis of these data represents the first application of our deblending approach to real data of crowded stellar fields. The scientific aims of our study set stringent requirements on the quality of the data reduction and the deblending of the individual stellar spectra. This work, discussed in Chapter 3, will provide us with large sets of stellar velocities in the sphere of influence of a putative IMBH. With the help of dedicated Jeans modelling, we want to verify whether our kinematical data does provide evidence for an IMBH in any of the clusters. Regardless of whether an IMBH is detected or not, our mass limits will yield valuable constraints on the population of IMBHs in globular clusters. The Jeans models and our constraints on black hole masses are presented in Chapter 4 together with a discussion about our findings in the context of the current state of research in this field.

While Chapter 4 is based on the results obtained from the velocities of the deblended stars, those are not the only stars present in our integral field datacubes, which contain an additional light contribution originating from fainter stars, too numerous to be resolved at seeing limited resolution. However, our analysis approach can uncover this "sea" of faint stars via subtraction of the dominating resolved stars. Chapter 5 is dedicated to the analysis of this stellar component. We aim to show that the analysis of its integrated light can yield additionally constraints on the presence of IMBHs in our target clusters.

Although this work has a strong emphasis on stellar kinematics, the application of PSF-fitting techniques to integral field data opens a lot of possibilities also in the field of chemical studies and stellar abundances. The results of our work in this field, carried out in close collaboration with Tim-Oliver Husser from the University of Göttingen, are outlined in Chapter 6.

Chapters 2 to 5 are meant to be stand-alone articles that are already accepted or being prepared for publication in *Astronomy & Astrophysics*. Each of these chapters includes a dedicated introduction that summarizes the state of research in this field. For this reason, it is unavoidable that some information that is already presented in this general introduction is reformulated again throughout the individual chapters.

References

Abadi, M. G., Navarro, J. F., & Steinmetz, M. 2006, MNRAS, 365, 747
Anderson, A. J. 1997, PhD thesis, University of California, Berkeley
Anderson, J. & King, I. R. 2000, PASP, 112, 1360
Anderson, J., Piotto, G., King, I. R., Bedin, L. R., & Guhathakurta, P. 2009, ApJ, 697, L58
Anderson, J., Sarajedini, A., Bedin, L. R., et al. 2008, AJ, 135, 2055
Anderson, J. & van der Marel, R. P. 2010, ApJ, 710, 1032
Antonov, V. A. 1962, Solution of the problem of stability of stellar system Emden's density law and the spherical distribution of velocities
Arp, H. C. 1955, AJ, 60, 317
Arp, H. C., Baum, W. A., & Sandage, A. R. 1953, AJ, 58, 4
Ashman, K. M. & Zepf, S. E. 1992, ApJ, 384, 50
Bacon, D., Sigurdsson, S., & Davies, M. B. 1996, MNRAS, 281, 830
Bacon, R., Accardo, M., Adjali, L., et al. 2010, in Society of Photo-Optical Instrumentation Engineers (SPIE) Conference Series, Vol. 7735, Society of Photo-Optical Instrumentation Engineers (SPIE) Conference Series
Bahcall, J. N. & Ostriker, J. P. 1975, Nature, 256, 23
Bahcall, J. N. & Wolf, R. A. 1976, ApJ, 209, 214
Battaglia, G., Helmi, A., Tolstoy, E., et al. 2008, ApJ, 681, L13
Baumgardt, H., Côté, P., Hilker, M., et al. 2009, MNRAS, 396, 2051
Baumgardt, H., Kroupa, P., & Parmentier, G. 2008, MNRAS, 384, 1231
Baumgardt, H. & Makino, J. 2003, MNRAS, 340, 227
Baumgardt, H., Makino, J., & Hut, P. 2005, ApJ, 620, 238
Baumgardt, H., Makino, J., Hut, P., McMillan, S., & Portegies Zwart, S. 2003, ApJ, 589, L25
Baumgardt, H. & Mieske, S. 2008, MNRAS, 391, 942
Bedin, L. R., Piotto, G., Anderson, J., et al. 2004, ApJ, 605, L125
Bekki, K. & Freeman, K. C. 2003, MNRAS, 346, L11
Bekki, K. & Norris, J. E. 2006, ApJ, 637, L109
Bellini, A., Bedin, L. R., Piotto, G., et al. 2010, AJ, 140, 631
Bender, R., Burstein, D., & Faber, S. M. 1992, ApJ, 399, 462
Binney, J. & Mamon, G. A. 1982, MNRAS, 200, 361
Binney, J. & Tremaine, S. 2008, Galactic Dynamics: Second Edition (Princeton University Press)
Binney, J. J., Davies, R. L., & Illingworth, G. D. 1990, ApJ, 361, 78
Borissova, J., Bonatto, C., Kurtev, R., et al. 2011, A&A, 532, A131
Brodie, J. P. & Strader, J. 2006, ARA&A, 44, 193
Buonanno, R., Buscema, G., Corsi, C. E., Ferraro, I., & Iannicola, G. 1983, A&A, 126, 278
Cannon, R. D. & Stobie, R. S. 1973, MNRAS, 162, 207
Carretta, E., Bragaglia, A., Gratton, R., D'Orazi, V., & Lucatello, S. 2009a, A&A, 508, 695
Carretta, E., Bragaglia, A., Gratton, R. G., et al. 2009b, A&A, 505, 117
Carretta, E., Bragaglia, A., Gratton, R. G., et al. 2010, A&A, 516, A55
Christensen, L., Jahnke, K., Wisotzki, L., & Sánchez, S. F. 2006, A&A, 459, 717
Cohen, J. G., Blakeslee, J. P., & Ryzhov, A. 1998, ApJ, 496, 808
Cohn, H. & Kulsrud, R. M. 1978, ApJ, 226, 1087
Cote, P., Marzke, R. O., & West, M. J. 1998, ApJ, 501, 554
Côté, P., McLaughlin, D. E., Cohen, J. G., & Blakeslee, J. P. 2003, ApJ, 591, 850
De Angeli, F., Piotto, G., Cassisi, S., et al. 2005, AJ, 130, 116
Denisenkov, P. A. & Denisenkova, S. N. 1989, Astronomicheskij Tsirkulyar, 1538, 11
D'Ercole, A., Vesperini, E., D'Antona, F., McMillan, S. L. W., & Recchi, S. 2008, MNRAS, 391, 825
Dinescu, D. I., Girard, T. M., & van Altena, W. F. 1999, AJ, 117, 1792
Djorgovski, S. & King, I. R. 1986, ApJ, 305, L61
Dolphin, A. E. 2000, PASP, 112, 1383
Dotter, A., Sarajedini, A., Anderson, J., et al. 2010, ApJ, 708, 698
Drukier, G. A., Fahlman, G. G., & Richer, H. B. 1992, ApJ, 386, 106
Dull, J. D., Cohn, H. N., Lugger, P. M., et al. 1997, ApJ, 481, 267
Duquennoy, A. & Mayor, M. 1991, A&A, 248, 485
Eckart, A. & Genzel, R. 1996, Nature, 383, 415
Eisenhauer, F., Genzel, R., Alexander, T., et al. 2005, ApJ, 628, 246
Evans, C. J., Taylor, W. D., Hénault-Brunet, V., et al. 2011, A&A, 530, A108
Fabian, A. C., Pringle, J. E., & Rees, M. J. 1975, MNRAS, 172, 15P
Fall, S. M. & Frenk, C. S. 1985, in IAU Symposium, Vol. 113, Dynamics of Star Clusters, ed. J. Goodman & P. Hut, 285–296
Fan, X., Narayanan, V. K., Lupton, R. H., et al. 2001, AJ, 122, 2833
Ferrarese, L. & Merritt, D. 2000, ApJ, 539, L9
Forbes, D. A. & Bridges, T. 2010, MNRAS, 404, 1203
Forbes, D. A., Brodie, J. P., & Grillmair, C. J. 1997, AJ, 113, 1652
Freeman, K. & Bland-Hawthorn, J. 2002, ARA&A, 40, 487
Freeman, K. C. & Rodgers, A. W. 1975, ApJ, 201, L71
Fregeau, J. M., Gürkan, M. A., Joshi, K. J., & Rasio, F. A. 2003, ApJ, 593, 772
Fusi Pecci, F., Ferraro, F. R., Bellazzini, M., et al. 1993, AJ, 105, 1145
Gao, B., Goodman, J., Cohn, H., & Murphy, B. 1991, ApJ, 370, 567

Gebhardt, K., Bender, R., Bower, G., et al. 2000a, ApJ, 539, L13
Gebhardt, K. & Fischer, P. 1995, AJ, 109, 209
Gebhardt, K. & Kissler-Patig, M. 1999, AJ, 118, 1526
Gebhardt, K., Pryor, C., O'Connell, R. D., Williams, T. B., & Hesser, J. E. 2000b, AJ, 119, 1268
Gebhardt, K., Rich, R. M., & Ho, L. C. 2002, ApJ, 578, L41
Gebhardt, K., Rich, R. M., & Ho, L. C. 2005, ApJ, 634, 1093
Gebhardt, K., Richstone, D., Tremaine, S., et al. 2003, ApJ, 583, 92
Geisler, D., Lee, M. G., & Kim, E. 1996, AJ, 111, 1529
Geisler, D. & Villanova, S. 2012, in American Astronomical Society Meeting Abstracts, Vol. 220, American Astronomical Society Meeting Abstracts #220, #102.02
Gerssen, J., van der Marel, R. P., Gebhardt, K., et al. 2002, AJ, 124, 3270
Gerssen, J., van der Marel, R. P., Gebhardt, K., et al. 2003, AJ, 125, 376
Ghez, A. M., Salim, S., Weinberg, N. N., et al. 2008, ApJ, 689, 1044
Giersz, M. & Heggie, D. C. 1997, MNRAS, 286, 709
Gill, M., Trenti, M., Miller, M. C., et al. 2008, ApJ, 686, 303
Gillessen, S., Eisenhauer, F., Trippe, S., et al. 2009, ApJ, 692, 1075
Glebbeek, E., Gaburov, E., de Mink, S. E., Pols, O. R., & Portegies Zwart, S. F. 2009, A&A, 497, 255
Goodman, J. & Hut, P. 1989, Nature, 339, 40
Goudfrooij, P., Mack, J., Kissler-Patig, M., Meylan, G., & Minniti, D. 2001, MNRAS, 322, 643
Gratton, R., Sneden, C., & Carretta, E. 2004, ARA&A, 42, 385
Gratton, R. G., Bonifacio, P., Bragaglia, A., et al. 2001, A&A, 369, 87
Gratton, R. G., Carretta, E., & Bragaglia, A. 2012, A&A Rev., 20, 50
Greene, J. E., Peng, C. Y., Kim, M., et al. 2010, ApJ, 721, 26
Gültekin, K., Richstone, D. O., Gebhardt, K., et al. 2009, ApJ, 698, 198
Gunn, J. E. & Griffin, R. F. 1979, AJ, 84, 752
Gürkan, M. A., Freitag, M., & Rasio, F. A. 2004, ApJ, 604, 632
Häring, N. & Rix, H.-W. 2004, ApJ, 604, L89
Harris, W. E. 1996, AJ, 112, 1487
Harris, W. E. 2001, in Saas-Fee Advanced Course 28: Star Clusters, ed. L. Labhardt & B. Binggeli, 223
Harris, W. E. & van den Bergh, S. 1981, AJ, 86, 1627
Hénon, M. 1971, Ap&SS, 13, 284
Herrnstein, J. R., Moran, J. M., Greenhill, L. J., & Trotter, A. S. 2005, ApJ, 629, 719
Hilker, M., Infante, L., & Richtler, T. 1999, A&AS, 138, 55
Hurley, J. R. 2007, MNRAS, 379, 93
Hut, P., McMillan, S., Goodman, J., et al. 1992a, PASP, 104, 981
Hut, P., McMillan, S., & Romani, R. W. 1992b, ApJ, 389, 527
Ibata, R. A., Gilmore, G., & Irwin, M. J. 1994, Nature, 370, 194
Ivanova, N., Belczynski, K., Fregeau, J. M., & Rasio, F. A. 2005, MNRAS, 358, 572
Jalali, B., Baumgardt, H., Kissler-Patig, M., et al. 2012, A&A, 538, A19
Johnson, J. A. & Bolte, M. 1998, AJ, 115, 693
King, I. R. 1966, AJ, 71, 64
King, I. R., Sosin, C., & Cool, A. M. 1995, ApJ, 452, L33
Kinman, T. D. 1959, MNRAS, 119, 538
Kissler-Patig, M. & Gebhardt, K. 1998, AJ, 116, 2237
Kissler-Patig, M., Grillmair, C. J., Meylan, G., et al. 1999, AJ, 117, 1206
Kissler-Patig, M., Richtler, T., Storm, J., & della Valle, M. 1997, A&A, 327, 503
Kong, A. K. H., Heinke, C. O., di Stefano, R., et al. 2010, MNRAS, 407, L84
Kormendy, J. & Richstone, D. 1995, ARA&A, 33, 581
Larsen, S. S., Brodie, J. P., Huchra, J. P., Forbes, D. A., & Grillmair, C. J. 2001, AJ, 121, 2974
Layden, A. C. & Sarajedini, A. 2000, AJ, 119, 1760
Lupton, R. H., Gunn, J. E., & Griffin, R. F. 1987, AJ, 93, 1114
Lützgendorf, N., Kissler-Patig, M., Gebhardt, K., et al. 2012a, ArXiv e-prints
Lützgendorf, N., Kissler-Patig, M., Gebhardt, K., et al. 2012b, A&A, 542, A129
Lützgendorf, N., Kissler-Patig, M., Noyola, E., et al. 2011, A&A, 533, A36
Lynden-Bell, D. & Wood, R. 1968, MNRAS, 138, 495
Mackey, A. D. & Gilmore, G. F. 2004, MNRAS, 355, 504
Madau, P. & Rees, M. J. 2001, ApJ, 551, L27
Magorrian, J., Tremaine, S., Richstone, D., et al. 1998, AJ, 115, 2285
Marconi, A. & Hunt, L. K. 2003, ApJ, 589, L21
Marín-Franch, A., Aparicio, A., Piotto, G., et al. 2009, ApJ, 694, 1498
Mashchenko, S. & Sills, A. 2005, ApJ, 619, 258
Mayall, N. U. 1946, ApJ, 104, 290
McLaughlin, D. E., Anderson, J., Meylan, G., et al. 2006, ApJS, 166, 249
McLaughlin, D. E. & van der Marel, R. P. 2005, ApJS, 161, 304
McNamara, B. J., Harrison, T. E., & Anderson, J. 2003, ApJ, 595, 187
McNamara, B. J., Harrison, T. E., Baumgardt, H., & Khalaj, P. 2012, ApJ, 745, 175
Merritt, D. 1993, ApJ, 413, 79
Merritt, D., Meylan, G., & Mayor, M. 1997, AJ, 114, 1074
Meylan, G. & Heggie, D. C. 1997, A&A Rev., 8, 1
Michie, R. W. 1963, MNRAS, 125, 127
Michie, R. W. & Bodenheimer, P. H. 1963, MNRAS, 126, 269
Mikkola, S. 1983, MNRAS, 203, 1107
Miller, M. C. & Hamilton, D. P. 2002, MNRAS, 330, 232
Miller-Jones, J. C. A., Wrobel, J. M., Sivakoff, G. R., et al. 2012, ApJ, 755, L1
Milone, A. P., Bedin, L. R., Piotto, G., et al. 2008, ApJ, 673, 241
Milone, A. P., Piotto, G., Bedin, L. R., et al. 2012a, A&A, 540, A16
Milone, A. P., Piotto, G., Bedin, L. R., et al. 2012b, ApJ, 744, 58
Miocchi, P. 2007, MNRAS, 381, 103
Moehler, S. & Sweigart, A. V. 2006, A&A, 455, 943
Moore, B. 1996, ApJ, 461, L13
Moore, B., Diemand, J., Madau, P., Zemp, M., & Stadel, J. 2006, MNRAS, 368, 563
Moretti, A., Piotto, G., Arcidiacono, C., et al. 2009, A&A, 493, 539
Morgan, W. W. 1959, AJ, 64, 432
Mouri, H. & Taniguchi, Y. 2002, ApJ, 566, L17
Norris, J. E., Freeman, K. C., Mayor, M., & Seitzer, P. 1997, ApJ, 487, L187
Noyola, E. & Baumgardt, H. 2011, ApJ, 743, 52
Noyola, E. & Gebhardt, K. 2006, AJ, 132, 447
Noyola, E., Gebhardt, K., & Bergmann, M. 2008, ApJ, 676, 1008
Noyola, E., Gebhardt, K., Kissler-Patig, M., et al. 2010, ApJ, 719, L60
Peebles, P. J. E. 1972, ApJ, 178, 371
Peebles, P. J. E. 1984, ApJ, 277, 470
Perlmutter, S., Aldering, G., Goldhaber, G., et al. 1999, ApJ, 517, 565
Piotto, G., Bedin, L. R., Anderson, J., et al. 2007, ApJ, 661, L53
Piotto, G., Milone, A. P., Anderson, J., et al. 2012, ApJ, 760, 39
Piotto, G., Villanova, S., Bedin, L. R., et al. 2005, ApJ, 621, 777
Portegies Zwart, S. F. & McMillan, S. L. W. 2002, ApJ, 576, 899
Pryor, C. P., Latham, D. W., & Hazen, M. L. 1988, AJ, 96, 123
Recio-Blanco, A., Aparicio, A., Piotto, G., de Angeli, F., & Djorgovski, S. G. 2006, A&A, 452, 875
Renzini, A. & Fusi Pecci, F. 1988, ARA&A, 26, 199
Richstone, D. O. & Tremaine, S. 1985, ApJ, 296, 370
Riess, A. G., Filippenko, A. V., Challis, P., et al. 1998, AJ, 116, 1009
Rosenberg, A., Saviane, I., Piotto, G., & Aparicio, A. 1999, AJ, 118, 2306
Sandage, A. & Wallerstein, G. 1960, ApJ, 131, 598
Sandage, A. R. 1953, AJ, 58, 61
Sarajedini, A. & King, C. R. 1989, AJ, 98, 1624
Sarajedini, A. & Layden, A. C. 1995, AJ, 109, 1086
Schechter, P. L., Mateo, M., & Saha, A. 1993, PASP, 105, 1342
Schwarzschild, M. 1979, ApJ, 232, 236
Searle, L. & Zinn, R. 1978, ApJ, 225, 357
Shapiro, S. L. & Lightman, A. P. 1976, Nature, 262, 743
Silk, J. & Rees, M. J. 1998, A&A, 331, L1
Sollima, A., Beccari, G., Ferraro, F. R., Fusi Pecci, F., & Sarajedini, A. 2007, MNRAS, 380, 781
Sommariva, V., Piotto, G., Rejkuba, M., et al. 2009, A&A, 493, 947
Spitzer, L. 1987, Dynamical evolution of globular clusters
Stetson, P. B. 1987, PASP, 99, 191
Strader, J., Chomiuk, L., Maccarone, T. J., et al. 2012, ApJ, 750, L27
Takahashi, K. & Lee, H. M. 2000, MNRAS, 316, 671
Tolstoy, E., Irwin, M. J., Helmi, A., et al. 2004, ApJ, 617, L119
Trager, S. C., King, I. R., & Djorgovski, S. 1995, AJ, 109, 218
Trenti, M., Ardi, E., Mineshige, S., & Hut, P. 2007, MNRAS, 374, 857
Ulvestad, J. S., Greene, J. E., & Ho, L. C. 2007, ApJ, 661, L151
van de Ven, G., van den Bosch, R. C. E., Verolme, E. K., & de Zeeuw, P. T. 2006, A&A, 445, 513
van den Bosch, R., de Zeeuw, T., Gebhardt, K., Noyola, E., & van de Ven, G. 2006, ApJ, 641, 852
van der Marel, R. P. & Anderson, J. 2010, ApJ, 710, 1063
van der Marel, R. P., Gerssen, J., Guhathakurta, P., Peterson, R. C., & Gebhardt, K. 2002, AJ, 124, 3255
Vesperini, E. & Heggie, D. C. 1997, MNRAS, 289, 898
Vesperini, E. & Trenti, M. 2010, ApJ, 720, L179
Villanova, S., Piotto, G., King, I. R., et al. 2007, ApJ, 663, 296
Volonteri, M. 2010, A&A Rev., 18, 279
Whitmore, B. C. & Schweizer, F. 1995, AJ, 109, 960
Wilson, C. P. 1975, AJ, 80, 175
Wisotzki, L., Becker, T., Christensen, L., et al. 2003, A&A, 408, 455
Wyller, A. A. 1970, ApJ, 160, 443
Zepf, S. E. & Ashman, K. M. 1993, MNRAS, 264, 611
Zinn, R. 1985, ApJ, 293, 424

Chapter 2

Resolving stellar populations with crowded field 3D spectroscopy[⋆]

Sebastian Kamann[1], Lutz Wisotzki[1], Martin M. Roth[1]

[1] Leibniz-Institut für Astrophysik Potsdam (AIP), An der Sternwarte 16, 14482 Potsdam, Germany

ABSTRACT

We describe a new method of extracting the spectra of stars from observations of crowded stellar fields with integral field spectroscopy (IFS). Our approach extends the well-established concept of *crowded field photometry* in images into the domain of 3-dimensional spectroscopic datacubes. The main features of our algorithm follow. (1) We assume that a high-fidelity input source catalogue already exists, e.g. from HST data, and that it is not needed to perform sophisticated source detection in the IFS data. (2) Source positions and properties of the point spread function (PSF) vary smoothly between spectral layers of the datacube, and these variations can be described by simple fitting functions. (3) The shape of the PSF can be adequately described by an analytical function. Even without isolated PSF calibrator stars we can therefore estimate the PSF by a model fit to the full ensemble of stars visible within the field of view. (4) By using sparse matrices to describe the sources, the problem of extracting the spectra of many stars simultaneously becomes computationally tractable. We present extensive performance and validation tests of our algorithm using realistic simulated datacubes that closely reproduce actual IFS observations of the central regions of Galactic globular clusters. We investigate the quality of the extracted spectra under the effects of crowding with respect to the resulting signal-to-noise ratios (S/N) and any possible changes in the continuum level, as well as with respect to absorption line spectral parameters, radial velocities, and equivalent widths. The main effect of blending between two nearby stars is a decrease in the S/N in their spectra. The effect increases with the crowding in the field in a way that the maximum number of stars with useful spectra is always ~0.2 per spatial resolution element. This balance breaks down when exceeding a total source density of one significantly detected star per resolution element. We also explore the effects of PSF mismatch and other systematics. We close with an outlook by applying our method to a simulated globular cluster observation with the upcoming MUSE instrument at the ESO-VLT.

2.1. Introduction

The observation of spatially resolved, but densely populated stellar fields, such as star clusters or the inner regions of very nearby galaxies, poses a severe challenge because of crowding. At finite angular resolution each star is represented by the point spread function (PSF) characteristic of the system. Observable is only the superposition of many scaled and shifted PSFs, according to brightness and position of the stars in the field of view. It is then a major task to disentangle the various overlapping PSFs in order to measure the corresponding stellar fluxes as accurately as possible.

In imaging photometry, this challenge was already addressed many years ago, and dedicated analysis tools have been developed to perform what is commonly termed “crowded field photometry”. `daophot` (Stetson 1987) is the most widely used of such tools and it has been applied extensively and with great success. At the core of `daophot` (and similar software) is a code that fits a PSF model simultaneously or in succession to all stars within a given field. The resulting photometry is unbiased with respect to overlapping stellar images (within the accuracy of the PSF model and as long as the list of fitted stars is complete), so that even heavily blended stars can be recovered.

However, the astrophysically desirable move from photometry to spectroscopy is still fraught with difficulties when it comes to crowded stellar fields. Traditional long-slit (or multi-slit) spectroscopy is clearly limited by the amount of blending within the slit aperture, which under conditions of heavy crowding may almost be impossible to control. The same is true for fibre-fed multiplexing spectroscopy using single apertures. Consequently, investigations using this type of equipment have typically restricted themselves to regions with modest crowding, such as the outer parts of star clusters or galaxies, and/or focused on the brightest sources in the fields of interest. A notable exception is the study by van der Marel et al. (2002) and Gerssen et al. (2002) who performed HST long-slit spectroscopy of the centre of the globular cluster M15. Here the improved spatial resolution of HST helped in dealing with the limitations of traditional spectroscopy.

Potentially much more powerful in this domain is the direct combination of imaging and spectroscopy. ‘Integral Field Spectroscopy’ (IFS) – often also called 3D or IFU spectroscopy (IFU = integral field unit) – has matured into a widely used observing technique over the last decade. It is particularly powerful for extended objects such as galaxies, by providing access to spectroscopic information across the full spatial extent of the target. Integral field spectroscopy has strongly advanced our knowledge of galaxies, both in the local universe (e.g., de Zeeuw et al. 2002; Cappellari et al. 2011) and at higher redshifts (e.g., Förster Schreiber et al. 2009).

[⋆] This Chapter is published in *Astronomy & Astrophysics*, V.549, 2013, p. A71+. Some references to the other Chapters of this thesis have been added, but the scientific content has not been changed.

Beyond the ability to trace the variation of observable properties across the field of view (FoV), IFS data also provide the user with an unprecedented access to single out individual objects surrounded by (and possibly blended with) other sources. This can be done in increasing levels of sophistication. A straightforward approach in stellar fields is to identify spatial pixels that are dominated by the contribution of a single star and obtain a spectrum of that star by summing the spectra in only those pixels. An example is the recent work by Evans et al. (2011), who used IFS to obtain spectra of massive stars in the Tarantula nebula (30 Doradus). A similar treatment was applied to near-infrared IFS observations of stars in the Galactic centre by Eisenhauer et al. (2005) and Pfuhl et al. (2011). While scientifically very successful, this approach is obviously still limited to moderate crowding conditions.

To facilitate the extraction of the spectra, knowledge of the spatial shape of the sources must be incorporated. Especially when dealing with barely resolved or still unresolved sources, a proper knowledge of the PSF becomes extremely important. Unfortunately, the fields of view of existing IFS instruments are so small that they often do not contain any undisturbed PSF calibrator. In order to proceed, it thus becomes necessary to estimate the PSF directly from the data. Several authors have presented solutions to this task, although ones usually restricted to specific science applications. For the severely background-limited spectrophotometry of planetary nebulae (PN) in the bulge of M31, Roth et al. (2004) estimated the PSF from a bright PN image in [O III] and fitted this to each wavelength bin of the datacube. Fabrika et al. (2005) applied the `cplucy` algorithm (Lucy 1994) with input from high spatial resolution HST images to extract spectra of LBV candidates in M33, while fully accounting for a highly variable unresolved background. Technical details of these two applications are discussed in Becker et al. (2004). In a similar spirit, the bright nuclear emission lines of quasars can be used to 'self-calibrate' the PSF for the analysis of quasar host galaxies (Jahnke et al. 2004; Christensen et al. 2006; Husemann et al. 2011). However, due to the lack of emission-line point sources, these procedures cannot be applied to arbitrary stellar fields. Another limitation lies in the fact that emission lines provide the PSF only at specific wavelengths, and an extrapolation to the full spectral range may be doubtful.

A more general approach was explored by Wisotzki et al. (2003) who deblended the four overlapping components of the gravitationally lensed QSO HE 0435-1223 from IFS data by assuming a purely analytic (but wavelength-dependent) PSF shape that was iteratively optimized. The main limitation of this particular solution was its computational inefficiency, which would make an application to fields with many more sources prohibitive. Sánchez et al. (2007) extended this approach to non-point sources in an IFS study of the galaxy cluster Abell 2218, where they used the morphological information on individual galaxies obtained from high-resolution imaging to deblend the overlapping data into individual galaxy spectra.

In this paper we present a new algorithm for the spectrophotometric analysis of generically crowded stellar fields observed by integral field spectroscopy. The algorithm determines a fully self-calibrated wavelength-dependent PSF model that is subsequently fitted to the entire datacube. In many aspects the algorithm is an extension of the well-established 'crowded field photometry' approach, but the spectroscopic dimension requires the addition of some genuinely new features. While we were completing this paper, Soto et al. (2012) published an analysis of IFS observations in the Galactic bulge, which includes PSF estimation and bears some generic resemblance to our approach. Unfortunately, not many details are provided in that paper on the algorithm itself and its performance.

The purposes of the present paper are twofold. Firstly, the paper provides the methodical foundations for a number of subsequent articles focusing on the central regions of globular clusters (Kamann et al., in prep., also Chapters 3-5 of this thesis). Here we use some of those data only for illustration purposes. Secondly, we also want to highlight the huge potential of IFS for crowded field spectroscopy in general, especially in view of the upcoming wide-field panoramic integral field spectrograph MUSE at the ESO-VLT.

The paper is organized as follows. In Sect. 2.2 we start by describing the basic considerations that went into developing our method. An overview of the observational data that motivated this study and of the simulated data that we created to test our algorithm is given in Sect. 2.3. The analysis algorithm itself is presented in detail in Sect. 2.4. Section 2.5 describes the extensive tests that we carried out to validate its performance. A discussion of potential sources that could systematically influence the performance of the algorithm is presented in Sect. 2.6. In Sect. 2.7 we briefly demonstrate the application of our method to data that will soon be obtained with the MUSE instrument. We wrap up our conclusions in Sect. 2.8.

2.2. Basic concepts

In a simplified picture, an integral field datacube can be considered a sequence of monochromatic images, hereafter called layers. A straightforward approach would then be to use existing methods to analyse the data cube layer by layer, i.e. to perform crowded field *photometry* individually on each layer, and combine the results afterwards, and yet, as we demonstrate in the following, such an approach does not use the full potential of IFS data.

The development of our new algorithm was guided by the following thoughts:

(1) For many objects, such as most globular clusters or several nearby galaxies, high-resolution images are already available (e.g., the HST/ACS survey of Galactic globular clusters by Sarajedini et al. 2007). The depth reached by these images is usually sufficient to assume that all stars that can be resolved with a (seeing-limited) IFU have been detected, and that their relative positions are known. Thus, an inventory of stars in the observed field already exists, and there is no need to perform sophisticated source detection on the integral field data. But of course the question remains which sources from an available catalogue can be recovered in the datacube. Given the typically lower spatial resolution of IFS data, only a subset of the catalogued sources will be accessible to the analysis. We describe in Sect. 2.4.5 how we derive an optimal subset of sources from a catalogue that can be extracted reliably.

(2) The individual monochromatic layers of a data cube are not independent of one another. Because all of them were observed simultaneously, temporal effects like seeing variability, atmospheric dispersion, and instrument flexure affect all images in such a way that properties such as the PSF or source positions are interconnected. While they may vary from layer to layer, these variations will be smooth with wavelength. We thus should use the whole datacube to determine one (wavelength-dependent) PSF model and one set of (wavelength-dependent) coordinates. The potential of IFS to obtain coordinates with a precision beyond that achievable with a single image at the same spatial resolution has been demonstrated previously (e.g., Mediavilla et al. 1998; Wisotzki et al. 2003).

(3) For the current generation of integral field spectrographs, the relatively small field of view often implies that sufficiently bright and isolated PSF calibrator stars are not available within a science exposure. Dedicated (i.e. non-simultaneous) observations of isolated stars are of very limited use for accurate PSF modelling because of the temporal variations in the PSF. In the future it may become possible to predict the PSF from adaptive optics wavefront sensor data (e.g., Jolissaint et al. 2010). For the present, however, we are bound to estimate the PSF directly from the crowded field science data. Nevertheless, this information is actually there – not in individual stars, but encased in the ensemble of all stars in the field. In Sect. 2.4.2 we present an iterative procedure to construct a global PSF model by simultaneous fitting of the full ensemble.

(4) Besides the spectra of individually resolved stars, an IFS data cube may also contain a background of fainter and possibly unresolved stars and/or nebular emission. This quasi-diffuse component can be a major nuisance as a source of systematic errors during the extraction of stellar spectra, but it is also possible that the scientific focus is mainly directed towards this component. For these reasons we made a special effort to find an appropriate solution to account for such a non-trivial background component in the analysis. This is explained in detail in Sect.2.4.

2.3. Data

2.3.1. Observations of globular clusters

We recently collected 3D spectroscopy data of a sample of Galactic globular clusters with the instruments PMAS (Roth et al. 2005) and ARGUS (Pasquini et al. 2002). In each cluster we mapped the central region out to a distance comparable to the core radius of the cluster. The main scientific aims are (1) to search for binary stars and (2) to place constraints on the possible presence of intermediate-mass black holes in the clusters. The results from these observations will be presented in forthcoming papers (Kamann et al, in prep., also Chapters 3-5 of this thesis).

The instrument setups in these observations varied a little from campaign to campaign, but were generally chosen to facilitate a kinematic analysis given the expected velocity dispersions of the clusters. The typical spectral resolution $R = \lambda/\Delta\lambda$ was ~8000, and the spectral range was targeted at the calcium triplet ($\lambda\lambda$8498 Å, 8542 Å, 8662 Å). To sample the PSF in the best possible way, we always selected the smallest available spaxel scale (spaxel = spatial pixel), $0\farcs3$ for ARGUS and $0\farcs5$ for PMAS. With 16×16 spaxels for PMAS and 22×14 for ARGUS, we thus covered an area per pointing of $8'' \times 8''$ and $6\farcs6 \times 4\farcs2$, respectively. The seeing conditions were variable, with $\sim 0\farcs7$ in the best and $1\farcs4$ in the worst case. Some whitelight images are presented in Fig. 2.1 to give an impression of the data. The crucial dependence of the data quality on the seeing during the observations is clearly visible.

2.3.2. Simulated data

To assess the the performance of our algorithm and to validate the quality of the deblended spectra we carried out extensive simulations. In line with our main scientific interest we focus on globular clusters, but the results are of course applicable to any sort of crowded stellar fields. At any rate the central regions of globular clusters display some of the most challenging cases of crowding that current instruments are capable of dealing with.

The preparation of the simulated data can be summarized as follows. We used the V- and I band photometry of the globular cluster 47Tuc from Sarajedini et al. (2007) and Anderson et al. (2008). To assign a realistic spectrum to each star, we constructed a single isochrone (t = 13 Gyr, Z = 0.0045), using the tool of Marigo et al. (2008)[1]. For each star we thus obtained estimates of T_{eff} and $\log g$ that were in turn used to select an appropriate spectrum from the stellar library of Munari et al. (2005). The library spectra have an intrinsic spectral resolution of $R = 20000$ and cover the entire wavelength range from 2500 Å to 10000 Å. In order to resemble our observational data, we extracted only the region around the calcium triplet and convolved the spectra with a Gaussian to obtain a final resolution of $R \sim 7000$.

To simulate realistic datacubes, random fields of $8'' \times 8''$ (the FoV of the PMAS instrument) were selected from the central region of 47Tuc. Stars in those fields were represented by their respective spectra, and a velocity drawn randomly from a normal distribution with σ = 10km/s, similar to the velocity dispersion in the centre of this cluster (McLaughlin et al. 2006), was assigned to each spectrum. Using an analytical PSF profile with a full width at half maximum (FWHM) corresponding to a seeing around 1.0″, cubes with 16 × 16 spatial pixels were prepared. Finally, appropriate noise was added. The resulting spatial sampling was 0.5″/pixel, again to resemble observational data obtained with PMAS. An example of the simulated data is given in Fig. 2.2. In the following, we refer to those datacubes as the *'crowded field datacubes'*.

Besides these rather realistic datacubes, we also prepared idealized cubes containing only two stars. We used these to investigate different aspects of the deblending procedure in isolation. The spectra of the stars were assigned using the same procedure as for the crowded field datacubes. We refer to these simulated data as the *'two star datacubes'*.

2.4. Deblending and extraction of spectra: Algorithm

2.4.1. Global model

We first clarify our adopted symbol and naming scheme. The datacube at hand is supposed to have pixel values $\mathfrak{d}_{i,j,k}$, where the first two indices relate to spatial coordinates and the index k to the spectral axis. To denote different stellar sources in the datacube we use the superscript n while background components have a superscript m. A model datacube is then described as the sum of all sources that contribute flux,

$$\mathfrak{m}_{i,j,k} = \sum_n f_k^n \ \mathrm{psf}_{i,j,k}^n + \sum_m b_{i,j,k}^m \, . \tag{2.1}$$

In Eq. 2.1, f_k^n is the total monochromatic flux of star n in layer k, and $\mathrm{psf}_{i,j,k}^n$ is the fraction of f_k^n in the considered pixel. This fraction is equal to the value of the normalized PSF of star n at the spatial position (i, j) and at spectral pixel k. The flux in each pixel of background component m is given by $b_{i,j,k}^m$. For a spatially constant background (such as the night sky), $b_{i,j,k}^m$ will only depend on k. An example for a background whose intensity varies across the field of view is the contribution of unresolved stars to the observed flux; this will be discussed in Sect.2.4.6. The second sum in Eq. 2.1 can be expanded further to also include spatially resolved sources that might be present in the datacube. An example for such a component might be gaseous line

---

[1] available at `http://stev.oapd.inaf.it/cgi-bin/cmd_2.3`

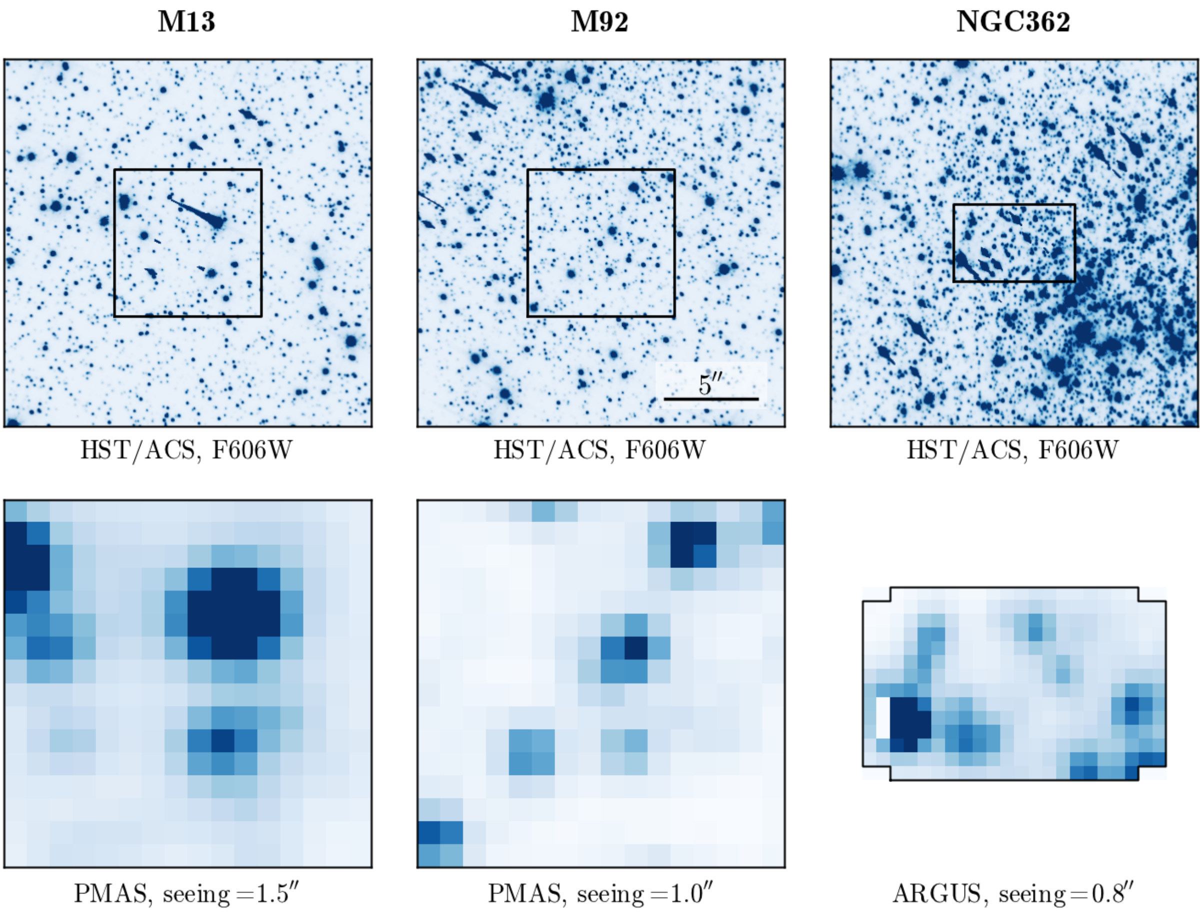

Fig. 2.1. Impressions from the observations of several globular clusters that we obtained using the integral field spectrographs PMAS and ARGUS. The upper row shows a 20″ × 20″ cut-out from an HST/ACS image with the footprint of a single integral field observation. A whitelight image of each integral field data cube is shown below. In each image, north is up and east is left.

emission in the observation of a young star cluster. Here we restrict the discussion to fields in where the flux is dominated by stellar continuum sources.

Starting from Eq. 2.1, we then search for the best (in a least-squares sense) model for a given dataset. We therefore have to minimize

$$\chi^2 = \sum_{i,j,k} \frac{\left(\mathfrak{d}_{i,j,k} - \sum_n f_k^n \ \mathrm{psf}_{i,j,k}^n - \sum_m b_{i,j,k}^m\right)^2}{\sigma_{i,j,k}^2} \,. \qquad (2.2)$$

Here, $\sigma_{i,j,k}^2$ is the variance tailored to each pixel value. Unfortunately, straightforward minimization of Eq. 2.2 is computationally very demanding for the large parameter space that needs to be covered: in each layer k, a stellar source will contribute three free parameters (f_k^n, x_k^n, and y_k^n), and a background component will contribute at least one additional free parameter. In addition, several free parameters might be needed to find a suitable model for the PSF of the observation. A further complication is that Eq. 2.2 represents a non-linear minimization problem.

To make the search for a solution feasible, we split the optimization into three tasks: (i) an optimization for the PSF, (ii) an optimization for the source coordinates, and (iii) an optimization for the fluxes. In each step, the model is optimized only with respect to one of these three properties, while the other two remain fixed to their current value. After one step has converged, the model parameters currently in focus are updated to their best-fit values and the model is optimized for the next set of parameters. On each layer k, the steps (i) to (iii) are then iteratively repeated until convergence is found for the fluxes of the sources.

The practical implementation of our approach can be summarized as follows. We start with an initial guess for the PSF and the source coordinates and use them to fit the fluxes in the central layer of the datacube. The reason for starting at the central layer is that the efficiency of the spectrograph should be highest at the centre of the covered wavelength range, and therefore the data should give the tightest constraints on the model. After the iteration has converged to a solution for the central layer, we continue with the two adjacent layers. In this way, the analysis proceeds simultaneously to the red and blue ends of the covered wavelength range. An integral field datacube provides a convenient structure for such an iterative approach, as the changes in the PSF or source coordinates between two adjacent layers are always small, so the best-fit model of the previous layer is already a very good starting point for the analysis of the next one. A potential drawback of this approach is that if a single layer returns a strongly deviating model, such as is caused by an undetected cosmic-ray hit or strong telluric absorption, it will affect the analyses of subsequent layers. To avoid this, we generate initial guesses by averaging over the best-fit models of the last N layers, with N typically being of the order of 10.

In general, we do not consider cosmic ray hits as a major problem. The structure of raw IFS data actually allows for a con-

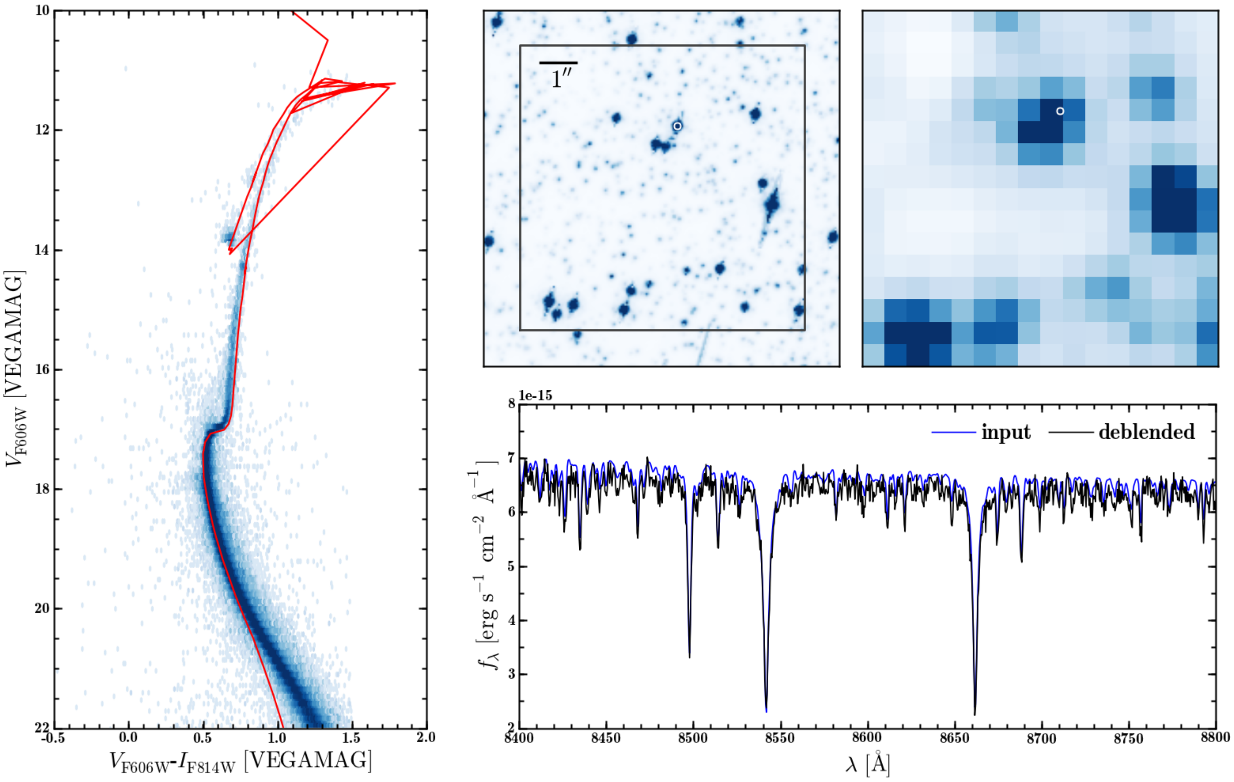

Fig. 2.2. Illustration of how the simulated data was produced and processed. Left panel: Input colour-magnitude diagram of 47Tuc. Overplotted is the isochrone that was used to assign spectra to the individual stars. Upper panels: Cut-out from an HST image of 47Tuc (upper middle); whitelight image of a simulated crowded field datacube centred on the HST footprint (upper right). The lower right panel shows the deblended spectrum of the star marked with a white circle. The input spectrum of this star is overplotted.

venient method to remove cosmic rays before performing the data reduction (Husemann et al. 2012). Additionally, it is possible to significantly reduce the influence of undetected cosmic rays in the analysis. Stetson (1987) presented a robust scheme that dynamically reduces the weights of pixels with strong residuals, and it is also applicable to IFS data.

After all layers of the cube have been processed, their respective best-fit models are combined to produce a coherent wavelength-dependent PSF model and to determine source coordinates as a smooth function of wavelength. Using this information, the datacube is then processed for a second time, yet this time only the fluxes are fitted and we obtain the final spectra of the sources.

After a few layers have been analysed, the analyses of the red and blue halves of the datacube proceed independently of each other. Thus, comparing the results obtained at the red and blue end can be used to check the reliability of the obtained model.

2.4.2. Modelling the PSF

The usual approach to determining the PSF in crowded field photometry is to select a number of relatively isolated stars and fit them with an analytical function. To account for possible mismatches between the analytical profile and the shape of the true PSF, an empirical look-up table correction is frequently applied afterwards.

As discussed above, this approach cannot be applied to IFS datacubes without modification, mainly because of the very small FoV. Our adopted approach is to instead use the full ensemble of resolved stars within a field to reconstruct a global PSF model, obtained by means of a least squares fit of Eq. 2.2 to the data. The approach to recovering the PSF using all stars in the field has previously been used by Schechter et al. (1993). A notable difference of our implementation is that the PSF is fitted to all stars simultaneously instead of in a sequential manner. Similar to Schechter et al. (1993), we restrict the PSF description to a purely analytical model, since the construction of a reliable look-up table requires not only sufficiently isolated stars, but also a very well-sampled PSF. With the somewhat coarse spatial sampling of many IFUs, this cannot always be taken for granted. But as the typical signal-to-noise ratio (S/N) per spectral pixel is much lower than in broad-band images, an analytical model should be adequate in most cases.

To define an analytical PSF model we follow the approach adopted in `GALFIT` (Peng et al. 2002). In general, the PSF will not be round but rather have an elliptical shape, with ellipticity e and position angle θ. To account for the ellipticity, the pixel coordinates x and y are first transformed into a coordinate system ($\hat{x}$, $\hat{y}$) centred on the origin of the star, and its $\hat{x}$-axis is aligned with the semi-major axis of the PSF:

$$\hat{x} = (x - x^n)\cos\theta - (y - y^n)\sin\theta, \tag{2.3}$$
$$\hat{y} = (x - x^n)\sin\theta + (y - y^n)\cos\theta, \tag{2.4}$$

with (x^n, y^n) being the pixel coordinates of source n. The distance to the centre of the PSF can now be written as as an angle-dependent quantity,

$$r(x, y) = \sqrt{\hat{x}^2 + \left(\frac{\hat{y}}{1-e}\right)^2}. \tag{2.5}$$

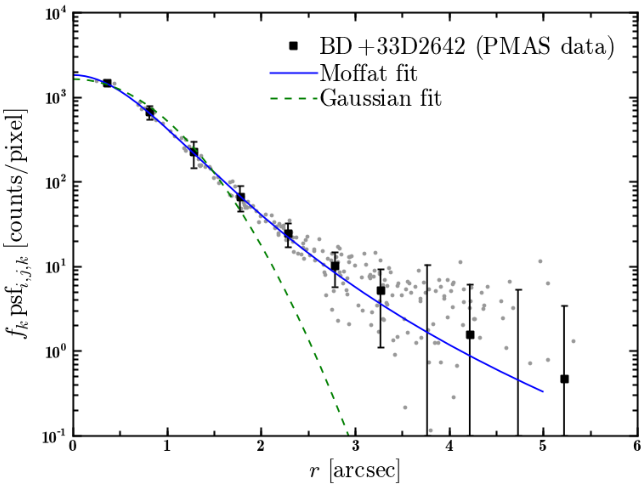

Fig. 2.3. Radial surface brightness profile of the star BD+33D2642 as measured in a PMAS datacube. Small grey dots show the flux in individual pixels, the black squares were obtained by radially binning the data. We used a Moffat profile and a simple Gaussian profile as the analytical PSF description and fitted the star with both PSF models. The blue solid line shows the best-fit PSF when using the Moffat, the green dashed line shows the best-fit PSF for the Gaussian profile.

To describe the radial shape of the PSF we adopt the Moffat profile, with a functional form given as

$$M(x,y) = \Sigma_0 \left(1 + \left(\frac{r(x,y)}{r_\mathrm{d}}\right)^2\right)^{-\beta} . \qquad (2.6)$$

The width of the Moffat profile is mainly determined by the dispersion radius r_d, while the β-parameter defines the kurtosis of the profile, i.e the broadness of the wings of the PSF. The FWHM of the Moffat profile can be expressed in terms of r_d and β as

$$\mathrm{FWHM} = 2\sqrt{2^{1/\beta} - 1}\, r_\mathrm{d} . \qquad (2.7)$$

This leaves us with four free PSF shape parameters per layer: β, FWHM, e, and θ. Depending on the quality of the data to be analysed, the number of free parameters can be reduced, for example by assuming a Gaussian instead of a Moffat profile or by enforcing a circular PSF. The central intensity Σ_0 of the PSF is directly tied to the monochromatic flux of a source.

For each star n in the analysis, an empty array of the same size as a layer of the datacube is created. Its pixel values are set to the intensity of a normalized PSF at a radius $r(x,y)$, using the current best-fit values for the source coordinates (x_k^n, y_k^n). Nonetheless directly using Eq. 2.6 to determine the pixel values $\mathrm{psf}^n_{i,j,k}$ can lead to systematic errors close to the origin of the profile if the sampling of the PSF approaches critical values. In such cases, the change of $M(x,y)$ within one pixel is so strong that its value at the centre of a pixel is not a good approximation for the integrated PSF intensity in that pixel. Currently, we solve this problem by supersampling each pixel within a certain distance to the centre of the PSF by a factor of typically 25–100 and calculating the intensity for each subpixel. The final value of each pixel is then obtained by summing over its subpixels. Numerical integration schemes such as the one presented by Buonanno & Iannicola (1989) can significantly reduce the number of required subpixels and will be considered in our ongoing development of the algorithm. Once a PSF has been prepared for each source, we can use Eq.2.2 to optimize the PSF model for each layer of the datacube. After all layers have been processed, the results of the individual layers are modelled as a smooth function of wavelength for each free parameter of the PSF model. Following Wisotzki et al. (2003), we use low order polynomials for this task. This way we finally obtain the wavelength-dependent PSF.

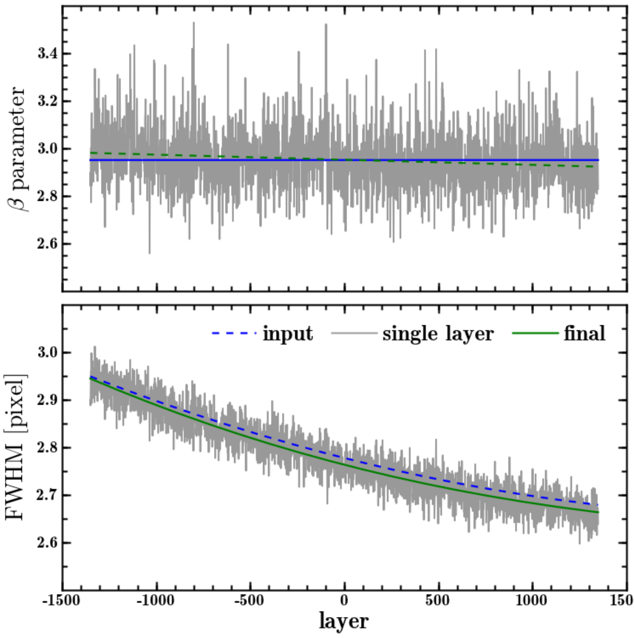

Fig. 2.4. Example for the recovery of the PSF in a datacube. Shown is the accuracy of the recovered PSF parameters β (*top*) and FWHM (*bottom*) in comparison to their true values (blue dashed line). The grey solid line gives the best-fit values of the PSF parameters obtained in each layer and the final parameters of the PSF model obtained from these values are shown as a solid green line. The analysis was started at the central image of the datacube and proceeded simultaneously to the red and blue ends of the cube.

To illustrate that our approach results in a valid description of the PSF in integral field data we analysed one of our PMAS datacubes of the standard star BD+33D2642. The datacube contains a single star and thus allows for a precise measurement of the PSF even in the faint wings. We analysed the data in the way just described, using a single point source and a background component. In Fig. 2.3 a comparison is shown between a PSF as it is measured from our PMAS data and our analytical profiles. It is obvious that a Moffat profile provides a good overall representation of the PSF. On the other hand, using a Gaussian severely underestimates the wings of the PSF.

We used the simulated ‘crowded field datacubes’ to investigate how well our approach can recover the PSF in a dense stellar field. We produced 100 cubes based on a wavelength-dependent PSF represented by a Moffat profile with constant β and varying FWHM. An example for the PSF recovery is shown in Fig. 2.4. It demonstrates that the constraints on the PSF in an individual layer are not very stringent, as can be seen by the large scatter especially for the β fits, and yet the final combination of all individual fits yields a wavelength-dependent model that is a very close representation of the true PSF.

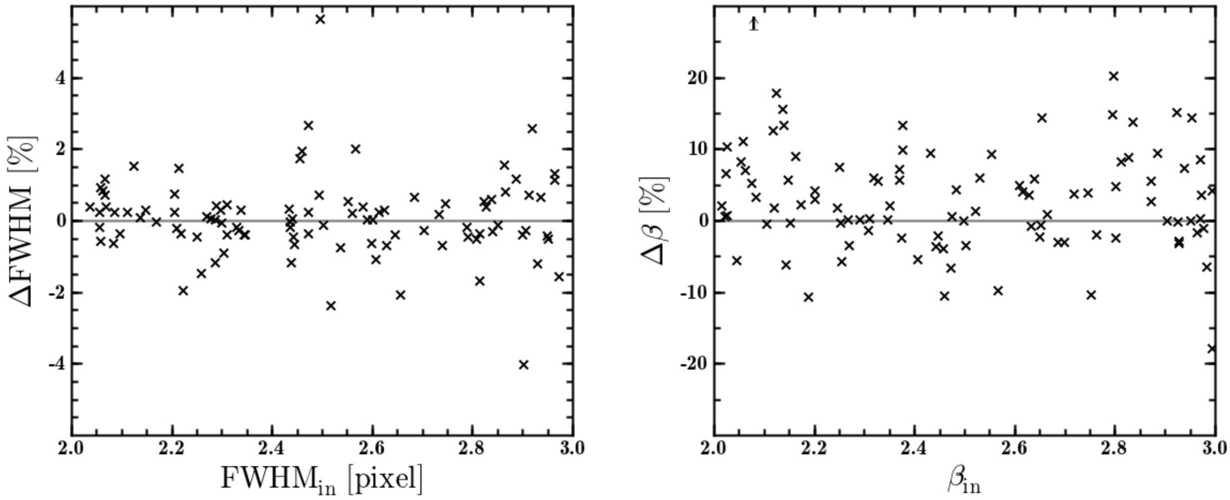

Fig. 2.5. Comparison between recovered and input PSF parameters for 100 simulated crowded field datacubes. The PSF was modelled using a Moffat profile with wavelength-dependent FWHM and constant β parameter. Shown is the mean fractional difference in percent, between recovered and true FWHM (*left*) and β parameter (*right*), respectively, as a function of the input values. A single outlier of $\Delta\beta \sim 60\%$ falls out of the plotted range and is shown as a lower limit.

To obtain a statistical impression of the accuracy of the PSF recovery, we analysed the full sample of 100 simulated 'crowded field datacubes' and compared the recovered PSF parameters to the input. The results of this comparison are shown in Fig. 2.5.

These plots show that the FWHM of the PSF can usually be recovered to an accuracy of 1–2%, while the recovered value of β usually agrees with the input value to within 10%. Thus, the PSF width is better constrained than the β parameter, similar to what we observed in Fig. 2.4. This is well known and is because β governs the outer wings of the PSF where the signal is generally low. But this also implies that errors in β do not influence the overall optimization (Eq. 2.2) as much as mismatches in FWHM.

Furthermore, it is reassuring that the recovered values of the FWHM are unbiased in the sense that they scatter around the 'true' value. This is not strictly the case for β, which tends to come out slightly too high (by a few percent), thus corresponding to a PSF with slightly less pronounced wings than was put into the simulations. This is probably because for high source densities, the ensemble of faint wings of each PSF can be misidentified as being part of the background; so apparently a very small fraction is, on average, transferred out of the wings of the stars used for the PSF estimation and into the background component. We discuss the consequences of the achievable PSF accuracy on the quality of the extracted spectra in detail in Sect. 2.5.

2.4.3. Source positions

We assume that a source catalogue based on high-resolution imaging already exists. The task is thus to find a global transformation from a reference system (i.e. the source coordinates in the catalogue) to the coordinate system of the datacube. At least four parameters are required to describe this transformation: a rotation angle α, a pixel scaling factor ξ, and a shift along both spatial axes, C and D. If we denote the coordinates of an object in the reference system by (u^n, v^n), we can write down the coordinate transformation for a single layer as

$$x_k^n = \xi_k\,(\cos\alpha_k\,u^n + \sin\alpha_k\,v^n) + C_k\,, \tag{2.8}$$

$$y_k^n = \xi_k\,(-\sin\alpha_k\,u^n + \cos\alpha_k\,v^n) + D_k\,. \tag{2.9}$$

Substituting $A_k = \xi_k \cos\alpha_k$ and $B_k = \xi_k \sin\alpha_k$, Eqs. 2.8 and 2.9 can be rewritten as

$$x_k^n = A_k\,u^n + B_k\,v^n + C_k\,, \tag{2.10}$$

$$y_k^n = A_k\,v^n - B_k\,u^n + D_k\,. \tag{2.11}$$

Equations 2.10 and 2.11 define a system of $2N$ linear equations, where N is the number of sources taken into account. While the transformation will be wavelength dependent, this dependency can be further constrained taking into account that:

(i) for instruments such as PMAS or ARGUS, where each spaxel is coupled to an optical fibre guiding the light into the spectrograph, neither α nor ξ should depend on wavelength, and

(ii) the variation in both C and D with wavelength due to atmospheric dispersion can be predicted using a model for the wavelength-dependent atmospheric refractive index during the observation. Such predictions as a function of airmass and parallactic angle have been derived, e.g., by Filippenko (1982); also see Sandin et al. (2012) for an overview of different approaches. For the range of airmasses ($\lesssim$ 2) of our PMAS data, an offset up to 0.″2 (equivalent to 0.4 spaxels) is predicted across the covered wavelength range, quite similar to the values we actually measure.

One might use this information to already eliminate the wavelength dependency in Eqs. 2.10 and 2.11 in the data reduction and then assume a single transformation for all layers of the cube. However, such a correction would involve resampling the data, which we believe is to be avoided as much as possible. Instead, we start by finding a best-fit solution for every layer separately and then use the information to constrain the transformation a posteriori: After all layers have been analysed, we determine the IFU coordinates x^n and y^n of every source as a smooth function of wavelength. To fix the rotation angle and the pixel scaling to a common value for all layers of the datacube, the polynomial fits can be coupled in such a way that the change in x^n and y^n with wavelength is the same for all sources n. Furthermore, that slope can be fixed to the one predicted by atmospheric dispersion. This approach is very flexible with respect to how much a priori information should be used in determining the coordinates (e.g., the determination of the refractive

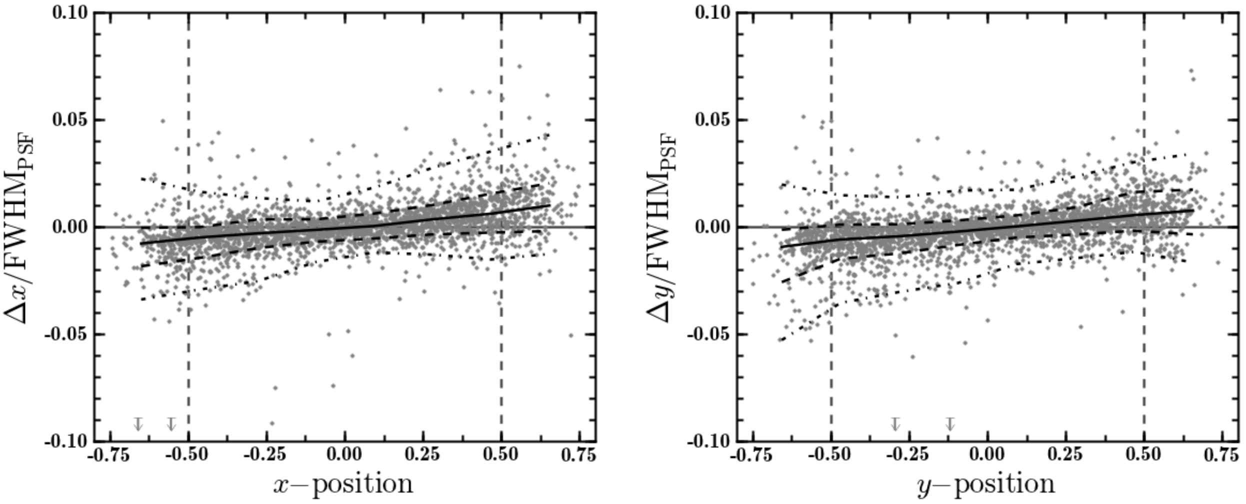

Fig. 2.6. Comparison between the recovered and true source coordinates for the sources in 100 simulated crowded field datacubes, expressed as the mean deviation in x- and y-direction relative to the FWHM of the PSF as a function of the position of each source, in units of the FoV size. Dashed vertical lines indicate the FoV edges. The median deviation along x and y is marked by a solid black line, the 68.3% and 95.4% percentiles of both distributions are indicated by the dotted and dashed black lines, respectively. A few outliers are out of the plotted range and indicated by upper limits.

index depends on an accurate knowledge of atmospheric properties such as humidity or air pressure that is not always available) and it uses the information from all layers together to obtain a final result.

Instead of fitting the parameters of Eqs. 2.10 and 2.11, we directly fit a low-order polynomial to each x^n and y^n. This is done because the variation in A to D with wavelength is not completely independent of one another. For example, to a certain extent a change in the scale factor ξ (and thus A and B) might be compensated by changes in the shifts C and D, especially when the S/N in a layer is low. Such correlated variations in the parameters on small wavelength scales would be washed out by a polynomial fit, causing larger errors in the recovered IFU coordinates.

In this simple linear model, Eqs. 2.10 and 2.11 do not account for distortions of the FoV. Given the small number of spatial pixels provided by most IFUs, this approximation should always be valid. If that should not be the case, a solution would be to expand the coordinate transformation to also include higher order terms of u^n and v^n. This will likely become important for more complex instruments such as MUSE (cf. Sect 2.7), where the FoV is split into 24 different parts that follow independent optical paths through the instrument before finally getting dispersed by different spectrographs.

One important feature in our procedure is that the global transformation model can include sources with centroids actually outside of the FoV. Of course the accuracy of the positions will decrease with increasing distance since the transformation itself can only be constrained inside the FoV, but we are mainly interested in sources close to the observed field that can still have an influence on the light distribution inside the FoV, especially in the case of bright stars.

Again, we used our 100 simulated crowded field datacubes to assess the accuracy of the recovered positions. In Fig. 2.6 we plot the offsets between the input and the recovered source positions, in units of the PSF FWHM in each cube, so that the results provide a generic measure of the achieved accuracy relative to the achieved spatial resolution.

We find that the standard deviations of the recovered coordinates from the true ones are ~ 1–2% of the FWHM of the PSF. The highest accuracy is achieved in the centre of the FoV where the coordinate transformation is best constrained. The scatter increases only slightly towards the edges of the FoV, but there is also a small systematic offset in the sense that at small x- or y-coordinates, the recovered values are on average lower than the true ones, while they are higher on average for large coordinates. With regard to the coordinate transformation, this implies that the scale factor of the transformation ξ_k is recovered too large. This behaviour can be attributed to the small FoV that we have to deal with. It leads to a significant fraction of sources that contribute to the observed flux distribution having their centres outside the FoV. In case of a small mismatch between the recovered and the true position, the strongest residuals will emerge in the region around those two positions. The more this region is pushed away from the observed field, the weaker its effect on χ^2 will be. Thus $\chi^2(\xi)$ is asymmetric towards higher values of ξ, causing the observed trend. One can obviously avoid this behaviour by making assumptions about the coordinate transformation and fixing the value of ξ_i. However, in this case the pixel scale of the integral field spectrograph must be known very precisely, to better than 0.01″ to achieve a comparable accuracy. We emphasize that this trend is extremely small and that in many cases the uncertainties of the individual high-resolution coordinates will already be higher.

2.4.4. Extraction of spectra

Once the PSF model and all source positions are known with sufficient accuracy, the least-square solution for the source spectra becomes a linear equation. We have to minimize

$$\chi^2 = |\hat{\boldsymbol{A}}\boldsymbol{a} - \boldsymbol{b}|^2 \,. \tag{2.12}$$

We denote $\hat{\boldsymbol{A}}$ the ‘PSF matrix’ because it contains the PSF of every source in the fit. $\boldsymbol{a}$ contains the object fluxes we aim at and $\boldsymbol{b}$ is the data. Note that, because of the 3-dimensional data structure, $\boldsymbol{a}$ and $\boldsymbol{b}$ are also 3-dimensional and $\hat{\boldsymbol{A}}$ is even

4-dimensional. We can then express the individual components of Eq. 2.12 as

$$A^n_{i,j,k} = \frac{\mathrm{psf}^n_{i,j,k}}{\sigma_{i,j,k}}, \tag{2.13}$$

$$a^n = f^n, \tag{2.14}$$

$$b_{i,j,k} = \frac{\mathfrak{d}_{i,j,k}}{\sigma_{i,j,k}}. \tag{2.15}$$

If we want to solve Eq. 2.12 in a least-squares sense we have to properly take into account the uncertainty $\sigma_{i,j,k}$ of each data value. To achieve this, both the data and the PSF coefficients have to be divided by the uncertainties (Press et al. 1992). It can easily be verified that substitution of Eqs. 2.13 to 2.15 into Eq. 2.12 yields Eq. 2.2.

The solution to Eq. 2.12 is obtained separately in each layer of the datacube without any coupling of the fluxes of an individual star in adjacent layers. In this sense, it is similar to performing photometry on each star in each layer (with known PSF and source coordinates) and obtaining the spectrum of each star as the combination of its individual monochromatic fluxes. However, in contrast to common crowded field photometry, the monochromatic fluxes in one layer are obtained simultaneously for all stars instead of measuring star after star.

For each spectrum that is obtained by solving Eq. 2.12 we can estimate the S/N per layer via

$$S/N_k = f_k \left(\sum_{i,j} \frac{\mathrm{psf}^2_{i,j,k}}{\sigma^2_{i,j,k}} \right)^{1/2}. \tag{2.16}$$

We note that Eq. 2.16 only takes the noise expected due to the pixel uncertainties $\sigma_{i,j,k}$ into account and therefore gives only an upper limit that does not include any noise contributions introduced by connecting the pixels in the analysis. As we show below, the true S/N in a deblended spectrum can be significantly lower.

It is worth spending a few more words on the handling of uncertainties in the analysis. Throughout this paper we assume that the uncertainties are known and correct, i.e that the true variance in each pixel is $\sigma^2_{i,j,k}$. The reduction of integral field data usually requires at least one step of resampling the data onto a regular grid. Resampling always introduces covariances between neighbouring pixels, although they are usually neglected in the further analysis. Consequently, the provided variance tends to underestimate the true uncertainty of a pixel value. However, this has no effect on the optimization, which is based on χ^2 minimization. Only the interpretation of absolute χ^2 values with respect to consistency between a model and the data may become doubtful.

Since Eq. 2.12 describes a linear least squares problem, its solution does not require any starting values and can be directly obtained by matrix inversion. For a realistic number of a sources this is not a computationally intensive process, even if applied to all layers in a cube. Furthermore, the computing time required for the solution of Eq. 2.12 can be very significantly decreased further by considering that the contribution of any star is limited to the pixels in its vicinity. Each element n of the PSF matrix $\hat{\boldsymbol{A}}$ therefore contains a large number of pixels with essentially zero values. For this reason, $\hat{\boldsymbol{A}}$ can be written as a sparse matrix, for which there are dedicated efficient algorithms available (e.g., Paige & Saunders 1982). With these provisions it becomes possible to fit the fluxes of even several thousand sources in a MUSE datacube simultaneously (see Sect. 2.7 below). The computation time required to analyse a datacube is almost exclusively determined by the time required to obtain the PSF and the coordinate transformation. The computation time scales linearly with the number of sources. When fitting ~ 20 sources for an instrument comparable to PMAS, one iteration on a single layer takes around 10 s on a single CPU. For the typical number of iterations and layers in a cube, the total time required for a whole datacube is around 10–20 hours on a single CPU. Some parts of the code have already been parallelized, others will be in the future, so that the actual time required for the analysis can be strongly reduced.

2.4.5. Construction of the source list

When the input catalogue of sources in the field is constructed from high-resolution imaging, it will typically reach magnitudes where the S/N level in the IFS data is too low to produce meaningful spectra. We thus need to construct a subsample of stars whose spectra can possibly be deblended in an available datacube. By design, this subsample will contain stars over a large range in magnitudes and expected S/N levels. Even if we are interested mainly in the stars bright enough to yield a spectrum with a sufficient S/N for some analysis, we also need to account for the effects of blending with the (more numerous) fainter objects. There is a limit, however: When true source confusion sets in, the deblending process and the flux assignment to individual sources becomes to some extent arbitrary. In Sect. 2.5 we explore quantitatively by means of simulations where this limit is reached.

The decision of whether or not to include a particular source will depend on several criteria: (i) the brightness of the source, (ii) the distance to other nearby sources and their relative brightnesses, (iii) the position of the source, in particular if it is located close to the edge of the FoV (or even outside, see below). Effectively, the first two criteria can be combined into a single one based on S/N, taking the degradation of S/N due to crowding into account.

The practical sequence of constructing a source list is as follows. We first estimate a limiting magnitude where confusion becomes dominant, based on a global characterization of the exposure, given its depth, resolution etc., in comparison with the input catalogue. We then select a preliminary source list on the condition that the source magnitudes are brighter than the confusion limit. For those sources we predict the continuum S/N using simulations as explained below, accounting for the overall effects of crowding, as well as for the influence of close-by bright stars. The final source list is then based only on the expected S/N of the spectra.

In this process there will be stars with magnitudes brighter than the confusion limit that do not pass the second selection stage, given their proximity to a brighter star. Yet the influence of those stars has to be taken into account in the analysis. In such cases we generate a modified PSF for the close-by bright star that approximates the contribution of its fainter companion using the broad-band magnitudes of the two stars and their distance. The extracted spectrum will then be a combined one, and will be flagged accordingly in the resulting catalogue of spectra.

We note that the selection using S/N ratios will also take care of picking the sources close to the edges of the FoV that contribute significantly to the observed data. Eq. 2.16 is a sum over all spatial pixels, the flux that enters in the S/N calculation is the fraction of flux that is recorded by the detector. For a given position, this fraction is determined by the PSF. The further a source is located outside the FoV, the smaller this fraction, and thus the S/N will be.

2.4.6. Treatment of background

So far we concentrated our discussion on the resolved sources. But the data will always contain some flux contribution from unresolved background components. One such contribution is the night sky, the intensity of which we assume to be constant over the field of view. Just like any other flux component that is spatially flat, it can be easily accounted for by expanding the PSF matrix $\hat{\boldsymbol{A}}$ by a component whose values are inversely proportional to the uncertainties $\sigma_{i,j,k}$

Of greater interest is another background component that is produced by stars below the confusion limit, i.e. those that are not included in our source list discussed in Sect. 2.4.5. This background will in general not be spatially flat, but instead the distribution of the stars will produce a grainy structure, known from the surface brightness fluctuations observed in nearby galaxies. Our approach allows us to actually model these fluctuations. The sources above the confusion limit provide us with a model of the PSF in the observation. Additionally, from the high-resolution imaging in combination with our model for the coordinate transformation discussed in Sect. 2.4.3, we obtain precise IFU coordinates even for the sources below the confusion limit. Furthermore, we can use the photometry provided by the high-resolution imaging to estimate the relative brightness of the sources. With PSF, positions, and relative brightnesses in hand, we can predict the relative brightness of the grainy background in every spatial pixel of the datacube. This prediction can then be included (again after division by $\sigma_{i,j,k}$) in the PSF matrix.

Another physical background component could be in the form of gaseous emission, e.g., from filaments in an H II region. Obviously, such a component is not to be expected in globular clusters, but we want to provide a tool that is useful in any kind of crowded stellar field. We also mention again that the scientific focus might actually not lie on the resolved stars but the nebular emission. One might be interested in the kinematics or emission line ratios and wish to remove the contamination of the bright stars. In their work on extragalactic planetary nebulae, Roth et al. (2004) show that integral field spectroscopy is capable of separating individual point sources from diffuse emission of the ISM. The ISM component will be line emission and thus be restricted to a few layers in the datacube, so even if it strongly biases the PSF fit in those layers, a reliable PSF model can be obtained by interpolation of the results obtained bluewards and redwards of the emission line. One might then start from some initial guess for the spatial intensity distribution of the gaseous emission that is included in Eq. 2.12 and iteratively improve it based on the residuals observed in the layers under consideration.

2.5. Performance of the deblending process

The quality of the spectrum extracted from a datacube containing a single isolated star will depend almost exclusively on the brightness of that star. This is different for the extraction from crowded fields, where several effects may contribute to degrade the spectrum. We investigated the performance of our deblending and extraction algorithm on the basis of our simulated datacubes. We employed several criteria to quantitatively measure the quality of the extracted spectra:

The first two criteria are purely formal indicators. (i) We measured how the S/N in the continuum behaves under crowding conditions, relative to the value in isolated stars of the same magnitude. (ii) We also tested how robustly the continuum level is recovered, in terms of a potential systematic error in the broad band magnitude.

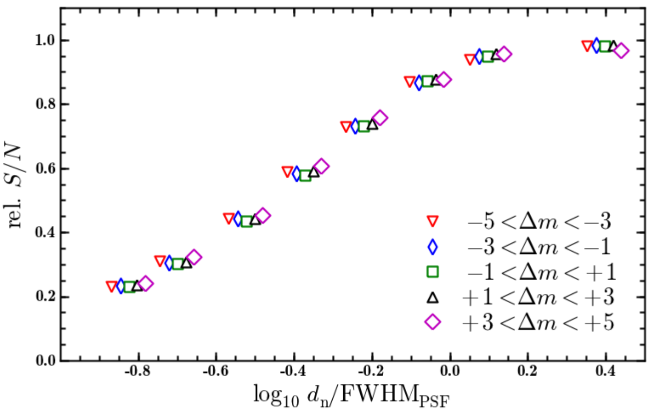

Fig. 2.7. Degradation of the S/N in the spectrum of a star with a nearby neighbour, as a function of the distance to the neighbouring source (normalized to the width of the PSF) and of the magnitude difference (star minus neighbour) between the two stars. We define the relative S/N as the ratio between the measured value and the value expected for an isolated star. For clarity, small horizontal offsets have been applied to the plotted datapoints for the different magnitude differences.

To facilitate a discussion of the astrophysical possibilities and limitations of crowded field spectroscopy, we also considered the behaviour of two types of derived spectral parameters on crowding: (iii) radial velocities, and (iv) equivalent widths of strong absorption lines.

In the following we illustrate and discuss the performance of our code for each of these parameters. We first illustrate and quantify crowding effects for the restricted scenario of only two stars within a cube, with varying angular distance and brightness difference. We then explore the global performance in realistic situations using the “crowded field datacubes” representing mock PMAS observations of a real globular cluster, constructed as described in Sect. 2.3.2.

2.5.1. “Crowding” of two stars

Signal to noise ratio and continuum level

To assess how the S/N is affected by crowding, we compared the S/N expected using Eq. 2.16 to the one actually measured in the deblended spectra. To measure the S/N of a deblended spectrum we did the following. We subtracted the (noise free) input spectrum from the deblended one. To account for possible mismatches in the continuum level and slope of the extracted spectrum we fitted the residuals with a low-order polynomial that was then also subtracted. The residuals should now scatter around zero with a standard deviation equal to the noise level of the deblended spectrum. We determined the standard deviation in a window around the central wavelength and divided the mean flux of the deblended spectrum in that window by it to yield an S/N.

For two stars of varying angular separation and magnitude difference, Fig. 2.7 shows the dependence of the S/N degradation on source separation d_n and flux ratio. For separations greater than the FWHM of the PSF, no degradation occurs as expected.

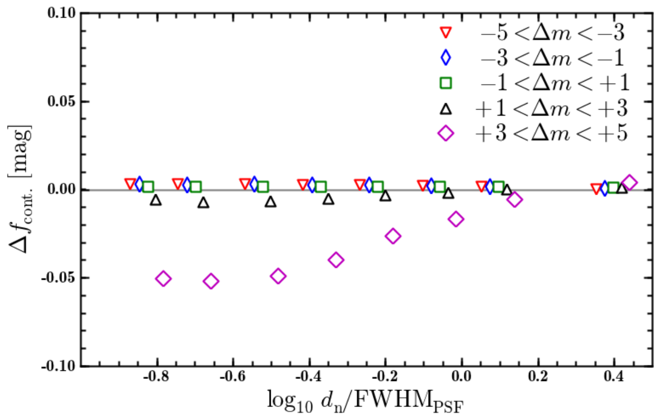

Fig. 2.8. The average error in the continuum level of the deblended spectra (expressed as a magnitude difference) as a function of the distance of the source to a neighbour (again normalized to the width of the PSF) and its relative brightness. As in Fig. 2.7, datapoints for different flux ratios are plotted with small horizontal offsets for clarity.

For smaller separations, the S/N decreases steadily and is only half that of an isolated star for $d_{12} \simeq 0.3$ FWHM. The reason for this degradation is an increasing degeneracy in Eq. 2.13. As the locations of the two stars approach each other, their PSF images become nearly the same, and the solution of Eq. 2.13 is no longer unique; any linear combination of the two stars that maintains the total flux will yield an almost equally likely result (in terms of χ^2). Practically speaking, this means that in every layer a different amount of flux will be transferred from one star to the other.

An interesting aspect revealed by Fig. 2.7 is that the decline in S/N seems to be almost independent of the flux ratio between the two stars. This is unexpected at first sight – one might expect a bright companion to have a higher impact on the deblended spectrum of a faint star than vice versa. But in fact the observed behaviour follows directly from Eq. 2.16. For small separations, the expected noise (the inverse of the square root in Eq. 2.16) will be almost the same for the two sources. But the final noise will also be the same for both sources because it is determined by the amount of flux that is shuffled back and forth between the two. Of course, the *absolute* S/N will still be higher for the brighter source because its signal is higher.

It is interesting to view the results depicted in Fig. 2.7 in light of the Rayleigh criterion, which states that two point sources are resolved if their separation is larger than the FWHM of the PSF. It is of course well known that this criterion is not a strict limit but only indicative for the spatial resolving power. Figure 2.7 shows that in the case where the relative positions of the two sources are known, it is possible to deblend stars with distances well below the FWHM of the PSF, although at the price of a reduced S/N.

We also investigated how well the continuum level of the stars could be recovered. To this aim we characterize the continuum by dividing each deblended spectrum by the corresponding input spectrum and converting the result into a magnitude. In Fig. 2.8 the dependence of the average continuum error on source separation and flux ratio is shown. It is remarkable that the strong decrease in S/N visible in Fig. 2.7 does not cause a similar degradation of the continuum level. This implies that the increase in noise is indeed purely random and does not introduce any systematics in the deblended spectra. That the actual deblending of the spectra (after PSF and source positions have been determined) does not require initial guesses makes it very robust against systematics. Especially in cases like those discussed above where the two stars are very close to one another and the χ^2 value becomes insensitive to the flux ratio between the two stars, the outcome of a fit that requires an initial guess would strongly depend on the value of that guess.

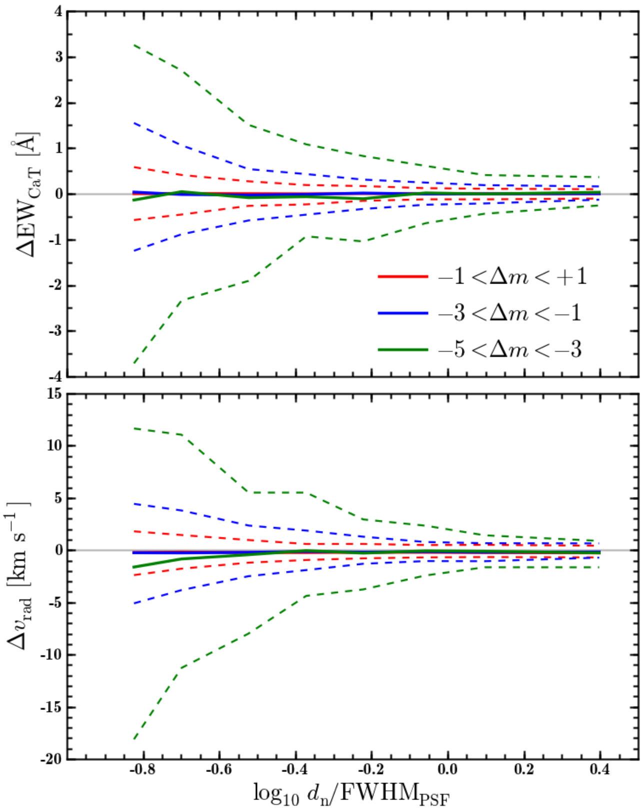

Fig. 2.9. Accuracy in the recovered radial velocities (*bottom*) and equivalent widths of strong absorption lines (*top*) for a blended star, as a function of source separation and for different flux ratios. The lines depict the median velocity difference (measured − true, thick solid) and the 75% percentiles (thin dashed) for a distribution of 1000 stellar pairs per separation value.

We do observe a small overestimation of the continuum level in the case of a very bright neighbour. However, the systematic error stays below 0.1mag and one should keep in mind that in this cases we are trying to measure the flux of a star that has a companion well inside the extent of the PSF that is at least 15× brighter.

Radial velocities and equivalent widths

We now consider the recovery of astrophysical quantities. We determined radial velocities by cross-correlating the extracted spectra with the noise-free input spectra used to generate the datacube. The quantity of interest is then the ’measured minus true’ velocity difference Δv. Recall that the spectral resolution adopted in the simulations was $\lambda/\Delta\lambda = 7000$, thus corresponding to a velocity resolution of 42.9 km/s (FWHM).

The outcome of running our deblending code on a large number of simulated “two star datacubes” (1000 realizations per separation setup) is depicted in the lower panel of Fig. 2.9. The scatter of the velocity differences increases as the source separation decreases, which is of course expected as an immediate consequence of the declining S/N. However, the median values of Δv stay comfortingly close to zero, although the two stars have randomly assigned velocity differences of the order of 10 km/s (see Sect. 2.3.2). This is even so if the neighbouring star is much brighter than the analysed source.

But Fig. 2.9 also shows clearly that the impact of partial blending in terms of the scatter on Δv is strongest if the nearby star is significantly brighter. At first sight this behaviour might be seen as different from what we observe for the S/N (cf. Fig. 2.7), but it can be easily explained by the fact that the accuracy in the radial velocity measurement depends on the actual S/N, rather than on the S/N degradation.

To check whether the deblending process might lead to a systematic error in Δv we divided our sample of stars into two subsamples, one with all stars that were assigned a positive 'true' velocity relative with respect to their neighbours and one with all stars with negative 'true' velocity. For both subsamples we found that the recovered median Δv values are statistically indistinguishable from zero.

To investigate the behaviour of absorption line equivalent widths we focused on the calcium triplet at $\lambda\lambda 8498$, 8542, 8662 Å. The equivalent width ($\mathrm{EW_{CaT}}$) of this feature is widely used to estimate the metallicity of stars (e.g., Battaglia et al. 2008), and it is therefore important to look into the integrity of this quantity under crowding conditions.

The behaviour that we observe for the recovered values of $\mathrm{EW_{CaT}}$ is very similar to what was just described for the radial velocities. The upper panel of Figure 2.9 shows the median deviation and 75% percentiles between the equivalent widths measured in the deblended spectra and those measured in the input spectra. On average there is again no bias, but the scatter increases with decreasing separation and with increasing brightness of the neighbouring star, as expected.

2.5.2. Performance in realistic crowded fields

In the last section, we showed how we can predict the expected S/N of a deblended spectrum under crowding (cf. Fig. 2.7), using the idealized case of only two stars. But when analysing a crowded stellar field, we have to take also another effect into account. Below a certain magnitude, the *confusion limit*, the stellar density of similarly bright stars will be so high that they form a 'pseudo background'. When this limit is reached, longer integration times will not lead to an increase in the number of resolved sources, though the average S/N will still increase.

To facilitate the following discussion, we first introduce the term *resolution element* as the area covered by a circle whose diameter is equal to the FWHM of the PSF. When dealing with source densities, it is quite useful to specify them as numbers of sources per resolution element because this measure is independent of the specific instrument characteristics (number of spaxels, spaxel size) and observing conditions (seeing). When stating source densities in the following, we refer to the density of stars brighter than a given limit.

Imaging studies are usually considered to be fairly complete down to source densities of 0.1 stars per resolution element. Of course, there is no sharp cut between detected and undetected sources at this limit as some brighter sources will already remain undetected, while some fainter ones will still be found. Our analysis is based on an existing inventory of sources, so there is no need for a source detection. Instead, we define a *resolvable* source as one that still improves the overall quality of the deblending process when it is included. Later, we also discuss the subset of *useful resolvable* sources, which are those for which physical parameters can be recovered to a given accuracy.

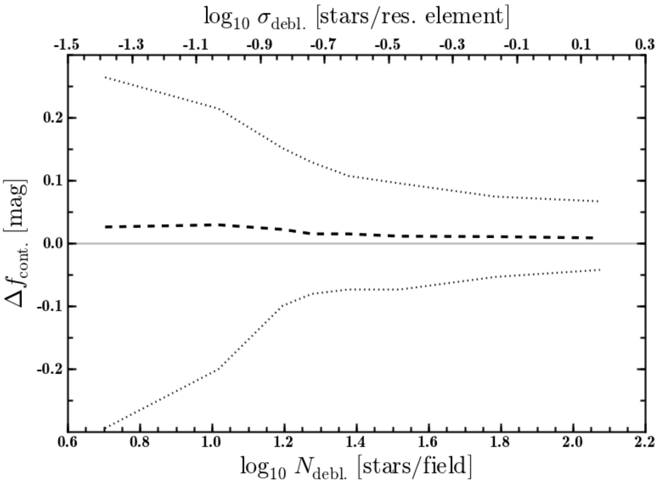

Fig. 2.10. The recovered continuum level of extracted spectra as a function of the number of stars in the source list, from the analysis of 100 simulated crowded field datacubes. The number of stars is given per datacube in the bottom and per resolution element in the top label. A thick dashed line is used to indicate the median continuum error of the brightest 10 stars per cube, and dotted lines enclose the 75% percentiles of the distribution.

The aims we pursue in this section are twofold. First, we want to obtain a well-founded determination of the confusion limit, i.e. the transition from resolvable sources to unresolvable sources, and investigate the effects of selecting either too few or too many stars. This is an important aspect for the source selection process that was presented in Sect. 2.4.5. Second, we want to verify whether the effects we discussed for the crowding of two stars (cf. Sect 2.5.1) can also be identified in realistic crowded stellar fields.

We used the crowded field datacubes and tested how the number of stars included in the deblending process influences the results by including all stars in the deblending process brighter than a limiting magnitude m_{cut}. m_{cut} was varied over a range that corresponded to average source densities between 5 and $>$ 100 stars per simulated datacube. In the following discussion, we use two measures for the source density: besides the number of sources per resolution element we also give the number of stars per datacube, since absolute numbers are quite intuitive. In our application cases, one crowded field datacube contains 256 spatial pixels (reproducing the characteristics of the PMAS instrument), and because the FWHM of the PSF is two pixels, the number of resolution elements per cube is ~80.

Continuum biases

We first checked whether the continuum level of the stellar spectra becomes biased after extraction from a crowded stellar field. Again we converted the fraction between recovered and true spectrum into a magnitude, so in the case of systematic flux transfer to or from other stars due to source confusion, we expect a non-zero offset Δf. We performed the deblending experiment on 100 simulated datacubes and measured the distribution of Δf for the set of the ten brightest stars in each datacube, as a function of the total number of stars in the source list. Recall that for each cube, the *total* number of stars in the source list was varied from a few to > 100 per field. The results are based on the ten brightest stars per cube to allow for a fair comparison between the individual simulations. Using all deblended stars would penalize the simulations in which many stars were included because stars with fainter magnitudes will on average have deblended a spectrum with a lower S/N.

Figure 2.10 shows the median and 75% percentiles of Δf and its dependence on the number of stars in the source list. The median value of Δf is nearly always very close to zero, implying that on average, the continuum level remains essentially unbiased under these crowding conditions. Only a very minor systematic offset to fainter magnitudes of ~ 0.01mag is observed. We expect that the missing flux is lost in the wings of the PSF and transferred into the background as it would agree with the fact that the PSF is recovered with slightly less pronounced wings (cf. Fig. 2.5).

It also becomes clear from Fig. 2.10 that individual stars can show significant deviations in their continuum levels. The accuracy in the recovered continuum is actually worst when only the few brightest stars (< 10 stars per simulated crowded field datacube) are extracted because in that case stars falling just below the selection cut are still well resolved, and yet their contribution is not accounted for during the deblending. m_{cut} is significantly brighter than the confusion limit and thus the stars are extracted against a very inhomogeneous ‘pseudo’-background. This behaviour is quite similar to what is reported by Moehler & Sweigart (2006) when performing multi-object spectroscopy of horizontal branch stars in the globular cluster NGC 6388: the contribution of close-by stars could not be accounted for and, as suggested by the authors, very likely did influence the results. Our results show that such problems are essentially avoided when applying PSF-fitting techniques on IFS datacubes. The recovery of the continuum level is significantly increased upon including more sources in the deblending process.

S/N degradation

The median relative S/N of the ten brightest sources in each cube is shown in Fig. 2.11. Apparently, the S/N in a given stellar spectrum decreases when the total number of sources taken into account is increased. This decrease can only be due to source confusion; in Sect. 2.5.1 we discussed the consequences of deblending sources with a small mutual distance. Now, if we increase the number of stars in the process without taking the environment of a selected source into account, it becomes more likely that stars are included whose mutual distance is close to or even smaller than the minimum distance at which the spatial resolution of the data allows for a clean separation of the two. If one tries to deblend those sources nevertheless, this will lead to an increase in the noise of the extracted spectra, but the comparison with Fig. 2.10 also shows that this flux reshuffling is essentially random, because individual stars on average do not receive flux or loose flux. Only their spectra get somewhat noisier.

In the source selection scheme that we have adopted, such behaviour is avoided by including the expected S/N in the selection process. For each source, the S/N is estimated using Eq. 2.16 and applying the correction found in Fig. 2.7. Then only sources above a threshold in S/N are considered resolvable whilst others are added to a brighter neighbour.

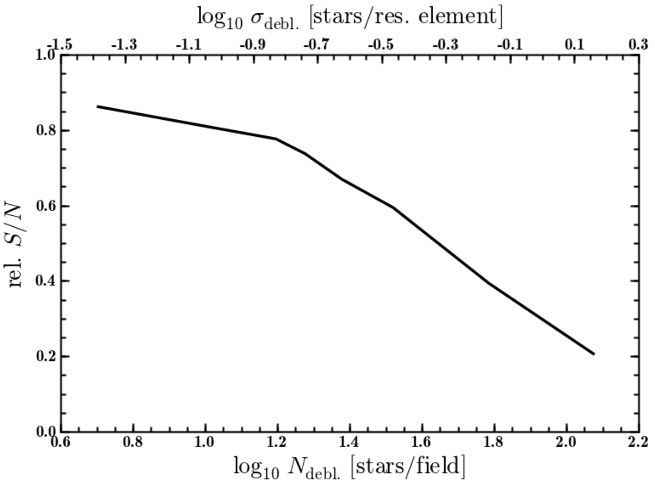

Fig. 2.11. Estimated S/N of extracted spectra as a function of the number of deblended stars per field or per resolution element, respectively, again using the 10 brightest stars per simulated cube. The thick solid line indicates the median of the distribution. As in Fig. 2.7, we show the ratio of the S/N measured in a deblended spectrum and that expected based on Eq. 2.16.

Recovery of spectral parameters

To quantify the influence of the number of deblended sources on our ability to recover physical parameters from the spectra, Fig. 2.12 shows the accuracy of measured radial velocities and equivalent widths as a function of the number of deblended sources.

When only the few brightest stars in each cube are deblended, the true $\mathrm{EW}_{\mathrm{CaT}}$ are underestimated. This can be easily explained as a consequence of flux transfer from unaccounted fainter to brighter stars, because the $\mathrm{EW}_{\mathrm{CaT}}$ increases as one moves up the red giant branch. Once the source list accounts for those fainter stars, this bias disappears entirely.

More interesting is the behaviour of the radial velocity accuracy Δv, which has a broad but clearly defined minimum. This suggests that there is actually an optimal number of stars to be used in the deblending process. The reason for the occurrence of such a minimum is that two counteracting effects influence the results, as we have identified previously. Inclusion of too few stars leads to systematic errors because the fluxes of fainter (yet still resolved) stars are not accounted for. Including too many stars, on the other hand, causes a drop in the S/N of the deblended spectra that renders the determination of stellar parameters less accurate.

The source density at which those two effects are best balanced is ~30 stars per simulated cube, corresponding to 0.4 stars per resolution element. If we adopt this number as the confusion limit and compare to the value of 0.1 stars per resolution element in crowded field photometry, we can quantify the improvement we get from using a pre-defined source catalogue instead of having to detect the sources in the datacube. Furthermore, we can use this value to give requirements on the quality of the input source catalogue in order to avoid being limited by the number of sources it contains: the stellar density of detected sources should be at least four times higher than the spatial resolution of the integral field data would allow for. Thus, the spatial resolution of the observation used to create the input catalogue must be at least twice the spatial resolution of the datacube.

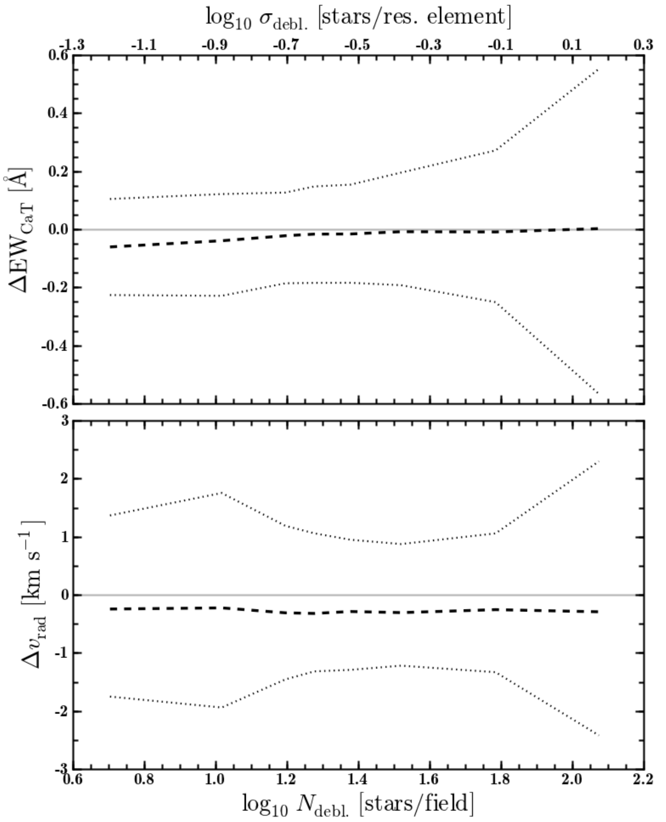

Fig. 2.12. Accuracy of the equivalent widths (*top*) and radial velocities (*bottom*) determined from the recovered spectra of the brightest 10 stars per cube as a function of the number of sources included. Line types are as in Fig. 2.10.

So far, we have counted all stars as resolvable that yielded on average better results when included in the deblending process. Clearly, not every single star of those will yield a useful spectrum. The subsample of *useful resolvable* stars will strongly depend on the science goals. To demonstrate this, we used the simulations that yielded the most accurate results, i.e., where 0.4 stars per resolution element were deblended and determined the recovery fraction as a function of source density when requesting different levels of accuracy in the recovered radial velocities. The recovery fractions we obtained are shown in Fig. 2.13. For the very stringent condition that uncertainties are $\lesssim$ 1km/s, the completeness already drops to 50% at 0.1 sources per resolution limit. On the other hand, under more relaxed conditions, the completeness drops to below 50% only at sources densities > 0.2 sources per resolution limit.

Finally, we note that the recovered velocities have a very small systematic offset of −0.2 km/s, independently of the number of stars; for the present study this is, however, of no concern.

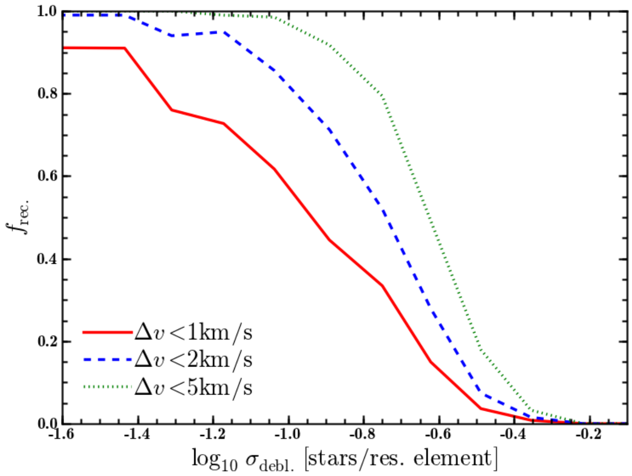

Fig. 2.13. The fraction of recovered sources plotted as a function of the source density, using three different values for the required accuracy in the recovered radial velocity. The curves have been obtained using the same data that yielded the most accurate results in Fig. 2.12.

2.5.3. Influence of crowding

Our crowded field datacubes represent realistic integral field observations of a globular cluster, with stellar densities typical for globular clusters. We now want to investigate the performance of our method in different regimes of crowding. Over a certain range in stellar density we expect a trade-off between the crowding and the achievable depth: The more crowded the stellar field, the more our analysis will have to be restricted to the brightest stars, but with increasing stellar density, it will also get more challenging to deblend clean single object spectra at all because the contrast between the individual sources decreases. In the limiting case the stellar density will already be so high for the brightest sources that the stellar field is entirely unresolved.

In this section we aim to quantify up to what amount of crowding our approach yields useful results before it breaks down. Quantifying this limit is important when making predictions about whether a stellar field can be accessed by means of crowded field 3D spectroscopy. This will not only be applicable to globular clusters but to any type of crowded stellar field. In nearby galaxies, for instance, projected stellar densities can significantly exceed those of a typical globular cluster. Thus it would be very helpful to know up to what source density we can still obtain good results.

To test the influence of the crowding, we modified our simulations of crowded field datacubes in the following way. We identified as a bright star every source in the catalogue with a visible magnitude brighter than the horizontal branch (F606W < 13.5 for 47Tuc), i.e we concentrated on the brightest giants. For each simulated datacube, we randomly picked stars from the catalogue and placed them in the datacube until a certain number of bright stars was reached. The number of bright stars picked varied between 4 and 400. The further processing of the cubes was then similar to the simulations described in Sect. 2.3.2.

In total, 200 datacubes were prepared that were all analysed using our algorithm. To quantify its performance for a single cube we counted the number of bright stars whose deblended spectra fulfilled an accuracy criterion. Two different accuracy criteria were used: an error in the recovered continuum of < 0.1mag and an offset in the recovered radial velocity of < 2km/s. In Fig. 2.14 we show the number of recovered sources as a function of the crowding. "Crowding" here is defined as the number of bright sources in a datacube. Furthermore, we again normalized the star counts by the number of resolution elements, for the reason mentioned above.

As Fig. 2.14 shows, both accuracy criteria yield comparable results: We observe that up to a crowding of 0.2 sources per resolution element, the number of accurately deblended sources

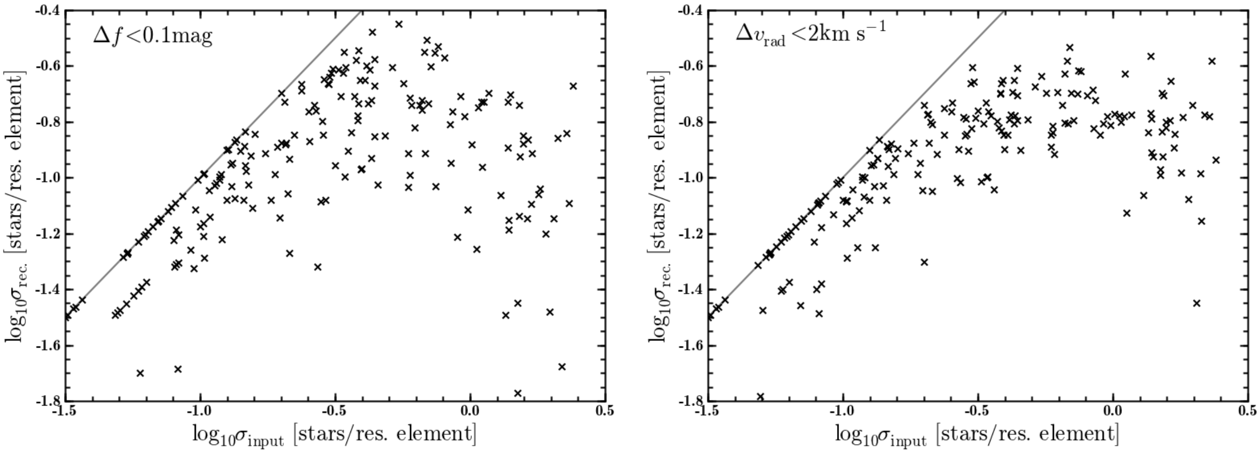

Fig. 2.14. The impact of crowding on the efficiency of the deblending algorithm. We show the number of useful deblended spectra as a function of the number of bright sources in the simulation. To obtain a measure of the crowding that does not depend on the specific simulation setup (seeing, size of the field of view) we have normalized the number of sources by the number of resolution elements. Two criteria were used to identify a usefully deblended spectrum: a magnitude offset < 0.1mag (*left*) and an offset in radial velocity < 2km/s (*right*) between the input spectrum and the recovered one. Each plotted datapoint corresponds to the analysis of one mock datacube. In both panels, a grey solid line indicates the optimal case where a useful spectrum could be deblended for every bright star in the field of view.

increases approximately linearly with the number of existing sources. For a higher crowding of 0.2-1.0 sources per resolution element, we observe a plateau with an average of ~ 0.2 accurately deblended sources per resolution element. If the crowding increases beyond one source per resolution element, the number of deblended sources that fulfil our accuracy criteria starts to decrease again, indicating that we have reached an "overcrowding regime" where our approach breaks down.

We note that the distributions shown in Fig. 2.14 can also be very helpful for judging whether single-star spectra can be deblended in a certain crowded stellar fields and for specifying what spatial resolution would be required for its investigation.

2.6. Potential sources for systematic errors

2.6.1. Influence of the PSF

In Sect. 2.4.2 we discussed to what accuracy the PSF can typically be determined in a crowded field datacube. We now investigate the effects of any possible mismatch between the true and the reconstructed PSF on the quality of the deblended spectra. To this aim, we modified the analysis of our two-star datacubes. The PSF assumed in the deblending process did now systematically deviate from the one that that was used to create the cubes. We describe the mismatch in terms of the FWHM of the PSF, as this is a quantity that is relatively easily accessible in observations. The analysis of Sect. 2.4.2 showed that we can recover the FWHM to an accuracy of usually ~1–2%, with some outliers at the 10% level. Based on these results, we simulated PSF mismatches of 1, 2, 5, and 10% in FWHM.

Qualitatively, we expect the effect of an inaccurate PSF to be the following: The deblending process will leave residuals in the vicinity of every star. The amplitude of such residuals will scale with the brightness of the star. Close-by stars will then be deblended on top of the residuals and the extracted spectrum will be a combination of the true spectrum and the residuals.

Quantitatively we wanted to know by how much these residuals bias a deblended spectrum and the derived astrophysical quantities. We again measured the radial velocities and Ca triplet equivalent widths in the deblended spectra, took the differences to the input values, and checked the ensemble of results for systematic deviations.

For obvious reasons the impact of any PSF mismatch will be strongest for relatively faint sources in the vicinity of significantly brighter ones. We therefore considered two cases: (i) A moderate brightness contrast between the source in question and its neighbour ($1 < \Delta m < 3$), and (ii) a strong brightness contrast of $3 < \Delta m < 5$. A contrast of 5 mag would be roughly the expected value for a star in the red clump of a globular cluster apparently close to a star at the tip of the red giant branch.

In Fig. 2.15, we present the median absolute difference between the measured and true radial velocities as a function of the degree of PSF mismatch, in two panels corresponding to the different contrast classes. To distinguish between random and possible systematic errors, the median absolute difference is also shown for the case of a perfect PSF (Fig. 2.15). In this case, the offset should be completely caused by random errors, i.e. the limited S/N of the deblended spectra. Any increase in the offset can then be attributed to the imperfect PSF. With increasing influence of the PSF residuals of the brighter neighbouring star, the median of the distribution will approach the assumed velocity dispersion.

As expected, the influence of the PSF increases with the brightness contrast between source and neighbour. This can be verified by comparing with the two panels of Fig. 2.15. For moderate brightness contrast, the introduced systematics are small if the FWHM of the PSF is determined to an accuracy of < 5%, whereas in the case of a strong brightness contrast, offsets of 2% already introduce measurable systematics. At this contrast level, the residuals caused by the PSF mismatch if the errors in the FWHM are ≥5% are so strong that the signal of the fainter star basically disappears and no useful spectrum can be deblended any more. On the other hand, Fig. 2.15 also shows that PSF mismatch only becomes an issue for source separations comparable to or smaller than the FWHM. We find similar results regarding the accuracy of the recovered values of $\mathrm{EW}_{\mathrm{CaT}}$.

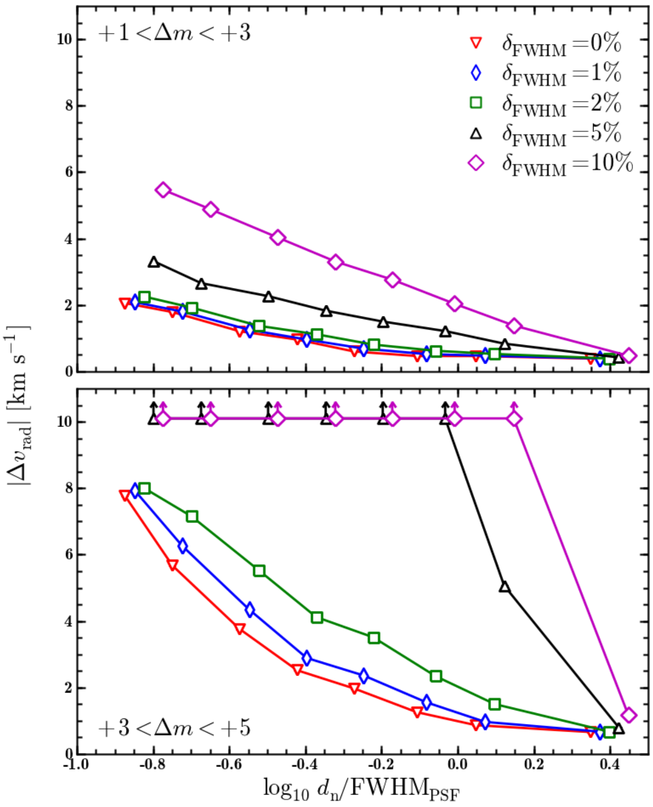

Fig. 2.15. Difference between recovered and true radial velocity of a simulated apparent binary star, as a function of source separation and of the degree of PSF mismatch, for two ranges of flux ratios between the two stars. The curves show the median of the *absolute* velocity difference of each stellar pair. Also shown is the median offset for the case of a perfect PSF (red line) to show the behaviour expected in the absence of any systematic error. For clarity, deviations larger than the velocity dispersion have been set to a value of 10km s^{-1}, the assumed velocity dispersion in the cluster.

Recall that for crowded fields in Galactic globular clusters we typically can recover the PSF width to an accuracy of $< 2\%$. The simulations presented in this subsection demonstrate clearly that this will be sufficient to deblend an unbiased spectrum of a star in the close vicinity, to even a small fraction of the PSF width, of a neighbour that is ~10× brighter. Only in the extreme case where the brightness contrast between the two stars is significantly greater than a factor of 10, significant biases are to be expected. Nevertheless, such cases will be known from the input catalogue and can thus be easily flagged and excluded from the further analysis.

2.6.2. Further sources for systematic errors

An imperfect PSF is not the only potential source of systematic errors. Another such source are the positions of the individual stars in the field. For reasons like measurement errors or proper motions, the source coordinates that are given in the input catalogue can be offset from their true values. The strength of such effects is essentially a property of the specific input catalog that is used and cannot be predicted like the achieved accuracy of the PSF. For this reason, we did not try to quantify the influence of these effects on the deblended spectra.

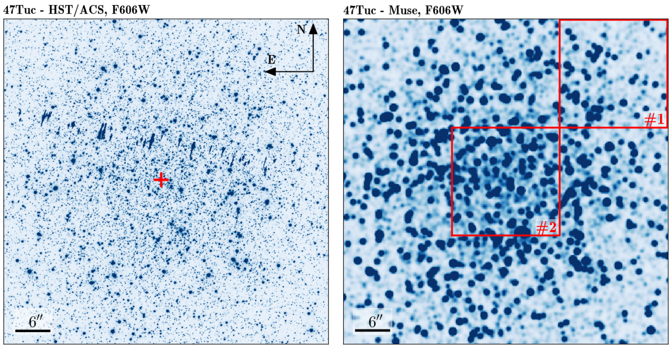

Fig. 2.16. Simulated MUSE observation of the globular cluster 47Tuc. *Left:* Cut-out from an HST/ACS observation of the central arcmin of the cluster in the F606W-passband. A red cross denotes the cluster centre. *Right:* Reconstructed broadband image from the mock MUSE data of the same region, obtained by integrating the datacube with the F606W filtercurve. The seeing in the simulation was set to 0.8arcsec. Red squares indicate the two 20 × 20 arcsec fields that are discussed in the text.

A further error source related to the input catalogue is the issue of missing stars or spurious detections. Those effects will occur mainly in the regime of the fainter stars that are inaccessible to the integral-field observations (that have a lower spatial resolution). Under certain circumstances, however, they might also play a role amongst the brighter stars that are accessible. One such example are catalogues that are compiled from observations with the Advanced Camera for Surveys (ACS) onboard HST. In the case of globular clusters, those observations are usually targeted at the numerous faint main-sequence stars, and the brightest giants appear heavily saturated in the exposures and cause strong bleeding features on the CCD that might cover relatively bright stars (see Fig 2.16 for an example). Again this effect will largely depend on the quality of the used input catalogue.

2.7. MUSE

MUSE (Bacon et al. 2010) is an integral field spectrograph currently being built by a consortium of 6 European institutes and ESO. It is scheduled to see its first light at the Very Large Telescope (VLT) in 2013. The instrument provides a FoV of 1arcmin^2 with spaxels of 0.2 × 0.2 arcsec^2, and a wavelength coverage of 4650–9300Å. The combination of a large FoV with a spatial sampling sufficient to properly sample the PSF even under good seeing conditions makes MUSE a unique instrument for a variety of science applications. Although the main motivation for developing this new instrument is the observation of faint galaxies at medium-to-high redshift, some very promising applications exist for investigating crowded stellar fields. To demonstrate this, we outline in the following the analysis of a simulated MUSE datacube of the globular cluster 47Tuc.

The simulations are again based on the HST-photometry obtained in the HST/ACS survey of Galactic globular clusters. Based on broadband colours and an isochrone fit to the colour magnitude diagram of 47Tuc, each star was assigned a spectrum based on a new library of model atmospheres and synthetic spectra calculated by Husser et al. (2013) using the stellar atmosphere code PHOENIX (Hauschildt & Baron 1999).

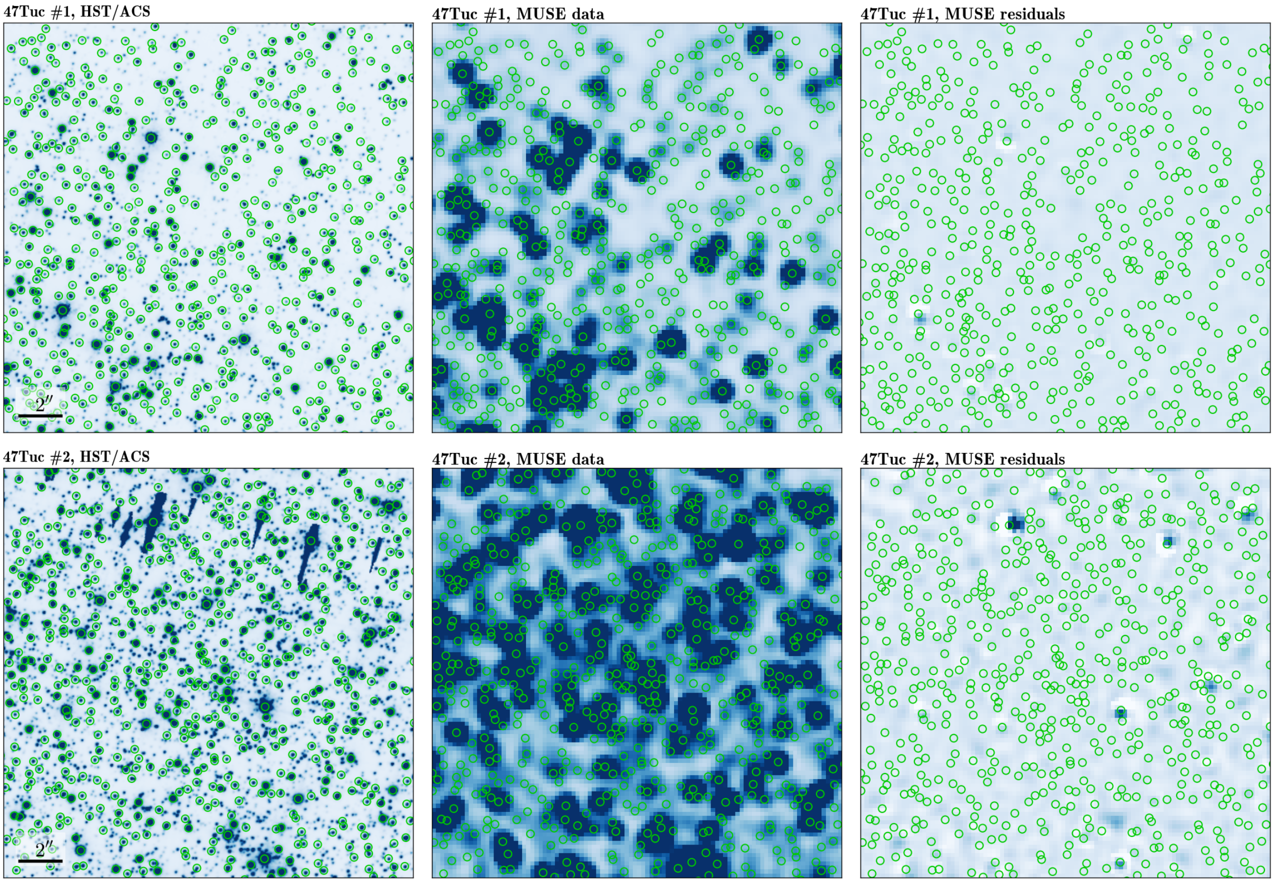

Fig. 2.17. Visualization of our source deblending algorithm applied to simulated MUSE data. For each of the two fields highlighted in Fig. 2.16, we show a cut-out from an HST/ACS image (*left*), a white light image of the simulated data (*centre*), and a residual image after fitting the sources (*right*). Each location where a useful spectrum was deblended has been marked by a green circle.

To simulate the effect of missing stars in the vicinity of brighter stars, we applied the following correction to the input catalogue. We counted the surface density of stars at a given magnitude in the vicinity of brighter stars and compared it to the overall density of those stars across the field covered by the catalogue. Stars were then randomly added in the vicinity of the brighter ones until the two densities matched.The catalogue that was later used in the analysis did not include those stars.

In the final step of the simulation, a datacube was created using dedicated software developed within the MUSE consortium (R. Bacon, private communication). It creates a datacube containing the provided sources and a sky spectrum. Each spectrum is convolved with the line spread function of MUSE. The seeing in the simulation was set to 0.8 arcsec. This value is internally translated to a wavelength-dependent PSF. The final simulated datacube is a combination of three snapshot exposures, each with an exposure time of 30 s. Figure 2.16 shows a whitelight image of this datacube together with an HST image.

We concentrate our discussion on two 20×20 arcsec subcubes, highlighted in Fig. 2.16 (*right*) by red squares. In both regions, we deblended the stellar spectra using our crowded field spectroscopy code.

The algorithm itself was slightly modified in order to handle the significantly larger amount of data of a MUSE cube compared to PMAS or ARGUS. The size of the FoV of MUSE is large enough that some relatively isolated bright stars should exist within the FoV that can be used as PSF calibrators. We therefore used the existing photometry to select suitable PSF stars on the condition that within a given radius there are no neighbours brighter than a given flux ratio. The search radius is chosen such that the PSF contribution outside this radius is essentially zero. After each fit to the object fluxes during the iteration, we then subtract all stars except those previously identified and determine the coordinate transformation and the PSF using only those stars. This significantly speeds up the analysis and we achieve computational times similar to our PMAS or ARGUS datacubes. Nevertheless, the actual extraction of the spectra still is performed on *all* stars simultaneously.

In Fig. 2.17 we show a close-up of the two regions, again using an HST/ACS image and a whitelight image of the mock MUSE data. We also show a whitelight image for each region with the MUSE data where the deblended sources were already subtracted. Closer inspection of these residuals reveals that some stars have been missed by our source selection; these are the stars added to the incomplete source catalogues as discussed above. Such sources can be easily identified in the residuals and then added manually to the catalogue.

To visualize the efficiency of our deblending approach we marked the position of every source for which a useful spectrum was deblended. Sources for which the extracted spectra have an S/N that is too low for a reliable radial velocity determination are not marked in Fig. 2.17. The total number of useful spectra that were deblended is 580 in subfield #1 and 610 in subfield #2. Interpolating these numbers to a full datacube, we estimate that from a single MUSE observation obtained under average seeing

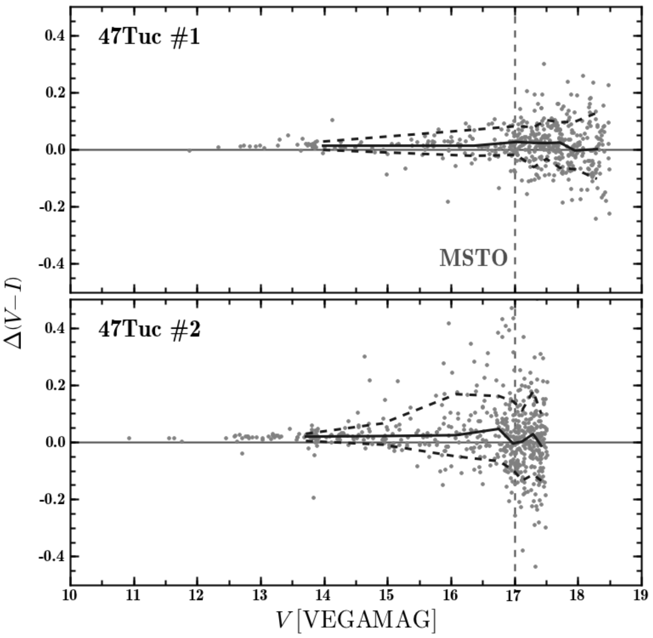

Fig. 2.18. Deviation in *V–I* colour recovered from the deblended spectra as a function of a stellar magnitudes for the two subfields highlighted in Fig. 2.16. The median of the distribution is shown as a thick solid line, dashed lines give the 75% percentiles of the distribution. A vertical dashed line is used to indicate the main-sequence turn-off in both panels.

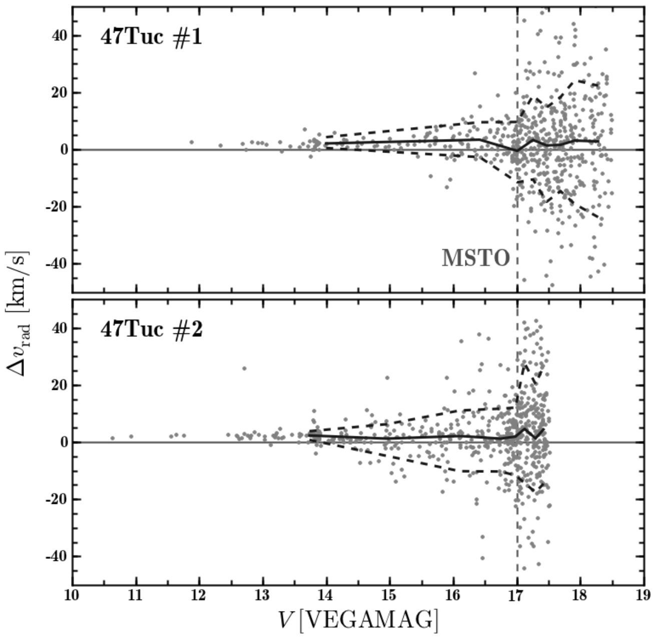

Fig. 2.19. Deviation of the radial velocities determined from the deblended spectra, again plotted as a function of a star's brightness for the two fields highlighted in Fig. 2.16. Radial velocities were determined by cross-correlating each deblended spectrum with its input spectrum. The line types are as in Fig. 2.18.

conditions we can obtain ~ 5000 useful spectra. Under very good seeing conditions this number may even be 3–4× higher.

The extended wavelength range of MUSE allows us to directly determine broadband colours from the spectra by applying the filtercurves of the HST/ACS $F606W$ and $F814W$ filters (hereafter called V and I, respectively) and compare them to the 'true' (i.e., input) colours. In Fig. 2.18, the deviation in $V - I$ is plotted as a function of V band magnitude. The comparison of the two fields gives a good impression of the effect of crowding. In the less crowded part of the simulated data (field #1), we obtain useful spectra for fainter stars than in the direct vicinity of the cluster centre (field #2), and yet in both fields we are able to probe below the main sequence turn-off. Taking into account that the simulation assumed only average seeing conditions and that MUSE is also designed to work with adaptive optics, this demonstrates the unique capabilities provided by the instrument.

Finally, we take a look at the accuracy achievable in the measured radial velocities. The spectral resolution provided by MUSE is lower than what we used in our previous simulations and that of our existing PMAS and ARGUS data. However, the wider wavelength range at least partly compensates for this. As Fig. 2.19 shows, radial velocities of bright giants can be determined with an accuracy of a few km/s. Around the main sequence turn-off of the cluster, the typical error of the obtained radial velocities is still comparable to the velocity dispersion.

2.8. Conclusions

The application of PSF-fitting techniques to integral field spectroscopy is a powerful approach to observe crowded stellar fields. We developed an algorithm to deblend the spectra of many stars within a single datacube simultaneously, and validated the method by applying it to realistic simulated observations of the central regions of globular clusters. The combination of linear least-squares fitting with the use of sparse matrices makes the code computationally efficient and affordable even for a modest workstation.

One central assumption for our algorithm is that an input catalogue of the sources in the field already exists. Typically this catalogue would be obtained by other means, such as by running a classical crowded field photometry code on high-resolution HST images. It is of course also possible to perform the source detection in the IFS datacubes themselves, e.g. from a collapsed white-light image. But our simulations show that by using prior knowledge of the locations of sources in the field, the number of correctly deblended sources is increased by up to a factor of ~4 compared to the case where the source detection is performed on the IFU data.

We extensively tested the performance of our code as a function of the degree of crowding, expressed as the number of sources per field or per spatial resolution element. A conventional rule of thumb for crowded field *photometry* states that deblending performs well up to a stellar density of ~0.1 per resolution element. We showed that the spectroscopic deblending works at even considerably higher source densities than that. This gain is partly due to the application of prior knowledge as discussed above, and partly due to the continuity enforcement over many simultaneously evaluated image layers in a datacube.

While unbiased spectra can be extracted even for heavily blended sources, such spectra will suffer from a significantly reduced S/N level, with the degradation being driven by the proximity to and the brightnesses of nearby stars. We showed that this reduction of S/N due to blending can be accurately modelled and predicted for a given dataset from the input catalogue. Consequently, an optimal source list for the final extraction can be constructed according to the expected S/N of the final spectra. This is a very useful feature for statistical investigations in crowded stellar fields, since it allows one to maximize the number of "meaningful" spectra that can be obtained from a given dataset.

Under conditions of strong crowding, the number of stars per field for which spectral parameters can be reliably determined is approximately independent of the actual source density and corresponds to roughly 0.2 stars per spatial resolution element. This 'plateau' exists because of the mutually opposing effects of higher source densities, on the one hand, and more severe S/N degradation due to crowding, on the other. Only when the observed density of stars of comparable brightness passes a definite "overcrowding limit" of ~1 star per resolution element, the extraction of useful individual spectra breaks down entirely.

The degree of crowding in a given field also depends, of course, on the depth and angular resolution of the data. We constructed our simulated datacubes in view of our own existing observations of Galactic globular clusters, using present-day IFUs under seeing-limited conditions. Even in the very central regions of these clusters we found that the source density of stars bright enough to produce meaningful spectra was still well below the overcrowding limit. However, this could change rapidly if the data were going deeper down the colour-magnitude diagram, especially once the main sequence is being probed. We demonstrated that with the upcoming MUSE instrument this domain will actually be reached. Improving the angular resolution, for example through ground-layer adaptive optics as envisaged for MUSE, will then become crucial.

The spectroscopy of crowded stellar fields may be of interest for other classes of astronomical objects, such as compact open clusters, dwarf galaxies, or dense regions in the bulge of the Milky Way. The methodical work presented in this paper will enhance the capabilities of 'crowded field 3D spectroscopy' beyond our own application topic of globular clusters. For the benefit of the community, we plan to make our code available to the public in the future. An overview of its current functionality and status is provided in Appendix A.

Acknowledgements. We thank the anonymous referee for a careful reading of the manuscript and for many useful comments that helped to improve this paper.

S. K. acknowledges support from the ERASMUS-F project through funding from PT-DESY, grant no. 05A09BAA.

The authors thank Eric Emsellem and Guiseppina Battaglia for providing a tool to facilitate the assignment of realistic spectra to the photometric data. We are grateful to Roland Bacon for sharing the QSim software to create realistic MUSE datacubes. Tim-Oliver Husser has been a great help in preparing the MUSE data.

Based on observations collected at the Centro Astronómico Hispano Alemán (CAHA) at Calar Alto, operated jointly by the Max-Planck Institut für Astronomie and the Instituto de Astrofísica de Andalucía (CSIC).

Based on observations made with the NASA/ESA Hubble Space Telescope, and obtained from the Hubble Legacy Archive, which is a collaboration between the Space Telescope Science Institute (STScI/NASA), the Space Telescope European Coordinating Facility (ST-ECF/ESA), and the Canadian Astronomy Data Centre (CADC/NRC/CSA).

References

Anderson, J., Sarajedini, A., Bedin, L. R., et al. 2008, AJ, 135, 2055
Bacon, R., Accardo, M., Adjali, L., et al. 2010, in Society of Photo-Optical Instrumentation Engineers (SPIE) Conference Series, Vol. 7735, Society of Photo-Optical Instrumentation Engineers (SPIE) Conference Series
Battaglia, G., Irwin, M., Tolstoy, E., et al. 2008, MNRAS, 383, 183
Becker, T., Fabrika, S., & Roth, M. M. 2004, Astronomische Nachrichten, 325, 155
Buonanno, R. & Iannicola, G. 1989, PASP, 101, 294
Cappellari, M., Emsellem, E., Krajnović, D., et al. 2011, MNRAS, 413, 813
Christensen, L., Jahnke, K., Wisotzki, L., & Sánchez, S. F. 2006, A&A, 459, 717
de Zeeuw, P. T., Bureau, M., Emsellem, E., et al. 2002, MNRAS, 329, 513
Eisenhauer, F., Genzel, R., Alexander, T., et al. 2005, ApJ, 628, 246
Evans, C. J., Taylor, W. D., Hénault-Brunet, V., et al. 2011, A&A, 530, A108
Fabrika, S., Sholukhova, O., Becker, T., et al. 2005, A&A, 437, 217
Filippenko, A. V. 1982, PASP, 94, 715
Förster Schreiber, N. M., Genzel, R., Bouché, N., et al. 2009, ApJ, 706, 1364
Gerssen, J., van der Marel, R. P., Gebhardt, K., et al. 2002, AJ, 124, 3270
Hauschildt, P. H. & Baron, E. 1999, Journal of Computational and Applied Mathematics, 109, 41
Husemann, B., Kamann, S., Sandin, C., et al. 2012, A&A, 545, A137
Husemann, B., Wisotzki, L., Jahnke, K., & Sánchez, S. F. 2011, A&A, 535, A72
Husser, T. O., Wende-von Berg, S., Dreizler, S., et al. 2013, A&A, submitted
Jahnke, K., Wisotzki, L., Sánchez, S. F., et al. 2004, Astronomische Nachrichten, 325, 128
Jolissaint, L., Christou, J., Wizinowich, P., & Tolstoy, E. 2010, in Society of Photo-Optical Instrumentation Engineers (SPIE) Conference Series, Vol. 7736, Society of Photo-Optical Instrumentation Engineers (SPIE) Conference Series
Lucy, L. B. 1994, in The Restoration of HST Images and Spectra - II, ed. R. J. Hanisch & R. L. White, 79
Marigo, P., Girardi, L., Bressan, A., et al. 2008, A&A, 482, 883
McLaughlin, D. E., Anderson, J., Meylan, G., et al. 2006, ApJS, 166, 249
Mediavilla, E., Arribas, S., del Burgo, C., et al. 1998, ApJ, 503, L27
Moehler, S. & Sweigart, A. V. 2006, A&A, 455, 943
Munari, U., Sordo, R., Castelli, F., & Zwitter, T. 2005, A&A, 442, 1127
Paige, C. C. & Saunders, M. A. 1982, ACM Trans. Math. Software, Volume 8, p. 43-71, 8, 43
Pasquini, L., Avila, G., Blecha, A., et al. 2002, The Messenger, 110, 1
Peng, C. Y., Ho, L. C., Impey, C. D., & Rix, H.-W. 2002, AJ, 124, 266
Pfuhl, O., Fritz, T. K., Zilka, M., et al. 2011, ApJ, 741, 108
Press, W. H., Teukolsky, S. A., Vetterling, W. T., & Flannery, B. P. 1992, Numerical recipes in FORTRAN. The art of scientific computing, ed. Press, W. H., Teukolsky, S. A., Vetterling, W. T., & Flannery, B. P.
Roth, M. M., Becker, T., Kelz, A., & Schmoll, J. 2004, ApJ, 603, 531
Roth, M. M., Kelz, A., Fechner, T., et al. 2005, PASP, 117, 620
Sánchez, S. F., Cardiel, N., Verheijen, M. A. W., Pedraz, S., & Covone, G. 2007, MNRAS, 376, 125
Sandin, C., Weilbacher, P., Fachreddin, T. V., Kamann, S., & Streicher, O. 2012, in Society of Photo-Optical Instrumentation Engineers (SPIE) Conference Series, Vol. 8451, Society of Photo-Optical Instrumentation Engineers (SPIE) Conference Series, ed. N. M. Radziwill & G. Ciozzi, 84510F–1–84510F–16
Sarajedini, A., Bedin, L. R., Chaboyer, B., et al. 2007, AJ, 133, 1658
Schechter, P. L., Mateo, M., & Saha, A. 1993, PASP, 105, 1342
Soto, M., Kuijken, K., & Rich, R. M. 2012, A&A, 540, A48
Stetson, P. B. 1987, PASP, 99, 191
van der Marel, R. P., Gerssen, J., Guhathakurta, P., Peterson, R. C., & Gebhardt, K. 2002, AJ, 124, 3255
Wisotzki, L., Becker, T., Christensen, L., et al. 2003, A&A, 408, 455

Chapter 3

Crowded field 3D spectroscopy in Galactic globular clusters: Radial velocity measurements in the central regions of M3, M13 and M92*

Sebastian Kamann[1]

[1] Leibniz-Institut für Astrophysik Potsdam (AIP), An der Sternwarte 16, 14482 Potsdam, Germany

ABSTRACT

We used the PMAS integral field spectrograph to obtain large sets of radial velocities in the central regions of three northern Galactic globular clusters: M3, M13 and M92. By applying the new technique of *crowded field 3D spectroscopy*, we could deblend useful stellar spectra for $\sim$ 80 stars within the central $\sim 10''$ of each target. Those are by far the largest spectroscopic data sets obtained in the innermost parts of the clusters so far. Radial velocities are determined using a cross-correlation technique that proves to yield reliable results for spectra with a signal-to-noise higher than 7. To obtain kinematical data across the whole extend of the cluster, we complemented our data with measurements available in the literature, yielding a total number of 227 stars in M3, 378 stars in M13 and 405 stars in M92. A comparison of the few stars in our PMAS sample that have measurements available in the literature reveals discrepancies for some stars that cannot be explained by measurement errors or variable radial velocities. Instead, we suggest that traditional spectroscopic techniques can lead to biased results in crowded stellar fields because stellar blending cannot be accounted for. In the PMAS data of M3, we uncover a star with a velocity relative to the cluster mean that is too high to be explained by the gravitational potential of the cluster. This raises the number of known high-velocity stars in this cluster to 3. We perform a careful identification of binary stars. Although the heterogeneity of our data set does not allow us to put stringent constraints on the binary fraction in either cluster, our detected binary rates are in agreement with previous findings that the binary fraction in globular clusters is significantly lower than in the field.

3.1. Introduction

Spectroscopic observations have significantly advanced our knowledge of globular clusters, ranging from the pioneering work by Gunn & Griffin (1979) and Lupton et al. (1987) on their internal dynamics to the more recent discovery of primordial abundance variations in light elements in clusters formerly thought to be homogeneous stellar populations (Gratton et al. 2001). Modern multi-object spectrographs allow the investigation of large samples of cluster stars with reasonable observing times (e.g. Lane et al. 2011; Carretta et al. 2009). An obvious limitation of multi-object spectroscopy is that it is generally limited to the relatively few and bright stars in a cluster that stick out of the rest of its population. Especially the dense central regions of the clusters cannot be efficiently probed. This becomes a severe limitation for dynamical studies of globular clusters because the central regions often are the most interesting ones. For example, the high stellar densities might lead to the formation of massive black holes in the cluster centres (Portegies Zwart et al. 2004). Long-slit spectroscopy might help to advance towards the cluster centres, as the spatial information is at least partially preserved, namely along the orientation of the slit. However, only with the superior spatial resolution offered by the *Hubble* Space Telescope (HST) it is feasible to obtain stellar samples large enough for a meaningful analysis (van der Marel et al. 2002; Gerssen et al. 2002).

Proper motion studies do not rely on spectroscopy, therefore preserving the spatial information is less of an issue. Such studies have for a long time been used to decide on the membership of stars to clusters (e.g. Cudworth & Monet 1979). With the advent of the Advanced Camera for Surveys (ACS) onboard HST it became feasible to carry out proper motion studies also in the dense cluster centres (McLaughlin et al. 2006; Anderson & van der Marel 2010). However, the controversy about the presence of an intermediate-mass black hole in ω Centauri (Noyola et al. 2008; van der Marel & Anderson 2010; Noyola et al. 2010) demonstrated the complementary nature of studies based on either proper motions or spectroscopy. Ideally one should use the full wealth of information.

Fabry-Perot imaging offers a possibility to perform spectroscopic studies that are fully spatially resolved through the scanning of individual spectral lines with monochromatic images that are observed in succession. For example, Gebhardt et al. (1995, 2000) combined Fabry-Perot observations with analysis techniques from crowded field photometry to unveil the central kinematics in a sample of Galactic globular clusters. Compared to a Fabry-Perot imaging, integral field spectroscopy (IFS) covers a significantly smaller field of view (FoV). However, the area observed by an integral field unit (IFU) is already comparable to the core region of a Galactic globular cluster. On the other hand, the structure of the data obtained with an IFU has some important advantages. The observation of an entire spectrum instead

---

* A version of this Chapter will be submitted for publication in *Astronomy & Astrophysics*. The preliminary list of co-authors includes Lutz Wisotzki, Martin M. Roth, Tim-Oliver Husser, Christer Sandin, Peter Weilbacher and Joris Gerssen.

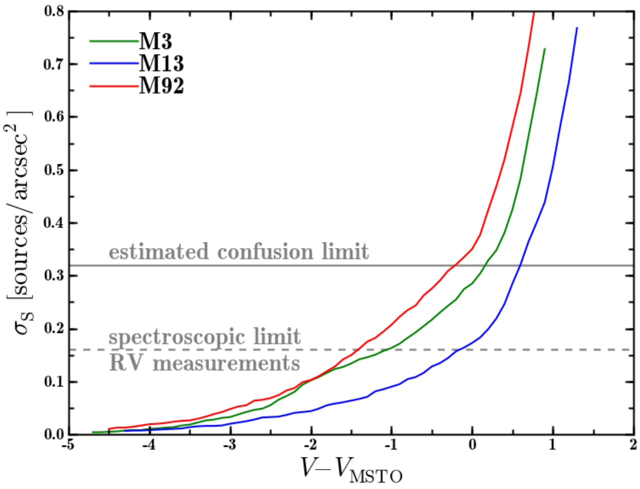

Fig. 3.1. Surface number density of sources brighter than a given magnitude for the three clusters in our sample. The densities were obtained by counting the stars in the central 20″ of each cluster. Magnitudes are given relative to the main sequence turn-off (MSTO) in each cluster. The solid horizontal line corresponds to the source density where we expect to hit the confusion limit. Below the density indicated by the dashed line the deblended spectra will likely have sufficient S/N for radial velocity determination.

of a single line allows one to accept lower spectral resolutions to achieve a sufficient resolution in velocity space. Furthermore, the whole IFS datacube is observed simultaneously, thus all the data is obtained at exactly the same observing conditions. This is a huge advantage because the information from the full datacube can be used in the analysis of every individual monochromatic layer.

In Kamann et al. (2013, hereafter Paper I; also Chapter 2 of this thesis), we recently presented a new method to analyse IFS data of crowded stellar fields. It extends the established analysis techniques for crowded field photometry into the domain of three-dimensional datacubes by fitting a wavelength dependent PSF to deblend the stellar spectra. In the present paper we apply our analysis to observations of three Galactic globular clusters: M3, M13 and M92. The paper is organized as follows: After a brief presentation of our observed sample in Sect. 3.2 we present our observations and the data reduction in Sects. 3.3 and 3.4. The analysis of the data, in particular the deblending of the stellar spectra, is outlined in Sect. 3.5. Sect. 3.6 is dedicated to the compilation of the final set of radial velocities, both from our IFS data and from the literature. A discussion on radial velocity variable stars is presented in Sect. 3.7 before we conclude in Sect. 3.8. The data presented in this paper is the basis for a search for intermediate-mass black holes in the clusters based on dynamical models that is carried out in an accompanying paper (Chapter 4 of this thesis).

3.2. Target selection

We searched the catalogue of Harris (1996) for globular clusters visible from Calar Alto observatory and selected the objects that were best suited for an analysis. This was done based on the following criterion. As we showed in Paper I, the confusion limit below which individual stellar spectra cannot be resolved any more is around ∼0.4 stars per resolution element. Assuming a typical seeing of 1.0″, this implies that we can resolve stars down to a density of 0.32/arcsec^2. Using the V- and I-band photometry obtained in the ACS Survey of Galactic globular clusters (Sarajedini et al. 2007; Anderson et al. 2008), we determined the I-band magnitude where the confusion limit would be reached and only considered clusters where spectroscopic observations down to this limit are feasible with a 3.5m telescope. Additionally, we looked at the confusion limit with respect to the stellar population in the cluster and restricted ourselves to clusters where the confusion limit in the central region was close to the main sequence turn-off (MSTO). The motivation for this selection criterion was that the number of stars per magnitude bin increases strongly below this point and we planned to analyse not only the resolved stars but also the unresolved stellar component that is uncovered after they have been subtracted. Now if we can resolve all stars on the red giant branch of the cluster, we make sure that the unresolved stellar component consists of many stars with similar brightness and is not dominated by a few bright stars. To illustrate this second criterion, we show in Fig. 3.1 the source density as a function of I-band magnitude for the three clusters that best fulfilled our selection criteria, M3 (NGC 5272), M13 (NGC 6205) and M92 (NGC 6341). The expected confusion limit in each cluster is indicated. We also provide the "usefulness" limit, motivated by the fact that we found in Paper I that roughly half of the deblended spectra will allow a measurement of the radial velocity of the star.

No preselection was performed based on photometric properties, such as the central slope of the surface brightness profile of the clusters. Baumgardt et al. (2005) suggested that the central slope might be used as an indicator for the presence of intermediate-mass black holes in the sense that clusters harbouring one should have a shallow cusp in theirs surface brightness profile. However, to obtain the complete picture about which clusters host massive black holes such a preselection might not be helpful.

Table 3.1 summarizes some fundamental properties of our sample clusters. The three targets are among the most massive clusters visible in the northern sky and are also located at relatively small distances to the sun.

3.3. Observations

We observed the three clusters using the PMAS instrument (Roth et al. 2005) at the Calar Alto 3.5m telescope. The data were obtained in 4 different observing runs with in 2010 and 2011. All observations were carried out using a spatial pixel ("spaxel") scale of 0.″5 on the sky and the R1200 grating in first order mounted backwards. With this configuration, we achieved a spectral resolution of $R = \lambda/\Delta\lambda \sim 7\,000$ around the infrared Ca II-triplet. The precise value of R varied with wavelength and from fibre to fibre. We discuss below in Sect. 3.4 how this variation was handled in the data analysis. In Table 3.2, we give a summary of the different observing runs. For M13 and M92, some observations were repeated in a later observing run, which enables us to search for stars with variable radial velocity.

PMAS covers a continuous area of 8″ × 8″ on the sky in the fine spatial sampling mode. For each of the observed targets, the aim was to completely cover the central region of the cluster, out to a radius of ∼ 15″. Due to weather losses, however, some fields could not be observed and the achieved coverage varies from cluster to cluster. Additionally, the final acquisition of the PMAS IFU has to be performed manually. In a crowded stellar field like a globular cluster, the precision of this procedure is limited to 1 − 2″ and constrains our final pointing accuracy.

Table 3.1. Fundamental properties of the observed clusters

Cluster	RA J2000	Dec J2000	distance kpc	$M_{\mathrm{V,t}}$ mag	σ_{c} km/s	Fe/H
M3 (NGC 5272)	13 42 11.62	+28 22 38.2	10.2	-8.88	5.5	-1.50
M13 (NGC 6205)	16 41 41.24	+36 27 35.5	7.1	-8.55	7.1	-1.53
M92 (NGC 6341)	17 17 07.39	+43 08 09.4	8.3	-8.21	6.0	-2.31

Notes. The values are taken from the database of Harris (1996).

Table 3.2. Summary of the PMAS observations

Run ID	Date		HJD		Target(s)
173	14 Mar 2010	18 Mar 2010	2455273	2455275	M3
184	07 May 2011	09 May 2011	2455690	2455691	M13
191	07 Jul 2011	10 Jul 2011	2455750	2455753	M13, M92
197	01 Oct 2011	02 Oct 2011	2455836	2455838	M92

Except for the first run (with ID 173), science observations were alternated with shorter observations of blank sky fields to allow for an accurate subtraction of sky lines during the data reduction. The sky subtraction procedure we have developed is presented below in Sect. 3.4.

3.4. Data reduction

The bulk part of the data reduction was performed using P3D, a dedicated software package to reduce fibre-fed integral field observations written by Sandin et al. (2010). It performs the basic parts of the reduction cascade, such as bias subtraction, tracing and extraction of the spectra, wavelength calibration and rebinning the data onto a regular grid. Recently, the dedicated cosmic-ray-rejection routine PYCOSMIC (Husemann et al. 2012) has been implemented into P3D and we followed the suggestions by Husemann et al. to efficiently clean our raw data from cosmic rays.

We used an optimal extraction method to obtain the individual spectra. Although optimal extraction is not strictly necessary for data observed with the PMAS lens array (the gaps between individual fibres are sufficiently large that crosstalk is a negligible issue), it has a big advantage over the simpler boxcar extraction: when determining the contribution of individual pixels to the extracted spectrum, P3D masks out the pixels affected by cosmic rays. Therefore, we do not rely on any interpolation scheme to assign values to those pixels.

All of our data was observed using the new PMAS CCD (Roth et al. 2010) that exhibits some features that require special treatment during the reduction. Moreover, our science goals impose stringent constraints on the data quality. For those reasons, some steps of the data reduction were performed outside of P3D. They will be discussed in the following.

3.4.1. Scattered light subtraction

Besides the traces of the individual science fibres and the bias level, we observed an additional light component in each of our exposures, scattered all over the CCD. This straylight component varies in strength and can reach intensities comparable to the science signal. Therefore we had to develop a method to subtract it. Using the trace mask, i.e., the position of each fibre in cross-dispersion direction as a function of wavelength, we first masked out all pixels around the traces. The remaining pixels should now contain only the scattered light. For each column of the CCD, we modelled the scattered light along the cross-dispersion direction by fitting a low order polynomial to the unmasked pixels. To obtain a smooth representation of the scattered light also as a function of wavelength, the sequence of one-dimensional fits was finally smoothed with a Gaussian kernel. Meanwhile, this procedure has also been implemented into P3D and we refer to the P3D homepage[1] for more details.

In Fig. 3.2, we show the crucial improvement in data quality after accounting for the scattered light. The difference image shows that the scattered light is not just a spatially flat component in the reduced datacubes but strongly influences the relative amount of light that is extracted for the individual fibres. Remember that our analysis relies on determining the PSF in an observation from the datacube and using this information to deblend stellar spectra. Any artefact in the data that changes the relative intensities of the spaxels would have a severe influence on the determination of the PSF because the intensities of the individual spaxels are not governed by the shape of the PSF any more.

3.4.2. Flatfielding

To get the relative intensities of the spaxels right, a high quality fibre-to-fibre flatfielding of the data is essential. A problem of PMAS is that the calibration data obtained during the night cannot be used to correct for the different efficiencies of the individual fibres because the calibration lamps do not illuminate the lens array homogeneously. Therefore, one has to rely on twilight flats. However, PMAS is mounted on the Cassegrain focus of the telescope, thus it is strongly affected by flexure. As a consequence, the sky flats cannot be used to correct the data for the fringing of the CCD because the fringing pattern is time-dependent.

We applied the following flatfielding procedure: starting from the reduced twilight flat, we divided each fibre by the mean of all fibres and fitted the resulting curves with Chebyshev polynomials of order around 10. Each science datacube was then flatfielded using the polynomial fits. This step corrects for the different efficiencies of the fibres, but it does not correct the fringing. The fringing pattern was removed using the night-time calibration data: each fibre in the continuum flat, originally used to trace the fibres across the CCD, was also fitted with a Chebyshev polynomial and afterwards divided by the fit. As a result, we obtained a normalized spectrum in each fibre that still included the

---

[1] `http://p3d.sourceforge.net/`

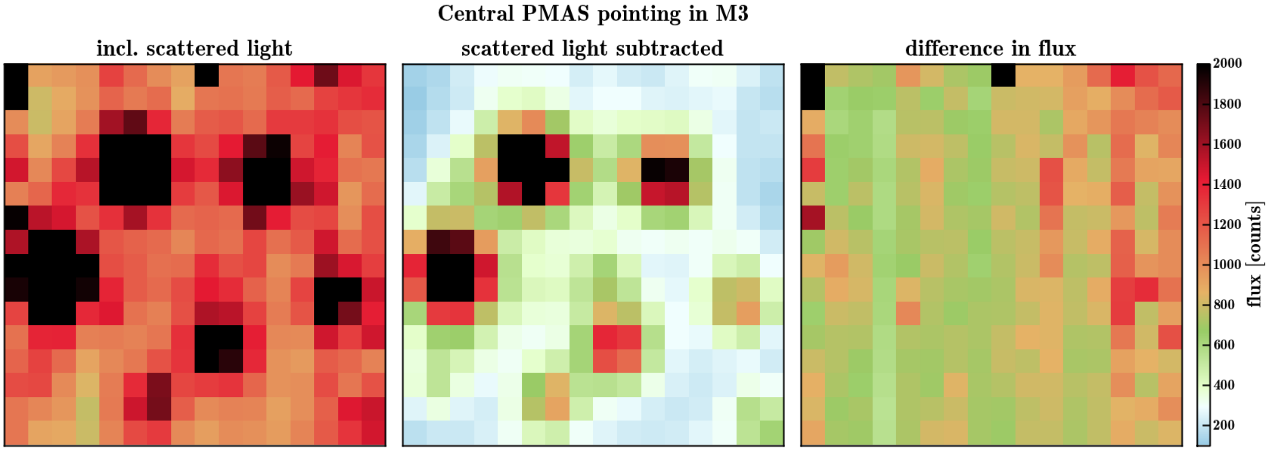

Fig. 3.2. Effect of scattered light in the PMAS data. We show a whitelight image of a reduced datacube of our central PMAS pointing in the cluster M3, once with the scattered light still included (left) and once with the scattered light subtracted (centre). The difference in flux between the two is shown in the right panel. All images are displayed using the same cuts.

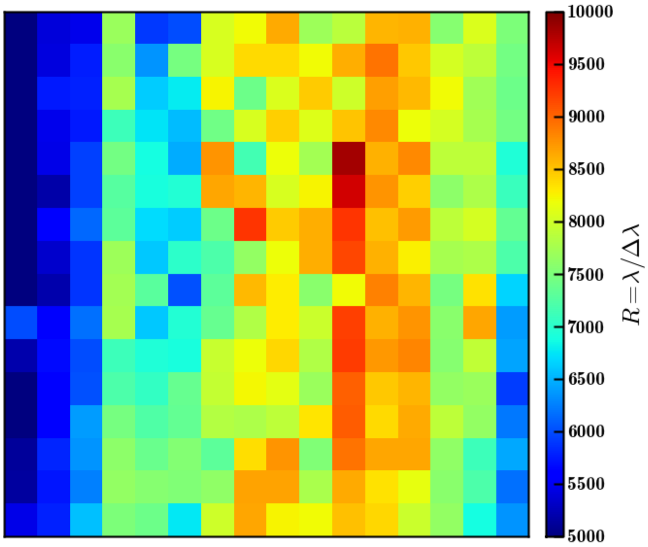

Fig. 3.3. Spectral resolution R in the calcium triplet as a function of position in the field of view. For each fibre, R was determined by fitting Gaussians to the individual arc lines and modelling the results as a smooth function of wavelength. The shown example is for M92, however, the pattern was similar in all observations.

fringes. Division of the science data by these spectra finally removed the fringes.

3.4.3. Determination of the spectral resolution

Some of our analysis requires an accurate determination of the spectral resolution R, both as a function of wavelength and position in the FoV. To determine R in a datacube, we used again the night-time calibration data. Each bright emission line in an arcframe was fitted with a Gaussian in every fibre. We then used Chebyshev polynomials to model the FWHM as a function of wavelength in every fibre and obtain an estimate of R in every pixel of a reduced datacube. To give an impression of how the spectral resolution changed across the field of view, we show in Fig. 3.3 the distribution of R in the calcium triplet. Note that the changes within a row are much stronger than within a column because the spectra within a column constitute a single package on the CCD and thus follow a comparable path through the spectrograph. The fibres that are located closest to the left edge of the field of view have the lowest spectral resolution. The likely reason for this is that they are not perfectly attached to the lenslets that focus the light into the fibres any more.

We emphasize that while strong differences up to a factor of ~ 2 are observed across the field of view, the pattern shown in Fig. 3.3 stayed fairly constant with time and also the absolute values did not change significantly. In the calcium triplet, we always found values from 5 000 to 10 000, depending on spaxel.

3.4.4. Subtraction of sky features

The last step in the data reduction was the sky removal. This step was omitted for the M3 data since no sky exposures were available for this cluster. For this cluster, we applied a method to subtract the sky during the data analysis that is presented in Appendix E.

All of our observations were carried out in dark time, therefore the sky spectrum mainly consisted of a faint continuum and telluric emission and absorption features. No evidence for a significant solar component was observed. The PMAS lens array does not have dedicated sky fibres, thus we had to rely on non-simultaneous sky exposures. It is well known that the intensity of the telluric lines changes during the night, so one cannot simply scale the observed sky with the exposure time and subtract it. Instead, we split the sky into an emission line component and a continuum component by fitting a polynomial to the continuum. The polynomial fit is scaled by the ratio of the exposure times of the science and the sky frames and subtracted from the science data. Our main concern, however, is an accurate removal of the strong OH lines. They are known to vary homogeneously, so we applied a constant scaling factor to the emission line component and subtracted it from the science data. The scaling factor was determined by performing a least squares fit to the regions around the OH lines and minimizing the squared residuals resulting from the subtraction of the sky lines.

To increase the signal in the sky, we binned the data beforehand. Given the strong variation of the spectral resolution across the field of view (cf. Fig. 3.3), one bin included all 16 fibres in a

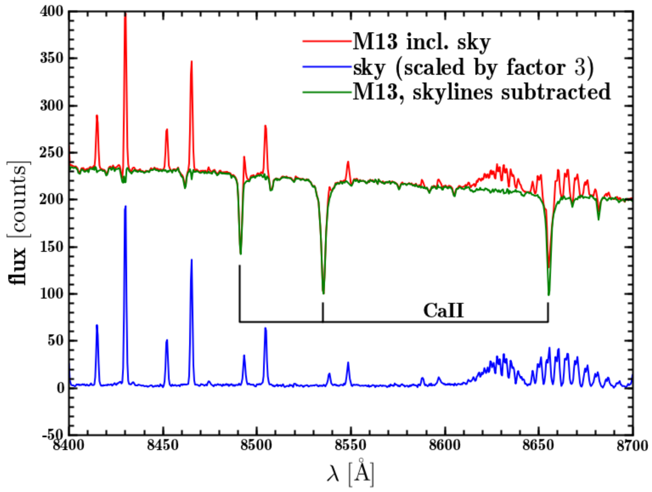

Fig. 3.4. Efficiency of skyline subtraction in PMAS data of M13. We show the average science spectrum of a datacube around the calcium triplet prior to the subtraction of telluric OH lines (red), the sky spectrum (blue) and the average science spectrum after the removal of the sky lines (green). The broad feature around the third line of the calcium triplet is telluric O_2 emission.

column and the procedure described above was repeated for all 16 columns.

We demonstrate the efficiency of our approach in Fig. 3.4. The broad sky feature visible around the third line of the calcium triplet is produced by telluric O_2 emission. Its intensity also changes during the night, but independently from the OH lines. Therefore an accurate subtraction of this feature was not always possible and the affected pixels had to be masked during some parts of the data analysis.

3.4.5. The final data sets

In Fig. 3.5, we show whitelight mosaics of our PMAS datasets in the three clusters together with an HST image of the central cluster region. The non-trivial mosaic pattern that we covered in the clusters has several reasons. We already mentioned the pointing inaccuracy of $1-2''$ that is a consequence of the acquisition procedure. Additionally, some fields were observed because they contained several bright stars and thus should allow for a good PSF reconstruction. One example of such a field is the isolated one to the south east in M13. The reason that in M3 our pointings are asymmetric with respect to the cluster centre is that the centre we used during the observations was offset from the one we assume in the analysis. This is discussed in more detail in Sect. 3.5.2.

Just counting the number of pointings, our richest dataset is that of M13. However, in terms of observing conditions, M92 is the most promising dataset as almost all of the observations were carried out with a seeing of $1''$or better while for the other two clusters, it usually varied between $1''$and $1\farcs5$. The provided seeing values were measured by the acquisition camera that operated in the V-band. The FWHM values that we measure in our datacubes are lower by $\sim 20\%$. In total, we obtained useful data for 5 fields in M3, 6 fields in M13 and 3 fields in M92. In each field, the number of exposures varied between 2 and 3. Data from different epochs exist for 5 of the fields in M13 and the central pointing in M92.

3.5. Data analysis

In Paper I, we presented an algorithm to deblend stellar spectra from IFS datacubes via PSF fitting. Starting from an inventory of the stars in the field (hereafter called "reference catalogue"), obtained, e.g., from HST imaging, we locate the sources in the datacube and determine the subset of sources for which spectra can be deblended at the (typically lower) spatial resolution of the IFS data. Using an iterative approach, we then determine the wavelength dependent PSF as well as the precise coordinate transformation from the reference catalogue to the datacube. In the final step, all the spectra of the resolved sources are simultaneously deblended using a linear least-squares fit. Further details are given in Paper I.

3.5.1. Generating a complete source list

To obtain a high quality reference catalogue, we started again from the photometry obtained in the ACS Survey of Galactic globular clusters, certainly the most comprehensive photometric dataset available for our set of clusters. We show a colour magnitude diagram of the three clusters based on this data in Fig. 3.6. However, one common issue of ACS observations is that the brightest stars are often heavily saturated and cause strong bleeding artefacts. Although the ACS survey included an observing strategy to overcome this effect as much as possible and saturated stars were treated separately in the analysis by Anderson et al. (2008), we decided to cross-check with a second dataset. In fact, a single PMAS datacube only contains 256 spaxels, so even a single star that is significantly detectable yet missing in the reference catalogue will have a strong effect on the analysis.

To cross-check the photometry we searched for data obtained with WFPC2. While probably being less accurate compared to ACS, WFPC2 data does not suffer so strongly from bleeding artefacts. For M13, we used the available photometry from Piotto et al. (2002). Unfortunately, neither M3 nor M92 are in the sample observed by Piotto et al.. For those two clusters, however, we found and obtained raw V- and I-band photometry from the archive and analysed them using DOLPHOT (Dolphin 2000). The available photometry for M13 covered the B- and V-bands, but our spectra are in the near infrared and we used I-band magnitudes in the source selection process for the deblending. To get I-band magnitudes for the M13 stars, we used Padova isochrones (Marigo et al. 2008), available for a wide range of magnitudes in the HST photometric system. We compared the magnitudes in B and V for every star in the HST photometry to those in the isochrone and then assigned it the I-band magnitude of the best match in the isochrone.

As expected, the ACS catalogue is quite complete at the magnitude levels that we are most interested in. However, we found that occasionally giant stars are missing. The reason for this becomes clear from Fig. 3.7, where we illustrate the result of the cross checking procedure for M3. The image shown in Fig. 3.7 is a combination of all data that were used to create the ACS catalogue. If bright stars were located directly on the bleeding artefacts caused by even brighter ones, they might have been missed. To avoid this, a single short exposure was taken as part of the ACS survey for every cluster observed. However, ACS has a gap of some arcseconds width in between the two chips and no short exposure data exists in that area. The stars we additionally detect using the second catalogue lie preferentially in the same area. The individual stars that we added to the reference catalogue for all three clusters are highlighted in the colour magnitude diagrams in Fig. 3.6.

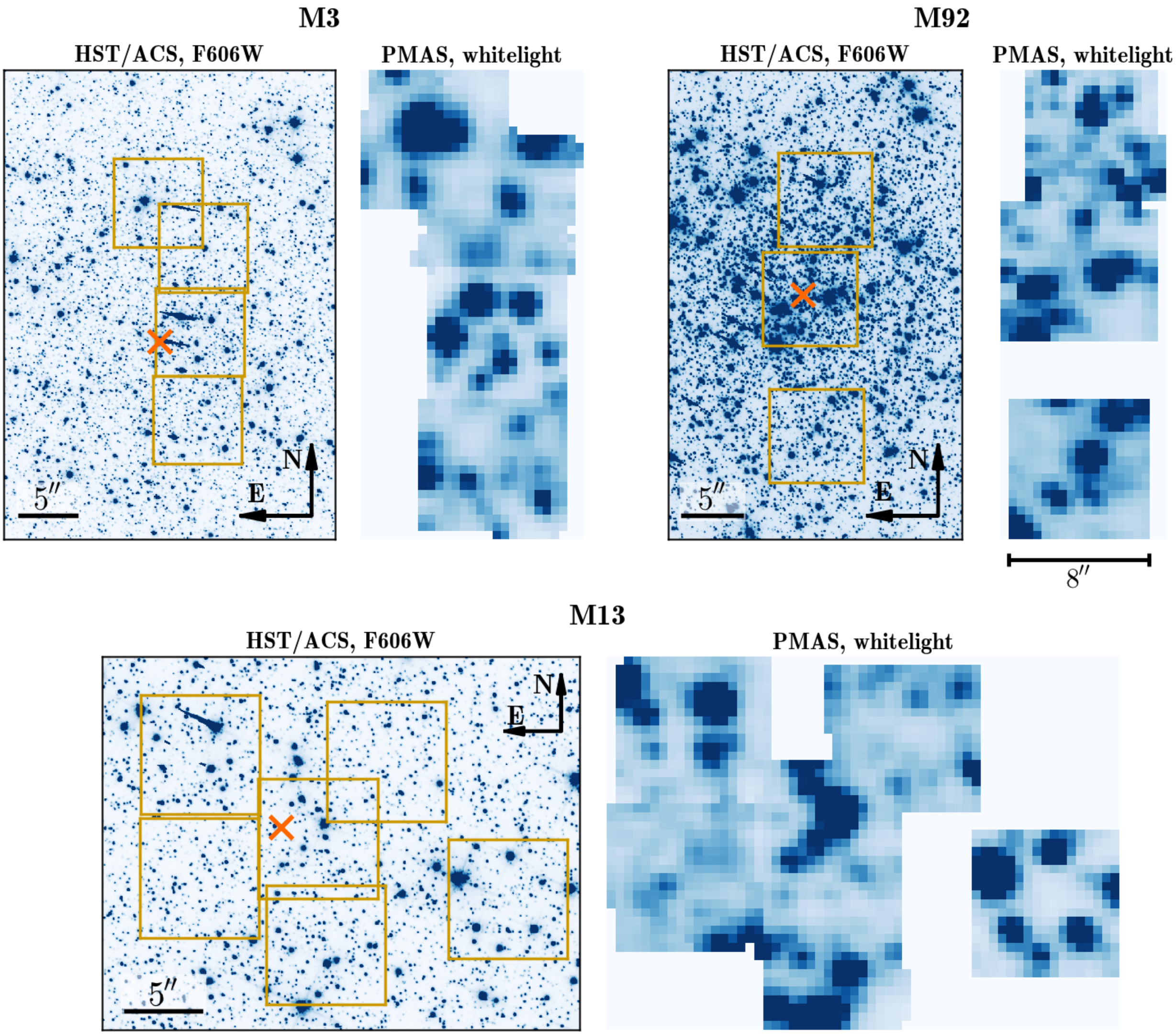

Fig. 3.5. The central region of the globular clusters M3, M13 and M92 as seen by HST and in our PMAS data. An orange cross in every HST panel panel marks the cluster centre as determined by Goldsbury et al. (2010). For this visualization, we collapsed the PMAS datacubes in dispersion direction. Note that one PMAS pointing in M3 is not shown because it is located further away ($\sim 30''$) from the centre.

3.5.2. Determination of the cluster centre

For the later analysis, a proper determination of the centre of each cluster is highly important. Measured cluster properties such as the surface brightness profile or the velocity dispersion profile can significantly deviate from the intrinsic ones if the true centre is offset from the assumed one. Several methods have been proposed in the literature to determine the (photometric) centre of a globular cluster, such as fitting ellipses to the number density contours of the cluster and determining the centre by averaging the centres of the different ellipses. Other methods exploit the symmetry of the density around putative centres. For the clusters in the ACS survey, these methods have been applied by Goldsbury et al. (2010). Since our photometry is based on more or less the same data (the few missing stars will have marginal influence) we adapt the centres reported by Goldsbury et al. and given in Table 3.1.

The central coordinates deviate slightly from those measured by Noyola & Gebhardt (2006). The offsets are $3\farcs9$ for M3, $2\farcs4$ for M13 and $0\farcs9$ for M92. A reason for this offset might be that all targets have rather large cores ($> 10''$, Harris 1996) so that measurements of the centre are less tighly constrained. The measurements performed by Noyola & Gebhardt are based on WFPC2 data that covers a smaller fraction of the central region than ACS does. Therefore, we rely on the Goldsbury et al. centre.

3.5.3. Deblending the spectra

Source selection

With a reference catalogue at hand for each cluster that should be complete at the brightness levels which we can probe with our PMAS data, the next step was to deblend the sources from the individual datacubes. The first step in this process was a determination of the expected confusion limit in each datacube, i.e., the magnitude below which no individual sources can be deblended any more. In Paper I, we found that the confusion limit is roughly equal to the magnitude when the density of brighter sources approaches 0.4 stars per resolution element. Due to the variable

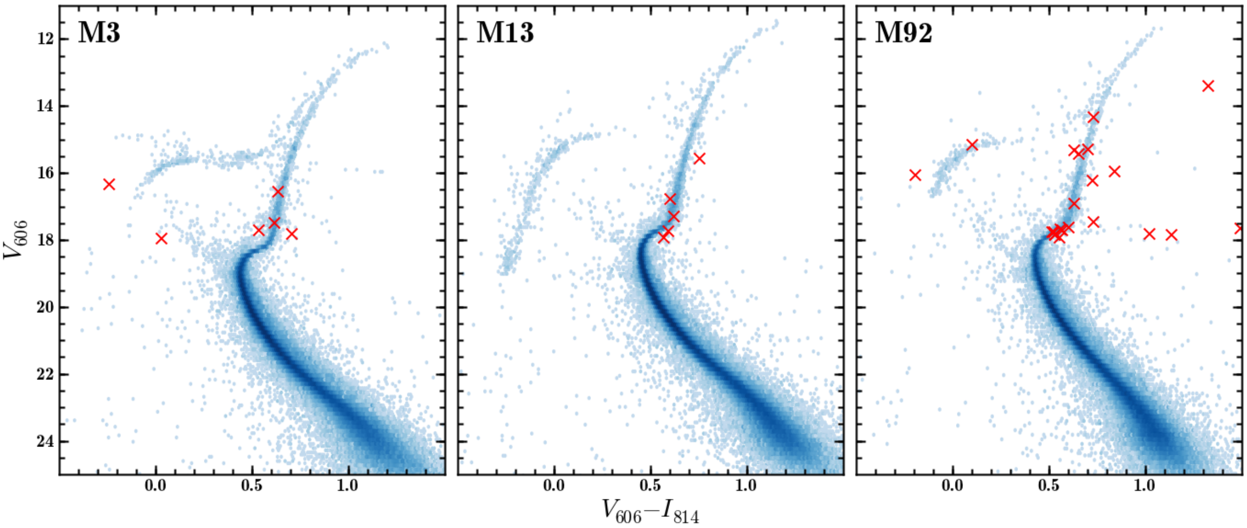

Fig. 3.6. Colour-magnitude diagrams of M3 (left), M13 (centre) and M92 (right). The photometry obtained in the ACS survey of Galactic globular clusters is shown as a blue density plot. Red crosses mark the individual stars we added based on the analysis of archival HST WFPC2 data.

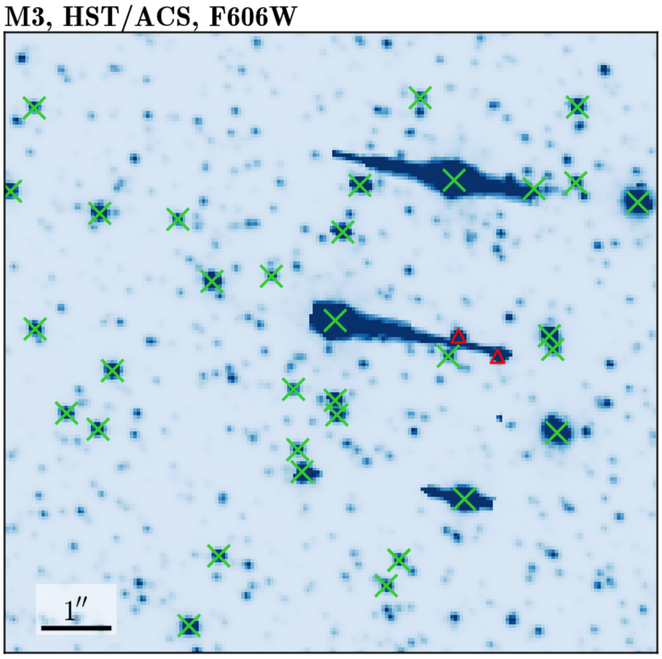

Fig. 3.7. Illustration of incompleteness in the ACS input catalogue, using the central region of M3. Green crosses indicate sources included in the ACS catalogue, sources marked by red triangles were added after a comparison with archival WFPC2 photometry. For clarity, only stars with an I-band magnitude brighter than 17 are highlighted. The cluster centre is located directly on the central bright star.

seeing conditions, this limit was variable even for a given cluster. In a second step, we then determined the expected signal-to-noise of each target above the confusion limit and only accepted stars above a certain threshold for which we used a S/N of 5.

Stars just below the confusion limit will still cause a grainy structure across the field of view. To account for this component, we used an additional component in the deblending process, containing all stars within 2 magnitudes below the confusion limit. The flux ratio of the individual stars in that component was fixed to their relative I-band brightnesses. Finally, a constant background component was included to account for even fainter sources and the night sky.

To visualize the results of the source selection process, we show in Fig. 3.8 a colour magnitude diagram of the covered area in each cluster and highlight the sources that passed the various selection criteria. In all three clusters, our data allow us to deblend spectra almost all the way down the red giant branch. Note that the few bright sources, marked by red triangles in Fig. 3.8, are those that fell below the S/N threshold because of their small distances ($\leq 0.3\times$ the seeing FWHM) to a brighter neighbour. For those sources we did not try to deblend individual spectra but accounted for their contributions by modifying the PSF of the neighbour as outlined in Paper I. The transitions between the individual selection categories in Fig. 3.8 are not sharp but rather smooth because the confusion limit varied with the observing conditions. One also has to keep in mind that the selection was carried out in the I-band while in Fig. 3.8 we plot V-magnitudes.

PSF

In the actual fitting procedure, we modelled the PSF as a Moffat function with up to 4 free parameters: the FWHM, the β parameter controlling the kurtosis of the profile, the position angle, and the ellipticity. For each observed datacube, the FWHM was a free parameter in the initial fit, using a prior guess from the seeing of the observation. In the majority of the cases, we also allowed β to vary. Exceptions were made for some observations where either no reasonably bright star was in the observed field or the seeing was rather poor ($\gtrsim 2''$). In those cases, the contrast was not high enough to yield useful constraints on the value of β and we fixed it to a typical value for the observations taken during the same night. Fig. 3.9 shows a summary of all the values we obtained for FWHM and β. The wide distribution of FWHM values gives a good impression of the different seeing conditions (and thus spatial resolutions) we are dealing with. As a side note, no correlation is observed between the FWHM and the airmass in the observation as one would expect the seeing to

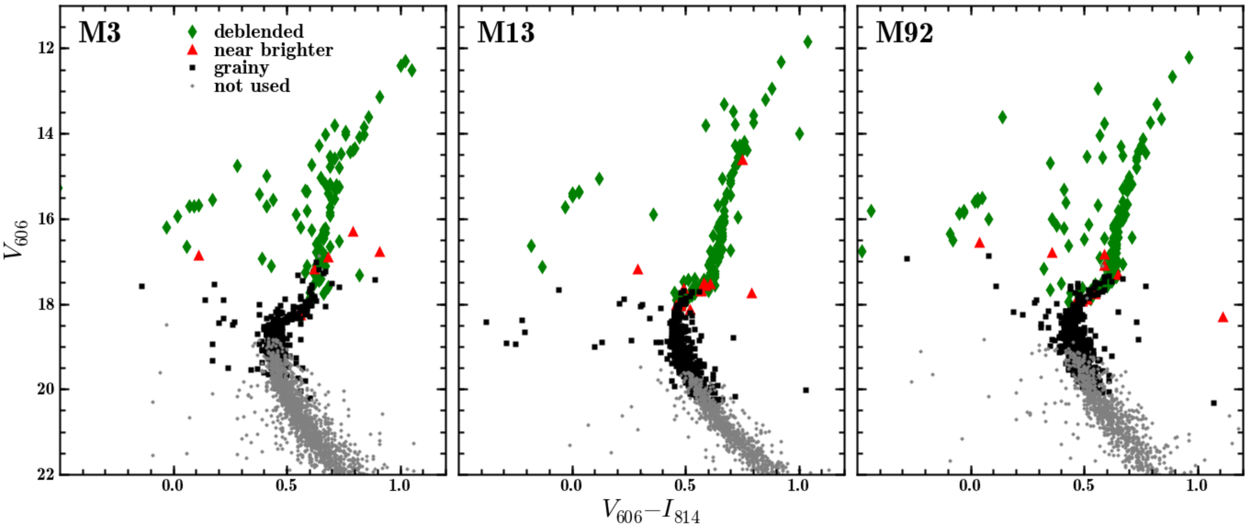

Fig. 3.8. Colour magnitude diagrams of the area covered by the PMAS observations, coding source categories by different colours and symbols: Individually deblended sources (green diamonds), sources deblended together with a brighter neighbour (red triangles), sources contributing to the grainy stellar background (black squares) and unused sources (grey circles).

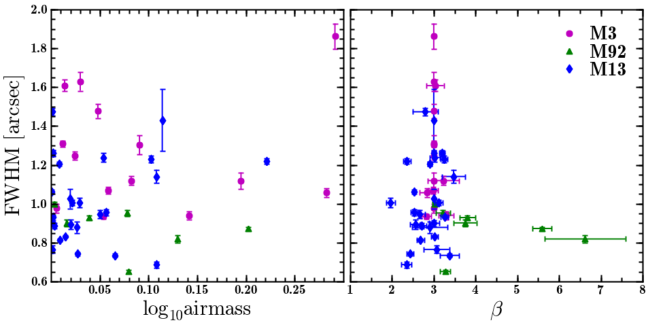

Fig. 3.9. Comparison of derived PSF parameters. Each panel shows the FWHM: As a function of the airmass of the observation (left), and as a function of β (right). Each plotted point corresponds to the mean value obtained in a datacube. Different symbols indicate different clusters as indicated in the legend. The error bars represent the standard deviations over the cubes, including variations with wavelength.

increase with airmass. Also, we observe no correlation between the FWHM and β and in most cases, the values of the latter scatter around $\beta \sim 3$. The rather low values of β indicate that the PMAS PSF has extended wings and that a Gaussian would not be a valid description of the PSF. There are two notable exceptions with rather values of $\beta \sim 6$. The two datacubes of M92 were observed within the same night in the October 2011 run. During this run, we observed only one additional datacube, also of M92, where we find a rather normal β value. So it remains unclear what caused the high values in the two mentioned cases.

Using an elliptical PSF did not significantly improve the results, so we always assumed a circular PSF.

Source coordinates

The coordinate transformation was always modelled using four free parameters: two parameters defining the scaling and rotation of the reference coordinates into a PMAS field of view and another two parameters describing a shift along the x- and y-axes. PMAS has a nominal spaxel scale of $0\farcs5$ and a fixed rotation angle of zero degrees. The reference coordinates have a pixel scale of $0\farcs05$ with the y-axis pointing north (Anderson et al. 2008), so we expect a scaling factor of $\xi = 0.1$ and zero rotation angle. As can be seen from Fig. 3.10, where we show the scaling factors and rotation angles for all our datacubes, this is not the case: on average, we obtain $\xi < 0.1$, indicating a slightly smaller scale of the PMAS spaxels. Simply taking the mean and standard deviation of all measurements gives $\xi = 0.0997 \pm 0.0002$. If we assume that the coordinates are correct in the centre of the PMAS field of view, this corresponds to an uncertainty near the edges of the field of view of ~3% of one spaxel, similar to what we found in our analysis of simulated PMAS data in Paper I.

We note that for the simulated PMAS data we also found a mild tendency that the recovered scaling factors came out to large. Compared to the nominal spaxel scale of PMAS, we now observe the opposite trend. However, differences in the scaling of the order that we observe can also occur within the instrument, e.g., caused by a temperature dependent focus. In our dataset, we do not find a significant correlation between the recovered scaling factor and the ambient temperature during the observation. Given the small spread in ξ, this is not surprising.

The observed increase of the uncertainty in the scaling factor with the seeing is well expected because the lower the spatial resolution, the smaller the contrast between individual stars and the larger the uncertainties on their measured centroids.

The rotation angle shows significant offsets from zero, up to a few degrees. We observe a bimodal distribution, with the values for the M3 data being consistent with an angle of $\theta = -3°$, while for M13 and M92, the values cluster around $\theta = +0.5°$. An explanation for this behaviour is that the M3 data were all obtained in 2010, before the telescope experienced a significant downtime and refurbishment, while the data for the other two targets was observed after that period. So we speculate that the telescope upgrade may have influenced the orientation of PMAS on the sky.

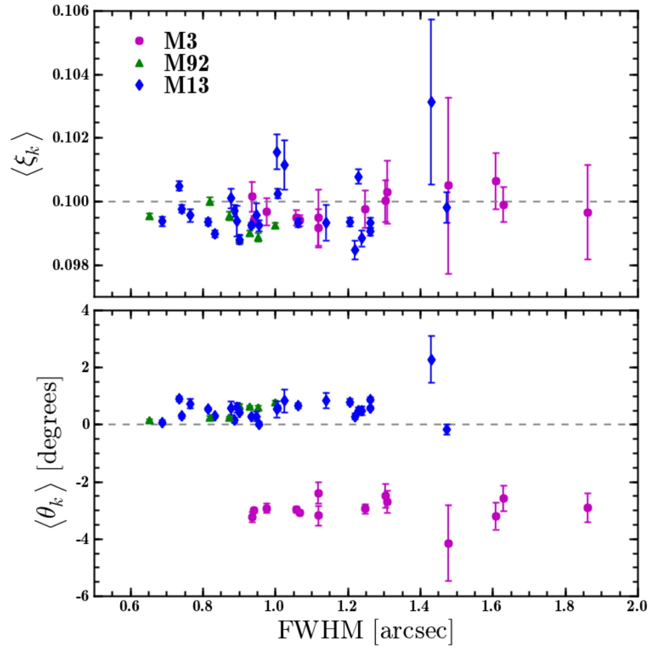

Fig. 3.10. Average spatial scaling factors (top) and rotation angles (bottom) of all the PMAS datacubes with respect to the reference catalogue. Symbols are the same as in Fig. 3.9. Dashed lines in both panels show the values expected for the nominal characteristics of PMAS in the instrument setup that was used.

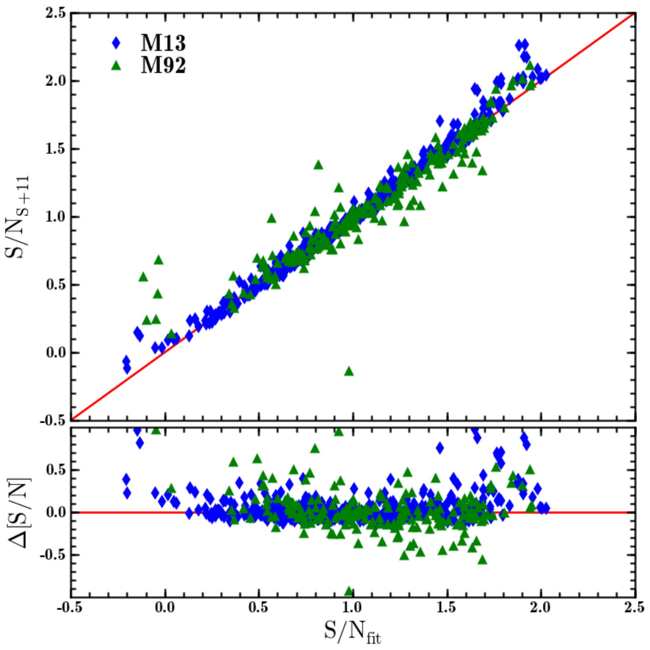

Fig. 3.11. Comparison between the signal to noise estimates obtained following the method by Siebert et al. (2011) and those when fitting the spectra with synthetic ones, using the deblended spectra in the clusters M13 and M92.

Extraction of spectra

With the wavelength dependent PSF parameters and coordinate transformations in hand, we deblended the spectra for the sources identified as outlined above. To assess the quality of the deblended spectra, we first looked at their S/N ratios. The signal-to-noise was determined following the prescription of Siebert et al. (2011): In an iterative approach, the spectrum was smoothed by a boxcar filter of 3 pixels size and clipped from pixels deviating by more than 2σ from the rms of the difference between the unsmoothed spectrum and the smoothed one. After convergence, the local standard deviation was determined for each pixel from the pixel itself and its two neighbours. The S/N was then estimated as the median of the ratio between the spectrum and the local standard deviation, normalized by a factor that depends on the data. To determine this factor, we compared our unnormalized values to those obtained when fitting the spectra with synthetic ones from the library by Husser et al. (2013). In the absence of template mismatches, those should closely follow the true S/N values. In Fig. 3.11 we compare the two S/N estimates for M13 and M92. To obtain a one-to-one relation, we have to normalize our provisional values by a factor of 0.48, reasonably close to the value of 0.36 obtained for RAVE data by Siebert et al. (2011).[2] It is reassuring that for two clusters with quite different metallicity (M13: $[Fe/H] = -1.53$, M92: $[Fe/H] = -2.31$, cf. Table 3.1), and over a wide range in S/N, we find a close to linear relation.

In Fig. 3.12 we present the results of the deblending process for the three clusters. Together with an HST image and a white-light mosaic of the integral field data, we also show the residuals after subtraction of the deblended sources. In each panel, we indicated every position where a stellar spectrum was deblended by a coloured cross, with the colour coding matched to the S/N of the spectrum. The number of stellar spectra we can deblend in such a small region of the sky is quite remarkable. As expected, the spectra cover a broad range in S/N, with the brightest stars having values of $S/N > 100$. That some spectra are deblended with a rather low S/N is generic to our approach: because we aim to obtain a spectrum for every single star that can possibly be resolved in a datacube, we inevitably pick up a lot of faint sources with a low S/N. This is similar to the increased spread that is observed in a colour-magnitude diagram of a globular cluster when moving down the main sequence. To illustrate this, we show in Fig. 3.13 some examples of the spectra that were deblended in the central pointing of M13 together with their positions in the cluster. For the brightest giant near the centre of the FoV we obtain a spectrum with a very high S/N as expected. The spectrum of the star uncovered from under the PSF wings of the bright star has a substantially lower S/N. Note that PSF fitting is the only technique that allows one to obtain an uncontaminated spectrum for this star at all. The same is true for stars of similar brightnesses close to each other. This is illustrated by the two stars towards the upper left corner of the FoV. As can be seen from the right panel of Fig. 3.13, one of them is a horizontal branch star and has a completely different spectrum from its neighbour, with no mutual contamination visible in the spectrum of either star. This highlights the power of our approach. Note that in a few cases (cf. Fig. 3.8) the distance between two stars is so small that even with PSF fitting techniques they cannot be accurately deblended because their PSF images become indistinguishable. In those cases we obtained a single spectrum for the two stars that was accordingly flagged during the further analysis.

---

[2] In fact, Siebert et al. (2011) determine two normalization constants: one determined from simulations with pure Poissonian noise and an additional one that accounts for the non-Poissonian nature of the observed spectra. For simplicity, we used the combination of the two.

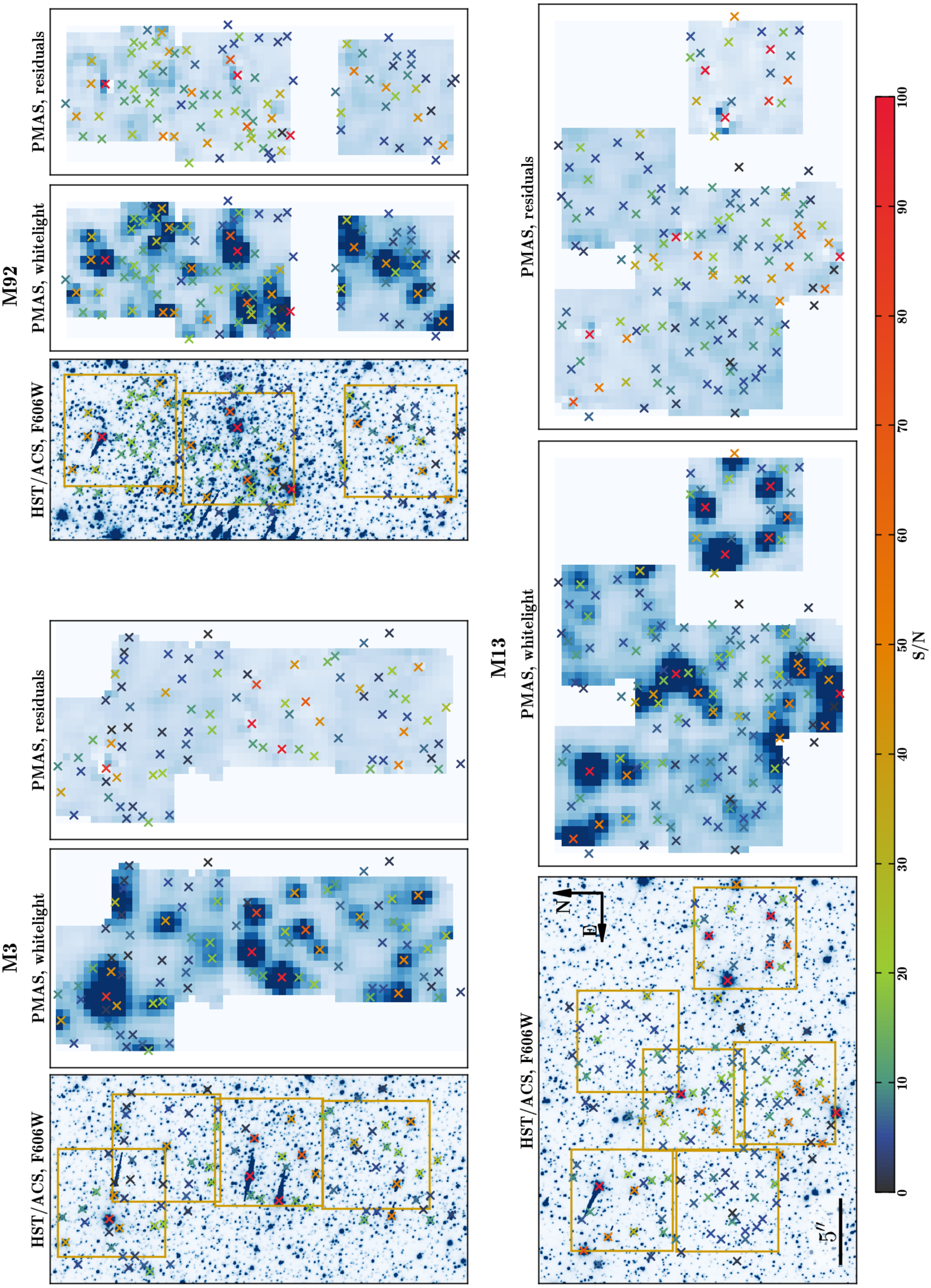

Fig. 3.12. Results of the deblending of the stellar spectra. For each cluster the panels show, from left to right: an HST image of the central region with the PMAS pointings overplotted, a whitelight image of the combined PMAS data, and the residuals from the PMAS data after the sources have been subtracted. In each panel we highlight the positions of the extracted spectra by coloured crosses, with the colour coding of the crosses matched to the S/N of the respective spectrum.

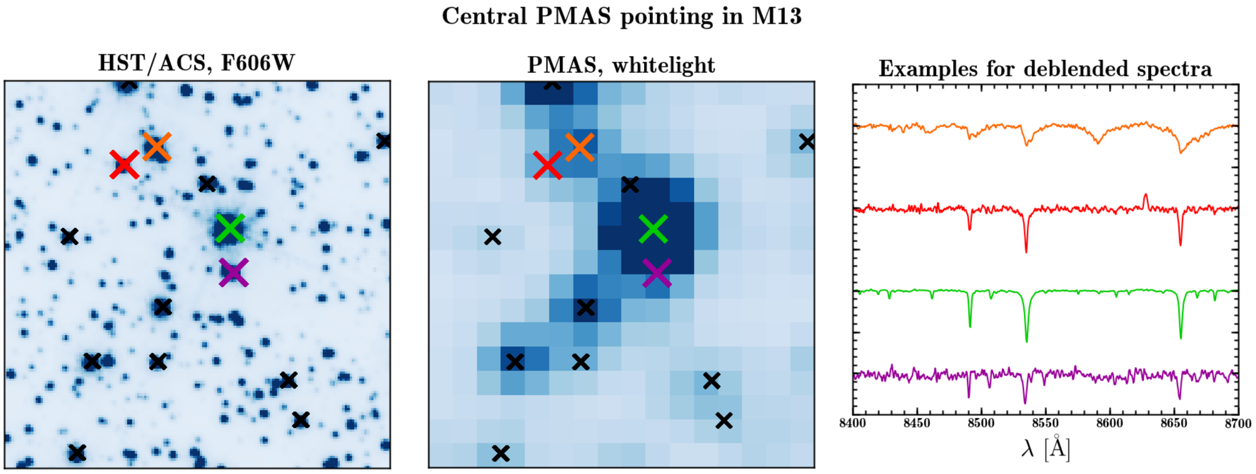

Fig. 3.13. Example spectra deblended from the central PMAS pointing in M13. The left panel shows an HST image of the region, a whitelight image of our PMAS data is shown in the central panel. In both panels, the locations of the deblended stars are shown using crosses. The spectra of the sources marked by coloured crosses are depicted in the right panel. The colour coding used to plot the spectra and to indicate their positions is the same in all three panels.

In total, we deblended spectra for 102 stars in M3, 141 in M13 and 98 in M92. The further analysis of those spectra will be discussed below.

When comparing the results for M92 with those obtained for M13 in Fig. 3.12, it becomes clear how crucial the seeing influences that quality of the data. As mentioned earlier and as is also visible from Fig. 3.9, the average seeing in the observations of M92 was significantly better compared to the observations of M13. As a consequence, relative to the number of pointings, we can deblend significantly more stars in the M92 data than in the M13 data. On average, the stars in M92 also have a higher S/N than those in M13. The observations of M3 were carried out under similar conditions as those of M13, but the average S/N of the stars is higher. The reason for this can be seen in Fig. 3.1, where we plot the stellar density as a function of magnitude. The density of M13 increases much steeper towards the confusion limit compared to M3 or M92. This implies that in M13 we select many stars of almost equal brightness right above the confusion limit.

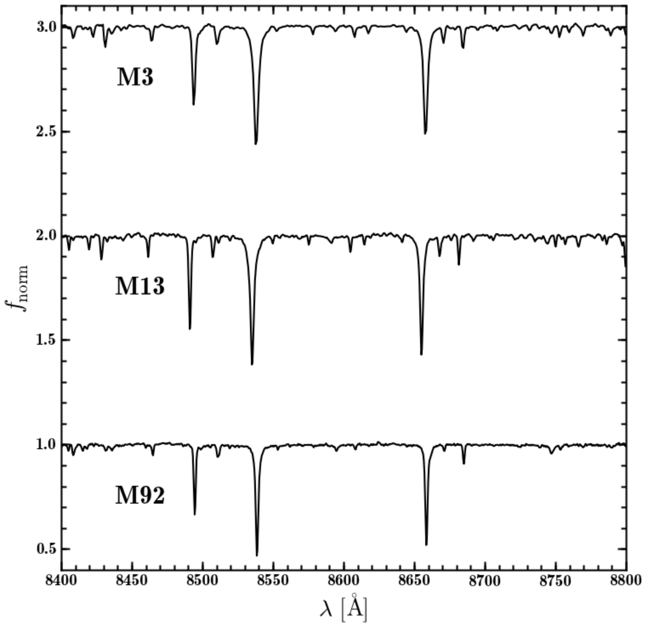

Fig. 3.14. Template spectra created for M3, M13 and M92. All spectra are normalized, but for clarity, horizontal offsets of +2 and +1 have been applied to the templates created for M3 and M13, respectively.

3.6. Radial velocities

3.6.1. Method

Cross-correlation of PMAS spectra

To determine radial velocities for our data, we cross-correlated all the spectra against a template spectrum. As no observations of a radial velocity standard star had been carried out, we created template spectra from the cluster stars themselves. For each cluster, we selected all the stars above a given cut in signal-to-noise and determined their average spectrum, with the input spectra being weighted by their respective S/N. Prior to the combination, all spectra were normalized, resampled into logarithmic space and corrected for the heliocentric velocity of the observation. To perform the continuum determination required to normalize the spectra we again followed Siebert et al. (2011): each spectrum was initially fitted with a polynomial (we used Chebyshev polynomials for this task), then κ-σ-clipping was performed on the residuals, using asymmetric κ-values for the upper and the lower threshold. While the upper threshold remained fixed at $\kappa_{\rm up} = 3$, the lower threshold $\kappa_{\rm low}$ was adjusted based on the S/N of the spectrum, with higher values being used for lower S/N values and vice versa. This is necessary because while spectral lines in high-S/N spectra must be clipped, noise spikes in low-S/N spectra should not be spuriously identified as spectral lines. The template spectra obtained in all three clusters are shown in Fig. 3.14

With the templates at hand, we determined a radial velocity for each spectrum by subtracting the continuum in the way just described, logarithmically rebinning it and cross-correlating it against the template spectrum of the respective cluster. The

Table 3.3. Literature data used to complement our radial velocities

Reference	Abbr.	Targets ($n_{\rm star}$)
Gunn & Griffin (1979)	GG79	M3 (111)
Lupton et al. (1987)	L+87	M13 (147)
Pryor et al. (1988)	P+88	M3 (111)
Soderberg et al. (1999)	S+99	M3 (87), M13 (150), M92 (35)^{a}
Pilachowski et al. (2000)	P+00	M3 (77), M13 (78), M92 (61)
Drukier et al. (2007)	D+07	M92 (306)
Mészáros et al. (2009)	M+09	M13 (123), M92 (64)

Notes. For each reference, the observed clusters are given together with number of stars observed per cluster.
$^{(a)}$ Excluded, see discussion in text.

cross-correlation peak was determined by fitting its central pixels with a Gaussian.

There are several criteria to assess the quality of a cross-correlation result. Obviously, the accuracy should scale with the height of the cross correlation peak. But the uncertainty also depends on the strengths and frequencies of spurious peaks, caused by the finite S/N of both template and spectrum. If we separate the cross correlation spectrum into a part that is symmetric about the true peak and one that is anti-symmetric about it, then only the antisymmetric part will contribute to the uncertainty in the determination of the centroid. Based on this idea, Tonry & Davis (1979) developed the r statistics for a cross correlation peak,

$$r_{\rm cc} = \frac{h}{\sqrt{2}\sigma_{\rm a}}\,, \tag{3.1}$$

where h is the height of the cross-correlation peak and $\sigma_{\rm a}$ is the normalized standard deviation of the antisymmetric component of the cross correlation spectrum. Tonry & Davis (1979) also showed that the uncertainty taylored to a measured radial velocity is proportional to $(1 + r_{\rm cc})^{-1}$. Based on this, Kurtz & Mink (1998) provide an estimate for the uncertainty,

$$\sigma_{\rm v} = \frac{3}{8}\frac{w}{1 + r_{\rm cc}}, \tag{3.2}$$

where w is the FWHM of the cross correlation peak.

A valid prescription of the uncertainties of the individual radial velocity measurements is essential to obtain a trustworthy value for the velocity dispersion within a cluster. We performed the following reliability check to test the validity of Eq. 3.2 when applied to our data.

First, we selected the spectra that were deblended with a S/N > 50 in each cluster, and created $N = 100$ realisations of each spectrum by applying a random velocity shift drawn from a Gaussian with standard deviation 10 km/s and then adding artificial noise to achieve a final S/N ratio that was between 2 and half of the initial S/N of the spectrum. We then performed the same cross correlation analysis on the simulated data as for our deblended spectra. To verify whether the values derived using Eq. 3.2 correctly describe the actual uncertainties we divided the offsets Δv between measured and true radial velocity by $\sigma_{\rm v}$, calculated using Eq. 3.2. The distribution of $\Delta v/\sigma_{\rm v}$ should be a Gaussian with a standard deviation of 1. We show this distribution in Fig. 3.15 as a function of $r_{\rm cc}$. Overall, Eq. 3.2 tends to overestimate the errors slightly, as our measured offsets are on average ~20% smaller, almost independent of $r_{\rm cc}$. We applied a correction factor of 0.8 to the uncertainties obtained from Eq. 3.2. We will also discuss the implications of under- or overestimated uncertainties when discussing the dynamic modelling of our targets.

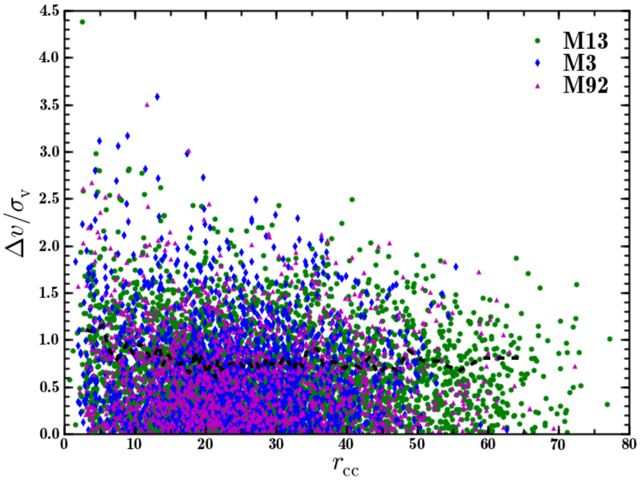

Fig. 3.15. Test for the validity of the adopted prescription to quantify the uncertainties of the radial velocity determination. We show the offset between measured and true radial velocities as a function of the cross-correlation statistics, $r_{\rm cc}$. The offsets are normalized by the uncertainty calculated using Eq. 3.2. A black dashed line shows the 68.3% percentile of the distribution. The results are based on simulated spectra as described in the text. Different symbols denote input spectra coming from different clusters, as indicated in the upper right corner.

Extending to larger radii – literature data

Our data are limited to the very central region of each cluster. Clearly, this is where our deblending approach is most efficient. To probe the kinematics over the full radial extend of our targets, we searched the literature for additional radial velocity data. At larger distances to the centre the source densities become significantly lower so that these regions can be more efficiently accessed also by means of traditional spectroscopy. When collecting these complementary data from the literature, we concentrated on studies that investigated a reasonable number of stars ($\gtrsim$50), and only selected data for which useful uncertainties were provided with the measured radial velocities. A summary of the catalogues that we included is provided in Table 3.3. For further information on the details of the observations and the determination of the radial velocities we refer to the publications given in Table 3.3.

To obtain the final set of radial velocities, we needed to combine the results from the individual studies of each cluster. Many stars were observed more than once in a single study and we obtained a combined velocity for such stars as

$$\bar{v} = \sum_i \frac{v_i}{\sigma^2_{\mathrm{v},i}} / \sum_i \sigma^2_{\mathrm{v},i} \, . \tag{3.3}$$

Eq. 3.3 corresponds to the calculation of the weighted mean of N measurements v_i with each measurement being weighted by the inverse of the square of its uncertainty $\sigma_{\mathrm{v},i}$. The uncertainty of the combined velocity is calculated as

$$\sigma_{\bar{\mathrm{v}}} = \left[\sum_i \frac{1}{\sigma^2_{\mathrm{v},i}} \right]^{-0.5} \, . \tag{3.4}$$

Eqs. 3.3 and 3.4 offer a convenient way to detect stars with variable radial velocities. The χ^2 value connected to Eq. 3.3 is

$$\chi^2 = \sum_{i=1}^{N} \frac{(\bar{v} - v_i)^2}{\sigma^2_{\mathrm{v},i}} \, . \tag{3.5}$$

For the scatter between individual measurements to be consistent with the uncertainties, the measured χ^2 should be comparable to the number of degrees of freedom N_{dof}, i.e., the number of observations minus one. For any combination of χ^2 and N_{dof}, the probability of consistency can be calculated from the probability density function of the χ^2 distribution for the given degrees of freedom. We identified as "RV variable" all stars with probabilities less than 1% and absolute offsets ≥2 km/s.

We also checked whether the individual studies yielded consistent results. This was done by defining a reference study for each cluster and identifying the subset of stars that was also observed by one or more of the other studies. For this subset, which contained $\gtrsim$20 stars for any given combination of two studies, we computed the difference in the measured radial velocities. In the case of consistent results, the differences should scatter around zero. If the mean of the distribution deviates from zero, this indicates that the studies obtained different systemic cluster velocities, a minor inconsistency that can be easily corrected for. We show the results of this comparison in Fig. 3.16. In most of the cases, the measured offsets were small ($\lesssim$1 km/s) and no systematic trends were observed. A notable exception is the data of Soderberg et al. (1999) in M92. As already mentioned by Drukier et al. (2007), the velocities measured by Soderberg et al. in M92 are biased towards the cluster mean, a trend likely caused by the presence of interstellar absorption lines in the spectra. We observe the same trend with respect to both comparison catalogues and therefore decided to omit this dataset. However, neither in M13 nor in M3 we observe a similar trend, likely because the spectra covered a different wavelength range. Therefore, we kept the data of Soderberg et al. for those two clusters.

We also used the comparison shown in Fig. 3.16 to check whether the uncertainties provided in the different studies are reliable. For this check, we assume that the individual data are reliable, i.e. no systematic measurement errors except for a constant offset are present. In that case, the scatter of the individual offsets should again be consistent with the measurement errors, i.e., the χ^2 value should be of the order of the number of degrees of freedom, in this case the number of stellar pairs minus one. Radial veloccity variables will bias this comparison. Therefore we iteratively cleaned the comparison samples from such stars. For each combination plotted in Fig. 3.16 the probability that the scatter is consistent with the uncertainties is provided. In some cases, the probabilities are quite small, indicating that the uncertainties may be underestimated. In such cases, we applied a constant correction factor to the uncertainties that yielded a $\chi 2$ value equal to the number of degrees of freedom. In doing so, we started from the data of Drukier et al. (2007) in M92 as it contains by far the largest sample of stars and uncertainties were determined very carefully. We then determined the correction factors successively for all other studies. The factors that we obtained were small (∼1.2-1.5).

In the next step, we combined the results of the individual samples. Eqs. 3.3 and 3.4 were used to obtain a single combined radial velocity for each star observed in more than one sample. Again, we flagged all stars that showed evidence for radial velocity variations, using the same criteria as before. This yielded the final set of stellar velocities that we will use in our subsequent analysis. We summarize the results of our literature search in the Appendix. Table B.1 contains the data for M3, Table C.1 the data for M13, and Table D.1 the data for M92.

3.6.2. Results

Velocities from the PMAS data

In Fig. 3.17 we plot the distribution of our measured radial velocities in the three clusters in the r_{cc}-v_{rad} plane. Kurtz & Mink (1998) called it the "blunder diagram" and proposed to use it in order to set a reliability threshold on r_{cc} in the sense that for lower values of r_{cc}, the measured radial velocities can be arbitrarily high. Gerssen et al. (2002) showed that a threshold in r_{cc} in combination with a cut in the S/N of the sources is an efficient way to clean a radial velocity sample of unreliable measurements. In our case, a combination of $r_{\mathrm{cc,min}} = 3$ and $\mathrm{S/N_{min}} = 7$ proved to be a good choice. As can be seen from Fig. 3.17, in all three clusters some stars with large velocity offsets are observed that have a high S/N and a reasonable r_{cc}-value. All of those stars lie on the horizontal branch. Not only do they have very broad absorption lines in the observed spectral window (cf. Fig. 3.13), their spectral shape is also very different from our templates. We excluded such stars based on the (V,I)-magnitude information in the reference catalogue.

After applying these selection criteria, we were left with 128 reliable velocity measurements for 50 stars in M3, 235 measurements for 80 stars in M13, and 152 measurements for 77 stars in M92. They are summarized in Tables B.2, C.2, and D.2 in the Appendix.

3.6.3. Comparing the two datasets

We matched the literature data to our reference catalogue to check whether some stars were covered by our PMAS footprint. This was done by overlaying both the sources and our reference catalogue objects on an HST footprint and visually identifying the counterparts. In the process of doing this, we found that some stars have quite inaccurate positional data in the literature, especially in M3, where we observe a mean scatter of $\sim 1''$. The scatter is in M13 is only $\sim 0.2''$, but some outliers with offsets around $2''$ are observed. The positions in M92 are the most accurate, showing a scatter of $\sim 0.1''$ and only some outliers with offsets $\sim 1''$. A likely explanation for this inaccuracy is that the input catalogues used in the literature studies reach back to, e.g., Ludendorff (1905). Such offsets render the measured radial velocities less reliable. In a crowded stellar field, such as a globular cluster, an observation will yield a spectrum even if the target star is (partly) missed. However, this spectrum will not only contain light coming from the target star but a growing contribution from the numerous fainter stars in its vicinity. Nearby ($\lesssim 1''$) bright stars can have a similar effect and are therefore equally

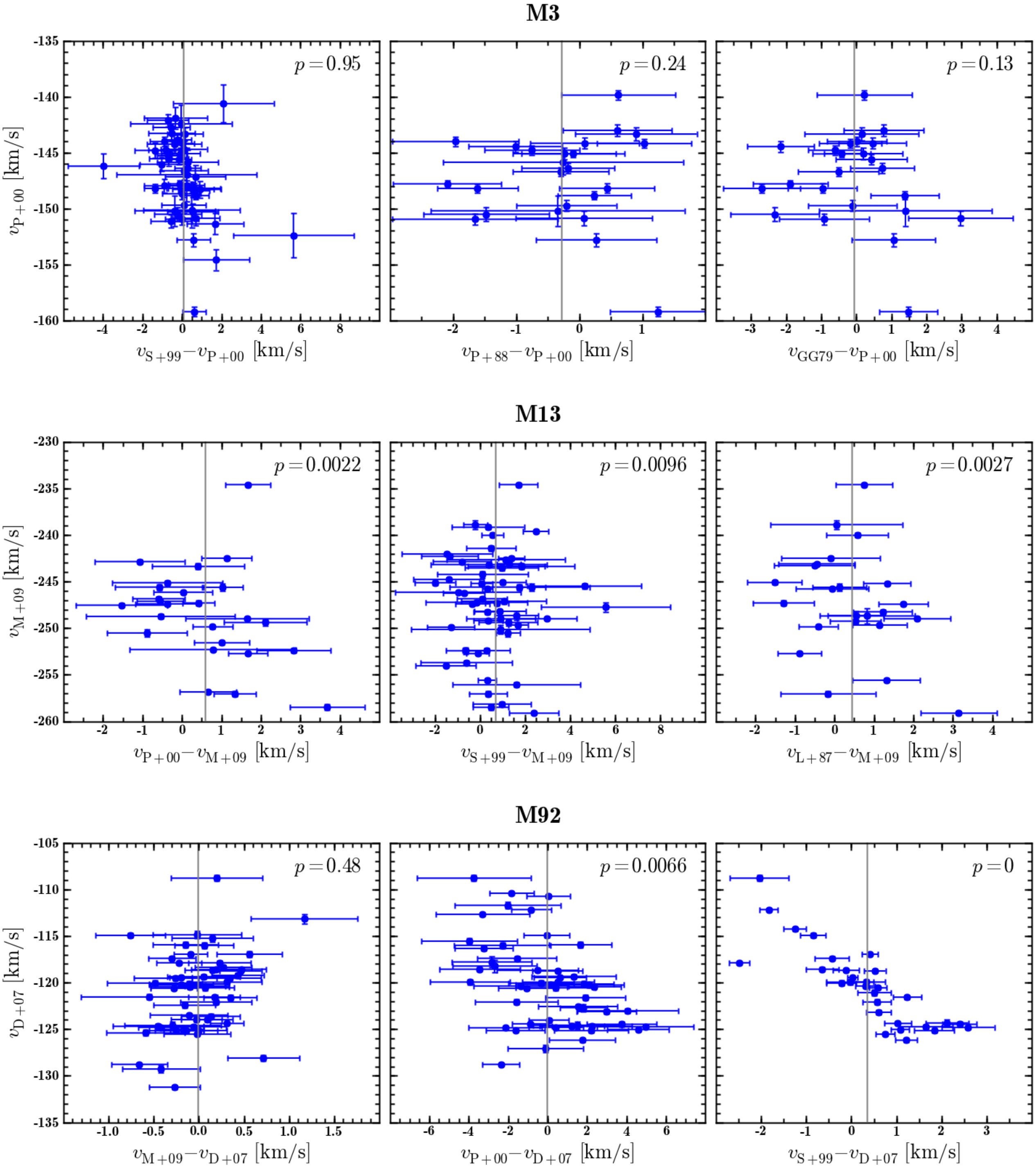

Fig. 3.16. Comparison of the different literature data sets in M3 (top), M13 (centre), and M92 (bottom). The different panels show the offset in the measured radial velocities between the various studies and the reference study for stars present in both samples. The probability that the scatter of the individual offsets is consistent with the provided uncertainties is given in the upper right corner of each panel. The abbreviations used to denote the individual studies are given in Table 3.3.

undesirable. We flagged all stars that (i) had bright neighbours that likely influenced the measurement of the radial velocity or (ii) were significantly offset from a bright HST counterpart or even had no obvious counterpart on the HST footprint at all. These stars were excluded from further analysis. The flags are also included in Tables B.1, C.1 and, D.1.

In M3 and M13, a few of the stars with radial velocity measurements available in the literature are located within our PMAS pointings: four in M13 and five in M3. When comparing our radial velocity measurement with those in the literature, we find an excellent agreement for the sources in M13, with a standard deviation of $\lesssim 1$ km/s that is well within the calculated uncertainty. However, in M3 the situation is more complex: for

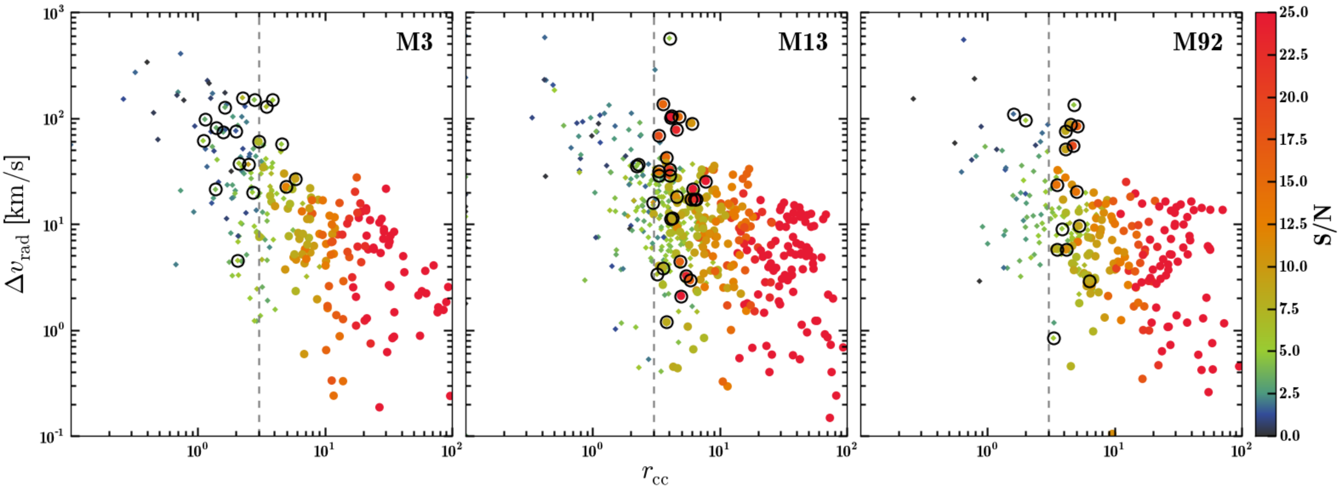

Fig. 3.17. Measured absolute radial velocities (relative to the template) as a function of the cross correlation statistic r_{cc}. The data are colour coded according to the S/N of the individual spectra. Spectra below the cut value of $\mathrm{S/N} = 7$ are plotted with small squares, those above with larger circles. Black annuli are used to label stars on the horizontal branch. The vertical line denotes the selected cut in r_{cc}.

four of the five stars the discrepancy is too large to be consistent with the error bars. Intrinsic RV variability is unlikely to be the reason for this; as none of the stars shows signs of variability, neither in the literature data nor in our dataset. In fact, we suspect that the literature values are affected by the influence of nearby stars. To illustrate this we show in Fig. 3.18 the situation for one of the suspicious stars. While our measurement yields a velocity very close to the cluster mean, the value in the literature is significantly higher. We suggest that this is caused by the influence of the two nearby fainter stars for which we indeed measure high relative velocities of 12.1km/s and 22.2km/s. This particular example clearly illustrates the gain achieved by using crowded field 3D spectroscopy: the full spatial information is preserved and allows us not only to remove the contamination from nearby sources but also to turn the "contamination" into a useful measurement. Note that all the 4 stars for which we observe a significant discrepancy between our data and the literature were also flagged when checking their positions in the HST image. They were therefore not included in the further analysis.

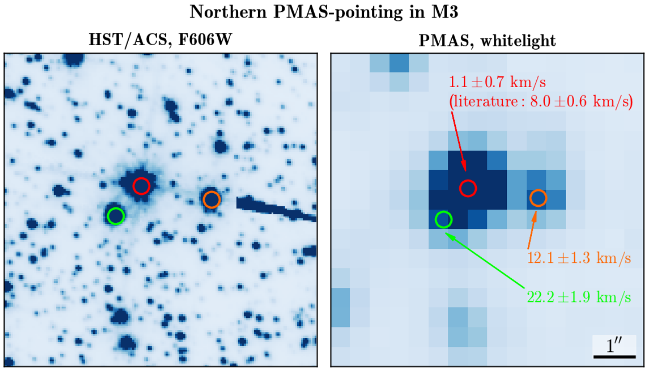

Fig. 3.18. Example of how traditional spectroscopy can give biased results in crowded stellar fields and how we can overcome such biases using crowded field 3D spectroscopy. The right panel shows one of our datacubes of M3, the seeing during the observation was ∼1.0″. The velocities of the stars marked with coloured circles are given relative to the cluster mean. On the left hand side we show the same area on an HST image.

One of the two stars in Fig. 3.18 that we "uncovered" is interesting by itself as its radial velocity is 22.2 km/s relative to the cluster mean. This makes it a $> 4\sigma$ outlier when using the velocity dispersion of the cluster determined by Gunn & Griffin (1979), also provided in Table 3.1. Gunn & Griffin (1979) found two other stars with similar offsets. The probability of finding three such stars in a sample of ∼200 stars by chance is $< 10^{-12}$, so there must be another explanation for their presence. Gunn & Griffin (1979) speculated on their origin and considered it unlikely that they were formed either via binary disruption or strong two-star encounters, suggesting that they might be remainders from the formation of the cluster (although the slowing down time due to dynamical friction is quite short). More recently, Lützgendorf et al. (2012) suggested that such a star can be formed in a single encounter between a main sequence binary star and a stellar-mass black hole.

In Fig. 3.19 we plot the radial velocities we obtained from our IFU data and from the literature as a function of the distance to the centre of each of the three clusters. It is obvious that the two datasets are very complementary: traditional spectroscopy is almost "blind" in the central regions of the clusters, while instruments such as PMAS are limited by their small field of view. However, at larger radii the limitations of traditional spectroscopy get less important for two reasons: On the one hand, the stellar density decreases so that crowding is less of an issue. On the other hand, the area covered by annuli around the centre increases with distance to the centre, so that it gets easier to pick a sufficient number of isolated stars in a radial bin of given width.

3.7. Radial velocity variable stars

As mentioned above stars with variable radial velocity are flagged in order to exclude them from the analysis of the cluster kinematics. Since radial velocity variations can either originate from intrinsic variability or the presence of binary stars, the measured velocities do not necessarily trace the cluster gravitational potential.

Intrinsic variability can easily cause variations of the order of the velocity dispersion of the cluster. For example, an RR Lyrae

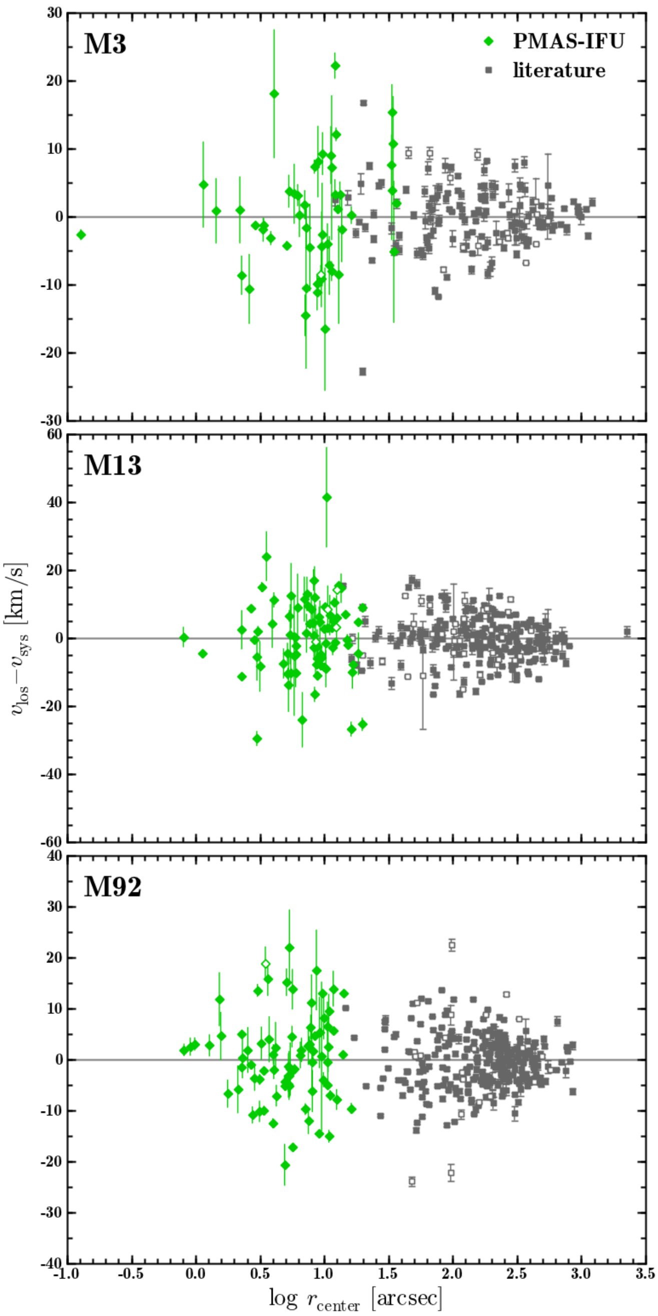

Fig. 3.19. Radial velocities of all stars in the three clusters as a function of distance to the cluster centre. Radial velocity measurements from our PMAS data are plotted using green diamonds, black squares refer to literature data. Open symbols are used to indicate stars that show variability, either photometrically or kinematically. All velocities are given relative to the cluster mean.

star with a period of 0.5 days will show variations by ±20km/s, assuming a change in radius by 0.5 solar radii (Kolenberg et al. 2010).

The importance of binary stars is expected to decrease with the density and the mass of the cluster. Kouwenhoven & de Grijs (2008) predicted the impact of binaries on the estimate of the dynamical mass of a cluster depending on its mass and half-mass radius. They found that the influence of binaries can be neglected if the central velocity dispersion is $\gtrsim$10 km/s while they dominate the dynamics in the regime $\lesssim$1 km/s. This puts our clusters right on the edge of where binaries become negligible.

Observational determinations of the binary fraction in the three clusters were carried out, e.g., by Milone et al. (2012) using HST photometry. They determined low binary fractions of $\sim$1–2%. Note that the fractions were determined using main sequence stars while our observations target giant stars. The determination of binary fractions based on spectroscopy is quite challenging and so far has been limited to less dense clusters (e.g., M4, Sommariva et al. 2009).

For the fields that were observed during two epochs (5/6 observed fields in M13; 1/3 fields in M92), we searched for stars with variable radial velocity in our PMAS data. We show in Fig. 3.20 the measured differences in the radial velocities between the two epochs for all observed stars. Again, we used an absolute offset $>$ 2km/s *and* a probability $<$ 1% that the offset is consistent with the measurement uncertainties as a criterion for a variable star. In Fig. 3.20, the candidates thus are the stars located above the horizontal dashed lines in *both* panels. We find 4 likely variables in M13 and none in M92. It is quite remarkable that the two stars with the highest measured S/N (with ID 58408 and 55692, respectively, in our reference catalogue) are both flagged as possible RV variable stars. They are also the brightest stars in the entire stellar sample of our PMAS data of M13, both lying at the tip of the red giant branch. Gunn & Griffin (1979) already noticed that such stars often showed stronger variability than expected based on the measurement uncertainties. They concluded that likely the stars experience a low magnitude pulsation and added an additional uncertainty of 0.8km/s to account for this "jitter". One of the two stars (with reference ID 55692) is also included in the compilation of variable stars in globular clusters by Clement et al. (2001) as a pulsating star. If we add a similar "jitter" to our measured uncertainty, this star falls below our significance threshold while the other one stays above it. We flagged both stars as variable.

Two other stars identified in the catalogue of Clement et al. (2001) as RR Lyrae stars were covered by our PMAS data, one in M92 and one in M3. For the one in M92 we have observations at two epochs and observe a change in the radial velocity by $\sim$ 10km/s. The probability that this is consistent with the uncertainties is $\sim$3%, just below our threshold. For M3 we only have single-epoch observations and the variation of the RR Lyrae star we observe within 3 observations over 2.5 hours is still marginally consistent with the uncertainties. We have flagged the two stars accordingly in Tables D.2 and B.2 and excluded them from further analysis.

In the literature data we find evidence for variable radial velocities in 16 out of 142 stars with multi-epoch data in M13, 4 of the candidates are known photometric variables. In M13, the numbers are 31 out of 200 with 11 photometric variables and in M92, 20 out of 250 with 2 photometric variables included.

Both, the integral field data as well as the literature data are consistent with low binary fractions. We did not try to estimate the binary fractions in the cluster from our datasets as we considered them too heterogeneous. For example, the number of observations per star varies between 1 and $>$ 10, but the efficiency of the binary detection increases with the number of observations.

3.8. Conclusions

We carried out integral field spectroscopy in the central regions of three Galactic globular clusters, M3, M13 and M92. Our observations cover the central $\sim$ $10''$ of each cluster and are

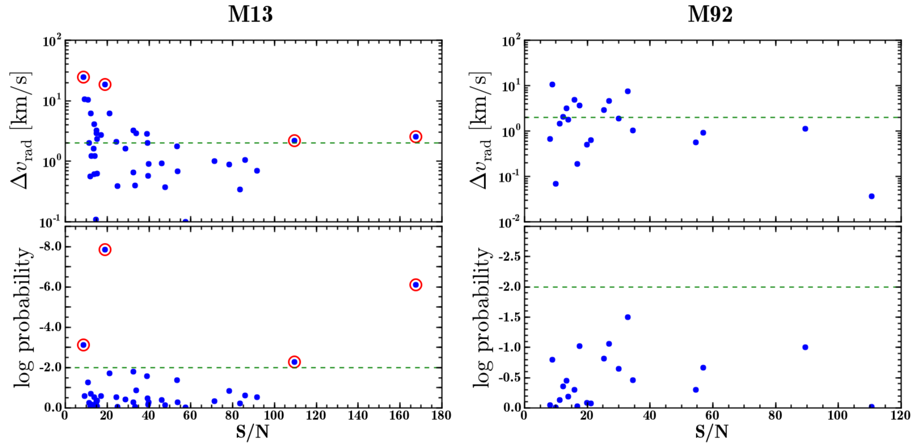

Fig. 3.20. Time variability in the measured radial velocities in our PMAS data for all stars that have been observed during two different epochs. M13 is left, M92 is right (no multi-epoch data exist for M3). For both clusters we show, as a function of the S/N of a star, the absolute velocity difference (upper panels) and the probability that the difference is consistent with the measurement uncertainties (lower panels). Horizontal green dashed lines indicate the thresholds used to identify variable stars. Only stars lying above both lines were considered variable. Each star identified as variable is marked by a red circle.

aimed at the kinematics of the cluster stars in these regions, especially regarding the question whether the clusters harbour massive black holes. To obtain reliable radial velocities of individual stars in the highly crowded regions, we applied a new dedicated algorithm for crowded field 3D spectroscopy, allowing us to deblend unbiased spectra for almost all stars on the red giant branch that are covered by our footprint. As expected, the S/N of the deblended spectra decreases as the stars get fainter, yet reliable radial velocity measurements are still possible for stars just below the horizontal branch. In total, we obtain useful spectra for ~ 80 stars in each cluster. Depending on the S/N, the uncertainty in the radial velocities varies between $\sim 1\mathrm{km/s}$ and $\sim 10\mathrm{km/s}$.

A substantial part of the data was obtained under seeing conditions $> 1''$. Since the amount of spectra we can deblend scales with the number of resolution elements and thus quadratically with the seeing, this significantly reduced the number of spectra we obtained. The effect becomes obvious from the fact that the sizes of the stellar samples with radial velocities from PMAS in M13 and M92 are comparable with one another although the area covered by the observations in M13 is almost twice as large. On the other hand, it shows that a (moderate) undersampling of the PSF is not a big issue in the analysis because most of the data in M92 were obtained with sub-arcsecond seeing and the spaxelsize of PMAS is $0\farcs5$.

For each of the clusters in our sample, we searched the literature for additional radial velocity data. The data we collected mainly cover the outer parts of the clusters and are thus very complementary to our dataset. In M3 and M13, some stars are available in both datasets. While the comparison of the velocity measurements in M13 yields a very good agreement, the offsets we find in M3 are significantly larger than expected in view of the uncertainties. We suggest that the literature values are affected by blending with nearby stars. Our findings show the limitations of traditional spectroscopy in crowded stellar fields and demonstrate the major advantages of integral field spectroscopy.

We performed a careful search for stars with radial velocity variations that might influence an analysis of the cluster kinematics. The number of possible binary stars is low, confirming previous findings about the binary fractions in globular clusters.

In a subsequent paper (Chapter 4 of this thesis), we will use the radial velocity data to perform dynamical modelling of the clusters, infer mass-to-light ratios and constrain the presence of intermediate-mass black holes. The signature of such a black hole would only be measurable within the few central arcseconds around the cluster centre. So our new data that we obtained is of utter importance for this task.

Finally, we want to emphasize that although we concentrated on radial velocities, the analysis approach that we applied can equally well be used to measure metallicities or element abundances, provided the spectra have sufficient resolution and spectral coverage for such a task.

Acknowledgements. S. K. acknowledges support from the ERASMUS-F project through funding from PT-DESY, grant no. 05A09BAA.
Based on observations collected at the Centro Astronómico Hispano Alemán (CAHA) at Calar Alto, operated jointly by the Max-Planck Institut für Astronomie and the Instituto de Astrofísica de Andalucía (CSIC).
Part of this work is based on observations made with the NASA/ESA Hubble Space Telescope, and obtained from the Hubble Legacy Archive, which is a collaboration between the Space Telescope Science Institute (STScI/NASA), the Space Telescope European Coordinating Facility (ST-ECF/ESA) and the Canadian Astronomy Data Centre (CADC/NRC/CSA).
Some of the data presented in this paper were obtained from the Mikulski Archive for Space Telescopes (MAST). STScI is operated by the Association of Universities for Research in Astronomy, Inc., under NASA contract NAS5-26555. Support for MAST for non-HST data is provided by the NASA Office of Space Science via grant NNX09AF08G and by other grants and contracts.

References

Anderson, J., Sarajedini, A., Bedin, L. R., et al. 2008, AJ, 135, 2055
Anderson, J. & van der Marel, R. P. 2010, ApJ, 710, 1032
Baumgardt, H., Makino, J., & Hut, P. 2005, ApJ, 620, 238
Carretta, E., Bragaglia, A., Gratton, R. G., et al. 2009, A&A, 505, 117
Clement, C. M., Muzzin, A., Dufton, Q., et al. 2001, AJ, 122, 2587
Cudworth, K. M. & Monet, D. G. 1979, AJ, 84, 774
Dolphin, A. E. 2000, PASP, 112, 1383
Drukier, G. A., Cohn, H. N., Lugger, P. M., et al. 2007, AJ, 133, 1041
Gebhardt, K., Pryor, C., O'Connell, R. D., Williams, T. B., & Hesser, J. E. 2000, AJ, 119, 1268
Gebhardt, K., Pryor, C., Williams, T. B., & Hesser, J. E. 1995, AJ, 110, 1699
Gerssen, J., van der Marel, R. P., Gebhardt, K., et al. 2002, AJ, 124, 3270
Goldsbury, R., Richer, H. B., Anderson, J., et al. 2010, AJ, 140, 1830
Gratton, R. G., Bonifacio, P., Bragaglia, A., et al. 2001, A&A, 369, 87
Gunn, J. E. & Griffin, R. F. 1979, AJ, 84, 752
Harris, W. E. 1996, AJ, 112, 1487
Husemann, B., Kamann, S., Sandin, C., et al. 2012, A&A, 545, A137
Husser, T. O., Wende-von Berg, S., Dreizler, S., et al. 2013, A&A, submitted
Kamann, S., Wisotzki, L., & Roth, M. M. 2013, A&A, 549, A71
Kolenberg, K., Fossati, L., Shulyak, D., et al. 2010, A&A, 519, A64
Kouwenhoven, M. B. N. & de Grijs, R. 2008, A&A, 480, 103
Kurtz, M. J. & Mink, D. J. 1998, PASP, 110, 934
Lane, R. R., Kiss, L. L., Lewis, G. F., et al. 2011, A&A, 530, A31
Ludendorff, H. 1905, Publikationen des Astrophysikalischen Observatoriums zu Potsdam, 50, 1
Lupton, R. H., Gunn, J. E., & Griffin, R. F. 1987, AJ, 93, 1114
Lützgendorf, N., Gualandris, A., Kissler-Patig, M., et al. 2012, A&A, 543, A82
Marigo, P., Girardi, L., Bressan, A., et al. 2008, A&A, 482, 883

McLaughlin, D. E., Anderson, J., Meylan, G., et al. 2006, ApJS, 166, 249
Mészáros, S., Dupree, A. K., & Szalai, T. 2009, AJ, 137, 4282
Milone, A. P., Piotto, G., Bedin, L. R., et al. 2012, A&A, 540, A16
Noyola, E. & Gebhardt, K. 2006, AJ, 132, 447
Noyola, E., Gebhardt, K., & Bergmann, M. 2008, ApJ, 676, 1008
Noyola, E., Gebhardt, K., Kissler-Patig, M., et al. 2010, ApJ, 719, L60
Pilachowski, C. A., Sneden, C., Kraft, R. P., Harmer, D., & Willmarth, D. 2000, AJ, 119, 2895
Piotto, G., King, I. R., Djorgovski, S. G., et al. 2002, A&A, 391, 945
Portegies Zwart, S. F., Baumgardt, H., Hut, P., Makino, J., & McMillan, S. L. W. 2004, Nature, 428, 724
Pryor, C. P., Latham, D. W., & Hazen, M. L. 1988, AJ, 96, 123
Roth, M. M., Fechner, T., Wolter, D., et al. 2010, in Society of Photo-Optical Instrumentation Engineers (SPIE) Conference Series, Vol. 7742, Society of Photo-Optical Instrumentation Engineers (SPIE) Conference Series
Roth, M. M., Kelz, A., Fechner, T., et al. 2005, PASP, 117, 620
Sandin, C., Becker, T., Roth, M. M., et al. 2010, A&A, 515, A35
Sarajedini, A., Bedin, L. R., Chaboyer, B., et al. 2007, AJ, 133, 1658
Siebert, A., Williams, M. E. K., Siviero, A., et al. 2011, AJ, 141, 187
Soderberg, A. M., Pilachowski, C. A., Barden, S. C., Willmarth, D., & Sneden, C. 1999, PASP, 111, 1233
Sommariva, V., Piotto, G., Rejkuba, M., et al. 2009, A&A, 493, 947
Tonry, J. & Davis, M. 1979, AJ, 84, 1511
van der Marel, R. P. & Anderson, J. 2010, ApJ, 710, 1063
van der Marel, R. P., Gerssen, J., Guhathakurta, P., Peterson, R. C., & Gebhardt, K. 2002, AJ, 124, 3255

Chapter 4

The search for intermediate-mass black holes in globular clusters: Dynamical models for M3, M13, and M92*

Sebastian Kamann[1]

[1] Leibniz-Institut für Astrophysik Potsdam (AIP), An der Sternwarte 16, 14482 Potsdam, Germany

ABSTRACT

It is a long standing question whether globular clusters host massive black holes in their centres. Finding these intermediate-mass black holes would shed light on how the supermassive ones that are observed in the centres of galaxies build up from smaller entities. However, the detection of such objects is a challenging task. Kinematic observations in the highly crowded cluster centres are required in combination with dedicated dynamical models to constrain the masses of intermediate-mass black holes. We recently obtained large sets of radial velocity measurements in the centres of three massive Galactic globular clusters, M3, M13, and M92. We combine our new kinematical data with surface brightness profiles to investigate the internal dynamics of every cluster using spherical Jeans models. By maximum likelihood means we constrain dynamical mass-to-light ratios and black-hole mass estimates. The surface brightness profiles reveal that all three clusters are consistent with having a shallow central cusp, although the data for M13 and M92 are almost equally well described by a core profile. In none of the three clusters, a massive black hole is required to explain the observed kinematics. We derive 1σ upper limits of $600 M_\odot$ for M3, $8\,900 M_\odot$ for M13 and $700 M_\odot$ for M92. Using more conservative 3σ limits increases these values to $2\,500 M_\odot$ (M3), $13\,000 M_\odot$ (M13) and $2\,000 M_\odot$ (M92). Our upper limits for M13 and M92 are the most stringent obtained for massive clusters so far. The dynamical mass-to-light ratios are quite heterogeneous, ranging from $\Upsilon = 1.00 \pm 0.10$ for M3 to $\Upsilon = 2.2 \pm 0.2$ for M13, with an intermediate value of $\Upsilon = 1.55 \pm 0.15$ for M92. A slight signature of rotation is observed in M13 as well as in M92. Finally, we find tentative evidence for tangential anisotropy in the core of the cluster M92.

4.1. Introduction

Over the last years, the search for intermediate-mass black holes (IMBHs) has gained remarkable attention. With $10^2 - 10^5$ solar masses, they would bridge the gap from stellar-mass black holes to supermassive ones (SMBHs). Constraining their population statistics might answer the question how SMBHs assemble their mass. The scaling relations observed between SMBHs and fundamental properties of their host bulges, such as luminosities (Kormendy & Richstone 1995), stellar masses (Magorrian et al. 1998; Marconi & Hunt 2003; Häring & Rix 2004) or stellar velocity dispersions (Ferrarese & Merritt 2000; Gebhardt et al. 2000; Gültekin et al. 2009) suggest that their growth is closely linked to the evolution of the host galaxy (Silk & Rees 1998, but see also Jahnke & Macciò 2011). The progenitors of SMBHs are likely to be found in the building blocks of present-day galaxies. The close connection of Galactic globular clusters to the build-up of the Milky Way was proposes already by Searle & Zinn (1978) and is supported by cosmological simulations (e.g., Moore et al. 2006). Globular clusters can therefore be considered as promising candidates to host IMBHs.

Interestingly, a simple-minded extrapolation of the SMBH scaling relations to the properties of globular clusters also yields black hole masses in the range $10^2 - 10^5$ solar masses. Clearly, such an extrapolation is a huge simplification, and there is evidence that the common relations disagree with the observations already in the regime of low-mass galaxies (Greene et al. 2010).

The runaway merging of massive stars in the early phases of cluster evolution has been suggested as a formation channel for IMBHs in dense star clusters (Portegies Zwart & McMillan 2002). However, it has been argued (e.g. Glebbeek et al. 2009) that strong stellar winds restrict the resulting black holes to stellar masses ($\gtrsim 10\ M_\odot$). An alternative formation scenario involves the collapse of massive population III stars (e.g. Madau & Rees 2001).

Observational evidence for the existence of IMBHs is still extremely scant. Gas accretion onto such a black hole would allow for its detection using radio or X-ray observations, such as in the case of the IMBH candidate HLX-1 in the galaxy ESO 243-49 (Farrell et al. 2009). G1 in M31, the most massive known globular cluster in the local group, was detected in both radio (Ulvestad et al. 2007) and X-ray observations (Trudolyubov & Priedhorsky 2004; Kong et al. 2010), although Miller-Jones et al. (2012) could not confirm the radio detection. Recent observations by Strader et al. (2012) place stringent upper limits on the amount of radio emission coming from Galactic globular clusters. Translating those into mass limits, however, requires making assumptions about the accretion physics that are not well understood.

Several authors investigated the possibility that IMBHs imprint their presence onto photometrically observable properties

---

* A version of this Chapter will be submitted for publication in *Astronomy & Astrophysics*. The preliminary list of co-authors includes Lutz Wisotzki, Joris Gerssen, and Martin M. Roth.

of a globular cluster. Baumgardt et al. (2005) and Noyola & Baumgardt (2011) found that a massive black hole should produce a shallow cusp in the central surface brightness profile of the surrounding cluster. A large ratio of core to half-mass radius was suggested as indirect evidence for the presence of an IMBH by Trenti et al. (2007). Furthermore, the existence of extreme horizontal branch stars has been proposed as a tracer for IMBHs by Miocchi (2007). Gill et al. (2008) investigated the influence of black holes on mass segregation among the cluster stars.

Arguably, the most direct way to not only find massive black holes, but also obtain their masses, is the detection of their kinematic fingerprints. The best SMBH mass estimates were obtained from stellar kinematics in our own galaxy (Gillessen et al. 2009) or gas kinematics in NGC 4258 (Herrnstein et al. 2005). However, obtaining meaningful kinematic measurements in the central regions of globular clusters is a challenging task: While the measurement of individual stellar velocities is hampered by crowding, integrated-light analyses can be significantly affected by shot noise from the few brightest giants. Kinematic studies of the centres of globular clusters remained ambiguous so far. Detections of IMBHs have been reported in a small number of massive clusters, G1 (Gebhardt et al. 2005) being one of them. In a sample recently studied by Lützgendorf et al. (2011, 2012b,a), the kinematics in 3 out of 8 clusters suggested the presence of an IMBH, while for the remaining clusters upper limits of typically $> 1\,000$ solar masses were derived. Similar mass limits were also reported in other studies, carried out for M15 by Gerssen et al. (2002) and van den Bosch et al. (2006), for 47Tuc by McLaughlin et al. (2006) or for NGC 6266 by McNamara et al. (2012).

The case of ω Centauri, the most massive cluster in the Milky Way, has been discussed controversially. Anderson & van der Marel (2010) and van der Marel & Anderson (2010) find no evidence for an IMBH while Noyola et al. (2010) and Jalali et al. (2012) claim the detection of one with a mass of $4 \cdot 10^4 \mathrm{M}_\odot$.

Clearly, a conclusive picture on which globular clusters host IMBHs is not established yet. Furthermore, the question whether the scaling relations established for SMBHs can be extrapolated into the regime of globular clusters remains to be answered. So far the results are still consistent with it. Alternatively, IMBHs might follow different scaling relations, as suggested by Miocchi (2007). More observations are the only way to make progress here.

We recently obtained large sets of stellar velocities in the centres of the three Galactic globular clusters M3, M13, and M92 with the PMAS (Roth et al. 2005) integral field unit (IFU). The observations as well as the data reduction and analysis are described in detail in an accompanying paper (Chapter 3 of this thesis). The velocities were obtained using a novel method that we developed (Kamann et al. 2013, also Chapter 2 of this thesis) to deblend stellar spectra from integral field spectroscopic observations of crowded stellar fields. It allows us to obtain reliable radial velocities even in the highly crowded central regions of Galactic globular clusters. In the present paper, we present the results of dynamical modelling of our three targets with the aim of constraining the presence of IMBHs. We note that M13 was identified by Miocchi (2007) as a possible candidate to host an IMBH according to its central surface brightness profile and extended horizontal branch.

Dynamical models have been previously derived for each of the three clusters. The kinematics in M3 were investigated already by Gunn & Griffin (1979) who found that King-Mitchie models provide a valid framework for the kinematical data available back then. The authors suggested a transition from an isotropic core to an anisotropic outer region occurring at ∼15 core radii (∼ 5′). This finding was confirmed by Cudworth (1979) from proper motions. In a similar fashion to Gunn & Griffin (1979), Lupton et al. (1987) studied the cluster M13 and found a transition to anisotropy occuriing at ∼5 core radii. Furthermore, the collected radial velocity data showed evidence for rotation at larger radii. Leonard et al. (1992) combined the kinematical data of Lupton et al. (1987) with proper motions collected by Cudworth & Monet (1979) to infer the mass and stellar content of M13, by analytically solving the spherical Jeans equation under the assumption of a Plummer density profile.

More recently, McLaughlin & van der Marel (2005) performed dynamical modelling on a large sample of 57 clusters, including M3, M13 and M92. To infer structural parameters, three different models were used that mainly varied in their behaviour at large radii, thus correspond to different strengths of a tidal cutoff. For the three targets investigated in this study, models with a moderate truncation (Wilson models) turned out to be a valid choice and we will refer to those when comparing our results with those of McLaughlin & van der Marel (2005). M92 was also included in the sample studied by Zocchi et al. (2012) who found it to be a relaxed cluster well described by an isotropic King model.

We give an overview on the theory behind our modelling approach in Sect. 4.2. After laying out the observational data that is required to constrain the models, namely the surface brightness profiles and the velocity distributions, in Sections 4.3 and 4.4, respectively, we present the comparison between our data and the models in Sect. 4.5. Our findings are discussed in Sect. 4.6 before we conclude in Sect. 4.7.

4.2. Jeans formalism

Jeans modelling is a widely used technique to investigate the dynamics of gravitationally bound stellar systems. It is discussed in detail in Binney & Tremaine (2008). A good overview is also given in van der Marel & Anderson (2010, hereafter vdMA10). We will restrict ourselves to a brief introduction into the general formalism in the following.

The basic idea behind this approach is to describe the entity of a collisionless stellar system by an unknown distribution function $f(\boldsymbol{x}, \boldsymbol{v}, t)$ that fulfils a continuity equation in phase space ($\boldsymbol{x}$, $\boldsymbol{v}$). Application of Hamilton's equations yields the collisionless Boltzmann equation. For a Hamiltonian $H = v^2/2 + \Phi(\boldsymbol{x}, t)$, with Φ the gravitational potential, it has the form

$$\frac{\partial f}{\partial t} + \boldsymbol{v}\,\frac{\partial f}{\partial \boldsymbol{x}} - \frac{\partial \Phi}{\partial \boldsymbol{x}}\frac{\partial f}{\partial \boldsymbol{v}} = 0 \tag{4.1}$$

in Cartesian coordinates. While constraining the entire distribution function f from observations is clearly not feasible, it is possible to measure individual moments of f that allow for the solution of Eq. 4.1 under simplifying conditions. The Jeans equations are a system of differential equations of the first and second order velocity moments, v_i and σ_{ij}. For a spherical system, one can derive the equation

$$\frac{d(\nu\overline{v_\mathrm{r}^2})}{dr} + 2\frac{\beta}{r}\nu\overline{v_\mathrm{r}^2} = -\nu\frac{d\Phi}{dr}\,. \tag{4.2}$$

Here, $\nu = \int d^3\boldsymbol{v} f$ is the probability of finding a star at location $\boldsymbol{x}$ and its multiplication with the total number of stars N yields the source density.

The anisotropy parameter β is defined as

$$\beta = 1 - \frac{\overline{v_\theta^2} + \overline{v_\phi^2}}{2\overline{v_\mathrm{r}^2}}\,. \tag{4.3}$$

A system with preferentially tangential orbits has $\beta < 0$, a system with $\beta > 0$ has preferentially radial orbits. For an isotropic system, $\overline{v_\phi^2} = \overline{v_\theta^2} = \overline{v_\mathrm{r}^2}$.

Equation 4.2 is a first-order linear differential equation of $\nu\,\overline{v_\mathrm{r}^2}$. Its solutions have the form

$$\nu(r)\,\overline{v_\mathrm{r}^2} = \frac{1}{I(r)} \int dr'\,\nu\,\frac{d\Phi}{dr'}\,I(r')\,, \tag{4.4}$$

with an integrating factor $I(r) = \exp\{2\int dr\,\beta(r)/r\}$ that depends on the functional form of the anisotropy parameter.

The gravitational potential going into Eq. 4.2 has a stellar contribution $\Phi_*(r)$ that is determined by the stellar mass density $\varrho_*(r)$. For a spherically symmetric density distribution, one finds

$$\Phi_*(r) = -4\pi G\left[\frac{1}{r}\int_0^r dr'\,r'^2\varrho_*(r') + \int_r^\infty dr'\,r'\varrho_*(r')\right]. \tag{4.5}$$

If a massive black hole is present in the cluster centre the gravitational potential will have an additional component $\Phi_\mathrm{BH} = -GM_\mathrm{BH}/r$. Further contributions, in particular a dark matter component, are negligible in globular clusters.

While the density within a cluster cannot be directly constrained from observations, it can be linked to the luminosity density $L(r)$ via the mass-to-light ratio $\Upsilon(r)$ of the system,

$$\varrho(r) = \Upsilon(r)L(r)\,. \tag{4.6}$$

A common approach to constrain the stellar gravitational potential from observations is therefore to measure the surface brightness profile $\mu_\mathrm{V}(\hat{r})$ of the system, as a function of projected radius $\hat{r}$. The surface brightness profile, described either in a parametric (e.g. vdMA10) or a non-parametric (e.g. Gebhardt & Fischer 1995) form can be deprojected into a luminosity density $L(r)$ via an Abel transform. In order to derive the probability density function $\nu(r)$ from the luminosity density $L(r)$ one has to make assumptions about the fraction of stars that contribute to the observed kinematics as well as about their average brightness. As long as the relation between $L(r)$ and $\nu(r)$ is independent of r, which is what we assume here, one can write the spherical Jeans equation (Eq. 4.2) as a first order linear differential equation of $L\,\overline{v_\mathrm{r}^2}$ and accordingly find its solutions by replacing $\nu(r)$ with $L(r)$ in Eq. 4.4.

In assuming proportionality between $\nu(r)$ and $L(r)$, we neglect mass segregation among the bright cluster stars. Most globular clusters have relaxation times that are significantly shorter than their ages (Djorgovski 1993; McLaughlin & van der Marel 2005). For the clusters in our sample, Harris (1996) list half-mass relaxation times of $\log(t_\mathrm{h}/\mathrm{years}) = 9.79$ (M3), 9.30 (M13), and 9.02 (M92). We cannot exclude mass segregation to be present in the clusters. Still the gradient in $\nu(r)/L(r)$ is supposed to be small (vdMA10).

Solutions to the spherical Jeans equation (cf. Eq. 4.4) yield the radial profiles of the second-order velocity moments of the distribution function. Translating them into observable quantities such as the velocity dispersion σ_los along the line of sight involves projection onto the plane of the sky. Prescriptions on how this is done can be found, e.g., in Cappellari (2008) or vdMA10.

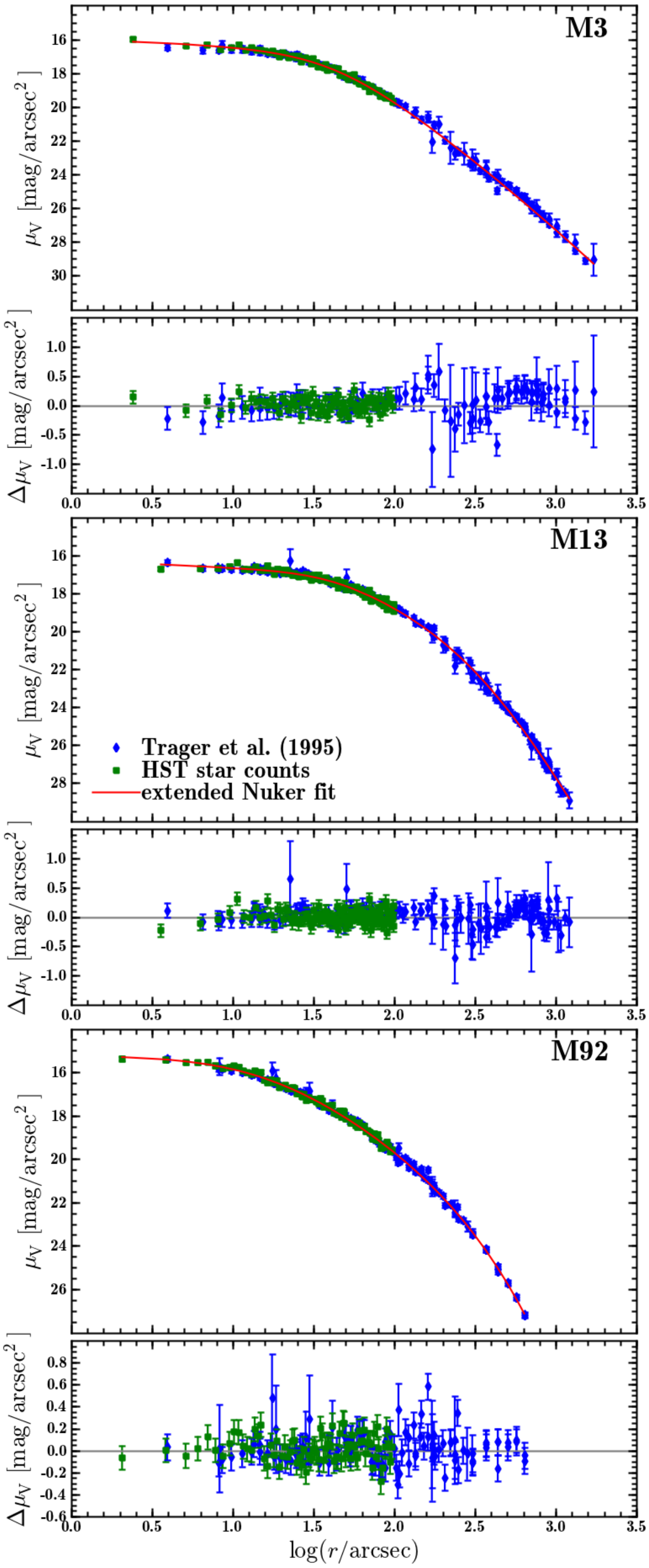

Fig. 4.1. The surface brightness profiles of the clusters M3, M13 and M92 are presented in the upper panels. Measurements based on star counts in the HST data are shown using green diamonds while blue squares represent the data of Trager et al. (1995). A solid red line shows the best-fit extended Nuker profile. In the lower panels, the residuals of the data with respect to the extended Nuker fit are shown. The shown surface brightness profiles are corrected for extinction.

4.3. Surface brightness profiles

A large set of surface brightness profiles for Galactic globular clusters was compiled by Trager et al. (1995). No uncertainties are provided with the data, only a relative weight is assigned to each datapoint. McLaughlin & van der Marel (2005) proposed a way to obtain meaningful uncertainties by scaling the weights with a constant factor until the measurements are consistent with a smooth function. We followed that approach and used the same scaling factors as McLaughlin & van der Marel and also omitted datapoints that were assigned a weight < 0.15.

The ground-based images of Trager et al. have limited spatial resolution, therefore we complemented them with *Hubble* Space Telescope (HST) data in the central region of each cluster. Our approach is based on star counts and similar to the one used by vdMA10 in ω Centauri. For each cluster, a reference catalogue was generated in Chapter 3, using the photometry of Anderson et al. (2008) and applying a correction for bright stars that have occasionally been missed. We used it to count the stars in concentric annuli around the cluster centre, which in each target was assumed to be at the location found by Goldsbury et al. (2010). The size of each annulus was chosen so that it contained 100 stars brighter than a magnitude $V = 19$ in order to have the same number statistics in each bin. The number density that we obtain this way is the projection of $\nu(r)$ into the plane of the sky. As we discussed in Sect. 4.2, we assume a constant relation between $\nu(r)$ and $L(r)$. Thus, the measured number density profile can easily be transformed into a surface brightness profile. This profile is then shifted vertically to match the one of Trager et al. in the region where the two overlap.

Alternatively, we could have also used to profiles obtained by Noyola & Gebhardt (2006) using HST data alone. However, we mentioned in Chapter 3 that the cluster centres that we assume slightly deviate from the ones used by Noyola & Gebhardt (by 3.″9 in M3, 2.″4 in M13, and 0.″9 in M92). It is not clear how this offset translates into the measured profiles. Also, our approach allows us to constrain the central profile for approximately the same subsets of stars for which we obtain kinematic measurements. The magnitude cut of $V = 19$ that we have chosen is slightly fainter than the limit of our spectroscopic observations (cf. Chapter 3) but this should have no effect. When we select a brighter magnitude the shapes of the profiles do not change significantly, only the number statistics get somewhat poorer. This also shows that the catalogues are quite complete at this brightness levels.

The resulting profiles were corrected for interstellar extinction and fitted with an extended Nuker profile whose functional form is given by

$$I(r) = I_{\mathrm{b}}\, 2^{\left(\frac{\beta-\gamma}{\alpha}\right)} \left(\frac{r}{r_{\mathrm{b}}}\right)^{-\gamma} \left[1 + \left(\frac{r}{r_{\mathrm{b}}}\right)^{\alpha}\right]^{-\left(\frac{\beta-\gamma}{\alpha}\right)} \left[1 + \left(\frac{r}{r_{\mathrm{c}}}\right)^{\delta}\right]^{-\left(\frac{\epsilon-\beta}{\delta}\right)} . \tag{4.7}$$

The “original” Nuker profile (omitting the second term in square brackets) was initially proposed by Lauer et al. (1995) to describe the surface brightness profiles of galaxies that showed a power-law cusp $I \propto r^{-\gamma}$ towards the centre and a logarithmic decline $\propto \beta$ for radii $> r_{\mathrm{b}}$. The generalized version given in Eq. 4.7 was used by vdMA10 to describe the surface brightness profile of ω Centauri. It has an additional break radius r_{c} where the logarithmic slope changes from β to ϵ. The physical justification for this second break is that many clusters have a rather well-defined truncation radius.

In Fig. 4.1 we show the results from fitting Eq. 4.7 to the surface brightness profiles. The parameters of the each best-fit Nuker profile are given in Table 4.1. The fits provide a good global representation of the measured profiles. In all three cases we obtain χ^2 values that suggest the fitted profile is fully consistent with the data (cf. Table 4.1).

A comparison of the core radii that we obtain with those listed in the catalogue of Harris (1996) (M3: 22.″2, M13: 37.″2, M92: 15.″6) shows remarkable agreement for M13 and M92, only the value we obtain in M3 is about twice as large. We performed another consistency check by calculating the integrated magnitude of each target, either by numerical integration of the data or Eq. 4.7. Again, the different values, included in Table 4.1, are largely consistent with one another.

The data of M92 is actually best fitted by a core profile with $\gamma = 0$. In the two other clusters, our fits suggest a shallow cusp in the central surface brightness profile. However, as pointed out by vdMA10, γ is not very well constrained in a fit of the whole surface brightness profile because its influence is limited to the innermost few datapoints. To obtain realistic confidence intervals on γ, we fitted the data within a distance of $0.5 r_{\mathrm{b}}$ to the centre with a simple power-law and obtained the range of slopes consistent with the data. We only allowed for γ values that still provided a reasonable fit to the overall profile within 90% confidence. This calculation yields $\gamma = 0.32 \pm 0.22$ in M3, $\gamma < 0.34$ in M13 and $\gamma < 0.43$ in M92. Hence, the surface brightness profile of M13 is also consistent with having a core.

The combination of a large core radius and a shallow surface brightness cusp led Miocchi (2007) to the conclusion that M13 is a good candidate to host an IMBH. Our photometric analysis confirms the large core. Also, the upper limit on the steepness of the cusp that we obtain is consistent with the value of $\gamma \lesssim 0.25$ suggested by Miocchi and others (Baumgardt et al. 2005; Noyola & Baumgardt 2011). Our analysis further suggests that the photometric properties of M3 are not so different from those of M13, in particular with respect to the large core radius. As the distance to M3 (10.2 kpc, Harris 1996) is a bit larger compared to M13 (7.1 kpc), the physical core radius is still somewhat smaller.

4.4. Kinematical data

In Chapter 3, we compiled large sets of radial velocities for each of the three clusters, M3, M13, and M92. Our PMAS IFU observations cover the central region of each cluster, out to distances of $\sim 20''$ from the cluster centre. These velocities were complemented with data at larger radii collected from various literature studies. The combination of the two datasets allows us to cover the full radial extend of each cluster.

Our spectra cover a large range in signal-to-noise ratios (S/N). Since the accuracy of the measured radial velocities is a function of the S/N, our radial velocities have non-uniform uncertainties, ranging from $\lesssim$1 km/s, well below the expected velocity dispersions of the clusters, to $\gtrsim$10 km/s, comparable to the expected dispersions. Large uncertainties, however, do not imply that the measurements are useless in the determination of the velocity dispersion. To demonstrate this we assume that for a sample of N stars, individual stellar velocities v_i with associated uncertainties σ_i ($i \in [1, N]$) have been measured. In that case, each measurement is taken from a distribution (Pryor & Meylan 1993)

$$f(v_i) = \frac{1}{\sqrt{2\pi(\sigma_{\mathrm{c}}^2 + \sigma_i^2)}} \exp\left\{-\frac{(v_i - v_{\mathrm{v}})^2}{2(\sigma_{\mathrm{c}}^2 + \sigma_i^2)}\right\} . \tag{4.8}$$

where σ_{c} is the velocity dispersion of the cluster at the location of star i and v_{v} is the systemic velocity of the cluster.

Table 4.1. Parameters of the best-fit Nuker profiles

ID	μ_b mag/arcsec^2	r_b arcsec	r_c arcsec	α	β	γ	δ	ϵ	χ^2	N_dof	$m_\mathrm{V,data}$	$m_\mathrm{V,Nuker}$
M3	16.8	41.5	273.5	2.10	2.15	0.03	0.57	3.94	167.7	161	6.50	6.54
M13	17.2	39.8	353.2	2.72	1.39	0.15	1.46	6.06	242.4	245	5.88	5.89
M92	16.1	15.1	2979.0	1.47	1.69	0.00	0.95	22.8	183.5	172	6.46	6.49

Equation 4.8 shows that the crucial aspect is not that the uncertainties are *small* but that they are *correct.* A significant under- or overestimation will bias the determination of the intrinsic dispersion, σ_c. Obviously, the need for accurate uncertainties increases with the ratio $\sigma_i/\sigma_\mathrm{c}$. We carefully determined the uncertainties in Chapter 3 and consider them reliable.

A basic assumption in Eq. 4.8 is that the line-of-sight velocity distribution (LOSVD) of the cluster can be described as a Gaussian distribution. Nevertheless its generalization to more complex distributions is straight forward, e.g. using a Gauss-Hermite expansion (van der Marel & Franx 1993).

The quantity of interest is the mean-squared velocity of the stars along the line-of-sight, which is the squared sum of the dispersion and a possible rotational component. We constrain a possible internal rotational component in the clusters in Sect. 4.4.3. For simplicity we refer to the projected mean-squared velocity as the velocity dispersion and denote it by σ_c in the remainder of the Chapter.

4.4.1. Maximum likelihood approach

A common way to solve Eq. 4.8 for the cluster properties v_c and σ_c is maximum likelihood estimation (e.g., Pryor & Meylan 1993; Baumgardt et al. 2009). The likelihood $\mathcal{L}$ of the model parameters (v_c, σ_c) given the observed data ($\boldsymbol{v}$, $\boldsymbol{\sigma}$) is the product of the probabilities of the individual measurements (v_i, σ_i), or equivalently,

$$\ln\mathcal{L} = \sum_{i=1}^{N} \ln\left(\frac{1}{\sqrt{2\pi(\sigma_\mathrm{c}^2+\sigma_i^2)}}\,\exp\left\{-\frac{(v_i-v_\mathrm{v})^2}{2(\sigma_\mathrm{c}^2+\sigma_i^2)}\right\}\right). \qquad (4.9)$$

Depending on the scientific application and the amount of information at hand, there are two ways to proceed from Eq. 4.9 that we discuss in the following. In absence of any model to compare to, it is possible to obtain the radial profile of the velocity dispersion by binning the data as a function of projected distance to the cluster centre. Below we use Jeans modelling to predict the radial velocity dispersion profile. In this case we can use Eq. 4.9 to (a) find the model with the highest likelihood and (b) estimate confidence intervals for the model parameters. We start with a discussion of of the radial profiles obtained from binning the data. The comparison with the Jeans models is discussed afterwards in Sect. 4.5.

4.4.2. Velocity dispersion in radial bins

The maximum likelihood estimates of the parameters (v_c, σ_c) given the observables (v_i, σ_i) are calculated via $\partial\mathcal{L}/\partial v_\mathrm{c} = \partial\mathcal{L}/\partial\sigma_\mathrm{c} = 0$, yielding two coupled formulae (Gunn & Griffin 1979; Pryor & Meylan 1993),

$$\sum_{i=1}^{N}\frac{v_i}{(\sigma_\mathrm{c}^2+\sigma_i^2)} - v_\mathrm{c}\sum_{i=1}^{N}\frac{1}{(\sigma_\mathrm{c}^2+\sigma_i^2)} = 0\,, \qquad (4.10)$$

$$\sum_{i=1}^{N}\frac{(v_i-v_\mathrm{c})^2}{(\sigma_\mathrm{c}^2+\sigma_i^2)^2} - \sum_{i=1}^{N}\frac{1}{(\sigma_\mathrm{c}^2+\sigma_i^2)} = 0\,. \qquad (4.11)$$

Equations 4.10 and 4.11 can be iteratively solved for v_c and σ_c. As an initial guess, the analytic solution obtained when neglecting the uncertainties σ_i is used. Then one parameter is fixed to its current value while the other is updated using either equation. Afterwards this parameter is held constant and the value of the second parameter is updated using the remaining equation.

Pryor & Meylan (1993) also provide formulae to determine the uncertainties in v_c and σ_c,

$$\mathrm{var}(v_\mathrm{c}) = \frac{I_{22}}{I_{11}I_{22}-I_{12}^2}\,, \qquad (4.12)$$

$$\mathrm{var}(\sigma_\mathrm{c}) = \frac{I_{11}}{I_{11}I_{22}-I_{12}^2}\,, \qquad (4.13)$$

$$\mathrm{cov}(v_\mathrm{c},\sigma_\mathrm{c}) = -\frac{I_{12}}{I_{11}I_{22}-I_{12}^2}\,. \qquad (4.14)$$

The $I_{j,k}$ are the coefficients of the information matrix, given by

$$I_{11} = \sum_{i=1}^{N}\frac{1}{\sigma_\mathrm{c}^2+\sigma_i^2}\,, \qquad (4.15)$$

$$I_{22} = \sum_{i=1}^{N}\left(\frac{1}{\sigma_\mathrm{c}^2+\sigma_i^2} - \frac{(v_i-v_\mathrm{c})^2+2\sigma_\mathrm{c}^2}{(\sigma_\mathrm{c}^2+\sigma_i^2)^2} - \frac{4\sigma_\mathrm{c}^2(v_i-v_\mathrm{c})^2}{(\sigma_\mathrm{c}^2+\sigma_i^2)^3}\right)\,, \qquad (4.16)$$

$$I_{12} = \sum_{i=1}^{N}\frac{2\sigma_\mathrm{c}(v_i-v_\mathrm{c})}{(\sigma_\mathrm{c}^2+\sigma_i^2)^2}\,. \qquad (4.17)$$

The velocity dispersion profiles for the three clusters obtained via radial binning of the data are shown in Fig. 4.2. The bin sizes used were 25 stars per bin in M92 and 30 stars in M13 and M3. The smaller bin size for M92 was chosen because the overall accuracy of the velocities in this cluster is slightly higher than in the other two. The comparison between our PMAS data and the literature shows a very good agreement between the two. This is a reassuring fact since the different datasets are quite heterogeneous. Note that the bins were created independently for our and the literature data, i.e., each bin only contains velocities from one dataset.

For M92, we also show two of the dispersion profiles determined by Drukier et al. (2007) using a Bayesian approach and radial velocity measurements of ~ 300 stars. The good agreement with our binned profiles is not too surprising given that their observations are the basis of the majority of our M92 data at larger radii. Drukier et al. (2007) found that the velocity dispersion is well described by a cored power-law with a scale radius

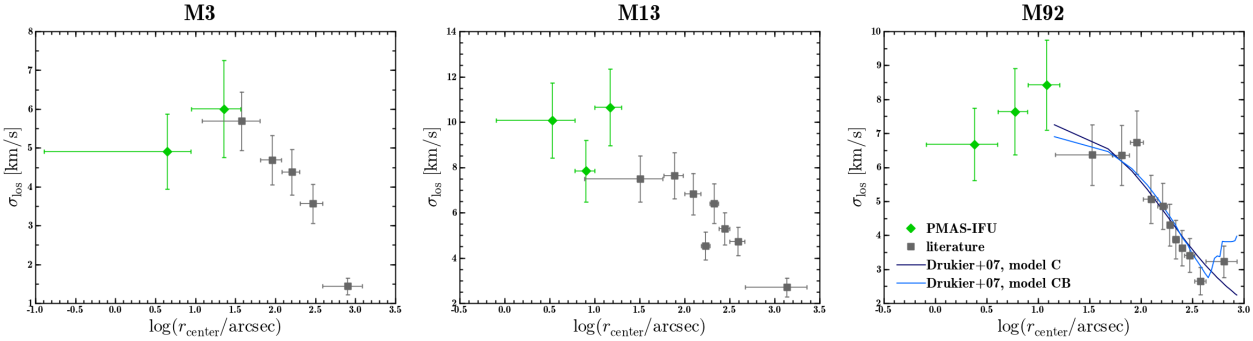

Fig. 4.2. The velocity dispersion as a function of projected distance to the cluster centre for M3, M13, and M92. In each cluster, the data was binned radially and Eqs. 4.10 and 4.11 were used to obtain the maximum likelihood estimate of the velocity dispersion per bin. We analysed our PMAS data and the literature data separately in the sense that no bin included data from both sets. For M92, we also show the velocity dispersion profile obtained by Drukier et al. (2007). Note that the horizontal error bars only indicate the full range in radii covered by the individual bins.

of 2′ (their model C). Their model CB includes an additional break radius that accounts for the possibility that escaping stars can yield a rise in the velocity dispersion profile in the very outskirts of the cluster. Such a rise is visible in M92, but not in the other two clusters. McLaughlin & van der Marel (2005) derive tidal radii of $r_{\rm t}$ =178 pc (M3), 74 pc (M13), and 59 pc (M92), respectively. For the distances of the clusters, those values correspond to projected radii of 60′, 36′ and 23′. A comparison with Fig. 4.2 shows that in M92, the rise in the velocity dispersion is observed at radii $\gtrsim 1/3 r_{\rm t}$. Neither in M3 nor M3 do we have sufficient kinematical data at such large radii to look for a similar effect.

The maximum likelihood estimates obtained upon solution of Eqs. 4.10 and 4.11 are known to be biased. The strength of this bias increases as the number of stars per bin decreases. It also grows when the measurement uncertainties grow relative to $\sigma_{\rm c}$. Some of the stars from our PMAS sample have velocity uncertainties higher than the intrinsic dispersion of the clusters. Therefore we checked the significance of a possible bias via Monte Carlo simulations: For each bin we created 1000 realizations by assigning each star a new velocity drawn from Eq. 4.8 and re-calculating $\sigma_{\rm c}$. We found that the velocity dispersions are slightly underestimated, but the offsets were always below 1 km/s and well within the error bars shown in Fig. 4.2. Not surprisingly, the bias was stronger for our IFU data (~0.5 km/s) than for the literature data (~0.2 km/s). This is a consequence of the wide range of velocity uncertainties in our data. We also used the simulations to verify that the uncertainties of the dispersions calculated using Eqs. 4.12 and 4.13 are useful by comparing them to the standard deviations of our Monte Carlo realizations. The agreement was remarkably good, with deviations $\lesssim$0.1 km/s.

4.4.3. Rotation in the clusters

We also checked if any of the clusters in our sample shows signs of rotation. To this aim we separated our data into 4 radial bins per cluster. In each bin the measured radial velocities were further divided into two halves with respect to an assumed rotation axis. We determined the mean velocity and its uncertainty in each half-bin as outlined above and calculated the difference in the mean velocities. This step was repeated assuming different rotation angles. In case of a non-zero rotational component, one expects a sinusoidal variation of the mean velocity difference with axis angle. The relation between the two quantities is shown in Fig. 4.3 for the different bins in the three clusters.

In M3, the measured offsets do not suggest any significant rotational component, at least the projected amplitude of it is $\lesssim$1 km/s. The situation is different in M13. Lupton et al. (1987) already reported that this cluster shows rotation. While no clear rotational signal is detected in the central bin, the three outer bins suggest rotation with a projected amplitude ~2 km/s, in reasonable agreement with the measurements of Lupton et al.. The rotation axis is tilted $\sim -30°$ with respect to the east-west direction. Finally, in M92 all four radial bins suggest a small rotational component, with a projected amplitude $\sim$ 1 − 2km/s. However, when comparing the curves depicted in the different panels shown for M92 in Fig. 4.3, the axis angle suggested by the data seems to be quite variable.

In summary, M13 and M92 both show signs of rotation within the clusters. However, a comparison between Figs. 4.2 and 4.3 shows that unless very unfortunate projection effects are at work, the dominant contribution to the observed line-of-sight velocity distribution is the velocity dispersion. This is important because our models assume spherical symmetry which would be broken in strongly rotating stellar systems. The generalisation to such systems can be done via axis-symmetric Jeans models that we do not consider here.

4.4.4. Comparison to models

When combining the data in radial bins, one has to select a useful bin size. Using too few bins might wash out some characteristics of the data. For example, the upturn in the velocity dispersion at the largest radii in M92 disappears when a size of 50 stars per bin is chosen. On the other hand, too many bins might introduce spurious features in the radial profile due to shot noise resulting from a low number of stars per bin. However, when a model prediction of $(v_{\rm c}, \sigma_{\rm c})$ is available as a function of radius, one does not necessarily rely on any binning of the data. Instead, the likelihood of each model given the data can be directly computed using Eq. 4.9. Following Gerssen et al. (2002), we define the quantity $\lambda \equiv -2\ln\mathcal{L}$. Inserting Eq. 4.9 we obtain

$$\lambda = \sum_{i=1}^{N} \ln\left[2\pi(\sigma_{\rm c}^2 + \sigma_i^2)\right] + \sum_{i=1}^{N} \frac{(v_i - v_{\rm c})^2}{\sigma_{\rm c}^2 + \sigma_i^2}\,. \qquad (4.18)$$

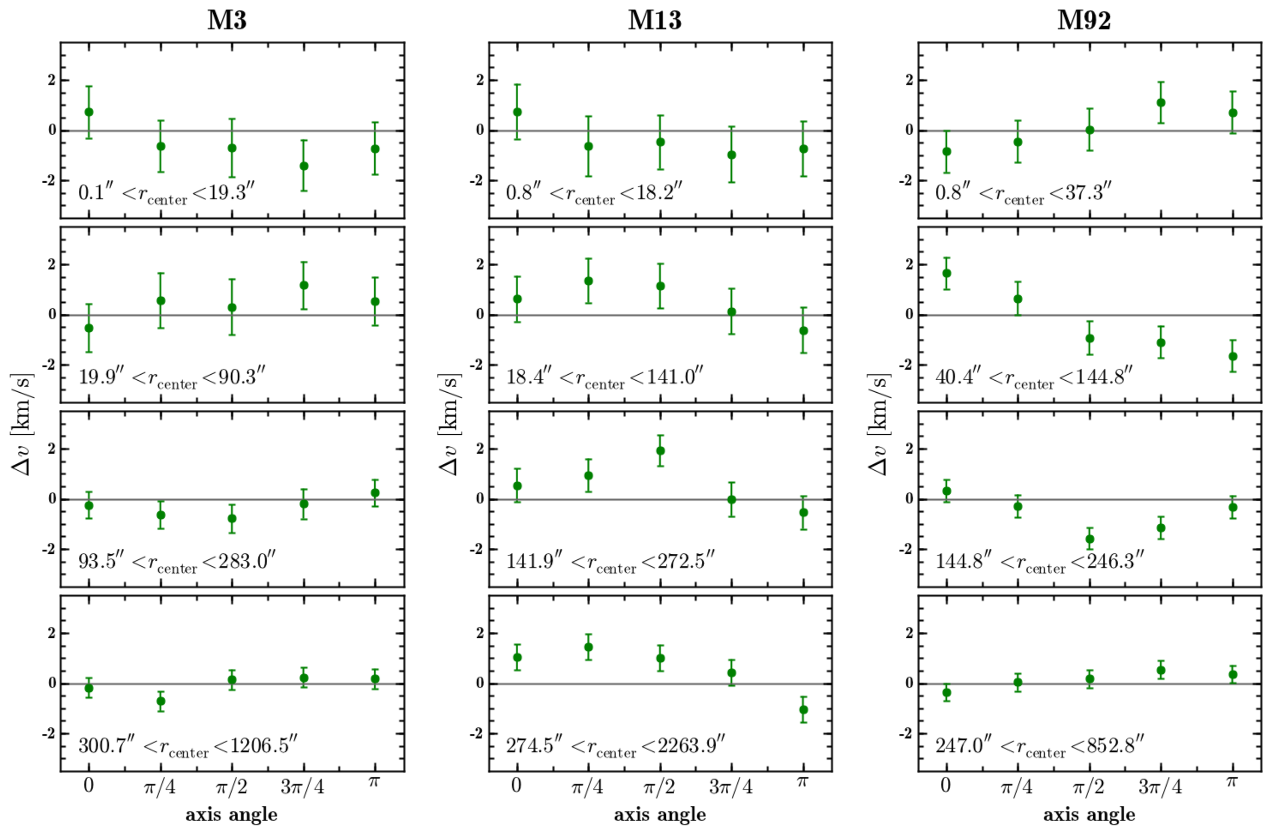

Fig. 4.3. Search for internal rotation of the clusters M3, M13, and M92. For each cluster, 4 radial annuli around the cluster centre are shown. In each bin, we plot the difference (divided by 2) in mean velocity after dividing the stars into two halves with respect to an assumed rotation axis that passes through the centre of the cluster. The axis angle is zero when aligned in east-west direction and increases in anticlockwise direction. The extension of the radial bins is indicated in each panel.

It can be shown that λ follows a χ^2 distribution with N degrees of freedom around the expectation value,

$$\langle\lambda\rangle = \sum_{i=1}^{N} \ln\left[2\pi(\sigma_c^2 + \sigma_i^2)\right] + N\,. \tag{4.19}$$

To illustrate that this is indeed the case for our data, we performed the following test. We used the positions and uncertainties of the stars in our sample in M13 ($N = 343$ stars), modelled the intrinsic radial velocity dispersion of the cluster as a power-law and then randomly drew samples of size N from a normal distribution following Eq. 4.8. The result of 10 000 realizations is shown in Fig. 4.4. The distribution of λ-values is statistically indistinguishable from the probability density function of the $\chi^2_{\rm N}$ distribution, a KS test yields a probability $\gtrsim$ 99%. Whether or not a model is statistically acceptable can thus be verified using the well-known characteristics of the $\chi^2_{\rm N}$ distribution.

Furthermore, likelihood ratio tests can be applied to discriminate between individual models in a statistical manner. We assume that the likelihood of models has been calculated on an m-dimensional grid and the model that maximizes the likelihood has $\lambda_{\rm min}$. If the range of models is restricted to an $\hat{m}$–dimensional subspace, the quantity $\lambda - \lambda_{\rm min}$ will be $\geq$0 for each model in $\hat{m}$. A well-known theorem from statistical theory (Wilks 1938) states that for large sample sizes N, the difference $\lambda - \lambda_{\rm min}$ is distributed according to a χ^2-distribution with $m - \hat{m}$ degrees of freedom. Therefore, confidence intervals can also be obtained using χ^2 statistics. This approach was also followed by, e.g., Merritt & Saha (1993) or Gerssen et al. (2002).

4.5. Dynamical modelling

Using the Jeans formalism outlined in Sect. 4.2, we created dynamical models for each of the clusters in our sample. The procedure we followed for every cluster can be summarized as follows. The surface brightness profile of the cluster was parametrized as an extended Nuker profile, cf. Sect. 4.3. Furthermore, we made an assumption about the anisotropy profile $\beta(r)$ in the cluster, starting from an isotropic profile, i.e. $\beta = 0$, and only considering anisotropy in cases where the comparison between the isotropic profile and the data suggested it. This was only the case for M92. For a given mass-to-light ratio $\Upsilon(r)$ and a given black-hole mass $M_{\rm BH}$, we then determined the radial velocity dispersion profile $\sigma_{\rm c}(r)$, as a function of projected distance to the cluster centre and projected into the line-of-sight. The code to preform the Jeans modelling was kindly provided by R. van der Marel (priv. comm.). We discuss our results for each cluster in the following.

4.5.1. M3

M3 is the most distant cluster in the sample, located at 10.2kpc (Harris 1996). In Sect. 4.3 we obtained an integrated V magnitude of 6.52. Combined with the distance, we obtain an absolute magnitude in V of $M_{V,\rm t} = -8.52$.

Regarding the kinematical data, we have the smallest number of velocity measurements in this cluster, 50 velocities from our PMAS data and 161 velocities collected from various literature

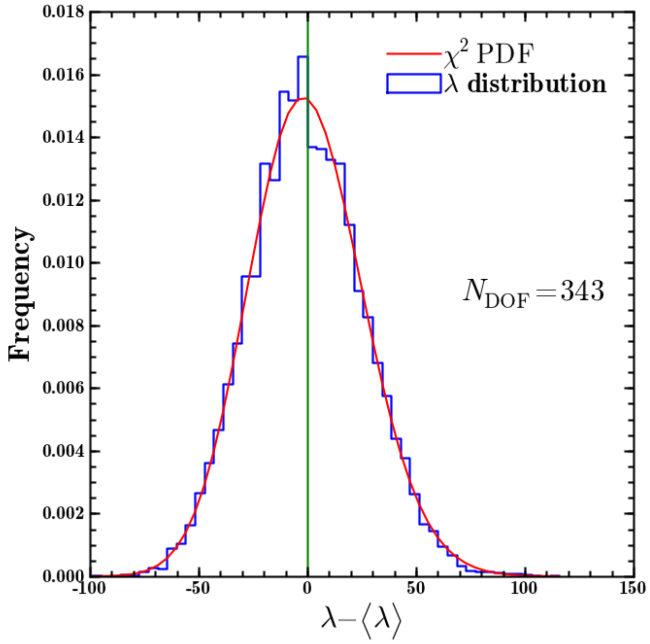

Fig. 4.4. Test for the validity of using χ^2 statistics in the comparison of modelled and measured velocity dispersion. The probability density function (PDF) of the χ^2 distribution with $N = 343$ degrees of freedom (the number of stars in the M13 sample) is plotted against the histogram of λ values obtained from 10 000 Monte Carlo realizations of our data. The simulations were performed using the positions and the uncertainties in the measured radial velocities of the M13 stars and then randomly drawing N velocities from a distribution according to Eq. 4.8. The dispersion profile of the cluster was modelled as a power law for this purpose.

studies. 17 stars were excluded because they showed signs of variability. Furthermore, three high velocity stars in our sample were eliminated because their velocities likely do not trace the cluster potential.

As input for the Jeans models we used constant mass-to-light ratios between ranging from $\Upsilon = 0.6 - 1.2 M_{\odot}/L_{\mathrm{V},\odot}$ and included contributions of a central black hole in the mass range $0 - 10\,000$ M$_{\odot}$ in the gravitational potential. For each model curve of $\sigma_{\mathrm{c}}(r)$, we calculated the λ value according to Eq. 4.18. Estimates and confidence intervals for M_{BH} and Υ were obtained by marginalizing the likelihoods over the other quantity. The likelihood of the individual models on the M_{BH}-Υ grid and the marginalized likelihoods of M_{BH} and Υ are shown in Fig. 4.5. The most likely model has no black hole and a mass to light ratio of $\Upsilon = 1.0$. With a value of $\lambda_{\mathrm{min}} = 1111.8$ it is statistically acceptable, given that $\langle\lambda\rangle = 1112.6$ for $N = 190$ degrees of freedom.

Marginalizing over models with identical mass-to-light ratio yields $\Upsilon = 1.00 \pm 0.11$. The difference to the value reported by McLaughlin & van der Marel (2005) ($\Upsilon = 0.77^{+0.35}_{-0.28}$) is within the uncertainties of the individual measurements. Combined with the luminosity our value yields a cluster mass of $M_{\mathrm{M3}} = (2.19 \pm 0.24) \cdot 10^5 \mathrm{M}_{\odot}$.

Our models do not suggest the presence of an intermediate-mass black hole in the cluster centre. We obtain a 1σ upper limit of $M_{\mathrm{BH}} < 600\,\mathrm{M}_{\odot}$ when marginalizing over the models with identical black hole mass. Using a more conservative 3σ limit increases the black hole mass allowed for by our modelling to 2 500 M$_{\odot}$. In Fig. 4.6 we show a comparison between the velocity dispersion derived from our data and the predictions of the various models with $\Upsilon = 1.0$. The distinction between the models with different black hole masses is almost exclusively based on the velocities of the stars in the innermost data bin. The velocity dispersion that we measure in the centre is slightly below the model prediction already in the case without any black hole. Therefore, an additional contribution to the velocity dispersion caused by any IMBH will always result in a reduced likelihood of the model given the data.

We emphasize that our innermost datapoint contains the velocities of 30 stars. It is an impressive demonstration of the power of our approach that we can obtain a substantial set of reliable radial velocities within the sphere of influence of an IMBH with a realistic mass estimate. Recall that our observations were obtained under mediocre seeing conditions of $\gtrsim 1''$using an IFU with only 16×16 spaxels.

We already mentioned that we find tentative evidence for even the model without an IMBH overestimating the measured velocity dispersion towards the centre. A possible explanation for such a behaviour is that the assumptions going into our model, such as a constant mass-to-light ratio or an isotropic velocity distribution, are not completely fulfilled. However, the discrepancy between model and data shown in Fig. 4.6 is not significant and our most likely model does provide an acceptable representation of the data. Given the restricted amount of kinematical data that is available for this cluster we did not calculate more complicated models. We discuss possible simplifications in our modelling and their consequences in Sect. 4.6.

4.5.2. M13

With a distance of 7.1 kpc M13 is the closest cluster in our sample. From Table 4.1 we obtain an absolute magnitude of the cluster of $M_{V,\mathrm{t}} = -8.45$, similar to the one found for M3. The relatively small distance is obviously an advantage when studying the central region of the cluster. Our dataset in M13 includes 343 stars with reliable radial velocity measurements, 80 obtained using PMAS integral field spectroscopy and 265 gathered from the literature. 2 stars are present in both samples. We excluded 40 stars because they showed variability.

We again calculated Jeans models using a range in constant mass-to-light ratios and for a range of black hole masses. The likelihood distribution of the different models is shown in Fig. 4.7 (left). The most likely model is obtained for a black hole with M_{BH}=4 000 M$_{\odot}$ and a mass-to-light ratio of $\Upsilon = 2.15$. It provides a statistically valid description of the data, we obtain $\lambda_{\mathrm{min}} = 2020.2$, well within the confidence interval around the expectation value, $\langle\lambda\rangle = 2026.0$ for $N = 302$ degrees of freedom.

We obtained confidence intervals for the black-hole mass and the mass-to-light ratio by marginalisation of the two-dimensional likelihood distribution. The results are shown in the central and right panel of Fig. 4.7, respectively. Our mass-to-light ratio estimate of $\Upsilon = 2.20 \pm 0.22$ is higher than the value found by McLaughlin & van der Marel (2005) for the same cluster ($\Upsilon = 1.20^{+0.54}_{-0.44}$). On the other hand, Lupton et al. (1987) found an even higher value of $\Upsilon = 3.63$ for their preferred model. The mass-to-light ratio is largely constrained in the outskirts of the cluster and in this region M13 seems to be quite complex as evidence for anisotropy and rotation has been found. Thus the exact value of the mass-to-light ratio depends on the details of the model. However, we do not expect a strong impact of these

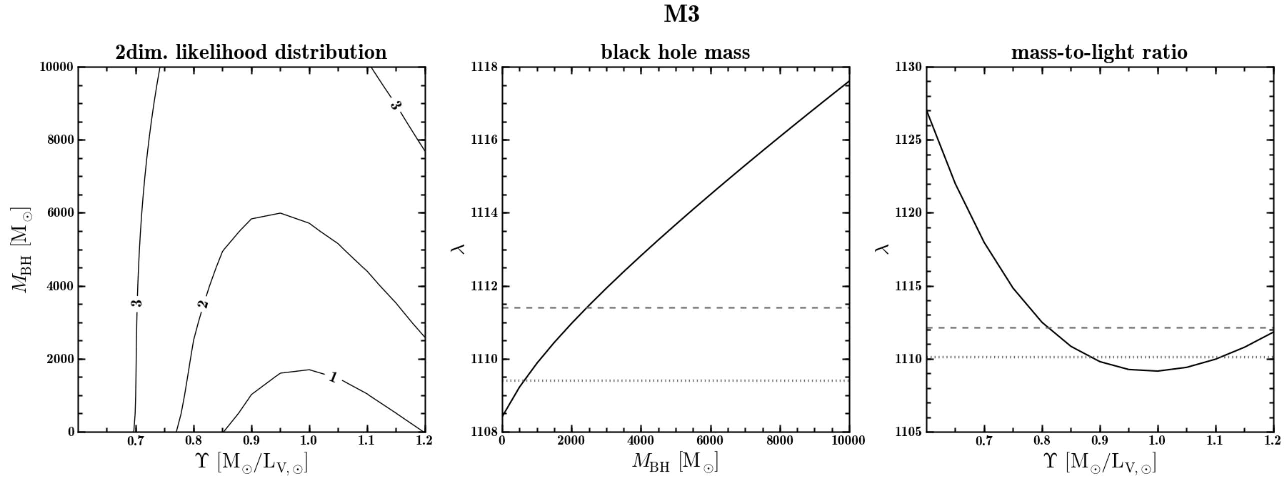

Fig. 4.5. The likelihood of the individual Jeans models calculated for M3. In each model calculation, a constant mass-to-light ratio Υ and a fixed black-hole mass $M_{\rm BH}$ was used.
Left: Distribution of likelihoods in the $M_{\rm BH}$-Υ plane. Contours trace the 1, 2 and 3σ confidence intervals.
Centre: Likelihood marginalized over the mass-to-light ratio as a function of black-hole mass. Horizontal lines indicate the 1 and 3σ confidence limits.
Right: Likelihood marginalized over the black-hole mass as a function of mass-to-light ratio. Again, horizontal lines indicate the 1 and 3σ confidence limits.

uncertainties on our analysis of the central kinematics. Using our estimate of the mass-to-light ratio, we obtain a cluster mass of $M_{\rm M13} = (4.51 \pm 0.45) \cdot 10^5 {\rm M}_\odot$.

The central panel of Fig. 4.7 shows that the increase of the likelihood when including an intermediate-mass black hole of 4 000 M$_\odot$ is not significant. After marginalising over the mass-to-light ratio, we obtain an upper limit of 8 300 M$_\odot$. A comparison between the velocity dispersion data and the model predictions for different black hole masses in M13 is shown in Fig. 4.8. The measured profile is well described by models with low black-hole masses. The scatter that we observe within the innermost 4 datapoints is still consistent with the uncertainties.

We found in Sect. 4.3 that the surface brightness profile allows for a range in central slopes, with $\gamma < 0.34$. We investigated the influence of the uncertainty in the measured surface brightness profile on our IMBH constraint by running the same grid of models as before, but using either a core (i.e. $\gamma = 0$) or a maximum cuspy ($\gamma = 0.34$) surface brightness profile as input. For a model with a core, we found only marginal changes in the deduced mass-to-light ratio and upper mass limit of an IMBH. However, if we use the maximum cuspy profile as input to the modelling we obtain that an IMBH of $M_{\rm BH} = 4\,000^{+4\,900}_{-3\,300}$ M$_\odot$ yields a better representation of the data at the 2σ level compared to the model without a black hole. As a conservative value we therefore adopt an upper mass limit in M13 of $M_{\rm BH} < 8\,900$ M$_\odot$ (1σ) or $M_{\rm BH} < 13\,000$ M$_\odot$ (3σ).

As isotropic models with a constant mass-to-light ratio already provide a valid description of the data we did not calculate more complicated Jeans models.

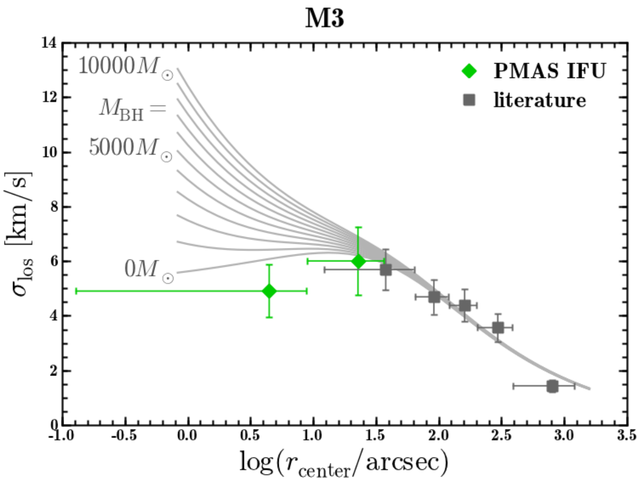

Fig. 4.6. Comparison between the velocity dispersion we measure from our data and the predictions of isotropic models of M3. Models with different black holes masses and a constant mass-to-light ratio of $\Upsilon_{\rm V,\odot} = 1.0$ are shown. The individual model predictions include central black holes with masses in the range of 0–10 000 M$_\odot$ in steps of 1 000 M$_\odot$. The data is the same as shown in Fig. 4.2.

4.5.3. M92

M92 is the cluster for which we have the best kinematical data. Our sample includes 77 stars with PMAS IFU spectra and 308 velocities collected from the literature. A total of 23 stars were excluded because we found evidence for variability in our analysis in Chapter 3. M92 is less luminous than M13 or M92, for a distance of 8.3 kpc we obtain absolute magnitude for the cluster of $M_{V,\rm t} = -8.18$. As such it is still one of the more luminous Milky Way globular clusters. Since it is also relatively nearby it is well suited for dynamical studies of its central region.

When calculating Jeans models for this cluster, we excluded stars with projected distances > 400″ to the cluster centre. The reason for this is the observed rise in the velocity dispersion at the largest projected radii (cf. Fig. 4.2), probably due to stars escaping from the cluster. The velocities of these stars obviously do not trace the gravitational potential of the cluster any more, but this is the quantity we want to constrain by our models.

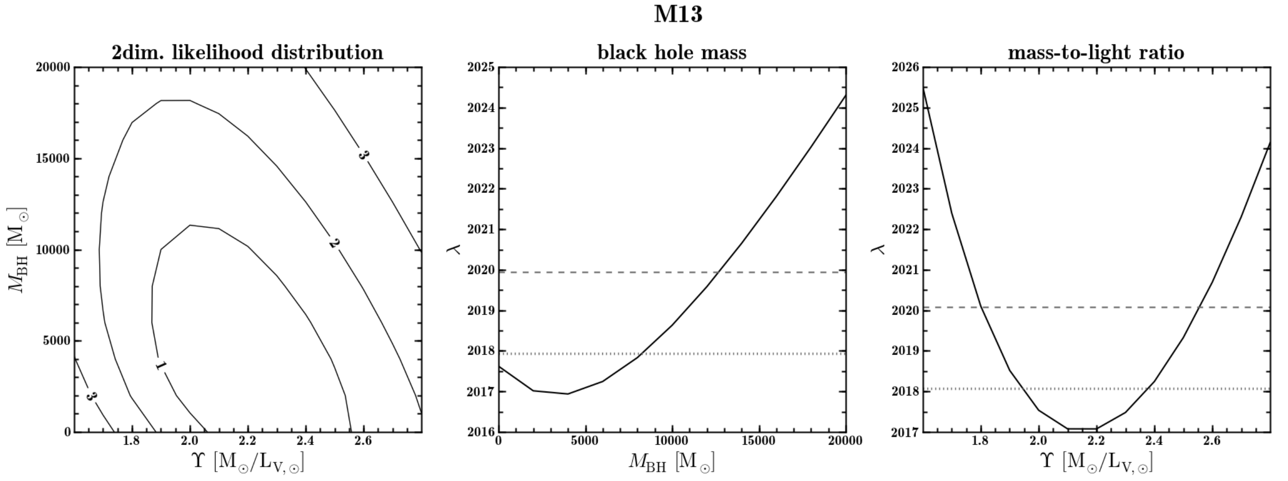

Fig. 4.7. The same as Fig. 4.5 for the globular cluster M13. Note the different ranges in black-hole mass and mass-to-light ratio compared to M3.

We proceeded in analogy to the other two clusters and solved the spherical, isotropic Jeans equation for a grid of models with constant mass-to-light ratios and including various masses of a putative IMBH. The distribution of likelihood values that we obtain is depicted in the left panel of Fig. 4.9. The model that maximizes the likelihood has no central black hole and a mass-to-light ratio of $\Upsilon = 1.55$. Its λ value of 2052.8 is well within the confidence interval around $\langle\lambda\rangle = 2051.0$ ($N_{\rm DOF} = 329$).

Our estimate of the dynamical mass-to-light ratio, $\Upsilon = 1.55 \pm 0.13$ (cf. Fig. 4.9, right) is again higher than the value obtained by McLaughlin & van der Marel (2005) for the same cluster, $\Upsilon = 0.78^{+0.38}_{-0.27}$, while it is slightly below the one obtained by Zocchi et al. (2012) for a King model, $\Upsilon = 1.83$. For our measurement we obtain a cluster mass of $M_{\rm M92} = (2.48 \pm 0.21) \cdot 10^5 {\rm M}_\odot$.

In Fig. 4.10 we show the velocity dispersion profiles that are predicted for the models with $\Upsilon = 1.55$ and a range in masses of a central IMBH and compare them to our data. As can be seen from the central panel of Fig. 4.9, our modelling does not favour a massive black hole in the cluster centre and yields a 1σ upper mass limit of 700 $M_\odot$. The 3σ limit is 2 000 $M_\odot$. Our PMAS dataset contains ~50 stars in the region where the models for different black hole masses diverge. Thanks to the more favourable seeing conditions the average S/N of the deblended spectra is higher than in the other two clusters. This allows us to put a stringent constraint to the mass of a possible IMBH in the cluster. The overall velocity dispersion profile that we measure is well reproduced by the model that does not include a central black hole. Similar to what is observed in M3, there is a slight tendency that the model overestimates the central velocity dispersions.

In Sect. 4.3 we found that the measured surface brightness profile was best represented using a core profile but that a profile with a central surface brightness cusp $\gamma < 0.43$ was also consistent with the data. Similarly to the case of M13 we investigated the influence of the different surface brightness profiles by computing the same suite of models, but using a cuspy profile with $\gamma = 0.43$ as input. We obtained a slightly smaller, yet consistent estimate of the mass-to-light ratio, $\Upsilon = 1.45 \pm 0.12$. Also the 1σ upper limit we obtained for the mass of a black hole decreased only slightly (500$M_\odot$).

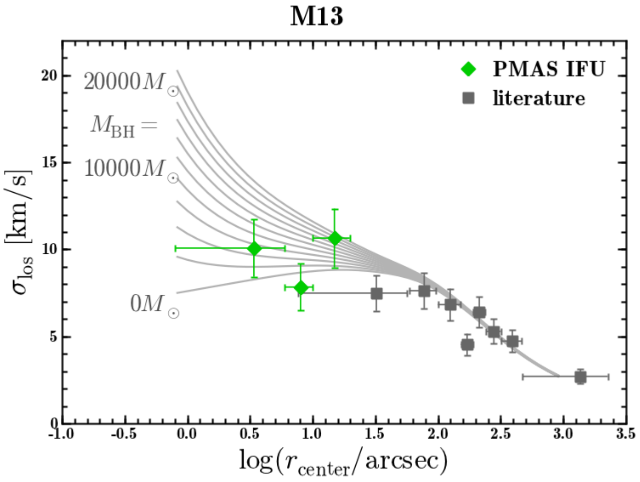

Fig. 4.8. Comparison between the data and the model predictions for the velocity dispersion along the line-of-sight for the cluster M13. Predictions are shown for Jeans models with a constant mass-to-light ratio of 2.2 and for black hole masses in the range 0–20 000 $M_\odot$ in steps of 2 000 $M_\odot$.

4.6. Discussion

We do not find strong evidence for the presence of an intermediate-mass black hole in any of the clusters that we studied. The upper limits that we obtain for M3 and M92 are very stringent. Any black hole with a mass $\gtrsim$1 000 $M_\odot$ would be difficult to explain in view of our measurements. The situation in M13 is a bit more complex, the upper limit of 8 900 $M_\odot$ that we obtain is an order of magnitude higher compared to the other clusters. Furthermore, the presence of an IMBH could even be suggested if we adopt a surface brightness profile with the steepest cusp that is consistent with the photometric data. Note that we refer to the 1σ mass limits of our modelling throughout this discussion in order to facilitate a comparison with other studies.

It is quite remarkable that the measurements in M13 are consistent with a significantly larger IMBH mass range than in M3 or M92. The cluster mass of M13 is only a factor 2 above that of M3 or M92, and also its structural parameters such as the

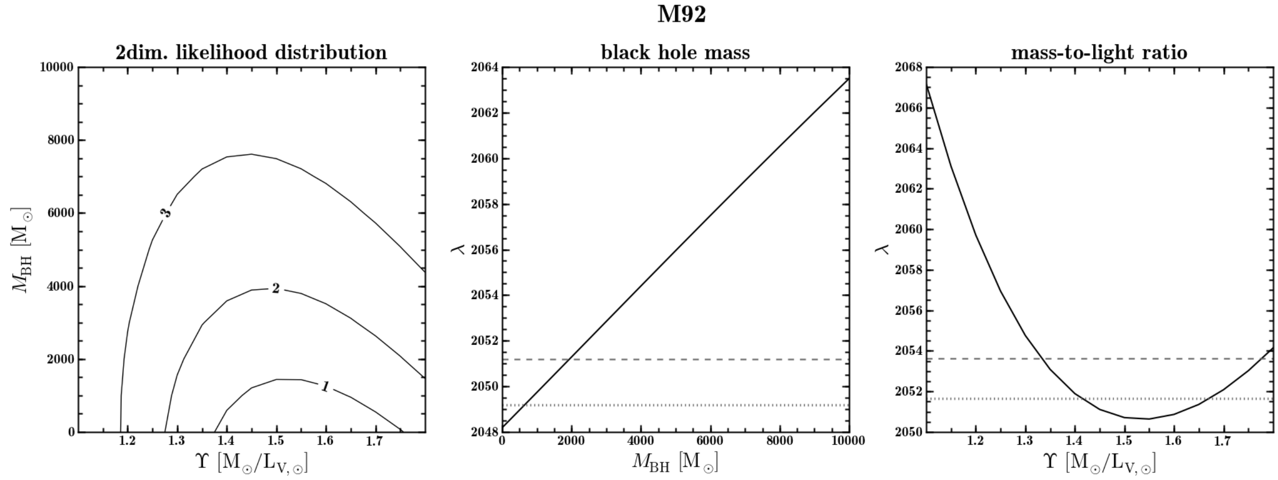

Fig. 4.9. The same as Fig. 4.5 for the globular cluster M92. Note the different range in mass-to-light ratios compared to M3.

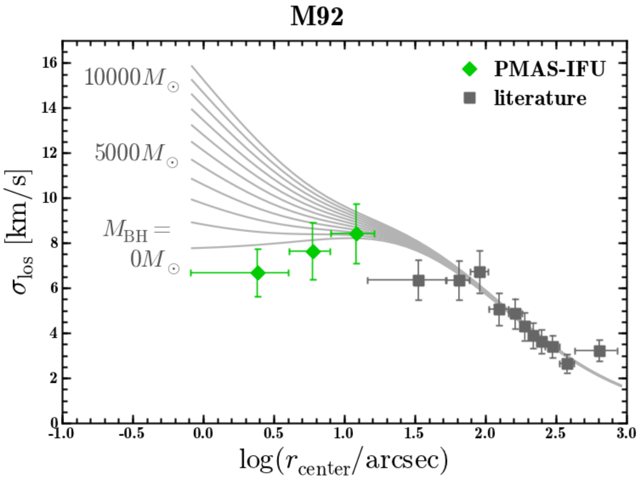

Fig. 4.10. The data and the model predictions for the velocity dispersion along the line-of-sight for the cluster M92 are compared. Predictions are shown for Jeans models with a constant mass-to-light ratio of 1.55 and for black hole masses in the range 0–10 000 M$_\odot$ in steps of 1 000 M$_\odot$. Note that stars in the outermost bin of the data were excluded when computing the likelihood of the individual models (see discussion in text).

core radius or the central surface brightness slope are not so different from those of M3. Moreover, the set of radial velocities close to the very centre is actually the largest in M13. However, as shown in Chapter 3, the observations of M13 were also carried out under unfortunate seeing conditions, at least compared to M92, and yielded a higher fraction of stars with low S/N than in M3 and M92. While we demonstrated that even stars with high uncertainties in their measured radial velocities are useful in the analysis of the cluster kinematics, they will on average contribute less to the models constraints. That this is the case in M13 can be verified by the larger error bars of the central measurements in M13 in Fig. 4.2. Still this alone does not explain the factor of 10 in black hole mass range. The comparison between model and data in Figs. 4.6, 4.8, and 4.10, shows that in M13 the central datapoints are on average above the model prediction without black hole, while they are below in the other two clusters. The discrepancy is still within the uncertainties so it might be just a statistical fluctuation. However, one might also speculate that the central kinematics in M13 are different from those in M3 or M92. At least we consider M13 the most promising candidate to potentially host a IMBH, still below our sensitivity limit but possibly detectable with better data.

We compare our measurements to other studies of intermediate-mass black holes in globular clusters in Table 4.2. Only studies based on the internal dynamics of the cluster are shown. The majority of the work that has been done so far focussed on the most massive clusters in the Milky Way (or M31 in the case of G1). While M3, M13 and M92 still belong to the more massive part of the overall globular cluster population in the Milky Way, they cover the lower end of the mass range studied so far. Compared to the limits on black hole masses found for more massive clusters, the upper limits we find in M3 and M92 are very stringent. To our knowledge, they are the lowest ones determined so far for massive globular clusters. This is quite remarkable given that our observations were carried out from the ground under average seeing conditions and with a 4m-class telescope. It shows the power of our technique to deblend stellar spectra from integral field datacubes.

To see if our new measurements provide more insight on the question whether globular clusters follow the same black-hole scaling relations as do galaxies, we compare them to the $M_{\rm BH}$–σ relation of Gültekin et al. (2009) and the $M_{\rm BH}$–$M_{\rm bulge}$ relation of Marconi & Hunt (2003) in Fig. 4.11. Even though these extrapolations should be taken with a grain of salt, their comparison to our upper limits is interesting. According to the velocity dispersions that we measure in the centres of the clusters, we should not expect to find a black hole at our sensitivity limit in any of the clusters studied. However, our upper limits for M3 and M92 are below the prediction based on the masses of the clusters. In this respect, it is interesting that Miocchi (2007) suggested that globular clusters follow a similar scaling relation between black-hole mass and cluster mass than galaxies do but that the scaling relation that includes the velocity dispersion might be fundamentally different. Our data may suggest the opposite.

The spherical Jeans modelling that we used to investigate the kinematics of our sample clusters does involve some simplifications. We now discuss the most important of those and check whether they are likely to affect our results significantly.

A constant mass-to-light ratio was assumed throughout our dynamical modelling. This is a simplification because the dy-

Table 4.2. Intermediate-mass black holes in globular clusters. Constraints from kinematical studies

Name	$M_{\rm GC}$ $\mathrm{M}_\odot$	$\Sigma(M_{\rm GC})$ $\mathrm{M}_\odot$	$\sigma_{\rm c}$ $\mathrm{km\,s^{-1}}$	$\Sigma(\sigma_{\rm c})$ $\mathrm{km\,s^{-1}}$	$M_{\rm IMBH}$ $\mathrm{M}_\odot$	$\Sigma(M_{\rm IMBH})$ $\mathrm{M}_\odot$	ref.
47 Tuc	1.1×10^6	1×10^5	11.5	2.3	$< 1.5 \times 10^3$		1
NGC 1851	3.7×10^5	2.6×10^4	9.3	0.5	$< 2 \times 10^3$		2
NGC 1904	1.4×10^5	1×10^4	8.0	0.5	3×10^3	1×10^3	2
NGC 2808	8.5×10^5	1×10^5	13.4	2.6	$< 7 \times 10^3$		3
ω Cen	2.5×10^6	2.3×10^5	16.0	3.2	$< 1.2 \times 10^4$		4
ω Cen	2.5×10^6	2.3×10^5	16.0	3.2	4.7×10^4	1×10^4	5
NGC 5694	2.6×10^5	3×10^4	8.8	0.6	$< 8 \times 10^3$		2
NGC 5824	4.5×10^5	3.1×10^4	11.2	0.4	$< 6 \times 10^3$		2
NGC 6093	3.4×10^5	1.6×10^4	9.3	0.3	$< 8 \times 10^2$		2
NGC 6266	8.2×10^5	1.7×10^4	13.7	1.1	$< 4 \times 10^3$		6
NGC 6266	9.3×10^5	2.1×10^4	15.5	0.5	2×10^3	1×10^3	2
NGC 6388	1.1×10^6	1.7×10^5	18.9	0.8	1.7×10^4	9×10^3	7
M15	6×10^5	4×10^4	12.0	2.0	$< 4.4 \times 10^3$		8
G1	1.1×10^7	4.4×10^6	25.1	1.7	1.8×10^4	5×10^3	9
M3	2.2×10^5	2.4×10^4	5.0	1.0	$< 6 \times 10^2$		This study
M13	4.5×10^5	4.5×10^4	10.0	2.0	$< 8 \times 10^3$		This study
M92	2.5×10^5	2.1×10^4	6.5	1.0	$< 7 \times 10^2$		This study

References. (1) McLaughlin et al. (2006); (2) Lützgendorf et al. (2012a); (3) Lützgendorf et al. (2012b); (4) van der Marel & Anderson (2010); (5) Noyola et al. (2010); (6) McNamara et al. (2012); (7) Lützgendorf et al. (2011); (8) Gerssen et al. (2002); (9) Gebhardt et al. (2005)

Notes. Upper limits on IMBH masses are 1σ-limits. We estimated them in cases where other confidence intervals were provided.

namical evolution of the cluster will lead to mass segregation. A rise of M/L in the outskirts is expected because of the increased abundance of low-mass stars. At the smallest radii, the situation might be more complex. The accumulation of heavy stellar remnants has been predicted to cause a central spike in the M/L profile. Gebhardt & Fischer (1995) found such a behaviour only in very concentrated clusters, where the M/L ratio had a minimum at distances around $1'$ towards the centre. In less concentrated clusters, M/L decreased monotonically with radius. A central increase in M/L would also increase the central velocity dispersion predicted by the model. In the cases of M3 and M92, such an increase would reduce the agreement with our measurements. So our data do not suggest that M/L increases towards the centre of either M3 or M92.

It is not fully understood how the inclusion of a dedicated mass-to-light ratio profile influences the search for an IMBH. While Gerssen et al. (2002, 2003) found that in M15 the need for an IMBH is diminished when including a model-predicted profile, Lützgendorf et al. (2012b) observed the opposite trend in NGC 2808. Note that in the latter case the largest changes occurred at radii $\gtrsim 10''$ where the predicted velocity dispersion profile underestimated the data. So their higher IMBH mass limit may well be a consequence of this mismatch.

We do not expect that the assumption of a constant mass-to-light ratio profile has led us to significantly underestimate the upper limits on the black hole masses that are large determined by the innermost datapoints. Minor discrepancies between the data and our models at larger radii, such as observed in M92 at distances $\sim 10'' - 100''$, might be hinting towards a more complex mass-to-light ratio profile. A possibility to obtain such a profile is via Fokker-Planck models (e.g. Dull et al. 1997, 2003, for M15) or N-body simulations. However, this is beyond the scope of this work. On the other hand, if all three components of the velocity dispersion are known, it is also possible to constrain the profile of the mass-to-light ratio directly from observations. Such has been done by van den Bosch et al. (2006) for M15 or van de Ven et al. (2006) for ω Centauri. The combination of our data with proper motions could be very promising in this respect.

We observed only one component of the velocity dispersion, namely the one along the line-of-sight. For this reason we cannot infer whether the velocity distribution is anisotropic in any of our target clusters. Anisotropy has been identified as a significant nuisance in the search for massive black holes. For example, a velocity distribution that is radially biased can mimic the presence of a black hole (Binney & Tremaine 2008). On the one hand, any initial anisotropy in a stellar system will decrease with time due to relaxation processes. The high stellar densities in the cluster centres imply relaxation timescales that are only a small fraction of the lifetime of a cluster (e.g. Meylan 1988). While evidence for anisotropy has been detected in M3 and M13, it is restricted to larger radii, so we do not expect it to strongly affect our analysis of the central kinematics.

However, the presence of a massive black hole can lead to a tangential bias because stars on high-eccentricity orbits are ejected by the black hole (Gebhardt et al. 2003). In M3 and M92 there is a tendency that the model prediction overestimates the velocity dispersion in the central region. Such a trend might be caused by tangential anisotropy in the centre. To test whether our data supports such a scenario, we ran anisotropic Jeans models with $\beta(r)$ parametrized as

$$\beta(r) = \beta_0 + (\beta_\infty - \beta_0)\frac{r^2}{r^2 + a^2}\,. \tag{4.20}$$

We selected M92 for this test because it has the best kinematical data. The anisotropy radius a was fixed to the core radius ($\sim 10''$, cf. Table 4.1) and β_∞ was set to zero because the cluster is known to be isotropic at larger radii (Cudworth 1976). The mass-to-light ratio and black hole mass of the model were fixed to the values that maximized the likelihood in the isotropic case, and β_0 was varied between -3 and 0. We find a confidence interval of $\beta_0 = -1.0^{-0.9}_{+0.8}$. Formally we find thus marginal evidence for tangential anisotropy in the core, but only with 1.6σ. A cluster whose velocity distribution becomes increasingly anisotropy when moving towards the centre is somehow counter-intuitive because the relaxation times are shorter in the centre. While a massive black hole might be an attractive solution for this, we think that more data is be needed to investigate this peculiarity. A combination of our data with proper motions might allow a direct determination of the anisotropy profile.

A valid dynamical modelling of the central regions depends critically on an accurate determination of the centre of the cluster. As mentioned in Chapter 3, we adopted the photometric cluster centres determined by Goldsbury et al. (2010) using two different methods. A correct localization of the centre is more difficult in clusters with a shallow central density gradient. In this respect, the large core radii found in M3 and M13 might be problematic. However, Goldsbury et al. give small uncertainties for all clusters that we studied ($0\farcs2$ for M3, $0\farcs1$ for M13 and $0\farcs3$ for M92). Our analysis is based on the assumption that the photometric centre of each cluster coincides with the kinematic centre. We do not find evidence that this is not the case.

Finally, we discuss the influence of binaries on our measurements. While binaries can have a strong impact on the dynamical analysis of star clusters, their influence is less of an issue in globular clusters than in open ones (Kouwenhoven & de Grijs 2008). Furthermore, we carefully cleaned our sample from binaries in Chapter 3. We do not expect that undetected binaries have a measurable impact on our analysis.

4.7. Conclusions

We investigated the internal kinematics in three massive Galactic globular cluster, M3, M13, and M92 using new radial velocity measurements for the inner $\sim 10''$. Compared to previous dynamical studies that were performed for these clusters, we have a significantly better coverage of the central regions with kinematical data. This allowed us to investigate whether the internal kinematics suggest the presence of an intermediate-mass black hole.

A careful analysis of the surface brightness profiles reveals that M13 and M92 are consistent with having a core profile. Only in M3 a surface brightness cusp is required to match the data. In all three cases, however, the measured surface brightness profiles are consistent with those that are predicted for globular clusters that harbour massive black holes based on theoretical work or simulations.

The analysis of the kinematical data in radial bins reveals a flat behaviour of the central velocity dispersion profile in all three clusters. A characteristic rise that might suggest the presence of an IMBH is observed in none of the clusters. On the contrary, in M3 and in M92 there is tentative evidence for a shallow decrease of the velocity dispersion towards the centre. Furthermore, we detect a weak rotational component in M13 and M92. While in M13 the rotation seems to disappear near the cluster centre, this might not be the case for M92. In all three clusters, however, the dynamics are dominated by random motions.

We calculated spherical Jeans models for each cluster in our sample. Isotropic models with a constant mass-to-light ratio provide a good overall representation of the cluster dynamics. In none of the targets a massive black hole is required to obtain agreement between the models and our data. Instead, we find stringent upper limits in M3 and M92, where any IMBH more massive than $\sim$1 000 solar masses is ruled out by our study. In M13, the upper limit is significantly more relaxed and we cannot rule out an IMBH with a mass $\lesssim$9 000 solar masses. We also discuss the possibility that the velocity distribution gets anisotropic towards the centre of M92. While our data does suggest tangential anisotropy we believe that more data will be needed to investigate this. In particular, a fully three-dimensional view of the cluster is possible when combining our data with proper motion studies.

Acknowledgements. The authors are grateful to Roeland van der Marel for providing his Jeans modelling code.
S. K. acknowledges support from the ERASMUS-F project through funding from PT-DESY, grant no. 05A09BAA.
Based on observations collected at the Centro Astronómico Hispano Alemán (CAHA) at Calar Alto, operated jointly by the Max-Planck Institut für Astronomie and the Instituto de Astrofísica de Andalucía (CSIC).

References

Anderson, J., Sarajedini, A., Bedin, L. R., et al. 2008, AJ, 135, 2055
Anderson, J. & van der Marel, R. P. 2010, ApJ, 710, 1032
Baumgardt, H., Côté, P., Hilker, M., et al. 2009, MNRAS, 396, 2051
Baumgardt, H., Makino, J., & Hut, P. 2005, ApJ, 620, 238
Binney, J. & Tremaine, S. 2008, Galactic Dynamics: Second Edition (Princeton University Press)
Cappellari, M. 2008, MNRAS, 390, 71
Cudworth, K. M. 1976, AJ, 81, 975
Cudworth, K. M. 1979, AJ, 84, 1312
Cudworth, K. M. & Monet, D. G. 1979, AJ, 84, 774
Djorgovski, S. 1993, in Astronomical Society of the Pacific Conference Series, Vol. 50, Structure and Dynamics of Globular Clusters, ed. S. G. Djorgovski & G. Meylan, 373
Drukier, G. A., Cohn, H. N., Lugger, P. M., et al. 2007, AJ, 133, 1041
Dull, J. D., Cohn, H. N., Lugger, P. M., et al. 1997, ApJ, 481, 267
Dull, J. D., Cohn, H. N., Lugger, P. M., et al. 2003, ApJ, 585, 598
Farrell, S. A., Webb, N. A., Barret, D., Godet, O., & Rodrigues, J. M. 2009, Nature, 460, 73
Ferrarese, L. & Merritt, D. 2000, ApJ, 539, L9
Gebhardt, K., Bender, R., Bower, G., et al. 2000, ApJ, 539, L13
Gebhardt, K. & Fischer, P. 1995, AJ, 109, 209
Gebhardt, K., Rich, R. M., & Ho, L. C. 2005, ApJ, 634, 1093
Gebhardt, K., Richstone, D., Tremaine, S., et al. 2003, ApJ, 583, 92
Gerssen, J., van der Marel, R. P., Gebhardt, K., et al. 2002, AJ, 124, 3270
Gerssen, J., van der Marel, R. P., Gebhardt, K., et al. 2003, AJ, 125, 376
Gill, M., Trenti, M., Miller, M. C., et al. 2008, ApJ, 686, 303
Gillessen, S., Eisenhauer, F., Trippe, S., et al. 2009, ApJ, 692, 1075
Glebbeek, E., Gaburov, E., de Mink, S. E., Pols, O. R., & Portegies Zwart, S. F. 2009, A&A, 497, 255
Goldsbury, R., Richer, H. B., Anderson, J., et al. 2010, AJ, 140, 1830
Greene, J. E., Peng, C. Y., Kim, M., et al. 2010, ApJ, 721, 26
Gültekin, K., Richstone, D. O., Gebhardt, K., et al. 2009, ApJ, 698, 198
Gunn, J. E. & Griffin, R. F. 1979, AJ, 84, 752
Häring, N. & Rix, H.-W. 2004, ApJ, 604, L89
Harris, W. E. 1996, AJ, 112, 1487
Herrnstein, J. R., Moran, J. M., Greenhill, L. J., & Trotter, A. S. 2005, ApJ, 629, 719
Jahnke, K. & Macciò, A. V. 2011, ApJ, 734, 92
Jalali, B., Baumgardt, H., Kissler-Patig, M., et al. 2012, A&A, 538, A19
Kamann, S., Wisotzki, L., & Roth, M. M. 2013, A&A, 549, A71
Kong, A. K. H., Heinke, C. O., di Stefano, R., et al. 2010, MNRAS, 407, L84
Kormendy, J. & Richstone, D. 1995, ARA&A, 33, 581
Kouwenhoven, M. B. N. & de Grijs, R. 2008, A&A, 480, 103
Lauer, T. R., Ajhar, E. A., Byun, Y.-I., et al. 1995, AJ, 110, 2622
Leonard, P. J. T., Richer, H. B., & Fahlman, G. G. 1992, AJ, 104, 2104
Lupton, R. H., Gunn, J. E., & Griffin, R. F. 1987, AJ, 93, 1114
Lützgendorf, N., Kissler-Patig, M., Gebhardt, K., et al. 2012a, ArXiv e-prints
Lützgendorf, N., Kissler-Patig, M., Gebhardt, K., et al. 2012b, A&A, 542, A129
Lützgendorf, N., Kissler-Patig, M., Noyola, E., et al. 2011, A&A, 533, A36
Madau, P. & Rees, M. J. 2001, ApJ, 551, L27
Magorrian, J., Tremaine, S., Richstone, D., et al. 1998, AJ, 115, 2285
Marconi, A. & Hunt, L. K. 2003, ApJ, 589, L21
McLaughlin, D. E., Anderson, J., Meylan, G., et al. 2006, ApJS, 166, 249
McLaughlin, D. E. & van der Marel, R. P. 2005, ApJS, 161, 304
McNamara, B. J., Harrison, T. E., Baumgardt, H., & Khalaj, P. 2012, ApJ, 745, 175
Merritt, D. & Saha, P. 1993, ApJ, 409, 75
Meylan, G. 1988, A&A, 191, 215
Miller-Jones, J. C. A., Wrobel, J. M., Sivakoff, G. R., et al. 2012, ApJ, 755, L1
Miocchi, P. 2007, MNRAS, 381, 103

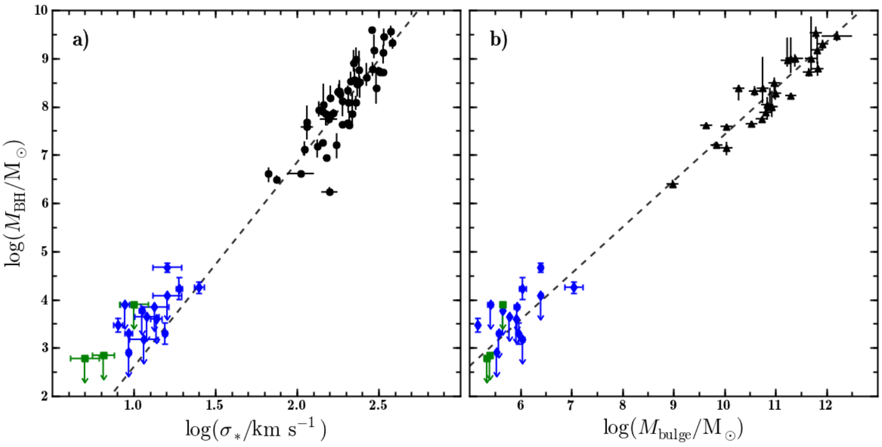

Fig. 4.11. Constraints on the masses of intermediate-mass black holes in globular clusters in the context of the $M_{\rm BH}$-bulge relations of galaxies. *Left:* Comparison to the data and the best-fit relation (dashed line) of Gültekin et al. (2009) in the $M_{\rm BH}$-σ plane. *Right:* Comparison to the data and best-fit relation of Marconi & Hunt (2003) in the $M_{\rm BH}$-$M_{\rm bulge}$ plane. In both panels, the data for the globular clusters are the same as in Table 4.2. For ω Centauri and NGC 6266, we included both studies listed in Table 4.2.

Moore, B., Diemand, J., Madau, P., Zemp, M., & Stadel, J. 2006, MNRAS, 368, 563
Noyola, E. & Baumgardt, H. 2011, ApJ, 743, 52
Noyola, E. & Gebhardt, K. 2006, AJ, 132, 447
Noyola, E., Gebhardt, K., Kissler-Patig, M., et al. 2010, ApJ, 719, L60
Portegies Zwart, S. F. & McMillan, S. L. W. 2002, ApJ, 576, 899
Pryor, C. & Meylan, G. 1993, in Astronomical Society of the Pacific Conference Series, Vol. 50, Structure and Dynamics of Globular Clusters, ed. S. G. Djorgovski & G. Meylan, 357
Roth, M. M., Kelz, A., Fechner, T., et al. 2005, PASP, 117, 620
Searle, L. & Zinn, R. 1978, ApJ, 225, 357
Silk, J. & Rees, M. J. 1998, A&A, 331, L1
Strader, J., Chomiuk, L., Maccarone, T. J., et al. 2012, ApJ, 750, L27
Trager, S. C., King, I. R., & Djorgovski, S. 1995, AJ, 109, 218
Trenti, M., Ardi, E., Mineshige, S., & Hut, P. 2007, MNRAS, 374, 857
Trudolyubov, S. & Priedhorsky, W. 2004, ApJ, 616, 821
Ulvestad, J. S., Greene, J. E., & Ho, L. C. 2007, ApJ, 661, L151
van de Ven, G., van den Bosch, R. C. E., Verolme, E. K., & de Zeeuw, P. T. 2006, A&A, 445, 513
van den Bosch, R., de Zeeuw, T., Gebhardt, K., Noyola, E., & van de Ven, G. 2006, ApJ, 641, 852
van der Marel, R. P. & Anderson, J. 2010, ApJ, 710, 1063
van der Marel, R. P. & Franx, M. 1993, ApJ, 407, 525
Wilks, S. 1938, Annals of Mathematical Statistics, 9, 60
Zocchi, A., Bertin, G., & Varri, A. L. 2012, A&A, 539, A65

Chapter 5

The search for intermediate-mass black holes in globular clusters: New constraints from the kinematics of the unresolved stars*

Sebastian Kamann[1]

[1] Leibniz-Institut für Astrophysik Potsdam (AIP), An der Sternwarte 16, 14482 Potsdam, Germany

ABSTRACT

We present a new method to spectroscopically study the unresolved light in a partially resolved stellar population such as a Galactic globular cluster. Our analysis makes use of the spatial information provided by an integral field spectrograph to subtract the light of the resolved stars and to reveal the integrated spectrum of the unresolved stars. This technique is applied to PMAS integral field spectroscopy of a sample of three Galactic globular clusters, M3, M13 and M92. We have previously analysed this data with the aim of constraining the presence of intermediate-mass black holes in the clusters based on the velocities measured for the resolved stars. Our current analysis is completely complementary as it is based on those stars that cannot be resolved by seeing-limited observations. We combine the spectra in radial bins around the centre of each cluster and measure the velocity dispersion in each bin. Our analysis shows that the dominant contribution to the spectra is indeed coming from the unresolved stars and that residuals from the subtraction of the bright stars play a negligible role. Therefore, our analysis is robust against shot noise.

Although the data we have available are limited by several factors like the limited spectral resolution or the lack of sky spectra observed simultaneously with the data, we are able to reliably measure the central velocity dispersion curve in M92. In agreement with our previous study, dedicated Jeans modelling shows that no black hole is required to fit the observed kinematics. Instead, the upper limit that we obtain on its mass, $500\mathrm{M}_\odot$ (1σ) or $1\,300\,\mathrm{M}_\odot$ (3σ), is the lowest obtained for a massive globular cluster so far. Unfortunately, for the other two clusters, the current data do not allow a similar analysis. However, our analysis approach is very promising, especially in combination with new data that overcome the limitations of ours.

5.1. Introduction

A common challenge in astronomical data analysis is to disentangle the light contributions of a point source and a spatially extended one in an observation. While the point source, either in form of a star or a quasar, will often constitute the dominant light contribution, the scientific aim, however, is often the study of the spatially extended source without contamination by its point-like counterpart. Quasar host galaxies are a good example in this respect. A bright quasar can be several magnitudes brighter than its entire host galaxy. With increasing redshift, the host galaxy appears more and more compact and its decomposition from the quasar becomes more challenging. Precise knowledge of the point spread function (PSF) during the observation is required to accurately remove the contribution of the quasar. In imaging studies, this knowledge might be obtained from the analysis of the light profiles of stars in the field of view (e.g. Croom et al. 2004). However, stars to calibrate the PSF might not always be available within the field of view. Non-simultaneously observed PSF stars are of limited use. As the PSF varies on short time scales, such calibrations can only be used in a statistical sense (Kuhlbrodt et al. 2005). In studies based on integral field spectroscopy (IFS), the observed field of view is usually so small that the quasar and its host fill the entire field of view. If the quasar shows broad emission lines, those lines provide a possibility to infer the PSF directly from the target because they originate from the direct vicinity of the nucleus (e.g. Christensen et al. 2006; Husemann et al. 2013).

In a similar manner, IFS can be used to deblend stellar and nebular emission in nearby galaxies, by using bright stellar emission lines to calibrate the PSF. In this case, the scientific focus can either lie on the star itself or on the gaseous emission around it. Roth et al. (2004) used this technique to study planetary nebulae in M31. A study of nebular emission around LBV stars in M33 was carried out by Fabrika et al. (2005).

A case that has barely been explored so far is the combined observation of a resolved stellar population and underlying extended emission. An intuitive example for such a case might be gaseous emission in a young stellar cluster. However, the continuous emission can also be in the form of stars. In a crowded stellar field, such as a globular cluster or a nearby galaxy, the brighter stars will be *resolved*, i.e., can be deblended from the rest of the population, while the more numerous fainter stars will form an *unresolved* stellar component in which no individual stars can be identified any more.

In imaging studies, such an unresolved stellar population is of marginal interest as it does not contain useful information except for an integrated magnitude. In IFS studies, however, the situation is different. Instead of an integrated magnitude, an integrated spectrum is obtained that might be used to measure a line-of-sight velocity dispersion (LOSVD), chemical abundances or to infer the star formation history. Yet uncovering such a population is a challenging task. Not only because it requires accurate knowledge of the PSF, but also because the techniques mentioned so far to recover the PSF cannot be applied. Suitable calibration stars are generally not available.

In Kamann et al. (2013, Chapter 2 of this thesis), we presented a new method to recover the PSF in a crowded stellar field. It does not require calibration stars and is therefore applicable to a wide range of crowded stellar fields. The application to PMAS (Roth et al. 2005) integral field data of M3, M13 and M92 in Chapter 3 showed that our method is capable of deblending high-quality spectra for the resolved stars in the highly crowded central regions of Galactic globular clusters. In Chapter 4, we constrained the presence of intermediate-mass black holes (IMBHs) in the three clusters based on the kinematic information extracted from those spectra.

The aim that we pursue in this Chapter is to investigate the dynamics of the clusters based on the integrated light of the unresolved stars, uncovered after the resolved ones have been subtracted. At seeing limited resolution, individual spectra can be deblended mainly for the stars above the main sequence turn-off (MSTO). The more numerous stars below the MSTO can only be resolved at significantly higher spatial resolution. For example, it is possible to measure their proper motions using *Hubble* space telescope (HST) photometry (e.g. Anderson & van der Marel 2010) to obtain kinematic information. The huge advantage of spectroscopy compared to photometry it that kinematic measurements are possible even if the stars are unresolved, using the LOSVD. For this reason, it might be possible to spectroscopically probe the cluster dynamics for stars along the main sequence even at seeing limited resolution.

IFS has successfully been used to measure the LOSVD and constrain the presence of IMBHs previously, e.g. by Noyola et al. (2010) or Lützgendorf et al. (2011, 2012). However, in those studies, no effort was made to subtract the resolved stars beforehand. Instead, spatial pixels ("spaxels") dominated by bright giants are excluded from the analysis. To our knowledge, the idea to combine a measurement of the LOSVD with a subtraction of the resolved stars based on PSF-fitting has not been used so far. A methodically similar approach approach was used by Wisotzki et al. (2003) who subtracted multiple lensed images of a quasar from IFS data to uncover the spectrum of the lensing galaxy.

This paper is organized as follows: We summarize the extraction of the spectra from the IFS data in Sect. 5.2. In Sect. 5.3, we present the template spectra used in the kinematic analysis that is discussed in Sect. 5.4. The results of this analysis are the subject of Sect. 5.5 and are used to revise the constraints about the presence of IMBHs in the clusters in Sect. 5.6. We conclude in Sect. 5.7

5.2. Uncovering the faint stars

The details of the data reduction and analysis are described in detail in Chapter 3. For the purpose of the current analysis, we recap the most important steps with respect to the uncovering of the unresolved light and discuss their implications on the further analysis.

5.2.1. Subtraction of the resolved stars

Removing the individually resolved brighter stars is the most crucial step in the estimation of an unbiased LOSVD. In general, the integrated light of a globular cluster will be dominated by stars on the red giant branch. As these stars are relatively few in number, their influence has to be considered carefully in the analysis. Otherwise, it might well be that the majority of the cluster light integrated over a certain area on the sky is contributed by a few bright giants, an unwanted effect that is referred to as *shot noise*. However, an accurate determination of the LOSVD is only possible if many similarly bright stars contribute comparably to the observed spectrum. While other methods have been proposed to overcome this problem, we are convinced that the best way to handle the shot noise is to accurately subtract the spectra of the bright giants from the data.

To estimate the strength of shot noise in our IFS data, we did the following. Under the assumption that N stars of equal brightness are present in an observed field, each star will contribute a fraction $s = (1/N)$ to the integrated flux. If we drop the simplification of all stars being equally bright, than the brightest among the N stars will contribute a fraction $s > (1/N)$. Therefore, if the integrated light can be attributed in large parts to a single bright giant, then $s \lesssim 1$. On the other hand, if many stars contribute comparably to the integrated flux, then $s \ll 1$. Thus, $s_{\max}$, defined as the fractional flux contribution of the brightest star, is a valuable indicator for the strength of shot noise and we refer to it as the *shot noise parameter*. The inverse value of $s_{\max}$ can be considered as the approximate number of stars with a measurable contribution to the observed flux.

Using the above definition, we demonstrate the significance of shot noise in our datasets in Fig. 5.1, where the distribution of $s_{\max}$ values prior to and after the subtraction of the resolved stars is shown. Including the resolved stars, shot noise has the most dramatic effect on our PMAS data of M3. The footprint of the data shown in Fig. 5.1(a) shows that a significant fraction of the flux in the majority of the spaxels can be attributed to individual stars. This is confirmed by the histogram shown in Fig. 5.1(c): in ~60% of the spaxels, more than 30% of the integrated flux comes from an individual star. After the resolved stars have been subtracted, the flux contribution of individual stars is below 30% essentially in all spaxels.

Our aim is to recover the LOSVD inside the cluster. A possibility to minimize the influence of shot noise in the recovered measurement is to integrate over a larger region on the sky. As we want to search for evidence for an IMBH in any of the three clusters, we need to probe the LOSVD inside its sphere of influence, which is $\sim 5 - 10''$ if one assumes a reasonable black hole mass (see Chapter 4). However, the PSF has a width of $\gtrsim 1''$ in our PMAS data, so the contribution from the bright giants is not restricted to individual pixels. The example of M3 shows that even after integration over the majority of the sphere of influence, the spectrum will be dominated by $5 - 6$ giants. On the other hand, there is no evidence for a comparable dominance of a few stars in the unresolved light.

A similar improvement after the subtraction is visible in the other two clusters. While in M13, some areas are uncontaminated by bright stars even without subtraction of the resolved ones, e.g., to the south-east of the centre, they account only for a minority of all available spaxels. In M92 the situation is comparable to M3, with only a small fraction of the spaxels being dominated by truly unresolved light prior to the subtraction.

The dominance of the resolved stars becomes also clear when determining the overall light fraction that can be attributed to the unresolved stars in each cluster. For each of the clusters in our datasets, we determined this fraction by summing up the counts in the spectra of the unresolved components and comparing it to the sum of counts of all deblended spectra of individual stars. This yielded fractions of ~25% in each of the three clusters. We also calculated the contribution of the unresolved stars by translating the magnitudes in the reference catalogue into fluxes and summing up the fluxes of the stars that are resolved and unresolved, respectively. This resulted in even lower fractions, ~15%. An explanation for the difference might be the

(a) Strength of shot noise from all stars

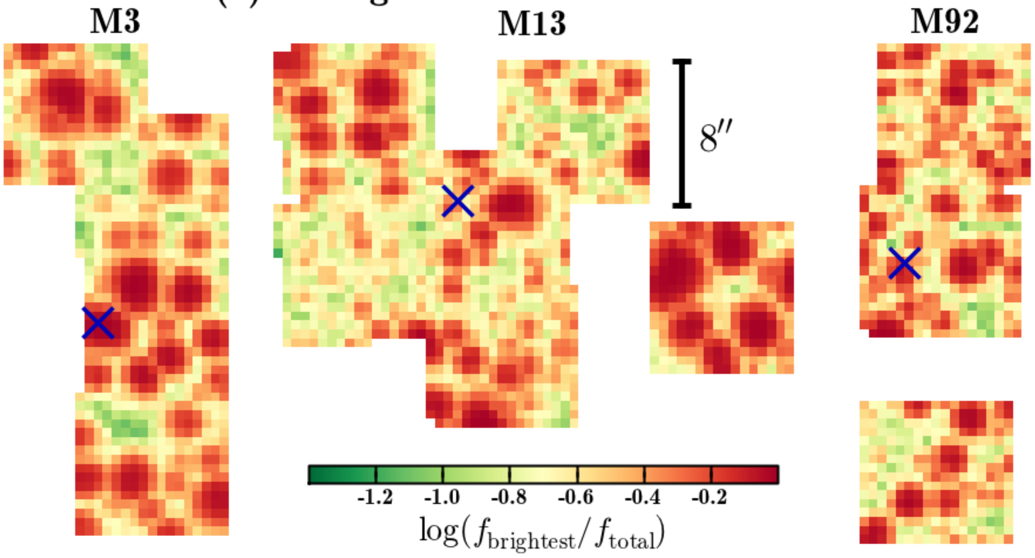

(b) Strength of shot noise from unresolved stars only

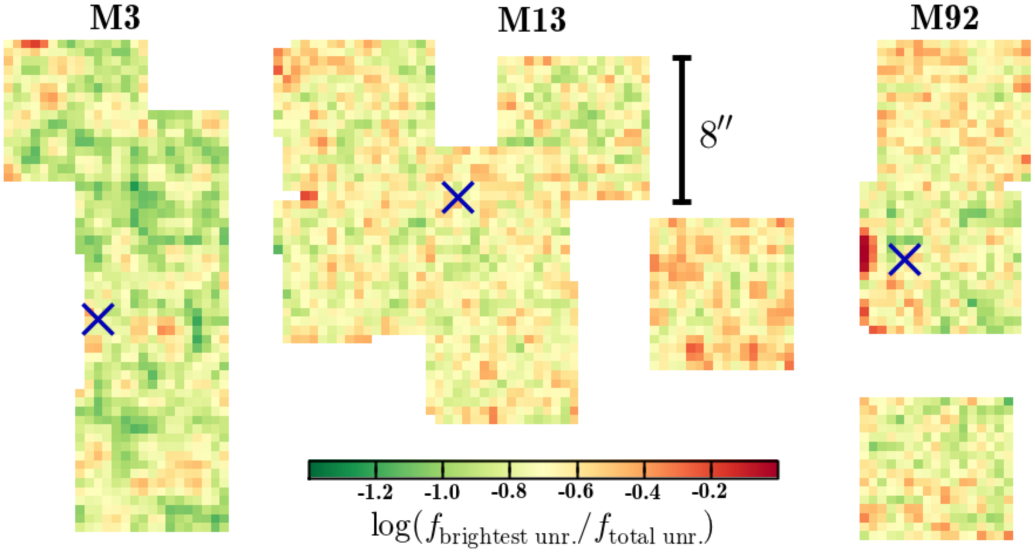

(c) Spaxel histograms

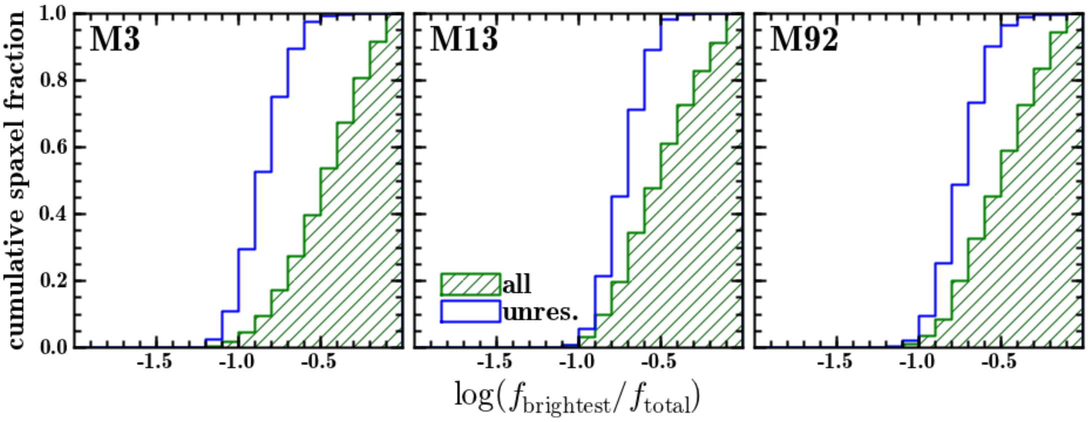

Fig. 5.1. Significance of shot noise in our integral field data. (a) The flux contribution of the brightest star to the integrated flux in each spaxel of the data in the three clusters. (b) The flux contribution of the brightest unresolved star, i.e. the brightest star for which no individual spectrum was deblended, to the overall unresolved flux in a spaxel. (c) The cumulative distributions of the spaxel values depicted in (a) and (b), respectively. In all datasets, north is up and east is left. A blue cross is used to indicate the centre of each cluster.

incompleteness of the photometric catalogue at fainter magnitudes.

It should be mentioned that the above discussions neglect the influence of residuals that remain after the subtraction of the bright stars. Our experience shows that such residuals can have a significant influence in individual spaxels. However, when integrating over several spaxels on the sky, there is a tendency for positive and negative residuals to cancel out. For this reason, we do not expect that the limited accuracy of the subtraction process biases the further analysis.

As mentioned earlier, the analyses of the unresolved light performed in other Galactic globular clusters, e.g. by Noyola et al. (2010) or Lützgendorf et al. (2011, 2012), are not based on PSF-fitting and subtraction of the resolved stars. Instead, an estimate of the seeing during the observation is used to identify spaxels that are strongly affected by shot noise that are in turn not used in the further analysis. This approach seems to yield valuable results in the clusters that the authors studied, but it is clearly not applicable to our data. The reason for this might be that the cluster we study are not as dense towards the centre so that the transition from resolved to unresolved stars occurs at fainter magnitudes in the colour magnitude diagram. For example, the clusters in the sample of Lützgendorf et al. (2012) typically have central luminosity densities above $10^{4.5}$ $L_\odot/pc^3$ (Harris 1996), whereas the densities in our targets all lie below that value ($10^{3.57}$ $L_\odot/pc^3$ in M3, $10^{3.55}$ $L_\odot/pc^3$ in M13 and $10^{4.38}$ $L_\odot/pc^3$ in M92).

Thus it is fair to say that the work done so far has limitations that we can improve on. Our approach makes the whole footprint covered by the observations accessible to an analysis of the integrated light and there is no need to to exclude a significant fraction of it. Furthermore, it is applicable to a larger set of clusters. The footprints depicted in Fig. 5.1 show that if all spaxels in the vicinity of bright stars were excluded, barely any spaxels would remain for an analysis. Also, in the unlucky situation where a bright star is located right at the centre of the cluster, like it is the case in M3, the region containing the most crucial information in view of a potential intermediate-mass black hole would be lost. All these limitations can be overcome by our approach.

5.2.2. Subtraction of sky emission lines

In Chapter 3 we discussed the contamination of the lines of the calcium triplet by telluric emission lines. Since PMAS does not have dedicated sky fibres and the strength of the telluric lines is time-dependent, sky subtraction is a challenging task. We implemented a method to subtract at least the telluric OH lines using dedicated, but non-simultaneous, exposures of blank sky. Unfortunately, such exposures are only available for the data of M13 and M92, but not for M3. For this reason, we cannot use the PMAS observations of M3 in the further analysis. Note that the sky subtraction is much more of an issue in the analysis of the unresolved stars than it is in the analysis of the resolved stars. The reason for this is that the resolved stars are accurately cleaned from telluric emission when they are deblended. We tried to decompose stellar and telluric emission also in the unresolved component of M3, using the recovered PSF together with the magnitudes and positions of the unresolved stars. This approach is presented in Appendix E. While it did yield promising results, the S/N in the final spectra was still too low for any analysis.

For M13 and M92, we have useful sky exposures that allow us to accurately subtract the telluric OH lines. A further complication is that the reddest of the calcium triplet lines is embedded in a complex of O_2 emission (see Chapter 3). Since the intensity of this feature varies independently from that of the OH lines, it is not possible to accurately subtract it together with the OH lines. We therefore concentrate in our analysis on the remaining two lines of the calcium triplet.

5.2.3. Combining the spectra in radial bins

To obtain spectra at a sufficient S/N in M13 and M92, we did the following. Using the results from the deblending process, i.e. the spectra of the resolved stars, the wavelength dependent PSF and the wavelength dependent source coordinates, we created datacubes with the resolved sources subtracted. In those, we binned the spaxels radially with respect to their distance towards the cluster centre. Before thy were coadded, we normalized the spectra in all spaxels. This was done using the same procedure to determine the continuum outlined in Chapter 3 for the normalization of the resolved stars. Note that the spectra were divided by the continuum in order to preserve the equivalent width of the absorption lines present in the spectra.

Some spaxels were manually excluded beforehand because their flux was obviously dominated by residuals from the PSF of a subtracted bright star. Only a handful of spectra were excluded in each cluster because of such strong residuals. Furthermore, we excluded the first three columns to the east of each datacube because the analysis performed in Chapter 3 showed that the spectral resolution in those columns is significantly lower than in the remaining spaxels. But even here the spectral resolution is quite variable. To get a handle on this, datacubes with an estimate of the spectral resolution in each pixel of the datacube were created (see Chapter 3 for details). The spaxels in those datacubes were combined in the same way as the science data to obtain the spectral resolution of each binned spectrum.

To get reliable uncertainties for each binned spectrum, we did not rely on the uncertainties that resulted from the data reduction. Obtaining correct uncertainties for integral field data is difficult because the data are rebinned onto a regular grid during the reduction and rebinning involves the transfer of power into the covariances between neighbouring pixels. Additionally, all the post-processing performed on the data, like sky subtraction, subtraction of the bright stars or radial binning, has to be taken into account. We conclude that an estimate of the uncertainty of a binned spectrum that is based on the uncertainties obtained during the data reduction is highly uncertain itself. Fortunately, the binning process itself offers a convenient way to obtain useful uncertainties via bootstrapping. In each bin, we created $N = 200$ realizations using random combinations of the available spaxel. N was roughly matched to the number of spaxels that went into a binned spectrum.

The bin sizes were chosen in order to achieve a S/N that is sufficiently high for a meaningful analysis. The expected velocity dispersion in either cluster is $\lesssim 10$ km/s. To accurately determine a velocity dispersion that small at a spectral resolution of $R \sim 8\,000$ requires a high S/N. However, the average contribution of the unresolved stellar component to the overall flux in the central datacubes is small according to the calculation presented in Sec. 5.2. Additionally, while our deblending procedure efficiently removes the flux contribution of the resolved stars, their noise contribution remains unaffected. For this reason, the S/N of the unresolved component in an individual spaxel is small ($S/N < 10$) and we had to make the bins reasonably large. The spectrum obtained in each bin is shown in Fig. 5.2. The radial extent of the bins as well as the S/N estimates are indicated. The

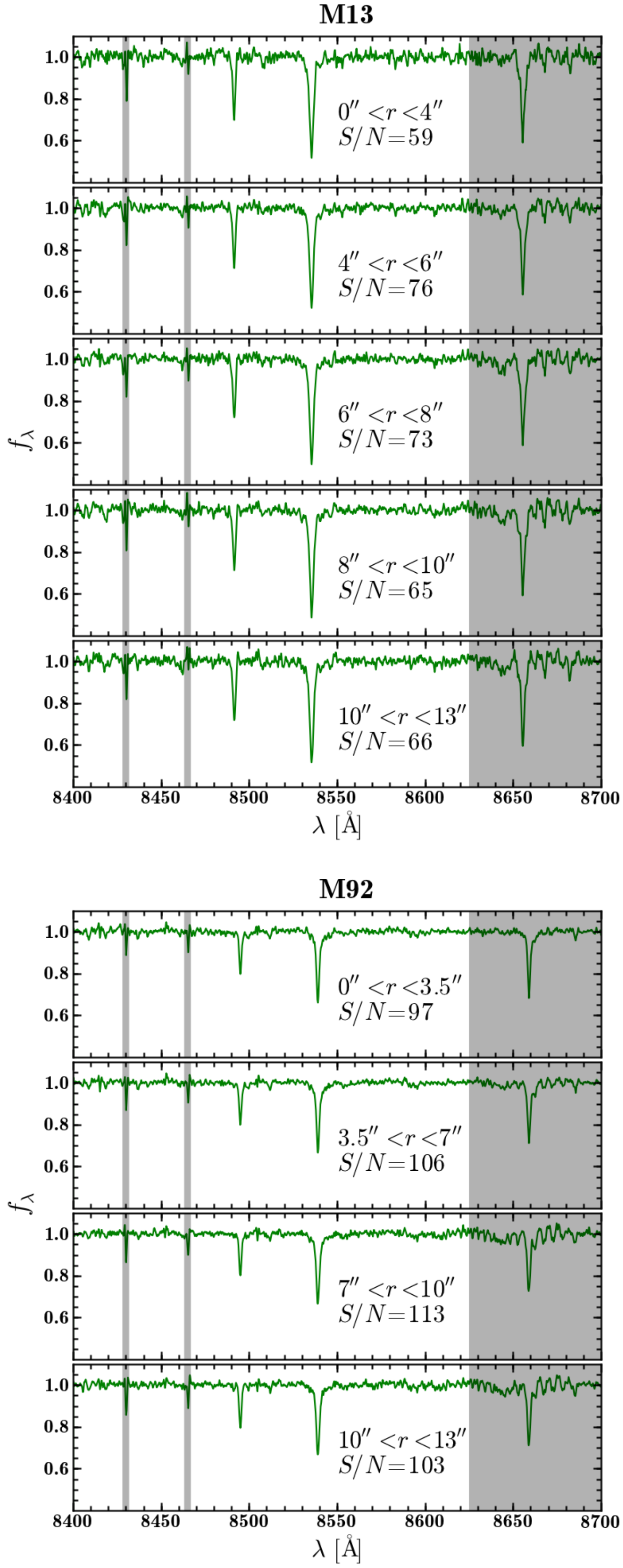

Fig. 5.2. Spectra obtained for the unresolved stellar component in M13 (top) and M92 (bottom). One spectrum is shown for each radial bin. The inner and outer limit of each bin are given below the spectrum together with the estimated S/N. Grey shaded areas indicate spectral windows that are contaminated by strong sky lines.

S/N was estimated with the help of the template spectra that were fitted to the data as explained below.

5.3. Compiling the template spectra

Obtaining a reliable template for further analysis is not trivial. The spectra of the resolved stars can generally not be used because they represent giant stars, while the unresolved starlight is dominated by stars around the main sequence turn-off. In particular, the stars for which the deblended spectra have S/N values sufficiently high to use the spectra as templates are the brightest giants. Thus the spectral mismatch compared to the spectra of the unresolved stellar component is largest for these stars.

No dedicated template stars were observed. The reason for this is simply that it would have been a significant observational effort to do so. Stars at the required position in the colour magnitude diagram can be observed at seeing limited resolution in the less dense outskirts of the clusters. Their apparent brightness in the desired spectral range is $I \sim 17.0$, and obtaining a spectrum with a sufficient $\mathrm{S/N} > 100$ for such stars at the requested spectral resolution and with a 3.5m telescope takes long exposure times. It deserves to be mentioned that an analysis of the unresolved stellar component was not the primary aim of the observations which were instead optimized for an analysis of the resolved stars.

For these reasons, we rely on synthetic template spectra. The set of template spectra was compiled following the procedure outlined in Chapter 2. Starting from the V- and I-band photometry obtained in the ACS survey of Galactic globular clusters (Sarajedini et al. 2007; Anderson et al. 2008), we matched a single isochrone to the observed colour magnitude diagram using the tool of Marigo et al. (2008). The physical information ([Fe/H], $\log g$, $T_{\mathrm{eff.}}$) provided in the isochrone was then used to obtain a set of templates from the library of Munari et al. (2005). This yielded a set of 34 templates for both objects, M13 and M92. The synthetic spectra have an initial spectral resolution of $R = 20\,000$. For our purposes, we degraded it to $R = 10\,000$ and rebinned the spectra logarithmically. We show a comparison between the templates and our data in M13 in Fig. 5.3.

5.4. Analysis of the spectra

5.4.1. Outline of fitting procedure

We analysed the spectra using the pPXF code (Cappellari & Emsellem 2004). It works by fitting the science spectra using either a single template spectrum or a linear combination of several template spectra in pixel space. For this reason, the spectra and template(s) have to be provided with a fixed sampling in velocity space, i.e. logarithmically sampled in wavelength space. pPXF provides a possibility to fit the continuum before performing the fit. As we relied on the accuracy of our normalization, we only allowed for a constant function of wavelength to be subtracted from the data. An advantage of pPXF is that the complexity of the LOSVD that is used in the fit can be adapted to the quality of the available data. This is done by modelling the LOSVD with a Gauss-Hermite expansion (van der Marel & Franx 1993) and penalizing the values of its higher order moments. However, as the expected velocity dispersion in either cluster is small ($\lesssim$10 km/s) compared to the spectral resolution of our data, we restrict our analysis to a Gaussian LOSVD. A reliable measurement of higher moments likely requires a higher spectral resolution than in our case where the line width is dom-

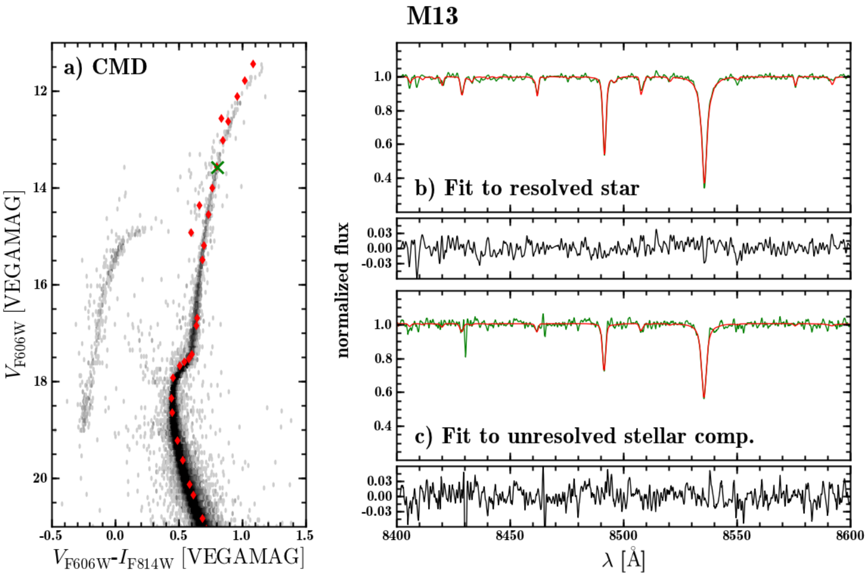

Fig. 5.3. Analysis of the data in M13 using synthetic template spectra. (a) The color-magnitude diagram of M13 is shown using the data from the ACS survey of Galactic globular clusters (Sarajedini et al. 2007; Anderson et al. 2008). The positions of the individual template spectra are indicated using red diamonds. A green cross marks the position of the star whose spectrum is shown in panel (b) together with a template and the fit residuals. In panel (c), we show a template fit to the spectrum of the unresolved stellar component in the central bin of our M13 data.

inated by the line-spread function (LSF) and the LOSVD only constitutes a minor contribution.

5.4.2. Verification of the results via calibration data

To judge the reliability of the kinematic information that we extract, we generated dedicated calibration spectra. The large sets of resolved stars that were deblended as described in Chapter 3 were used for this purpose. We selected all spectra that were deblended with a S/N $\gtrsim 30$ and convolved them with a Gaussian LOSVD. The width of the LOSVD was matched to the velocity dispersion we expect for each cluster ($5 - 15$km/s). In total ~ 30 input spectra were used in each cluster, M13 and M92. These spectra were then subjected to the same analysis with pPXF as the binned spectra of the unresolved component.

There are two potential caveats in using synthetic spectra that we want to check for with our calibration data. (i) The templates are based on a modelling of the stellar atmospheres. Differences in the shape or depths of the spectral lines between the modelled and the observed spectra might be compensated for with the LOSVD during the pPXF analysis. (ii) The templates will have a different LSF than the science spectra. As the final line width is the convolution of the LOSVD with the LSF, this difference might lead to a systematic mismatch of the fitted LOSVD. Note that because the PMAS LSF varies significantly from fibre to fibre, this would be an issue also for observed templates.

5.4.3. The best matching templates

Before moving to the kinematic analysis, we discuss the results in view of the template spectra that provided the best fit to our calibration data and the spectra of the unresolved stellar components in the different radial bins. This is a useful exercise as it allows us to verify whether the spectra we obtained for the unresolved stellar component are indeed dominated by the light from the numerous faint stars. In that case, the template fit should also give the largest weights to templates representing faint stars. On the other hand, if the residuals from the brightest giant stars dominate the spectra, then templates from this region of the colour magnitude diagram should have a strong contribution.

In Fig. 5.3 it is already visible that in M13 the spectrum of the unresolved stellar component is quite different from that of the bright giant that we use as a calibration star. In particular, the equivalent width of the strong calcium triplet lines is much smaller for the unresolved stellar component. It is well known that for red giants of the same metallicity, the equivalent width of the calcium triplet increases with the brightness of the star relative to the horizontal branch (Armandroff & Da Costa 1991). The smaller equivalent width might therefore indicate that the stars that contribute to the spectrum of the unresolved light are fainter than the resolved giants. However, the correlation between brightness and equivalent width is not valid for main sequence stars. In fact, during the fit to the spectrum of the unresolved light, the largest weight is given to templates that represent upper main sequence stars. This result is reassuring because we expect that the transition between resolved and unresolved stars in our data occurs near the MSTO. On the other hand, the fit to the resolved stars is dominated by the contribution from templates of bright giant stars as expected. For this reason, we are confident that the residuals of the bright resolved stars do not contaminate the spectrum of the unresolved stellar component significantly. Similar results are obtained for our data of M92.

Comparing the data and the fitted templates in Fig. 5.3, we do not identify any strong signs of a template mismatch. Thus the set of templates that we selected should give a valid representation of the observed spectra.

5.5. Kinematic results

To obtain the intrinsic LOSVD of a spectrum, we need to account for the difference in the spectral resolution between template and spectrum. This was done using the dedicated spectral resolution data that we prepared for each spectrum. For simplicity, we assumed that each spectrum has a constant spectral resolution. This is not strictly true, but in the small wavelength range that we consider, the variation is only of the order of $1 - 2\%$, so this simplification should have no measurable effect on the results.

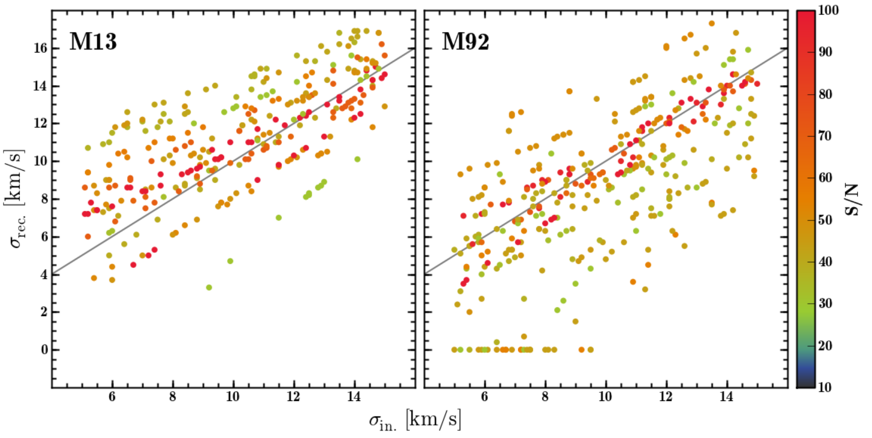

Fig. 5.4. Comparison between the input velocity dispersion and the recovered one for the calibration spectra. The calibration data was created by convolving spectra of resolved stars in M13 (*left*) and M92 (*right*) with Gaussian line-of-sight velocity distributions of varying width and analysed using pPXF. The individual data points are colour-coded with respect to the signal-to-noise of the spectra. Solid lines indicate a one-to-one relation between input and recovered values.

Table 5.1. Results of the kinematical analysis

Cluster	$r_{\rm min}$ arcsec	$r_{\rm max}$ arcsec	$\sigma_{\rm ppxf}$ km/s
M13	0.5	4.0	$12.3^{+2.1}_{-2.6}$
	4.0	6.0	$14.6^{+1.0}_{-1.3}$
	6.0	8.0	$14.7^{+1.0}_{-1.1}$
	8.0	10.0	$15.2^{+0.9}_{-1.1}$
	10.0	13.0	$14.3^{+1.4}_{-1.5}$
M92	0.5	3.5	$7.2^{+0.9}_{-1.8}$
	3.5	7.0	$8.4^{+1.2}_{-1.4}$
	7.0	10.0	$9.7^{+1.6}_{-2.2}$
	10.0	13.0	$8.0^{+1.9}_{-2.5}$

5.5.1. Calibration data

First, we investigate the reliability of the measured velocity dispersions using our calibration data. To this aim, we compare the measured velocity dispersion to the one we initially used in the preparation of the spectra. In the absence of systematic errors introduced by the templates the offset between the measured velocity dispersion and the one used to prepare the spectra should scatter around zero. The comparison between the measured velocity dispersion and the initial one is shown in Fig. 5.4 for both clusters.

The right panel of Fig. 5.4 suggests that the analysis of M92 is largely unbiased. The recovered velocity dispersion scatter around the input values. As expected, the scatter of the individual data points decreases with the S/N of the spectra. In M13, the situation is a bit more complex as for velocity dispersions $\lesssim$ 10 km/s, the velocity dispersions are recovered systematically too high. Although this trend disappears at higher velocity dispersions, we cannot exclude slight systematic effects to be present in the analysis of the M13 data.

In both clusters, we observe that above a S/N of ~ 60, the recovered velocity dispersions closely follow the initial ones (when neglecting the systematic offset in M13). This result may serve as an a posteriori justification of the bin sizes we selected for the unresolved light as the S/N in those spectra is at least ~60 (cf. Fig. 5.2). For M92 we selected the bin sizes a bit more conservative as the low metallicity of the cluster implies weaker spectral lines.

5.5.2. The unresolved stellar component

The results of the kinematic fit for the individual bins are summarized in Table 5.1. The provided uncertainties were obtained from the analysis of the bootstrapping realizations we created in every bin.

We compare our measurements to those we obtained using the resolved stars in Chapter 4 in Fig. 5.5. For M92, our new results yield a remarkable agreement with the velocity dispersion based on the velocities of the resolved stars. Larger discrepancies are observed for the M13 data, however. Compared to the velocity dispersions calculated from the resolved stars, the results obtained from the unresolved stellar component seem to be systematically higher. This behaviour seems to be at odds with the results from the calibration data. Although there is tendency that the recovered velocity dispersions are overestimated (cf. Fig. 5.4), this trend is too weak to explain the high values obtained in the analysis of the unresolved light spectra. An explanation could be that the weak overestimation of the velocity dispersion observed for the giant stars becomes more severe when moving down towards the main sequence. Unfortunately, we do not have the data to test this hypothesis. Therefore, we consider the new estimates of the velocity dispersion obtained for M13 doubtful. However, we are confident that our new measurements in M92 are reliable. This view is also supported by the fact that an analysis of the spectra of M92 with an independent software package for kinematical analyses developed by Rix & White (1992) and Walcher et al. (2009), kindly provided by J. Walcher, yielded statistically indistinguishable results. This was not the case for M13, where the measured velocity dispersions were systematically lower.

5.6. New constraints on the presence of intermediate-mass black holes

In Chapter 4, we constrained the masses of possible IMBHs using only the kinematic information extracted from the spectra of the resolved stars in the cluster. In summary, the results for both clusters, M13 and M92, were consistent with no black hole. The upper mass limit found for M92 was by a factor ~10 more stringent than the one found for M13. In M13, the 1σ limit was 8 900 $M_{\odot}$ and the 3σ limit was 13 000 $M_{\odot}$, whereas in M92, limits of 700 $M_{\odot}$ (1σ) or 2 000 $M_{\odot}$ (3σ) were derived. We now want to check whether the information that we extracted from the unresolved stellar component can provide additional insights. In view of the doubtful results we obtained for M13 (cf. Fig. 5.5), we restrict the following discussion to M92.

As mentioned before, the comparison of the velocity dispersion obtained for the resolved and the unresolved stars in M92 reveals a good agreement. Therefore, the conclusion from

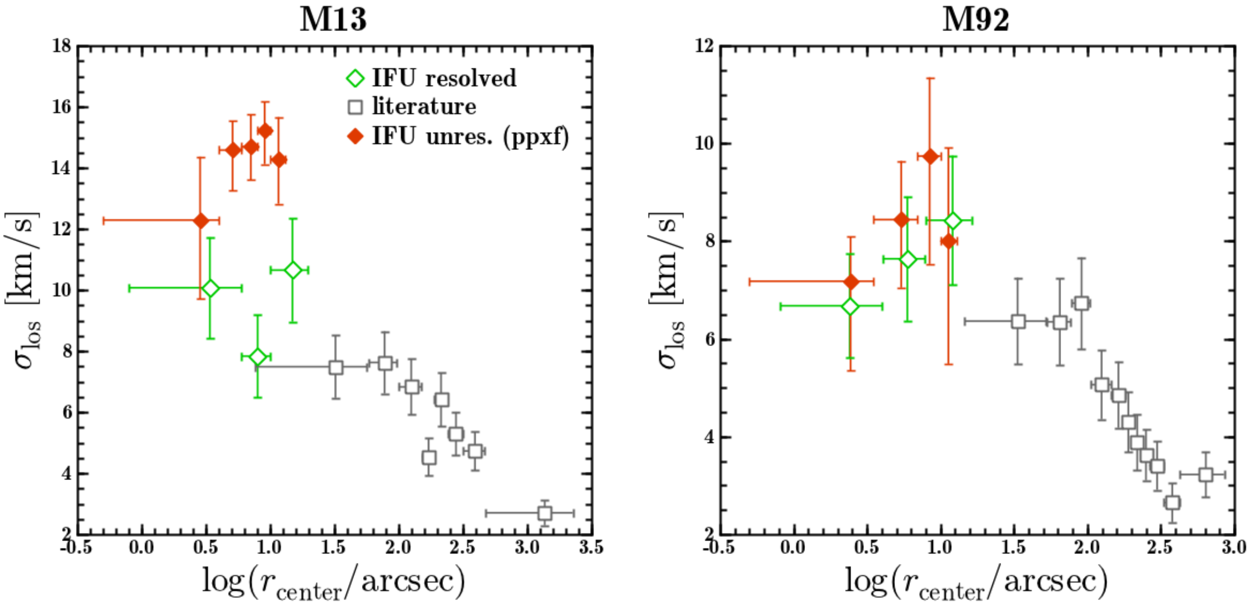

Fig. 5.5. Comparison between the velocity dispersion determined using the unresolved stellar component and the one measured from the resolved stars, in M13 (*left*) and M92 (*right*). Filled diamonds show the results obtained for the unresolved stars using pPXF. Open symbols represent results based on resolved stars, with grey squares corresponding to literature data and green diamonds corresponding to our IFU measurements. Note that these IFU measurements are based on the same datacubes that we use for the measurement of the unresolved light.

Chapter 4 that no black hole is required to explain the observed kinematics is still valid. However, the additional data might help to lower the upper mass limit. Although both measurements are based on the same datasets, they are in fact independent from one another because different stars contribute to them.

We used the same Jeans modelling approach as in Chapter 4 and determined the agreement between the predicted velocity dispersion and the available kinematical data. Compared to the previous analysis, we have to slightly modify our approach to estimate the agreement between our data and a given model curve. As the velocity dispersion measurements obtained from the unresolved component are binned by default, the maximum likelihood approach we used with the resolved stars is not applicable. Instead, we directly used the velocity dispersion in the radial bins presented in Fig. 5.5 and perform a χ^2 minimization. The results of this minimization are shown in Fig. 5.6.

A model with a mass-to-light ratio of $\Upsilon = 1.45$ and no black hole provides the best representation of the available data. As in our previous analysis, we determined confidence intervals for either parameter by marginalizing over the other. This yields an upper limit on the mass of an IMBH of 500 $M_\odot$ (1σ) or 1 300 $M_\odot$ (3σ) and a mass-to-light ratio of $\Upsilon = 1.40^{+0.15}_{-0.10}$. In Fig. 5.7, we compare the predictions of the models with a constant mass-to-light ratio of 1.40 and varying black hole masses, ranging from no black hole to 5 000 $M_\odot$.

The new data allows us to lower our upper mass limit on any IMBH in M92 by ~ 30%. The reason for this is obvious. As can be seen from Fig. 5.7, the measurements from the unresolved light roughly double our kinemtic constraints inside the sphere of influence of a putative IMBH.

The data also seems to confirm that even the models without a black hole overestimate the measured velocity dispersion at the smallest radii. As mentioned in Chapter 4, one possibility to explain this would be tangential anisotropy. In principle, one possibility to test this hypothesis would be to examine the line profiles in the spectra of the unresolved stellar component. Anisotropy could be inferred using the higher order moments of the LOSVD. However, with the currently available data, such measurements are probably not possible at sufficient significance. The tendency for overestimation at the smallest radii can also can explain why the mass-to-light ratio that we obtain ($\Upsilon = 1.40$) is slightly lower than the one we measured using only the resolved stars, $\Upsilon = 1.55$. Our new data put more weight on the inner kinematics.

5.7. Conclusions

In this Chapter, we investigated the feasibility of analysing an unresolved population of stars that is hidden underneath a dominant resolved population. Integral field spectroscopy is an outstanding observing technique in this respect for two reasons. (i) In contrast to traditional spectroscopy, the possibility to apply PSF-fitting techniques to subtract the resolved stars can provide an unbiased view of the unresolved stars. (ii) As opposed to imaging studies, the unresolved light contains a wealth of information. Its spectrum can be used to determine velocity distributions, abundances or star formation histories that can be compared to the information extracted from the resolved stars.

Using PMAS data of the three Galactic globular clusters M3, M13 and M92, we made an effort to determine the line-of-sight velocity distribution of the unresolved stellar component after subtracting the resolved stars. In our observations of all three targets, the bulk part of the spatial pixels is dominated by the light contribution of the resolved stars and the unresolved component is uncovered only after they have been subtracted.

To obtain spectra with a sufficiently high S/N in the final spectra, the data were binned in annuli around the assumed cluster centre. We analysed the spectra using a set of synthetic tem-

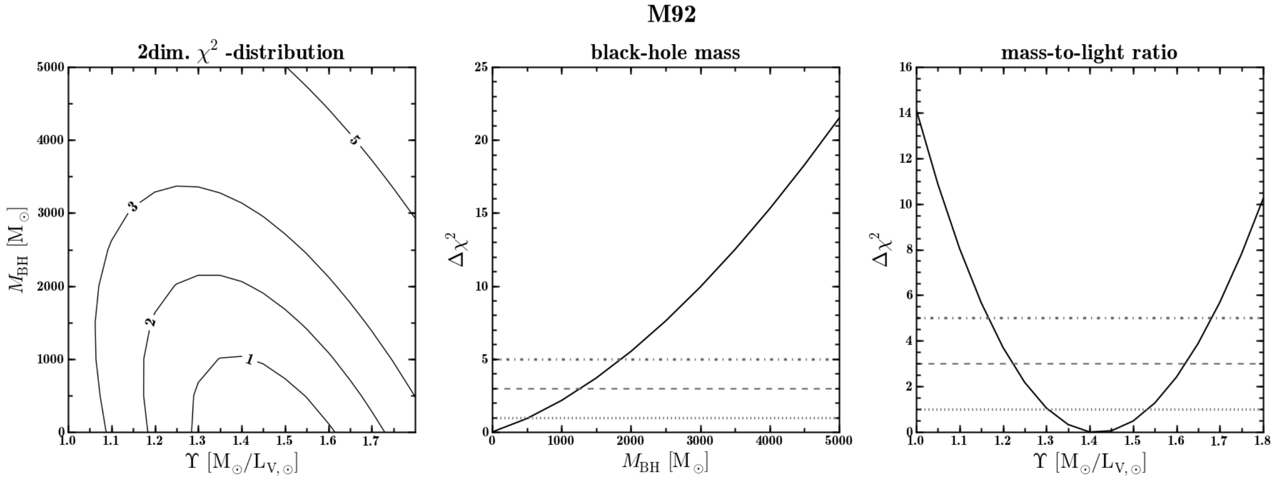

Fig. 5.6. Comparison between the extended data set in M92 and Jeans models with different black hole masses and mass-to-light ratios. The left panel shows the two-dimensional distribution of χ^2 values as a function of black hole mass and mass-to-light ratio. Solid lines give the confidence intervals in units of σ. In the central and right panels, the one-dimensional χ^2 distributions as a function of black hole mass and mass-to-light ratio are shown, obtained by marginalising the two-dimensional distribution over the other parameter. Horizontal lines denote the 1 (dotted), 3 (dashed) and 5σ (dash-dotted) confidence intervals. The data used in this comparison is the binned velocity dispersion of the resolved stars and the kinematic information extracted from the pPXF analysis.

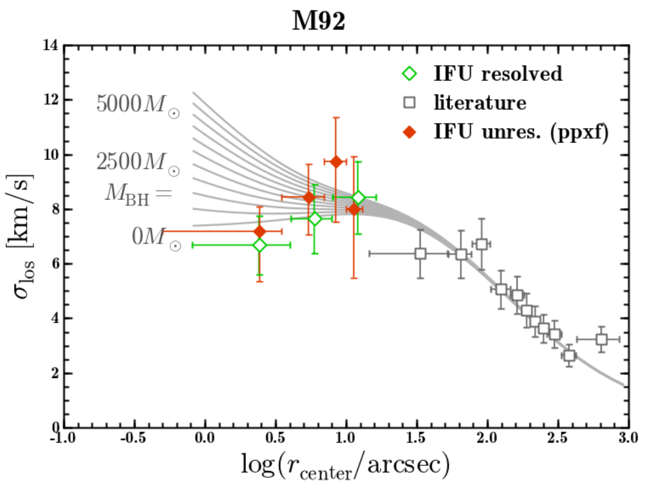

Fig. 5.7. Comparison between the velocity dispersion measured from the data in M92 and the predictions by Jeans models with different black hole masses and a constant mass-to-light ratio of $\Upsilon = 1.45$. The model curves show the prediction with black hole masses ranging from 0 M$_\odot$ to 5 000M$_\odot$ in steps of 500 M$_\odot$. The symbols used to display the data are the same as in Fig. 5.5.

plates and found that indeed the major contribution comes from stars around or below the main sequence turn-off. Any contribution from the residuals of the bright stars is small and thus our analysis is robust against shot noise.

We carefully checked whether our data allow for a reliable measurement of the velocity dispersion of the unresolved stellar component. Calibration data were prepared by convolving the spectra of resolved stars that were deblended with sufficiently high S/N with a Gaussian velocity distribution and processed in the same way as the spectra of the unresolved component.

While the results for M13 remain doubtful, we obtain a reliable velocity dispersion for M92. The fact that it is in perfect agreement with our analysis of the resolved stars is remarkable. The two measurements are statistically independent in the sense that the kinematics of different stars inside the cluster are probed. Therefore, we can combine them to constrain the mass of a potential IMBH in the cluster. By comparing the full set of kinematical information to dedicated Jeans models, we confirm our previous finding that no massive black hole is needed to explain the observed kinematics. Our analysis limits the mass of such a black hole to $< 500\,{\rm M}_\odot$ (1σ) or $1\,300\,{\rm M}_\odot$ (3σ). To our knowledge, this limit is the most stringent obtained for any massive globular cluster so far.

This analysis shows the prospects of the deblending algorithm that we developed, although the measurements are at the edge of what is possible with the data we have at hand. In particular, the following limitations apply to our data.

1. The resolved stars dominate the overall light in the clusters and even though their light contribution can be removed via PSF fitting, their noise contribution remains. Thus long exposure times are required to study the unresolved light. PMAS was designed to provide a high throughput at short optical wavelengths whereas our observations are carried out in the near infrared where the efficiency is somewhat lower. It is also attached to a medium-sized telescope only, so that with the limited observing time we had available, we had to make a compromise between covering a sufficiently large area around the cluster centres and exposing long enough on a single field.
2. PMAS does not offer the possibility to observe the sky simultaneously to the science fields. For this reason, we had to rely on non-simultaneous sky exposures that only allow us to remove part of the telluric emission features. In particular, this limitation prevents us from an analysis of the M3 data because no useful sky exposures are available, whereas in the other two clusters, we can only use two of the calcium triplet lines in the analysis.
3. In view of the small velocity dispersion in either cluster, the spectral resolution of our observations is barely high enough for a useful analysis. Additionally, the fact that the spectral

resolution varies significantly from one fibre to the other further complicates the analysis.

Future observations that diminish these limitations will be very promising, not only for kinematical studies but also for investigations targeted on chemical analyses. A good instrument for such studies might be ARGUS (Pasquini et al. 2002) as it provides a higher spatial resolution than PMAS does, has dedicated sky fibres and is attached to an 8m-class telescope.

Acknowledgements. The authors are grateful to J. Walcher for many helpful discussions.
S. K. acknowledges support from the ERASMUS-F project through funding from PT-DESY, grant no. 05A09BAA.
Based on observations collected at the Centro Astronómico Hispano Alemán (CAHA) at Calar Alto, operated jointly by the Max-Planck Institut für Astronomie and the Instituto de Astrofísica de Andalucía (CSIC).

References

Anderson, J., Sarajedini, A., Bedin, L. R., et al. 2008, AJ, 135, 2055
Anderson, J. & van der Marel, R. P. 2010, ApJ, 710, 1032
Armandroff, T. E. & Da Costa, G. S. 1991, AJ, 101, 1329
Cappellari, M. & Emsellem, E. 2004, PASP, 116, 138
Christensen, L., Jahnke, K., Wisotzki, L., & Sánchez, S. F. 2006, A&A, 459, 717
Croom, S. M., Schade, D., Boyle, B. J., et al. 2004, ApJ, 606, 126
Fabrika, S., Sholukhova, O., Becker, T., et al. 2005, A&A, 437, 217
Harris, W. E. 1996, AJ, 112, 1487
Husemann, B., Wisotzki, L., Sánchez, S. F., & Jahnke, K. 2013, A&A, 549, A43
Kamann, S., Wisotzki, L., & Roth, M. M. 2013, A&A, 549, A71
Kuhlbrodt, B., Örndahl, E., Wisotzki, L., & Jahnke, K. 2005, A&A, 439, 497
Lützgendorf, N., Kissler-Patig, M., Gebhardt, K., et al. 2012, ArXiv e-prints
Lützgendorf, N., Kissler-Patig, M., Noyola, E., et al. 2011, A&A, 533, A36
Marigo, P., Girardi, L., Bressan, A., et al. 2008, A&A, 482, 883
Munari, U., Sordo, R., Castelli, F., & Zwitter, T. 2005, A&A, 442, 1127
Noyola, E., Gebhardt, K., Kissler-Patig, M., et al. 2010, ApJ, 719, L60
Pasquini, L., Avila, G., Blecha, A., et al. 2002, The Messenger, 110, 1
Rix, H.-W. & White, S. D. M. 1992, MNRAS, 254, 389
Roth, M. M., Becker, T., Kelz, A., & Schmoll, J. 2004, ApJ, 603, 531
Roth, M. M., Kelz, A., Fechner, T., et al. 2005, PASP, 117, 620
Sarajedini, A., Bedin, L. R., Chaboyer, B., et al. 2007, AJ, 133, 1658
van der Marel, R. P. & Franx, M. 1993, ApJ, 407, 525
Walcher, C. J., Coelho, P., Gallazzi, A., & Charlot, S. 2009, MNRAS, 398, L44
Wisotzki, L., Becker, T., Christensen, L., et al. 2003, A&A, 408, 455

Chapter 6

Chemical analyses using crowded field 3D spectroscopy[⋆]

Sebastian Kamann[1] and Tim-Oliver Husser[2]

[1] Leibniz-Institut für Astrophysik Potsdam (AIP), An der Sternwarte 16, 14482 Potsdam, Germany
[2] Institut für Astrophysik, Universität Göttingen, Friedrich-Hund-Platz 1, 37077 Göttingen, Germany

ABSTRACT

Spectroscopy is a very versatile observing technique and the information that can be extracted from stellar spectra is not limited to radial velocities. Stellar parameters, metallicities or element abundances shed light on the environment in which a star was formed. Therefore, they are indispensable tracers for the formation and evolution of stellar populations such as star clusters or galaxies. Since these populations often appear as crowded stellar fields, we believe that our algorithm to deblend stellar spectra has a huge potential in this respect. To explore this potential, we analyse simulated and observed spectra using a new tool for stellar synthesis. The simulated data represent realistic MUSE observations and we show that despite its low resolution, MUSE will allow us to derive accurate parameters, like effective temperatures or α-element abundances for $\gtrsim 1\,000$ stars in a single observation. The application of stellar synthesis to PMAS spectra of the globular cluster M13 demonstrates its feasibility to work with observed data.

6.1. Introduction

While integral field units (IFUs) are routinely used nowadays in population studies of unresolved stellar populations (e.g. Sánchez et al. 2012), multi-object spectroscopy is still the preferred technique to study their resolved counterparts (e.g. Carretta et al. 2009). Its advantages are obvious: the high multiplex capabilities of multi-object spectrographs in combination with their wide fields of view allow one to collect large sets of high signal-to-noise (S/N) spectra in reasonable amounts of telescope time. However, this "cherry picking" approach to study a stellar population becomes more challenging as crowding increases. As we demonstrated in the previous Chapters, integral field spectroscopy (IFS) in combination with a sophisticated deblending approach offers a convenient way to overcome this issue for kinematical studies. Yet to take full advantage of the power of spectroscopy, one should combine dynamical with chemical analyses. The latter usually require a higher spectral resolution and a higher S/N than the former do. Most IFUs provide a low to medium spectral resolution and spectra are unavoidably deblended over a large range in S/N, so the question is whether IFS proves to be a powerful tool also for the chemical investigation of crowded stellar fields.

A high spectral resolution is not always needed to gain insight into the chemical composition of a stellar population. Armandroff & Da Costa (1991) advocated the equivalent width of the calcium triplet lines as a powerful tracer of metallicity that can be accurately measured already at moderate spectral resolution. For this reason, it is also less demanding in terms of observing time and can be used even with rather faint stars. Not least of because of that, medium resolution spectroscopy has proven to be an indispensable tool in the study of dwarf galaxies (see Tolstoy et al. 2009 for a review). Furthermore, the work done by Kirby et al. (2008) showed that one can go beyond metallicities even at modest resolution and also infer, e.g., α-element abundances by using spectral synthesis. In his PhD thesis, Husser (2012) recently presented a new method to perform spectral synthesis. It implements an approach to fit all parameters simultaneously that was initially developed by Koleva et al. (2009). In this small Chapter, we apply this method to spectra deblended from IFU data. We use both, simulated and observed data for this analysis. Sect. 6.2 is dedicated to the analysis of simulated MUSE data, and in Sect. 6.3 we briefly discuss the analysis of our observed PMAS data.

6.2. Analysis of simulated MUSE data

The Multi-Unit Spectroscopic Explorer MUSE (Bacon et al. 2010) was described already in Chapter 2. After its commissioning at the ESO VLT, currently foreseen by the end of 2013, it will provide a unique combination of a large field of view ($1' \times 1'$) and a high spatial sampling ($0\farcs2$). MUSE covers a large spectral range (4650 − 9300Å), yet its spectral resolution of $R \sim 2\,000$ in the blue part and $R \sim 4\,000$ in the red part is rather low. To verify what MUSE can provide with respect to element abundances and stellar parameters, we performed dedicated simulations.

6.2.1. The simulated datacube

The preparation of the datacube was carried out as described in Chapter 2. Starting from the photometry of 47Tuc in V_{606} and I_{814} obtained in the ACS survey of Galactic globular clusters (Sarajedini et al. 2007; Anderson et al. 2008), we assigned each star in the central arcminute of the cluster a synthetic spectrum based on the PHOENIX library (Hauschildt & Baron 1999;

[⋆] This brief Chapter contains a summary of the topic and is currently not intended for separate publication. More details can be found in the PhD thesis by T.-O. Husser (2012), University of Göttingen.

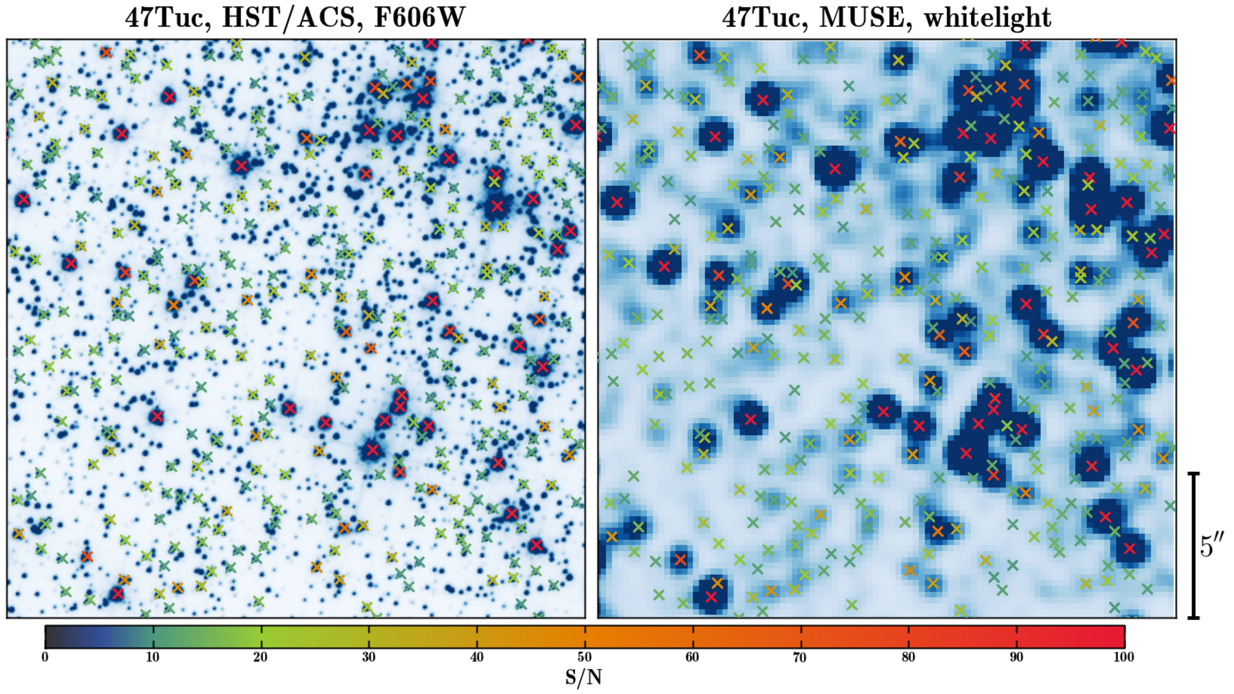

Fig. 6.1. 20″ × 20″ cut-out from the simulated MUSE datacube of 47Tuc. The left panels shows the region as it appears in an HST observation, the right panel shows the datacube assuming a seeing of 0.″8. The sources for which spectra were deblended with a $S/N > 10$ are marked by crosses. The colour-coding of the crosses is matched to the S/N of the spectra. In both panels, north is up, east is left. The centre of 47Tuc is located 14″ to the north-west of the displayed field-of-view,.

Husser et al. 2013). For the purpose of the following analysis, we used spectra that covered a broad range in metallicity and α-element abundance. Clearly, this is not a realistic scenario for 47Tuc. However, our aim in doing these simulations is to test how well stellar parameters can be recovered from MUSE spectra that have been deblended from a crowded field datacube and this is best done by covering a large parameter space.

The final datacube was again created using the QSIM tool (R. Bacon, priv. comm.) that takes the object spectra and the source coordinates as input. It convolves the spectra internally with a model of the MUSE line spread function (LSF) and generates a wavelength dependent PSF that is used to place the stars in the datacube. In the last step, a sky model is included and noise is added to the cube.

6.2.2. Analysis

To deblend the stars, the datacube was split into 9 subcubes, each of which had a field of view of 20″ × 20″. The reason for doing this is that across the full MUSE field-of-view, the stellar density varies significantly and the crowding limit changes rather strongly. Note, however, that thanks to the efficient memory usage of the deblending algorithm, the analysis of the full cube is also possible. In the following discussion, we restrict ourselves to the results obtained from the subcube that is shown in Fig. 6.1. In total, ~ 900 spectra were deblended. For clarity, only the ~ 400 sources for which the deblended spectra have a $S/N > 10$ are marked in Fig. 6.1. Spectra with a lower S/N will likely not yield useful results in terms of abundances or stellar parameters.

The spectra of the ~ 200 brightest stars were analysed using the spectral analysis code of Husser (2012). In brief, it works by fitting the deblended spectra on a grid of synthetic ones. The grid covers a multi-dimensional parameter space in stellar parameters and abundances and the best match is found by means of an advanced interpolation scheme. The fitting process itself includes a convolution of the synthetic spectra with the assumed LSF and a line-of-sight velocity distribution. To determine α-element abundances, the fit is restricted to spectral windows where these elements show strong features. This approach is similar to the one developed by Kirby et al. (2008).

6.2.3. Results

We obtained effective temperatures, surface gravities, metallicities and α-element abundances from the fit that we compared to the intrinsic ones of the input spectra. The results of this comparison are summarized in Fig. 6.2. They show that for spectra with a $S/N \gtrsim 40$, an accurate recovery of chemical properties should be possible despite the low spectral resolution of MUSE. Both, metallicities and α-element abundances are recovered to a precision of ~ 0.15dex without any significant systematic trends. Furthermore, the recovery of stellar parameters seems to be feasible with MUSE spectra at high S/N values. The scatter in the recovered effective temperatures amounts to ~ 50K and the standard deviation in the recovered surface gravities is around 0.1dex in $\log g$.

6.3. Analysis of PMAS data of M13

The PMAS data of the globular cluster M13 were obtained only for kinematical purposes. The details of the data reduction and analysis are fully described in Chapters 3 to 5 and not repeated

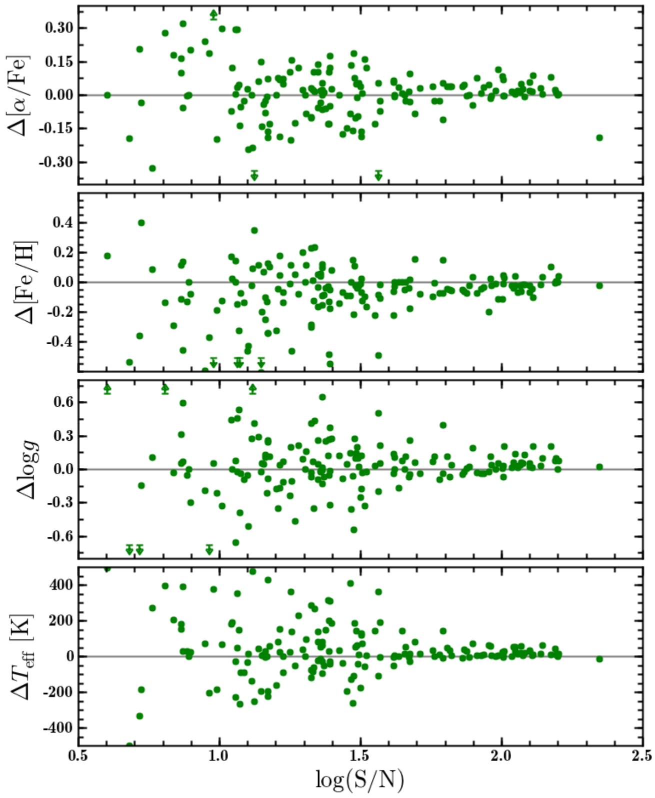

Fig. 6.2. Results from the spectral synthesis of ∼ 200 spectra deblended from the simulated MUSE data. The individual panels show, from top to bottom, the accuracy of the recovered α-abundance, metallicity, surface gravity, and effective temperature as a function of the S/N of the spectra. For clarity, a few outliers that are outside of the plotted range are marked by upper or lower limits, respectively.

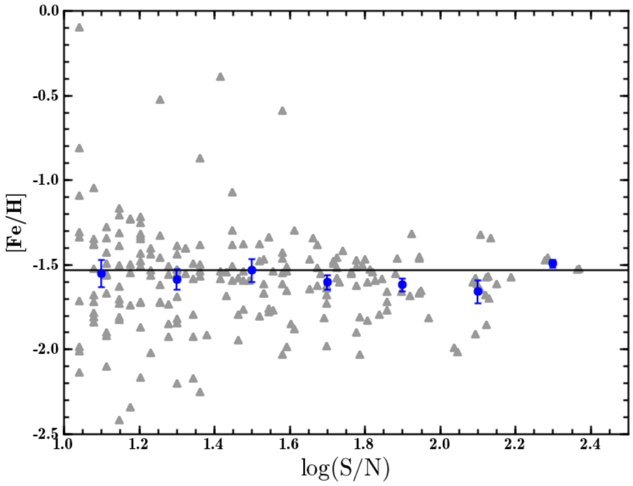

Fig. 6.3. Metallicities obtained from the PMAS spectra in M13. Grey triangles show the [Fe/H] measurements for individual spectra, blue circles represent the mean values after combining the measurements in bins of width 0.2 in log(S/N). The error bars show the 95% confidence intervals of the means in each bin. A horizontal line marks the tabulated metallicity of M13.

here. Although the PMAS IFU (Roth et al. 2005) can work at a higher spectral resolution than MUSE, the covered wavelength range is very limited in the high resolution mode. Our spectra cover the calcium triplet at a resolution of $R \sim 7000$. Therefore, they should be suited for a determination of the metallicity. As M13 is known to show no spread in [Fe/H] at the level that we can probe with our data, all that we can test is whether we are able to recover the global metallicity of $[\mathrm{Fe/H}] = -1.53$ (Harris 1996) of the cluster.

As the spectral range covered by the data is so small, we had to use a prior in the spectral analysis. Using the tool of Marigo et al. (2008), an isochrone was fitted to the available photometry to obtain useful initial guesses for the metallicity and the stellar parameters. In the following parameter fit, the surface gravity was held fixed to its initial guess and only the metallicity and the effective temperature were varied. A similar approach has been used by Kirby et al. (2009) in the analysis of medium resolution spectra of the Sculptor dwarf galaxy. The spectra were fitted using the *cflib* (Valdes et al. 2004) stellar library that contains 1 273 observed spectra, and an interpolation scheme provided by P. Prugniel (Prugniel et al. 2011). Note that another possibility to determine the metallicities would be to measure the equivalent width of the calcium triplet.

We show the [Fe/H] measurements we obtained for the individual spectra in Fig. 6.3 and compare them to the cluster value. We only show results for spectra with a $\mathrm{S/N} > 10$ since no useful measurements were possible below this cut. Overall, the agreement between our measurements and the tabulated value is good. Despite the restricted wavelength range, we are able to reproduce the metallicity of the cluster to an accuracy of 0.1dex. We observe a weak yet significant trend that the metallicities are slightly underestimated. As the underestimation is most significant for the spectra with a high S/N, it likely hints towards weak systematic effects introduced by the analysis. However, it is reassuring that no strong trend is observed with S/N because it adds another piece of evidence that no systematic errors are introduced when the spectra are deblended, even for spectra with a low S/N.

6.4. Conclusions

We demonstrated the feasibility to use MUSE spectra for the determination of stellar metallicities, α-element abundances, surface gravities, and effective temperatures. Despite the low spectral resolution provided by MUSE, we are able to recover such parameters in spectra with a $S/N > 40$. The large spectral range that is covered by the MUSE spectra proves to be a huge advantage in the analysis because many spectral features are included in the spectra.

Clearly, such detailed studies will by possible only for a subset of the deblended spectra. In the example that we discussed above, ∼ 70 out of the ∼ 900 spectra that were deblended in total have a sufficient S/N. However, extrapolating this number to a whole MUSE datacube yields an impressive number of ∼ 600 useful targets in a single observation. The exact number will obviously depend on the crowding of the observed field, the seeing and the exposure time. In the MUSE simulation, we assumed an average seeing of 0.″8 and set the exposure time to 90s in order not to saturate the bright stars. So our estimate on the total number of useful stars is rather conservative. Even more so because the S/N values of many sources can be significantly increased by repeated visits. One idea for an observing strategy might be the following. The observations are split up into several epochs to facilitate a search for stars with variable radial velocities. As the requirements for radial velocities measurements are somewhat lower, the exposure time per visit would be short. Yet the spectra obtained during different epochs can be combined afterwards to yield a S/N high enough for a detailed chemical analysis.

Finally, we note that even though the scientific usability of our PMAS spectra for chemical analyses is limited we can use them to illustrate that the combination of existing IFUs and medium resolution spectroscopy can be a powerful approach for such studies.

References

Anderson, J., Sarajedini, A., Bedin, L. R., et al. 2008, AJ, 135, 2055

Armandroff, T. E. & Da Costa, G. S. 1991, AJ, 101, 1329

Bacon, R., Accardo, M., Adjali, L., et al. 2010, in Society of Photo-Optical Instrumentation Engineers (SPIE) Conference Series, Vol. 7735, Society of Photo-Optical Instrumentation Engineers (SPIE) Conference Series

Carretta, E., Bragaglia, A., Gratton, R. G., et al. 2009, A&A, 505, 117

Harris, W. E. 1996, AJ, 112, 1487

Hauschildt, P. H. & Baron, E. 1999, Journal of Computational and Applied Mathematics, 109, 41

Husser, T. O. 2012, PhD thesis, University of Göttingen

Husser, T. O., Wende-von Berg, S., Dreizler, S., et al. 2013, A&A, submitted

Kirby, E. N., Guhathakurta, P., Bolte, M., Sneden, C., & Geha, M. C. 2009, ApJ, 705, 328

Kirby, E. N., Guhathakurta, P., & Sneden, C. 2008, ApJ, 682, 1217

Koleva, M., Prugniel, P., Bouchard, A., & Wu, Y. 2009, A&A, 501, 1269

Marigo, P., Girardi, L., Bressan, A., et al. 2008, A&A, 482, 883

Prugniel, P., Vauglin, I., & Koleva, M. 2011, A&A, 531, A165

Roth, M. M., Kelz, A., Fechner, T., et al. 2005, PASP, 117, 620

Sánchez, S. F., Kennicutt, R. C., Gil de Paz, A., et al. 2012, A&A, 538, A8

Sarajedini, A., Bedin, L. R., Chaboyer, B., et al. 2007, AJ, 133, 1658

Tolstoy, E., Hill, V., & Tosi, M. 2009, ARA&A, 47, 371

Valdes, F., Gupta, R., Rose, J. A., Singh, H. P., & Bell, D. J. 2004, ApJS, 152, 251

Chapter 7

Conclusions & Outlook

7.1. Results of this work

The work carried out in the course of this thesis explores the possibilities of using integral field spectroscopy (IFS) to study resolved stellar populations. By means of their combined spatial and spectral coverage, integral field spectrographs bridge the gap between high resolution photometry on the one hand side and classical spectroscopy on the other hand side. The former technique has the capability to observe large samples of stars simultaneously, yet the information collected for each individual star is limited. While traditional spectroscopy can provide much more information about individual stars, it lacks the spatial information required to deblend the sources in crowded stellar fields. For this reason, it is limited to the analysis of the few isolated, usually reasonably bright stars in such fields. Although the potential of IFS to overcome this limitation has been recognized for some time, few efforts have been made in this direction. In particular, the transfer of techniques developed for photometric observations of crowded stellar fields that incorporate the point spread function (PSF) in the analysis has been barely studied so far. The small number of spatial pixels as well as the complex structure of IFS data have hampered this development.

7.1.1. A new method to study crowded stellar fields

We performed the first systematic study on the feasibility of using PSF-fitting techniques to deblend stellar spectra in IFS observations of crowded stellar fields. In view of the relatively small number of spatial pixels available in most integral field units (IFUs), measuring a reliable PSF from a datacube is a challenging task. The solution that we found works by assuming an analytical representation of the PSF that is optimized in a simultaneous fit to all resolved stars in the field. It provides a precise estimate of the PSF in almost all situations that we studied. Furthermore, we could show that by combining the data from all monochromatic layers that build up the datacube, we can significantly increase the precision of our PSF model compared to the analysis of a single layer. The same is true for the source positions. To determine the positions of the stars in a datacube, we make use of the fact that most of the crowded stellar fields that are probed spectroscopically have been imaged beforehand at a higher spatial resolution. The usage of this a priori information allows us to probe deeper into the stellar field than would be possible otherwise. Depending on the scientific aims, we can deblend around 0.2 useful stellar spectra per resolution element. Dedicated simulations show that this value remains essentially unchanged over a large range in stellar crowding and that our approach breaks down only if the number of equally bright stars exceeds the number of resolution elements. In this case, already the brightest stars form a pseudo-continuum across the field-of-view and we enter the domain of unresolved stellar populations.

The analysis method that we developed can be divided into three distinct steps that are iterated: an optimization for the PSF, one for the positions of the sources and one for their fluxes. This division has some strong advantages. As the optimization for the source fluxes is a linear least squares fit, it does not require any initial guesses and is computationally not very demanding. The latter advantage allows us to deblend the entity of the resolved sources simultaneously. Via the usage of sparse matrices, we made sure that this statement holds even if several thousand sources are involved in the optimization. The sparse matrices also make sure that the memory usage is limited even for huge data.

In the development of the analysis scheme, we paid special attention to a proper treatment of the background. As opposed to imaging studies, a background component consisting of the unresolved fainter stars can contain valuable information in IFS studies as its spectrum contains kinematic as well as chemical information about the stellar population.

The results of our systematic study will be very useful guidelines for future applications of crowded field spectroscopy. To facilitate such applications, we wrote a software package that performs the data analysis in an automatic manner after an initial setup has been defined by the user. It is called PampelMuse and will be made publicly available soon.

7.1.2. Putting theory into practice: The application to PMAS IFU data

We applied our analysis method to a set of three Galactic globular clusters, M3, M13 and M92, that were observed with the PMAS IFU. The observations targeted the central regions of the clusters where crowding is severe and traditional spectroscopy is essentially blind. Yet we are able to deblend clean stellar spectra for almost all red giant stars covered by the footprint of our observations. The datasets, consisting of $\sim$80 stars per cluster, are among the largest spectroscopic samples obtained so far in the centres of Galactic globular clusters. By combining our data with radial velocity measurements from the literature we are able to collect kinematic information across the whole radial extend of each cluster.

It is reassuring that the predictions about the number of resolvable stars in a datacube that we obtained in our systematic study are confirmed in the analysis of real IFS data. Furthermore, we find no evidence that our method to recover the PSF fails in any of the datacubes. Even if no bright star is available in the field of view, we are able to obtain realistic values for the parameters that govern the shape of the PSF model.

The accuracy of the PSF recovery is also reflected by the fact that we are able to uncover the unresolved stellar component in the clusters, even though it contributes only ~25% of the total light that is dominated by the resolved stars. The characteristics of the PMAS data, like the lack of sky fibres, the limited spectral resolution or the limited signal-to-noise ratio of the background component, constrain our possibilities to analyse the unresolved starlight. After all, PMAS is not attached to an 8m-class telescope and was never designed for this type of study. But the analysis that is feasible with the data already shows the prospects of the deblending scheme that we have developed. To our knowledge, such a combined analysis of the resolved and unresolved light in a crowded stellar field has never been done before.

7.1.3. The search for intermediate-mass black holes in globular clusters

Over the course of this thesis the question whether massive black holes reside in the centres of globular clusters has received quite some attention. Yet no conclusive answer can be given on which globular clusters host intermediate-mass black holes. In the largest sample studied so far, Lützgendorf et al. (2012) recently found evidence for the presence of black holes only in some clusters although the sample that was studied preferentially contained objects that were considered likely host candidates based on their photometric properties. The results of Lützgendorf et al. are based on measurements of the integrated cluster light. This method is applicable to the subset of clusters where the projected stellar density on the sky is high enough so that the integrated light is not dominated by a few bright giants. Our work shows how this approach can be developed further so that it works in arbitrary Galactic clusters, as it makes the resolved and the unresolved stars available for an analysis.

In none of the three clusters that we studied, an intermediate-mass black hole is required to explain our kinematic measurements. Based on isotropic Jeans models, we are able to set upper mass limits on a central black hole that might be present in either cluster. In M13, which was identified as as a likely host cluster by Miocchi (2007), our observations can rule out any black hole that is more massive than $8\,900\,\mathrm{M}_{\odot}$ (1σ). In M3 and M92, however, the limits are remarkably more stringent, yielding $< 1\,000\,\mathrm{M}_{\odot}$. In M92, where a combined analysis of the resolved and unresolved stars is possible despite the limitations of the PMAS data, we obtain an final upper mass limit of $500\,\mathrm{M}_{\odot}$. It is the lowest limit so far obtained for a massive globular cluster. This is quite a remarkable result given that our observations are neither supported by adaptive optics (AO), nor obtained with an 8m-class telescope nor based on multi-cycle *Hubble* space telescope (HST) observations. Thus, our approach is observationally quite "cheap" compared to other approaches to measure stellar velocities in the strongly crowded cluster centres, like HST proper motions (McLaughlin et al. 2006), HST long-slit spectroscopy (van der Marel et al. 2002) or AO-supported Fabry-Perot imaging (Gebhardt et al. 2000).

The rather large discrepancy in the upper limit derived for M13 compared to M3 and M92 is surprising as all three clusters have comparable masses or densities. It might suggest that the internal structure of M13 is different compared to the other two clusters. This is also supported by the higher central velocity dispersion that we measure for this cluster and the higher mass-to-light ratio.

Finally, if we view our results in the context of the relations that exist between the supermassive black holes and the surrounding bulges in galaxies, we find that our upper limits are still consistent with an extrapolation of the relation between black-hole mass and stellar velocity dispersion, yet the clusters M3 and M92 are below the extrapolated relation between black-hole mass and stellar mass.

7.2. Outlook and future prospects

The work that we carried out in the course of this thesis can only be a first step in exploring the full potential of IFS in the observation of crowded stellar fields. Furthermore, there are several ways we can think of to extend our observational campaign to search for intermediate-mass black holes in globular clusters. In the following, we highlight some important next steps in either of the two fields.

7.2.1. Constraining intermediate-mass black holes in globular clusters

We can think of two avenues to make further progress towards answering the question if and which globular clusters contain intermediate-mass black holes.

Gathering more data

Building up on the experience we obtained with our PMAS data, we successfully applied for observing time with the ARGUS IFU at the Very Large Telescope (VLT) to observe two globular clusters on the southern sky, 47Tuc and NGC 362. These observations were designed to overcome the main limitations of our currently available PMAS data as ARGUS offers a higher spectral resolution, has dedicated sky fibres and is attached to an 8m-class telescope. In particular, the analysis of the unresolved stellar component would benefit from these improvements. Additionally, the higher spatial sampling would allow us to better sample the PSF under good seeing conditions and therefore to increase the number of resolvable stars. We also implemented a dedicated multi-epoch observing strategy to systematically identify binary stars. Unfortunately, only about 1/3 of the planned observations were carried out in period 88 (October 2011 to March 2012). We handed in a second proposal for the remaining observations that was granted observing time in the currently ongoing period, so this new data should be available soon.

Another promising idea for future progress is the combination of the radial velocity data with proper motions. The full 3-dimensional velocity information would allow us to directly measure anisotropies and rotational velocity components. It might also be used to constrain the run of mass-to-light ratio with cluster radius as done by van den Bosch et al. (2006).

More sophisticated dynamical models

We compared our measurements to predictions obtained from spherical Jeans models. While those provided a valid framework for the data we have currently available, extended data sets might require more advanced modelling approaches. Axis-symmetric Jeans models or even Schwarzschild models have the advantage that they can be calculated for a larger range of gravitational potentials. In addition, evolutionary approaches such as N-body models or Fokker-Planck calculations can help to get a better handle on the mass-to-light ratio in the cluster.

7.2.2. Spectroscopy is not all about radial velocities – Measurements of stellar parameters

The scientific work carried out in this thesis is mainly focussed on stellar dynamics. Yet kinematic measurements represent one out of many possibilities to extract information from spectroscopic data. Determinations of metallicities, element abundances or star formation histories all rely on spectroscopy. Our deblending approach allows us to perform these measurements for stars that are inaccessible to traditional spectroscopic observations. One might argue that in a globular cluster, one can always find reasonably isolated stars in the outskirts of the cluster. However, because of the preselection of target stars that is required if one wants to perform multi-object spectroscopy, there is always the danger involved of obtaining a biased view of the cluster. As crowded field spectroscopy using IFUs does not require any preselection, it is robust against such biases. In fact, it offers the prospect of obtaining a "spectroscopic colour magnitude diagram" of a cluster, i.e. an inventory of all stars down to a limiting magnitude with a full spectrum included for each star instead of a magnitude and one or a few colours.

A current limitation for such studies in globular clusters might be that because of their large degree of chemical homogeneity, uncovering the subtle star-to-star variations like the anticorrelation between oxygen and sodium (Carretta et al. 2009) seems to require a high spectral resolution. Yet most IFUs have been designed for extragalactic purposes, so that instruments that combine a high spatial sampling with a high spectral resolution are rare. A notable exception in this respect is the ARGUS IFU. It still has a limited field of view though, so that it is a huge observational effort to cover a larger part of a cluster.

7.2.3. From globular clusters to general crowded stellar fields

Globular clusters only represent one object class where one encounters a crowded stellar field. Other examples in our own galaxy are open stellar clusters or the Galactic bulge. The bulge has a much more diverse star formation history and much larger abundance spreads than most globular clusters. The same is true for nearby galaxies that are still partially resolvable into individual stars. As such, these objects offer a larger range of applications for spectroscopy at lower resolution. The work done by, e.g., Tolstoy et al. (2001) or Battaglia et al. (2008) showed that metallicities based on the equivalent width of the calcium triplet can provide valuable insights into the star formation history of a galaxy. Furthermore, medium-resolution spectroscopy in combination with spectral synthesis can by used to measure the abundances of individual α-elements. The prospects of this technique, introduced by Kirby et al. (2008), for crowded field spectroscopy using IFUs are currently being investigated by Tim-Oliver Husser at the University of Göttingen (Husser 2012). The deblending algorithm that we developed allows such measurements for significantly more stars even in strongly crowded fields and obviates any preselection of the target stars.

Crowded field spectroscopy might also help to bridge the gap between galaxy studies based on either individual stars or integrated light. Similar to globular clusters, nearby galaxies are partially resolved, i.e., a transition from resolved to unresolved stars occurs at a given magnitude. The unique possibility to study both of these components using the same observations might help in the calibration of star formation rates, ages or metallicities determined from integrated light spectra. In the limiting case between resolved and unresolved stars, the stellar population will have a grainy structure, similar to the surface brightness fluctuations observed in imaging studies of galaxies. New analysis methods might be developed based on spectroscopic surface brightness fluctuations.

The analysis of crowded stellar fields apart from globular clusters will require some modifications of the deblending algorithm. We previously mentioned that gaseous emission like it is found in star forming regions in local galaxies can be a nuisance in the data analysis. Yet it can at the same time be an interesting science target. For this reason, it is worth to spend some efforts in a convenient handling of such non-stellar emission in the future development of the code.

Furthermore, the development of a dedicated source finding algorithm can be a useful task for the future. It will not only be needed in (rare) cases where no high-resolution images of an observed field are available but will also be helpful to adopt the code to AO-assisted IFUs. The structure of IFS data, with around 1 000 monochromatic images that are observed simultaneously and show a continuous shift of the source coordinates with wavelength should be of great help in reliably detecting the sources.

7.2.4. Future instrumentation – MUSE

Many of the applications that we proposed as possible future endeavours will strongly benefit from upcoming instrumentation. To cover a reasonably large fraction of a globular cluster or even a nearby galaxy requires panoramic IFUs that combine a large field of view with a high spatial sampling. MUSE will be such an instrument. After its commissioning at the VLT by the end of 2013, it will provide a field of view of one square arcminute at a sampling of $0.2''$. As it is also designed to work with AO, it will probably be the most promising IFU for crowded field spectroscopy in the near future. The simulations that we have performed in Chapter 2 showed that it is realistic to deblend several 1 000 stellar spectra from a single MUSE datacube. The instrument will provide a much higher throughput than any other IFU that is currently available on a large telescope. This efficiency opens new and exciting observing possibilities. For example, surveying the bulk part of a globular cluster for radial velocity variations will be an affordable observational effort. Thus, it will become possible to constrain the distribution of binary periods inside the cluster. The sample sizes that can be obtained within a single crowded stellar field will increase from a few hundred stars to 10 000 stars and more. These huge sample sizes will likely also allow one to break new ground in chemical analyses. One idea could be to develop clever combination algorithms that make use of the different radial velocities of the individual stars to combine their spectra into one that has a much higher spatial resolution than what will be provided by MUSE ($R \sim 3\,000$).

In fact, much of the methodical work that was carried out in this work was initially motivated by the development of MUSE. When developing our algorithm, we paid special attention to design it in such a way that in can handle the huge datacubes ($> 3 \times 10^8$ pixels containing $\sim 10\,000$ resolvable stars) that will be delivered by MUSE. We also actively participated in the ongoing development and testing of the data reduction pipeline. So when MUSE will become available, we will be ready to exploit the data.

References

Battaglia, G., Irwin, M., Tolstoy, E., et al. 2008, MNRAS, 383, 183
Carretta, E., Bragaglia, A., Gratton, R. G., et al. 2009, A&A, 505, 117
Gebhardt, K., Pryor, C., O'Connell, R. D., Williams, T. B., & Hesser, J. E. 2000, AJ, 119, 1268
Husser, T. O. 2012, PhD thesis, University of Göttingen
Kirby, E. N., Guhathakurta, P., & Sneden, C. 2008, ApJ, 682, 1217
Lützgendorf, N., Kissler-Patig, M., Gebhardt, K., et al. 2012, ArXiv e-prints
McLaughlin, D. E., Anderson, J., Meylan, G., et al. 2006, ApJS, 166, 249
Miocchi, P. 2007, MNRAS, 381, 103
Tolstoy, E., Irwin, M. J., Cole, A. A., et al. 2001, MNRAS, 327, 918
van den Bosch, R., de Zeeuw, T., Gebhardt, K., Noyola, E., & van de Ven, G. 2006, ApJ, 641, 852
van der Marel, R. P., Gerssen, J., Guhathakurta, P., Peterson, R. C., & Gebhardt, K. 2002, AJ, 124, 3255

Appendix A

PampelMuse – A dedicated software package for crowded field 3D spectroscopy

ABSTRACT

To automate the complicated process of deblending stellar spectra from integral field data, we developed a software package named PampelMuse, the "**P**otsdam **a**vanced **m**ulti **PSF** **e**xtraction a**l**gorithm for **Muse**". It is designed to perform the selection of the sources that are included in the deblending process, to determine the PSF and the source coordinates and finally to extract the stellar spectra. Graphical user interfaces are provided to help the user in the steps of the data analysis that require human interaction. In the following, we provide a brief description of PampelMuse.

A.1. General concept

The formalism behind our approach to perform crowded field spectroscopy was described in detail in Chapter 2 and is not repeated here. Instead, we aim to explain how we translated it into a software package that is easy to use. To design a user-friendly tool, the development of PampelMuse was guided by the following principles. (i) It should be freely available and not depend on external software that involves expensive licence fees. (ii) It should be easy to install and executable on a normal PC or laptop. (iii) It should be intuitive to use. In view of the first two principles, we considered it the best choice to write the code in *python*. A further advantage of *python* is that many powerful libraries for scientific programming are available.

The functionality of PampelMuse is split up into several subroutines that can be called from the command line. In general, the analysis of a datacube can be split up into three distinct stages: an initial stage where the deblending process is set up, the actual deblending of the spectra, and a verification stage where the results of the deblending process are inspected. However, as is shown below, the latter two stages can be iterated to improve the results. In the following, we describe these three core routines in more detail.

A.2. The source selection stage

As discussed in Chapter 2, we assume that a catalogue of sources present in the observed field of view is available. In the first step of the data analysis, the aim is to select the subset of catalogued sources that can be deblended at the spatial resolution of the datacube. To this aim, the datacube must be provided together with the input catalogue. The input catalogue should be a plain text file containing an ID, a magnitude and x- and y-coordinates. The magnitude can be provided in any filter, yet it is recommended to use a filter that covers a similar wavelength range as the datacube. The coordinates should be given in a plain reference system, such as HST/ACS pixel coordinates.

The routine will create a mock image from the catalogue. To this aim, it uses the spaxel scale of the integral field data together with an estimate of the PSF in the datacube. Therefore, the simulated image should resemble the observed field of view. A GUI is opened and the simulated image is plotted together with a whitelight image of the datacube. The GUI allows one to interactively locate the exact position of the datacube by identifying the same stars in both images. This step is illustrated in Fig. A.1. To increase the accuracy of the positions measured on the whitelight image of the datacube, the routine will calculate first and second order moments for every selected star. However, since this calculation only works for relatively bright and isolated stars that are not always available, it can be switched off. Note that the comparison between the whitelight image and the mock image created from the datacube allows the user also to check whether the assumed PSF is reasonable and whether any bright stars are missing in the catalogue.

Based on the sources that were identified via the GUI, the routine will determine an initial guess of the coordinate transformation from the catalogue to the datacube. Recall from Chapter 2 that instead of fitting the positions of individual stars, we assume that the positions of the sources in the datacube can be obtained via a transformation of the catalogued positions that is governed by 4 parameters. This transformation basically describes a rotation and a scaling followed by a shift along x and y.

Afterwards, it performs the actual source selection process. The individual stars are classified according to their brightness, expected signal-to-noise (S/N) ratio and position within the field-of-view. The classification uses the following numbering scheme.

2: A "resolved" source, i.e. a star for which an individual spectrum can be deblended
1: A "nearby" source, i.e. a source that is resolvable with respect to its brightness and expected S/N but too close to a neighbouring brighter source. Therefore, a combined spectrum will be deblended for the two sources.

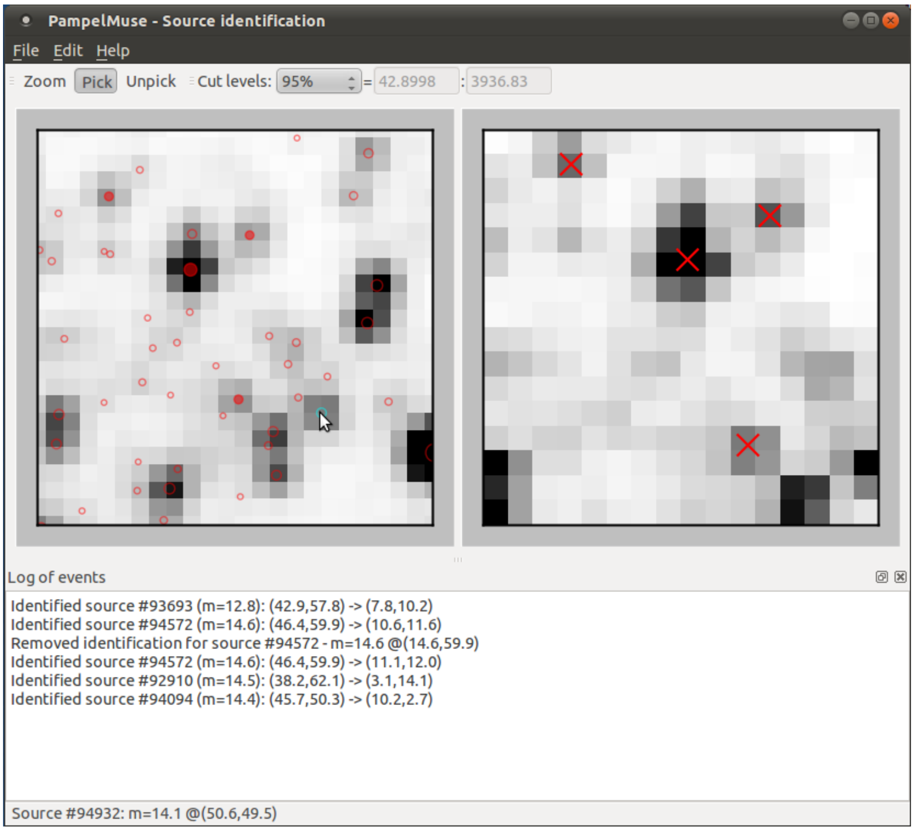

```
Identified source #93693 (m=12.8): (42.9,57.8) -> (7.8,10.2)
Identified source #94572 (m=14.6): (46.4,59.9) -> (10.6,11.6)
Removed identification for source #94572 - m=14.6 @(14.6,59.9)
Identified source #94572 (m=14.6): (46.4,59.9) -> (11.1,12.0)
Identified source #92910 (m=14.5): (38.2,62.1) -> (3.1,14.1)
Identified source #94094 (m=14.4): (45.7,50.3) -> (10.2,2.7)
```

```
Source #94932: m=14.1 @(50.6,49.5)
```

Fig. A.1. Illustration of the source identification process in PampelMuse. To obtain an initial guess of the coordinate transformation, the user interactively identifies sources in a mock image created from the input catalogue (left image) and a whitelight image of the datacube (right image). The data shown in this example is taken from one of the PMAS datacubes of M92.

0: A "grainy" source, i.e. a source for which no individual spectrum can be deblended but that contributes to the grainy structure of the unresolved light.
−1: A source that is not used in the further analysis.

The location of the individual classes in the colour magnitude diagrams of the three PMAS clusters is shown in Fig. 3.8.

In the final step, a multi-extension FITS-file, hereafter called *parameter file*, is created that contains all the information about the sources, i.e. IDs, catalogue positions or classifications, the PSF parameters and the coordinate transformation. The parameter file is used as input by the other core routines described below.

A.3. Fitting the datacube

The fitting scheme works as follows. For every component in the fit (either a resolved star or a background component), a sparse matrix is prepared of the same size as a monochromatic layer of the datacube. Using the current estimate of the coordinate transformation, the central coordinates of each resolved source on its matrix are located and based on the current parameters of the PSF model, a normalized PSF is added finally added to each matrix. Background components are treated separately. During the fit, the routine tries to minimize the mismatch between a linear combination of the matrices and the data in a layer.

To make this optimization feasible, we follow an iterative approach in which the fluxes, coordinate transformation parameters and PSF parameters are fitted individually while the other two are kept fixed at their current values. Since the optimization for the monochromatic fluxes of the resolved stars (and the background components) is a linear least squares fit, no initial guesses for the individual fluxes must be provided.

The initial guess for the parameters of the coordinate transformation are obtained in the source selection stage as described above. The initial guesses of the parameters that govern the shape of the PSF are provided by the user. The user can also control which parameters of the coordinate transformation and of the PSF are fitted. Note that the initial guesses are only used for the analysis of the very first layers that are analysed. Afterwards, the routine will create initial guesses by averaging over the results obtained in adjacent layers.

As already mentioned, every monochromatic layer of the datacube is considered separately in this process. Only the layer that is currently being analysed is loaded into memory, therefore even the analysis of datacubes with sizes similar to those that will be delivered by MUSE is feasible on a normal PC. The analysis is started on the central layer of the cube and then proceeds simultaneously to its red and blue ends.

A flowchart of the analysis is shown in Fig. A.2. The results of the fit, i.e. object spectra, the PSF model, and the coordinate transformation, will be stored in the provided parameter file.

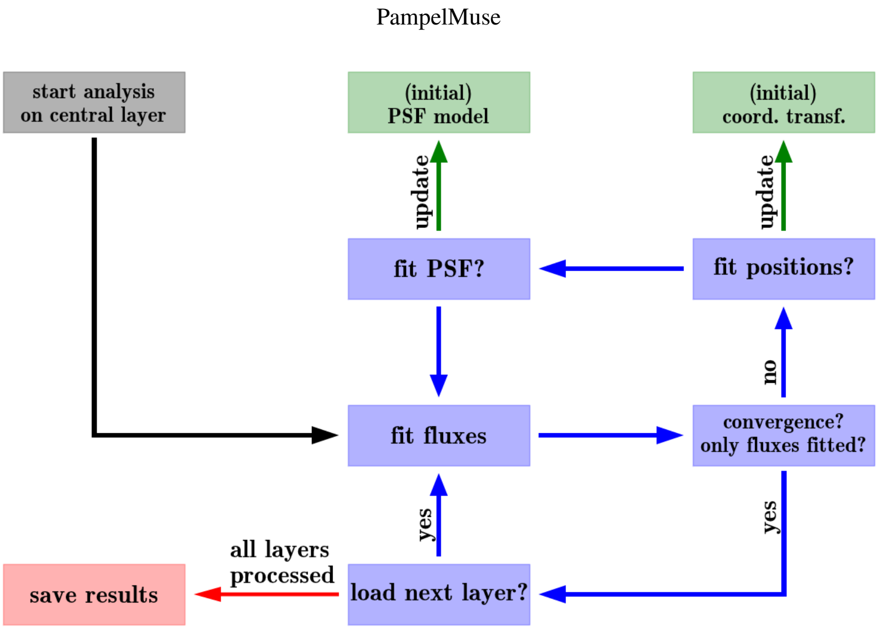

Fig. A.2. Flowchart of how PampelMuse analyses a datacube. The steps that are executed during the iterative fit of the monochromatic layers are colour-coded in blue.

A.4. Inspecting the results

After a full datacube has been successfully processed by the deblending routine of PampelMuse, a GUI can be started that serves two purposes.

(i) It allows the user to inspect the quality of the deblended spectra.
(ii) It can be used to obtain a wavelength dependent PSF model and coordinate transformation. Recall that when PampelMuse scans through a datacube and either the parameters of the PSF or the coordinate transformation are fitted, they are determined individually for every layer. With the help of the GUI, the PSF and the source coordinates can be modelled as smooth functions of wavelength using polynomials.

The spectrum viewer of PampelMuse is shown in the left panel of Fig. A.3. Besides a pure visualization of the spectra, the GUI provides the possibility to mask out parts of the wavelength range covered by the data. Those regions are then excluded from the polynomial fits to the PSF parameters or the coordinates of the stars. This is useful for example if strong undetected cosmic ray hits affect the results in some layers or telluric absorption diminishes the flux at a certain wavelength. In some cases, it might also be useful to exclude strong stellar absorption lines, such as the calcium triplet lines, because the lower flux results in a lower S/N of the observed stars and the constraints on the PSF or the positions of the stars are less stringent.

The right panel of Fig. A.3 gives an impression of the polynomial fitting process. The degree of the polynomial can be changed by the user. Furthermore, several orthogonal polynomial bases, such as Chebyshev or Legendre polynomials are available. Note that instead of fitting the parameters of the coordinate transformation, the spaxel coordinates of the individual sources are fitted. As we mentioned in Chapter 2, this is done because the parameters sometimes show correlated variations on small wavelength scales that would be washed out by a polynomial fit. The GUI allows the user to set a flag that forces the polynomial fits to all source coordinates in either x or y to have the same slope. The results of the polynomial fits can be stored in the parameter file.

A.5. A strategy for successful data analysis

To obtain optimal results with PampelMuse, we recommend the following approach. After a source list has been compiled and a parameter file has been generated, perform an initial deblending run in which the PSF parameters and the parameters of the coordinate transformation are allowed to vary. Afterwards inspect the results and replace the positions of the sources in the datacube and the parameters of the PSF with polynomial fits. Finally, perform the deblending for a second time. In this second run, all parameters except for the fluxes should be fixed. The routine will then use the wavelength-dependent PSF model and source coordinates to deblend the spectra.

A.6. Requirements

The software requires *python v2.7* or later to be installed. As it builds up on the functionality provided by standard python libraries such as *numpy*, *scipy* and *matplotlib*, those must also be available on the system. The graphical user interfaces (GUIs) are designed using *PyQt*. Some auxiliary routines also require *pyraf* to be installed. These routines can for example by used to add world coordinates to a datacube. However, when PampelMuse is started, it checks whether *pyraf* is available and if this is not the case disables the affected auxiliary routines without affecting the functionality of the core ones.

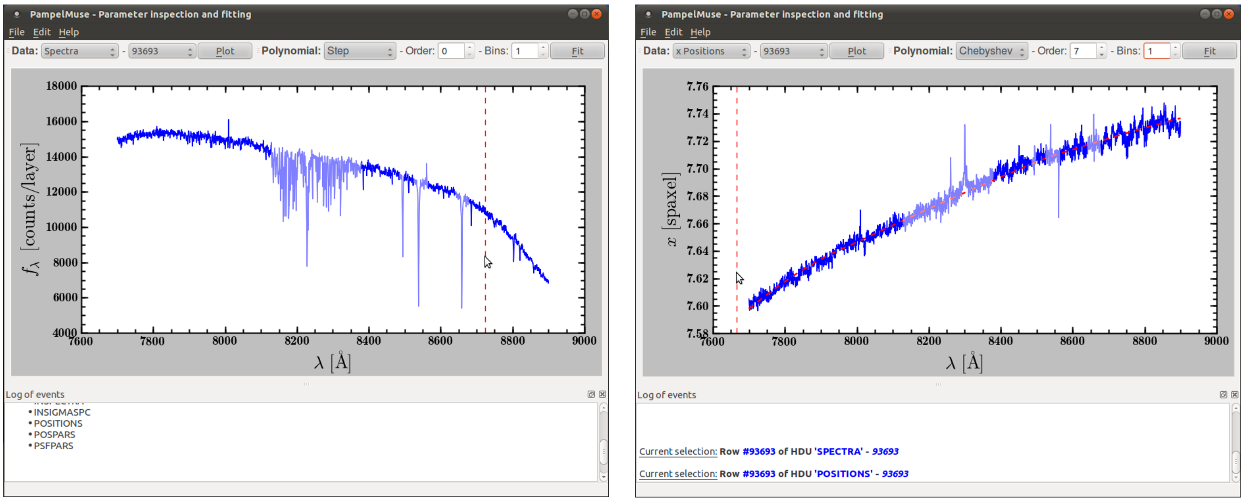

Data: Spectra - 93693 Polynomial: Step - Order: 0 - Bins: 1

- INSIGMASPC
- POSITIONS
- POSPARS
- PSFPARS

Data: x Positions - 93693 Polynomial: Chebyshev - Order: 7 - Bins: 1

```
Current selection: Row #93693 of HDU 'SPECTRA' - 93693
Current selection: Row #93693 of HDU 'POSITIONS' - 93693
```

Fig. A.3. Impressions from the GUI provided by PampelMuse to visualize the deblended spectra and to fit the spaxel coordinates of the sources or the parameters of the PSF model with polynomials. A deblended spectrum is displayed in the left panel. Regions shown in lighter blue have been masked out and are not used in the polynomial fits. In the right panel, the x coordinate of a source is shown together with a polynomial fit as a function of wavelength. The data shown is this example were obtained again from a PMAS datacube of M92.

A.7. The PampelMuse configuration file

The behaviour of the individual routines that are part of PampelMuse can be influenced by several configuration parameters. A basic configuration is stored in an XML file that can be accessed via dedicated *python* routines. The advantage of this approach is that validity checks can be carried out every time a parameter is updated. Besides this, every routine accepts a user specified configuration that can be provided via command-line arguments. In Table A.1, we give an overview of the individual configuration parameters.

Table A.1. The configuration parameters of PampelMuse

Parameter	Default value	Description
VERBOSE	2	The chattiness of PampelMuse, i.e. the amount of information that is printed out
IFU	pmas	The IFU used in the observations. This parameter is not stringly needed to run the code but it is useful to account for some instrument-specific features like the missing edges of the ARGUS IFU.
USEQT	True	Flag indicating whether Qt loaded to provide a graphical interface for the analysis. Requires a system with PyQt4. Note that currently parallelization does not work with Qt.
CPUCOUNT	1	The number of CPUs PampelMuse should use in the parallelized parts of the analysis. Set CPUCOUNT to -1 to use all available CPUs.
SMALLIFU	True	This flag defines how the determination of the PSF and the coordinate transformation is performed during the fit. If SMALLIFU is enabled, all sources are used for this purpose (recommended for IFUs with a small number of spatial pixels), otherwise bright, isolated stars are used (recommended for MUSE)
CFPCOLS	(0, 1, 2, 3)	The columns of the crowded-field photometry file that contain: ID, x position, y position and magnitude of the stars
PASSBAND	F814W	The photometric passband in which the provided magnitudes are given.
PIXSCALE	10.0	The scaling of the IFU pixels with respect to the input coordinates. Same as the IFU spaxelsize if the input coordinates are given in acrseconds. If the input coordinates are given in pixels, it is the ratio of IFU spaxelsize to input pixelsize.
APERRAD	3.0	Radius (in spaxels) used for aperture spectrophotometry. Only used if SMALLIFU=False.
APERNOIS	0.1	The maximum allowed fraction of contaminating flux within APERRAD around a star that is selected as PSF star. Only used if SMALLIFU=False.
RESLIM	16.0	An estimate of the magnitude down to which stars can possibly be resolved in the datacube.
UPDATERL	True	If UPDATERL-flag is set, PampelMuse will determine the confusion limit and update RESLIM accordingly.
CONFDENS	0.4	The confusion limit, i.e the number of stars per resultion element. A resolution element is defined as the circle with radius 0.5 × FWHM (in spaxel). Only used if UPDATERL-flag is set.
SNRCUT	3.0	The cut in expected signal-to-noise below which no sources are selected. The S/N is determined from the estimated FWHM and the provided broad band magnitudes.
BINRAD	0.3	The minimum spatial separation [measured in units of the expected FWHM of the PSF] of two resolved sources. Resolved sources with distances smaller BINRAD are combined.
USEUNRES	False	Flag indicating whether the contribution from the unresolved sources should be included as an additional component in the analysis.
UNRESBIN	2.0	Only has an effect if USEUNRES is enabled. In that case the contribution of the sources in the magnitude interval of width UNRESBIN below the confusion limit is combined in an unresolved stellar component.
GLOBSKY	True	Flag determines whether a global sky background (i.e a component with constant surface brightness over the FoV) is included in the fit.
PSFRAD	10.0	The radius out to which the PSF of a source will be defined. Should be large enough to avoid annuli of flux around the brighter sources in the residuals.
POSFIT	0	Defines how source positions are handled in the fit: 0 - Sources are fixed to their input positions; 1 - Only a global offset is fitted; 2 - A global offset and scaling are fitted; 3 - Individual positions are fitted.
PSFTYPE	moffat	The analytical profile that is used to model the PSF.
PSFPARS	(2.5, 3.0, 0.0, 0.0)	The initial values of the PSF shape parameters. The meaning of the parameters for a Moffat profile is (β, FWHM, ellipticity, position angle)
PSFFIT	6	The degree of PSF variablility, given as $\Sigma_N 2^N$, with N being the position in the PSFPARS array (starting with 1) of a PSF shape parameter that should be fitted.
MAXITER	1	The maximum number of iterations performed for a single layer. Set to 1 to skip the iteration on individual layers.

Appendix B

Radial velocity measurements in M3

ABSTRACT

We summarize the radial velocity measurements of the stars in our sample for the globular cluster M3. For our PMAS measurements and for the literature data, a one-page excerpt from the full catalogue is shown. The full data sets will be provided in the version of Chapter 3 that will be submitted for publication in *Astronomy & Astrophysics*.

B.1. Literature data

Table B.1. Archival radial velocity measurements in M3

SIMBAD ID	RA	Dec	$v_{\rm rad}$	$\sigma_{\rm v}$	$n_{\rm meas}$	variability		references	ID
	J2000	J2000	km/s	km/s		vel.	pho.		
2MASS J13420078+2810427	205.5032959	28.1785278	-145.7	0.3	5	n	n	1, 2, 3	
2MASS J13422219+2823435	205.5924988	28.3954449	-137.7	0.8	4	y	n	2, 3, 4	
2MASS J13423482+2826148	205.6450806	28.4374714	-147.5	1.1	2	y	n	1, 2	
2MASS J13424150+2819081	205.6732330	28.3189049	-146.6	0.1	8	y	y	2, 3, 4	
2MASS J13424471+2823456	205.6863403	28.3960285	-144.7	3.5	1	y	y	2	
Cl* NGC 5272 AC 968	205.5469127	28.3778075	-140.9	1.0	1	n	n	3	111888[a]
Cl* NGC 5272 GYB 618	205.5452671	28.3825870	-145.9	0.9	3	n	n	3, 4	113884[a]
Cl* NGC 5272 KUST 107	205.4992523	28.3820419	-151.1	1.4	14	y	y	3, 4	
Cl* NGC 5272 KUST 154	205.5127716	28.3695087	-143.6	0.6	2	n	n	1, 2	
Cl* NGC 5272 KUST 166	205.5141732	28.3955811	-151.2	0.9	2	n	n	3, 4	174510
Cl* NGC 5272 KUST 247	205.5280371	28.3490946	-151.4	0.6	7	y	n	3, 4	27591
Cl* NGC 5272 KUST 256	205.5289457	28.3748400	-150.0	0.6	2	n	n	1, 2	75220
Cl* NGC 5272 KUST 278	205.5317206	28.3570647	-155.8	0.4	4	n	n	2, 3, 4	26067
Cl* NGC 5272 KUST 287	205.5326883	28.3997806	-141.2	0.9	7	y	n	3, 4	166964
Cl* NGC 5272 KUST 293	205.5330529	28.3900931	-149.6	0.1	9	n	n	1, 2, 3, 4	166641
Cl* NGC 5272 KUST 300	205.5338905	28.3703472	-152.2	0.7	4	n	n	3, 4	71096
Cl* NGC 5272 KUST 308	205.5354174	28.3659042	-152.5	0.7	5	n	n	3, 4	69705
Cl* NGC 5272 KUST 315	205.5350994	28.3844633	-146.6	0.5	4	n	n	3, 4	124801
Cl* NGC 5272 KUST 325	205.5365111	28.3535048	-145.8	0.2	3	n	n	1, 2, 4	23427
Cl* NGC 5272 KUST 330	205.5363832	28.3632783	-150.8	0.6	3	n	n	3, 4	68952
Cl* NGC 5272 KUST 331	205.5363402	28.3765624	-149.7	0.5	5	n	n	3, 4	123464
Cl* NGC 5272 KUST 352	205.5372893	28.3964225	-142.6	0.6	5	n	n	3, 4	164219
Cl* NGC 5272 KUST 358	205.5381450	28.3929559	-145.2	0.8	4	n	n	3, 4	163682
Cl* NGC 5272 KUST 359	205.5384734	28.3554720	-154.7	0.4	4	y	n	2, 3, 4	22467
Cl* NGC 5272 KUST 375	205.5397491	28.3314171	-149.7	0.4	6	n	n	1, 3, 4	
Cl* NGC 5272 KUST 378	205.5396889	28.3678943	-136.4	0.6	3	n	n	3, 4	65753[a]
Cl* NGC 5272 KUST 433	205.5428551	28.4012501	-144.3	0.6	3	n	n	3, 4	160616
Cl* NGC 5272 KUST 442	205.5432885	28.3952092	-147.1	0.9	3	n	n	3, 4	160270
Cl* NGC 5272 KUST 470	205.5452873	28.3962471	-144.3	0.6	8	n	n	3, 4	159080

References. (1) Pilachowski et al. (2000), AJ, 119, 2895; (2) Soderberg et al. (1999), PASP, 111, 1233; (3) Pryor et al. (1988), AJ, 96, 123; (4) Gunn & Griffin (1979), AJ, 84, 752

Notes. Results are shown for 29 out of 179 stars. For each source the primary identifier in the SIMBAD database is provided. In cases where the star was on the footprint of our reference catalogue, we provide the corresponding ID in the last column. In those cases, we also updated the RA- and Dec-coordinates to those given in the reference catalogue. The radial velocities and their uncertainties were obtained by combination of the data of the different studies. Velocities are given relative to the cluster mean. radial velocity variables and stars included in the catalogue of photometric variables of Clement et al. (2001), AJ, 122, 2587 are flagged.

(a) The position of the source in the HST image suggests significant contamination from one or more bright neighbours.

(b) The source has no obvious counterpart in the HST data.

B.2. PMAS IFU data

Table B.2. Radial velocity measurements from our PMAS IFU data in M3

ID	RA J2000	Dec J2000	HJD days	S/N	r_{cc}	v_{rad} km/s	σ_{v} km/s	SIMBAD ID
57102	205.5488312	28.3741746	2455274.5895	9.9	7.7	5.4	6.7	
			2455274.6440	11.4	7.8	12.1	5.5	
57509	205.5483651	28.3744691	2455274.6440	7.4	3.8	-16.2	9.1	
57945	205.5479859	28.3748693	2455274.3911	24.3	19.5	-13.1	2.7	
			2455274.5895	32.8	29.2	-8.4	1.9	
			2455274.6440	49.9	29.2	-8.9	1.9	
58330	205.5477288	28.3743996	2455274.3911	7.7	7.5	-7.4	6.1	
			2455274.5895	16.9	8.0	-12.5	6.2	
			2455274.6440	23.8	17.6	-1.1	2.8	
58746	205.5474334	28.3740266	2455274.3911	7.5	5.2	7.7	7.8	
			2455274.5895	17.8	15.6	4.9	3.6	
			2455274.6440	26.8	17.6	2.0	3.1	
58782	205.5472402	28.3748338	2455274.3911	8.9	8.9	-16.9	7.2	
			2455274.5895	13.3	10.2	6.5	5.4	
			2455274.6440	19.1	15.1	-5.4	3.5	
59564	205.5465195	28.3745806	2455274.3911	25.0	18.5	-11.4	2.8	
			2455274.5895	37.0	24.4	-5.7	2.4	
			2455274.6440	47.9	28.8	-7.2	1.9	
67097	205.5386756	28.3735273	2455274.6210	17.9	13.1	15.8	4.1	
67525	205.5381769	28.3748921	2455274.6210	10.1	6.9	4.2	7.4	
67526	205.5382751	28.3746724	2455274.6210	20.1	12.6	7.9	4.5	
67885	205.5379799	28.3742677	2455274.6210	11.3	5.7	-4.8	10.4	
68228	205.5373390	28.3744242	2455274.6210	106.1	90.3	1.8	0.7	NGC 5272 610
			2455274.6713	49.3	35.1	0.9	1.6	
108046	205.5500400	28.3799628	2455273.6791	16.2	14.0	-2.9	4.1	
			2455273.7009	13.1	11.9	-11.6	4.5	
109139	205.5494714	28.3807600	2455273.6791	8.9	6.2	-8.2	7.2	
109167	205.5493552	28.3817076	2455273.5536	24.1	20.6	1.2	2.5	
			2455273.6791	38.7	30.9	0.6	1.7	
			2455273.7009	16.9	12.3	-1.4	3.8	
109381	205.5487392	28.3749753	2455274.3911	24.4	21.9	5.7	2.4	
			2455274.5895	36.9	32.9	7.7	1.7	
			2455274.6440	52.3	35.1	8.4	1.5	
109384	205.5488310	28.3755389	2455274.5895	9.1	6.3	7.2	7.7	
			2455274.6440	14.6	13.1	-0.9	3.6	
109573	205.5489239	28.3796828	2455273.5536	8.6	7.6	-11.1	6.4	
			2455273.6791	21.0	15.6	-11.2	3.2	
			2455273.7009	8.5	6.7	-8.0	7.8	
109584	205.5489682	28.3798702	2455273.5536	9.8	8.2	-6.2	5.8	
			2455273.6791	23.1	18.1	-6.1	3.1	
			2455273.7009	8.5	7.7	-21.7	5.9	
109609	205.5488128	28.3808053	2455273.4761	10.5	11.4	-8.0	4.4	NGC 5272 807
			2455273.5536	76.8	62.8	2.2	0.9	
			2455273.6791	87.0	77.1	1.5	0.7	
			2455273.7009	60.7	56.1	0.9	1.0	
109610	205.5490214	28.3805940	2455273.5536	21.5	17.3	20.1	3.1	
			2455273.6791	41.8	30.3	21.5	1.9	
			2455273.7009	17.5	17.8	27.4	2.9	
109920	205.5485366	28.3766581	2455273.3960	13.6	7.0	-5.8	6.8	
			2455273.4481	20.7	19.3	-4.3	2.9	
			2455273.4993	21.3	18.0	-12.7	2.9	

Notes. Results are shown for 22 out of 50 stars. The first column gives the identifier of each star in the photometric catalogue of Anderson et al. (2008), AJ, 135, 2055. RA- and Dec- coordinates are given in decimal degrees and are also taken from Anderson et al (2008). The velocities are measured relative to the template that was used in the analysis. Uncertainties are estimated using equation Eq. 3.2 and applying the correction found in Fig. 3.15. SIMBAD identifiers are only provided for sources with radial velocity measurements available in the literature.

[(a)] The identification of the star is difficult due to the large positional errors in the ground-based imaging data.

[(b)] Stars with identifiers > 900000 were added from our WFPC2 data.

[(v)] The star is included in the catalogue of variable stars of Clement et al. (2001), AJ, 122, 2587.

Appendix C

Radial velocity measurements in M13

ABSTRACT

We summarize the radial velocity measurements of the stars in our sample for the globular cluster M13. Again, a one-page excerpt from the full catalogue is shown for the PMAS data and the literature values. The full data sets will be provided in the version of Chapter 3 that will be submitted for publication in *Astronomy & Astrophysics*.

C.1. Literature data

Table C.1. Archival radial velocity measurements in M13

SIMBAD ID	RA	Dec	v_{rad}	σ_{v}	n_{meas}	variability		references	ID
	J2000	J2000	km/s	km/s		vel.	pho.		
2MASS J16404298+3627418	250.1790924	36.4616318	-245.2	0.2	4	n	n	1, 3, 4	
2MASS J16405637+3622185	250.2349091	36.3718071	-250.3	0.3	4	n	n	1, 2, 3	
2MASS J16410260+3626158	250.2608643	36.4377251	-243.4	0.3	5	n	n	1, 2, 3	
2MASS J16410507+3628208	250.2711487	36.4724579	-242.4	0.4	3	n	n	1, 3	
2MASS J16410615+3625227	250.2756500	36.4229736	-247.5	0.2	4	n	n	1, 2, 3	
2MASS J16410648+3628136	250.2770386	36.4704704	-249.6	0.2	5	n	n	1, 3, 4	
2MASS J16410966+3626448	250.2902832	36.4458008	-256.8	0.1	4	n	n	1, 2	
2MASS J16411359+3630333	250.3066406	36.5092773	-242.9	0.2	4	n	n	1, 2, 3	
2MASS J16411389+3625026	250.3078918	36.4174118	-249.0	0.2	4	n	n	1	
2MASS J16411521+3629240	250.3134155	36.4900017	-251.4	0.3	3	y	n	1, 3	
2MASS J16411550+3631028	250.3146210	36.5174561	-242.2	0.3	3	n	n	1	
2MASS J16411570+3627500	250.3154449	36.4639091	-249.3	0.3	5	n	n	1, 2, 3	
2MASS J16411583+3633177	250.3159790	36.5549393	-245.6	0.3	5	n	n	1, 2, 3	
2MASS J16411700+3625479	250.3208618	36.4299889	-242.4	0.2	8	n	n	1, 2, 3, 4	
2MASS J16411772+3629298	250.3238525	36.4916382	-239.2	0.2	3	n	n	1, 3	
2MASS J16411827+3620496	250.3261261	36.3471298	-245.3	0.4	5	n	n	1, 2, 3	
2MASS J16411831+3626407	250.3262939	36.4446640	-245.5	0.4	3	n	n	1, 3	
2MASS J16411863+3628434	250.3276367	36.4787254	-250.4	0.4	2	n	n	1	
2MASS J16411882+3628232	250.3284302	36.4731369	-239.5	0.3	2	n	n	1	
2MASS J16411923+3627144	250.3301239	36.4540215	-246.3	0.2	3	n	n	1, 3	
2MASS J16411983+3624381	250.3326263	36.4106102	-257.0	0.3	8	n	n	1, 2, 3, 4	
2MASS J16412353+3630173	250.3480682	36.5048180	-238.6	0.6	9	y	n	1, 3, 4	
2MASS J16412408+3625306	250.3503571	36.4251823	-245.9	0.9	11	y	y	1, 2, 3, 4	
2MASS J16412452+3630492	250.3522034	36.5136757	-234.8	0.6	2	y	n	1	
2MASS J16412464+3625449	250.3526611	36.4291649	-233.8	0.5	5	n	n	2, 3, 4	
2MASS J16412677+3623256	250.3615417	36.3904495	-253.9	0.1	2	n	n	1	
2MASS J16412684+3625286	250.3618317	36.4246292	-243.4	0.2	1	n	n	1	
2MASS J16412707+3626508	250.3627930	36.4474525	-249.1	0.1	2	n	n	1	
2MASS J16412709+3628002	250.3628845	36.4667473	-237.9	0.6	7	y	y	1, 2, 3, 4	
2MASS J16412729+3632226	250.3637390	36.5396194	-244.3	0.3	5	n	n	1, 3	
2MASS J16412735+3629304	250.3639832	36.4918022	-237.8	0.3	2	n	n	1	
2MASS J16412815+3625274	250.3673096	36.4242973	-248.5	0.4	5	n	n	1, 3, 4	
2MASS J16412825+3630017	250.3677216	36.5004807	-243.5	0.2	3	n	n	1, 3	
2MASS J16412826+3623005	250.3677826	36.3834839	-242.7	0.1	5	n	n	1, 3	
2MASS J16412837+3627038	250.3682098	36.4510574	-253.5	0.6	2	n	n	3, 4	

References. (1) Mészáros et al. (2009), AJ, 137, 4282; (2) Pilachowski et al. (2000), AJ, 119, 2895; (3) Soderberg et al. (1999), PASP, 111, 1233; (4) Lupton et al. (1987), AJ, 93, 1114

Notes. The same as Table B.1 for the literature data collected in M13. Again, only part of the final data set (35 out of 274 stars) is shown.

C.2. PMAS IFU data

Table C.2. Radial velocity measurements from our PMAS IFU data in M13

ID	RA J2000	Dec J2000	HJD days	S/N	r_{cc}	v_{rad} km/s	σ_v km/s	SIMBAD ID
52895	250.4248404	36.4583785	2455691.5874	7.4	5.4	-12.8	5.5	
52945	250.4248422	36.4598975	2455691.5874	8.4	5.8	-6.3	5.1	
53254	250.4243537	36.4586614	2455690.6477	7.3	3.8	0.1	7.7	
			2455691.5042	7.4	5.4	-16.9	5.9	
			2455691.5874	10.9	7.6	-11.5	3.9	
			2455751.5465	9.0	6.4	13.2	6.2	
53255	250.4242378	36.4585982	2455691.5874	7.0	4.1	8.2	9.2	
53587	250.4236978	36.4581803	2455690.6477	8.0	3.6	-3.9	8.3	
			2455691.5042	7.4	6.2	-0.7	5.1	
			2455691.5874	9.4	6.3	5.4	6.0	
53611	250.4236954	36.4591904	2455690.6477	11.3	6.5	-13.6	5.1	
			2455691.5042	10.1	8.8	-20.6	3.8	
			2455691.5874	12.9	9.2	-7.6	3.9	
53863	250.4233272	36.4577335	2455690.6477	12.7	7.0	-10.0	5.2	
			2455691.5042	12.7	13.5	-13.6	2.8	
			2455691.5874	18.1	13.0	-16.2	2.8	
			2455751.4667	7.7	7.9	-18.1	4.2	
			2455751.5465	11.1	15.1	-14.6	2.5	
54239	250.4231571	36.4590722	2455690.6477	7.0	4.4	-10.3	7.3	
			2455691.5874	8.5	6.9	-11.8	5.5	
54607	250.4225361	36.4576307	2455690.4685	18.2	6.8	-7.4	5.9	
			2455690.5367	32.8	25.8	-0.6	1.7	
			2455690.6477	39.9	20.1	-2.2	2.1	
			2455691.5042	38.8	32.6	-3.3	1.3	
			2455691.5874	47.8	34.3	-2.9	1.2	
			2455750.4719	23.8	19.0	-4.6	2.3	
			2455750.5423	39.6	36.8	-3.7	1.2	
			2455751.4667	27.7	35.6	-3.2	1.1	
			2455751.5465	23.3	24.8	-2.0	1.6	
54624	250.4223685	36.4584196	2455690.5062	7.1	3.6	-2.7	8.9	
54955	250.4222255	36.4566965	2455690.4685	60.3	34.5	-0.0	1.4	
			2455690.5367	55.3	37.7	-0.6	1.2	
			2455750.4719	51.9	44.2	-1.1	0.9	
			2455750.5423	47.5	48.7	-0.9	0.9	
54978	250.4219552	36.4578029	2455690.4685	39.6	27.5	6.9	1.6	
			2455690.5367	27.4	16.4	5.6	2.6	
			2455750.4719	26.9	25.3	4.2	1.6	
			2455750.5423	20.7	20.0	6.0	2.0	
55001	250.4219846	36.4583376	2455690.4685	7.2	4.5	8.7	9.6	
55037	250.4220386	36.4597360	2455690.4398	13.8	10.7	-2.5	3.7	
			2455690.5062	15.4	7.9	5.3	4.9	
			2455750.4358	9.5	9.0	-8.6	4.5	
			2455750.5093	9.8	8.5	-3.6	4.0	
55328	250.4216518	36.4574363	2455690.4685	52.9	38.1	-12.7	1.1	
			2455690.5367	37.8	25.5	-10.4	1.6	
			2455750.4719	37.1	43.2	-11.7	0.9	
			2455750.5423	30.4	35.1	-11.0	1.1	
55375	250.4217495	36.4590271	2455690.5062	11.5	4.6	-9.3	7.0	
55376	250.4218740	36.4590146	2455690.4398	28.1	24.6	0.4	1.7	
			2455690.5062	27.2	22.4	1.4	1.9	
			2455690.5595	28.0	18.1	-0.7	2.4	
			2455750.4358	42.0	37.1	-3.3	1.1	
			2455750.5093	37.9	37.9	-2.3	1.1	
55692	250.4213923	36.4563853	2455690.4685	111.4	68.5	12.2	0.7	Cl* NGC 6205 CGY 4982[v]
			2455690.5367	106.9	65.2	11.1	0.7	
			2455750.4719	122.0	55.3	9.6	0.7	
			2455750.5423	97.7	52.4	9.4	0.8	

Notes. The same as Table B.2 for the cluster M13. Results are shown for 18 out of 80 stars in the final data set.

Appendix D

Radial velocity measurements in M92

ABSTRACT

We summarize the radial velocity measurements of the stars in our sample for the globular cluster M92. As for M3 and M92, a one-page excerpt from the full catalogue is shown for the PMAS data and the literature values. The full data sets will be provided in the version of Chapter 3 that will be submitted for publication in *Astronomy & Astrophysics*.

D.1. Literature data

Table D.1. Archival radial velocity measurements in M92

SIMBAD ID	RA	Dec	$v_{\rm rad}$	$\sigma_{\rm v}$	$n_{\rm meas}$	variability		references	ID
	J2000	J2000	km/s	km/s		vel.	pho.		
2MASS J17163427+4307363	259.1428223	43.1267624	-120.3	0.1	6	n	n	1, 2, 3	
2MASS J17163748+4306155	259.1561890	43.1043282	-118.4	0.1	7	y	n	1, 2, 3	
2MASS J17163772+4308411	259.1571960	43.1447678	-125.3	0.2	6	n	n	1, 2, 3	
2MASS J17164330+4304161	259.1804504	43.0711517	-121.3	0.1	8	n	n	1, 2, 3	
2MASS J17164395+4307318	259.1831360	43.1255150	-107.8	0.4	7	y	n	1, 2, 3	
2MASS J17164791+4306160	259.1996460	43.1044464	-127.7	0.4	6	n	n	1, 2	
2MASS J17164867+4306240	259.2027893	43.1066933	-112.3	0.5	3	n	n	1, 2	
2MASS J17165035+4305531	259.2097778	43.0980873	-118.4	0.2	5	n	n	1, 2, 3	
2MASS J17165118+4306434	259.2132568	43.1120758	-116.0	0.1	5	n	n	1, 2, 3	
2MASS J17165187+4306371	259.2161560	43.1103249	-125.2	0.1	4	n	n	1, 2, 3	
2MASS J17165284+4303294	259.2201843	43.0581894	-119.8	0.2	8	n	n	1, 2	
2MASS J17165471+4310263	259.2279968	43.1739731	-119.3	0.2	6	n	n	1, 2	
2MASS J17165519+4301588	259.2300110	43.0330238	-125.1	0.2	7	n	n	1, 2	
2MASS J17165551+4305034	259.2313232	43.0842972	-118.7	0.1	6	n	n	1, 2, 3	
2MASS J17165601+4304478	259.2333984	43.0799675	-123.5	0.2	4	n	n	1, 2	
2MASS J17165652+4310314	259.2355347	43.1754112	-125.7	0.3	3	n	n	1, 2	
2MASS J17165658+4307229	259.2357788	43.1230545	-122.5	0.2	4	n	n	1, 2	
2MASS J17165738+4307236	259.2391052	43.1232491	-124.3	0.1	4	n	n	1, 2	
2MASS J17165772+4314115	259.2405396	43.2365417	-119.5	0.0	29	n	n	1, 2, 3	
2MASS J17165883+4315116	259.2451477	43.2532310	-125.0	0.2	6	y	n	1, 2, 3	
2MASS J17165912+4308238	259.2463170	43.1400002	-117.2	0.4	3	n	n	1	113080
2MASS J17165963+4313309	259.2484741	43.2252502	-116.5	0.1	2	n	n	2	
2MASS J17165967+4301058	259.2486572	43.0182915	-125.0	0.1	9	n	n	1, 2, 3	
2MASS J17170033+4311478	259.2513733	43.1966171	-117.6	0.1	5	n	n	1, 2, 3	
2MASS J17170043+4305117	259.2518311	43.0865860	-127.9	0.6	6	y	n	1, 2, 3	
2MASS J17170081+4310251	259.2533875	43.1736641	-120.2	0.2	4	n	n	1, 2, 3	
2MASS J17170394+4302031	259.2664490	43.0342026	-123.5	0.1	7	n	n	1, 2	
2MASS J17170398+4313579	259.2666016	43.2327538	-124.1	0.3	1	n	n	2	
2MASS J17170577+4305456	259.2740479	43.0960236	-131.4	0.1	3	n	n	1, 2	
2MASS J17170588+4310171	259.2745056	43.1714439	-118.6	0.1	4	n	n	1, 2	
2MASS J17170647+4306029	259.2769775	43.1008186	-116.6	0.3	2	n	n	1, 2	
2MASS J17170722+4310341	259.2800903	43.1761513	-124.4	0.3	1	n	n	2	
2MASS J17171122+4310102	259.2967755	43.1695384	-114.9	0.2	3	n	n	1, 2	139545
2MASS J17171140+4306027	259.2975464	43.1007576	-122.0	0.2	4	n	n	1, 2, 3	
2MASS J17171199+4312252	259.2999878	43.2070274	0.0	0.0	0	n	n		

References. (1) Drukier et al. (2007), AJ, 133, 1041; (2) Mészáros et al. (2009), AJ, 137, 4282; (3) Pilachowski et al. (2000), AJ, 119, 2895

Notes. The same as Table B.1 for the literature data collected in M92. Results are shown for 35 out of 312 stars in the sample.

D.2. PMAS IFU data

Table D.2. Radial velocity measurements from our PMAS IFU data in M92

ID	RA J2000	Dec J2000	HJD days	S/N	$r_{\rm cc}$	$v_{\rm rad}$ km/s	$\sigma_{\rm v}$ km/s	SIMBAD ID
48531	259.2821070	43.1348212	2455837.3898	29.7	22.9	-4.0	1.5	
48781	259.2819538	43.1315117	2455753.4781	46.1	38.9	-7.7	0.9	
			2455753.5467	40.0	35.0	-9.9	0.9	
48902	259.2816791	43.1346331	2455753.4393	89.7	72.9	-1.2	0.5	
			2455753.5109	105.6	95.7	-0.5	0.4	
			2455837.3898	72.9	59.3	0.4	0.6	
48907	259.2816566	43.1350094	2455753.5109	11.1	9.6	0.1	3.3	
			2455837.3898	16.7	14.2	-1.7	2.2	
48920	259.2820419	43.1351904	2455753.5109	10.8	9.6	-7.0	3.3	
			2455837.3898	11.7	10.6	-5.6	2.8	
48926	259.2819840	43.1356933	2455837.3898	15.5	10.3	4.1	3.2	
48929	259.2816142	43.1354485	2455753.4393	12.0	9.7	-10.7	3.5	
			2455753.5109	11.3	8.2	-12.8	3.6	
			2455837.3898	16.9	11.8	-8.6	2.2	
48930	259.2817678	43.1354285	2455753.4393	10.9	9.8	-4.2	2.8	
			2455753.5109	20.3	19.8	-2.9	1.6	
			2455837.3898	28.3	21.4	-2.7	1.6	
49185	259.2811774	43.1320224	2455753.4781	44.2	30.7	14.4	1.1	
			2455753.5467	39.8	27.8	13.3	1.1	
49298	259.2811997	43.1350149	2455753.4393	33.1	14.6	19.3	2.3	Cl* NGC 6341 SAW V30[a]
			2455753.5109	43.5	16.5	15.5	2.3	
			2455837.3898	22.3	12.3	24.9	2.9	
49299	259.2811313	43.1349593	2455837.3898	8.6	8.8	16.8	3.4	
49307	259.2812827	43.1353974	2455837.3898	10.0	8.4	1.3	4.1	
49316	259.2814285	43.1355207	2455753.4393	44.0	45.6	-0.6	0.7	
			2455753.5109	54.7	37.3	-1.2	0.9	
			2455837.3898	64.9	55.0	-0.3	0.6	
49618	259.2808685	43.1326772	2455753.4781	8.0	8.0	14.8	3.5	
49647	259.2810405	43.1336000	2455753.4781	23.3	21.7	6.1	1.4	
			2455753.5467	25.6	27.3	5.2	1.1	
49713	259.2807988	43.1351013	2455753.4393	17.0	20.8	16.5	1.4	
			2455753.5109	21.0	18.6	10.5	1.7	
			2455837.3898	25.6	22.5	14.6	1.4	
49723	259.2810665	43.1355458	2455753.5109	7.4	5.2	13.1	6.4	
			2455837.3898	10.4	6.6	2.6	4.0	
49735	259.2810693	43.1361065	2455753.4393	13.6	14.8	2.5	2.0	
			2455753.5109	16.2	17.2	1.7	1.8	
			2455837.3898	22.8	17.4	5.7	1.7	
49737	259.2809979	43.1357682	2455753.4393	11.6	10.6	4.4	2.8	
			2455753.5109	14.7	15.4	1.8	2.0	
			2455837.3898	23.9	18.5	2.9	1.8	
50006	259.2803689	43.1320622	2455753.4781	29.4	30.8	1.4	1.0	
			2455753.5467	25.1	19.1	3.1	1.6	
50025	259.2805819	43.1324838	2455753.4781	19.1	17.3	-5.3	1.7	
			2455753.5467	17.8	13.7	-9.5	2.2	
50030	259.2803308	43.1326740	2455753.4781	46.1	39.4	7.0	0.8	
			2455753.5467	41.2	34.8	6.0	0.9	
50061	259.2804565	43.1337103	2455753.5467	7.6	6.4	-5.3	4.1	
50105	259.2805105	43.1348443	2455753.4393	20.9	18.7	1.0	1.6	
			2455753.5109	25.4	20.1	-3.7	1.5	
			2455837.3898	34.3	23.0	3.0	1.3	
50133	259.2804034	43.1357367	2455753.5109	10.1	10.1	3.7	2.8	
			2455837.3898	9.6	9.2	3.6	3.5	
50433	259.2798765	43.1333297	2455753.4781	54.5	56.7	13.6	0.6	
			2455753.5467	49.6	48.5	14.1	0.6	

Notes. The same as Table B.2 for the cluster M92. Results are shown for 26 out of 77 stars in the final data set.

Appendix E

Sky subtraction in the PMAS data of M3

ABSTRACT

The analysis of the unresolved stellar component in the globular cluster M3 was significantly hampered by telluric line emission. As no observations of blank sky are available for this cluster, we could not subtract the sky prior to the data analysis. Instead, we tried to implement a sky subtraction in the deblending process. It is based on the idea that the unresolved stellar sources should form a grainy structure across the field-of-view while the sky should be entirely flat.

E.1. Idea

The stars in a datacube can roughly be divided into three categories: resolved stars, stars just below the confusion limit and stars far below the confusion limit. After the resolved ones have been subtracted, the stars just below the confusion limit will still create a grainy structure across the field of view. Even though these stars are too faint to be resolved individually, we can still collect many informations for them. The fit to the resolved stars provides us with the PSF and the coordinate transformation that can be used to pin-point their spatial position in the datacube. Finally, we can use the available magnitudes to estimate their relative fluxes and to model the graininess across the field of view. We therefore included two background components when running the deblending software, one that was spatially flat and one "grainy", composed of the stars within two magnitudes below the confusion limit. The sky emission should contribute only to the former component because it should not vary on spatial scales as small as the PMAS field of view. Note, however, that this component will also include stellar light, emitted by the stars more than two magnitudes fainter than the confusion limit.

E.2. Results

We compare the spectra of the two unresolved components obtained in the analysis of a central datacube of M3 in the left panel of Fig. E.1. It is reassuring to see that barely any contamination from telluric lines is visible in the spectrum of the "grainy" component.

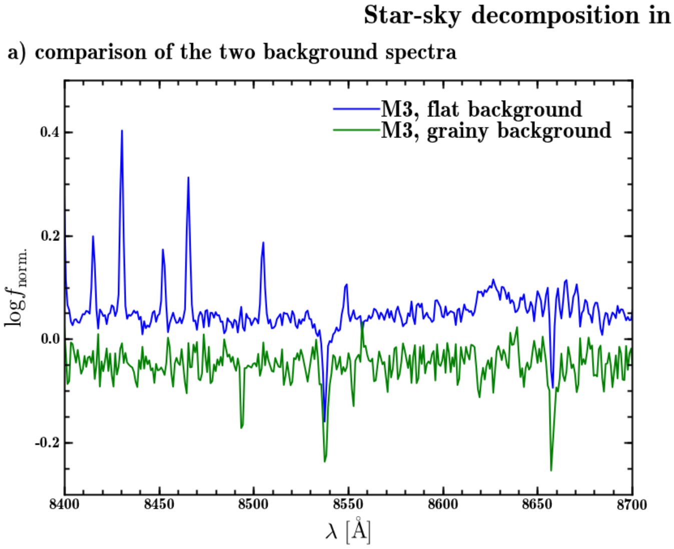

Fig. E.1. (a) Comparison of the two spectra obtained for the grainy and the flat background component, respectively, in a central datacube of M3. The green line depicts the spectrum obtained for the stars within 2 mag below the confusion limit. Stars even fainter and the night sky produce the spectrum shown as a blue line. Both spectra are normalized, but for clarity, vertical shifts have been applied. (b) The normalized cross-correlation function of the two spectra, calculated for the continuum around the calcium triplet lines. The x-axis corresponds to the shift between the spectra in spatial pixels.

Unfortunately, the spectra of the two unresolved components cannot be deblended at a sufficient signal to noise (S/N). In Chapter 2 we discussed the case of two stars with a mutual distance that is significantly smaller than the resolution of the data, i.e. the FWHM of the PSF. In such a case, the PSF matrices of the stars used in the deblending algorithm are almost identical. For this reason, the outcome of the fit will mainly depend on the sum of the two fluxes but not strongly on their ratio. The two spectra are deblended with strong anticorrelated noise because in the fit to each monochromatic layer, a certain amount of flux will be shuffled back and forth. The effect is similar for the separation of the two background components. The graininess caused by the stars below the confusion limit is weak (after all, that is what we are trying to achieve by deblending as many bright stars as possible) and the contrast to the flat background component is low. That this does indeed lead to anticorrelated noise is demonstrated in the right panel of Fig. E.1, where the cross-correlation function of the two background spectra in the continuum around the calcium triplet is shown. A strong negative spike at zero pixels offset indicates a significant anticorrelation.

Another factor that limits the S/N in the grainy background spectrum is that a lot of stellar light is still included in the flat background component, as can be seen from the presence of calcium lines in the spectrum. It is coming from stars far below the confusion limit. Thus, with the currently available data we cannot obtain spectra of the unresolved stellar component at a sufficient S/N in M3 for a kinematical analysis of the unresolved light. We emphasize that this is not caused by an issue with our data analysis but by the limitations of the data we currently have available.

Acknowledgements

There are many people that I would like to thank for helping me to get to the point where I am now – writing the acknowledgements on the last page of a finished thesis on the evening before the day I hand it in.

First of all, I am very grateful to my supervisor Lutz Wisotzki who has been an immeasurably great help for the 4 years of my thesis. I have benefited in so many ways from working together with him over such a long time, scientifically as well as personally. Without his guidance, support and countless advices I could not have finished this work. We managed to write successful observing proposals, publish a paper and finally complete a thesis on a science topic we both were no experts in some years ago. I think this accounts for an excellent supervisor!

Another person that deserves my special thanks is Martin Roth whose contribution to starting this project and bringing it to a successful end can hardly be overestimated. Not only was he largely responsible for the successful proposal that founded this PhD project, he also gave me the possibility to observe "my" globular clusters with PMAS. Additionally, his seemingly inexhaustible knowledge about integral field spectroscopy was extremely valuable for me.

I want to thank my colleagues from the AIP who have supported me during the different stages of this work. There is Andreas Kelz, whose knowledge about PMAS rivals that of Martin. Christer Sandin and Peter Weilbacher have been a tremendous help in reducing the PMAS data. I am grateful to Olivier Schnurr for sharing his knowledge about star clusters and polishing our observing proposals. Joris Gerssen has been a great help with his expertise on stellar dynamics. Finally, I profited a lot from discussions with Jakob Walcher about the analysis of the unresolved stellar light.

I am grateful to all the members of the Galaxies' group, past and present. Over the 4 years of my PhD, I have experienced help by so many people from our group that it is probably impossible to mention all of them and not forget about one or two. However, I should not forget to mention Josie Kerutt who helped me a lot with the MUSE simulations, Tanya Urrutia and Christian Herenz for taking the time to proofread parts of my thesis, and Andreas Schulze who guided us safely through Beijing last summer. My special thanks go to my long-time office mates Daniel Kupko and Bernd Husemann who endured me for such a long time. Bernd, I will definitively miss the daily coffee!

Some people from other institutes have contributed to this this thesis and I really appreciate their help. First of all, I want to thank Tim-Oliver Husser and Stefan Dreizler from Göttingen. Working together with them was a very valuable experience over the past years and will surely continue to be like this in the future. The exchange with Tim-Oliver about extracting every bit of information out of a datacube helped me a lot in finishing this thesis. Some of the work of this thesis would also not have been possible without contributions from the MUSE consortium, especially by Roland Bacon and Eric Emsellem. I am also grateful to Roeland van der Marel for sharing his Jeans modelling code.

Writing a PhD thesis is never easy, but sometimes it can be very tough. Over the last 4 years, I often got the impression that I spend too much time working and forget about what is really important in life. For this reason, the final sentences of this thesis are reserved my girlfriend Elly McGill and my family, in particular my parents Petra and Friedhelm Kamann. None of the work I carried out and wrote about would have been possible if it wasn't for their wonderful support and their countless encouragements. I cannot thank you enough for this!